Multiple Volume Scattering in Random Media and Periodic Structures with Applications in Microwave Remote Sensing and Wave Functional Materials

by

Shurun Tan

A dissertation submitted in partial fulfillment
of the requirements for the degree of
Doctor of Philosophy
(Electrical Engineering)
in the University of Michigan
2017

Doctoral Committee:

Professor Leung Tsang, Chair
Associate Research Scientist Roger De Roo
Professor Anthony Grbic
Associate Professor Dragan Huterer
Professor Kamal Sarabandi

To my family,
With love and gratitude.

ACKNOWLEDGEMENTS

I would like to express my sincere gratitude towards my research advisor, Prof. Leung Tsang, whose talent and enthusiasm has inspired me to devote myself into the path of seeking truth and knowledge. I learned from him how to analyze a problem from the first physical principle, and to move upon a solution / conclusion based on careful logical deduction, experienced mathematical derivation, and genuine physical insights. Those following chapters are merely applications and testimonies of this general methodology. I thank for his mentorship and guidance. It is through answering his harsh questions that I learned to question and defend myself, and to argue my own viewpoint and to explain it to others. I thank for his training in writing, in making a presentation, and in choosing a topic. I thank for his support in building up my research career. I owe my deepest respect to him.

I would also thank Prof. Kamal Sarabandi, Prof. Anthony Grbic, Prof. Dragan Huterer and Dr. Roger De Roo for serving in my dissertation committee and providing valuable suggestions to improve the thesis.

I would like to thank the two universities, University of Washington and University of Michigan, that I have spent my years in pursing my PhD degree. They offer me complementary perspectives. The beautiful mountain view of the Seattle campus made me fall in love with nature and art. The quiet, friendly, and enthusiastic Ann Arbor inspires my imagination in the scientific and engineering world. I treasure for my life those friends I met and got acquainted.

I feel indebted to the scientific community to which I belong. The projects supported me financially, enriched my life and mind, and the researchers offered me an agreeable friendship rooted in similar scientific goals and interests. The problems and questions faced and raised in these communities are the sources of inspirations. Thank for all those scientists and engineers that shared with me their insightful thoughts, invaluable data, and incentive encouragements. To name a few, this includes Dr. Chuan Xiong from the Institute of Remote Sensing and Digital Earth, Chinese Academy of Sciences, Dr. Xiaolan Xu, Dr. Seung-Bum Kim, Dr. Simon H. Yueh and Dr. Son. V. Nghiem, from Jet Propulsion Laboratory, Dr. Kung-Hau Ding from the Air Force Research Laboratory, Dr. Juha Lemmetyinen from the Finnish Meteorological Institute, Prof. Joel T. Johnson, Prof. Kenneth C. Jezek, Prof. Michael Durand, Dr. Mustafa Aksoy and Dr. Yuna Duan from Ohio State University, Dr. Marco Brogioni and Dr. Giovanni Macelloni from the "Nello Carrara" Institute of Applied Physics (IFAC) of the National Research Conncil (CNR), Italy, Dr. Ludovic Brucker, Dr. Do Hyuk Kang, and Dr. Edward Kim from the Goddard Space Flight Center, Prof. Hans-Peter Marshall from the Boise State University, Dr. Henning Lowe and Dr. Martin Proksch from the WSL Institute for Snow and Avalanche Research SLF, Switzerland, and Dr. Joshua King and Chris Derksen from Environment and Climate Change Canada.

I won't let my emotion go unless I mention the names of those closest colleagues and friends who sit beside me and argue with me inexhaustibly about Maxwell's equations and the meaning of life. They really helped me a lot in shaping my ideas and in supporting me for lots of tedious data analysis. Those includes, incompletely, for those who have been in our research group, Dr. Tien-Hao Liao, Dr. Wenmo Chang, Dr. Xin Chang, Xudong Li, Chenxin Su, Huanting Huang, Tianlin Wang, Tai Qiao, Jiyue Zhu, Haokui Xu, Weihui Gu, Mohammadreza Sanamzadeh, and Maryam Salim; and for those RadLab-mates, just to name a few, Dr. Jiangfeng Wu, Dr. Yang Liu,

Dr. Adib Nashashibi, Dr. Leland Pierce, Francesco Foglia Manzillo, Mostafa Zaky, Mohammad Mousavi, Mani Kashanianfard, Zhanni Wu, Xiuzhang Cai, Han Guo, Weitian Sheng, and Shuo Huang. I appreciate all the helps I received from all the RadLab and ECE friends, faculties and staffs (especially Jennifer Feneley), for their friendship, and for their help to improve my knowledge, and to make every day and every travel as smooth as it could be.

Among the many friendships, I would especially mention my former advisor Prof. Tie Jun Cui, who mentored me when I was a master student. His envisioning that my one-year exchange program at University of Houston would certainly embark more is proved true. I am grateful for his constant interests and encouragements and supports in my personal development.

Last but not least, I am mostly grateful to the love I received from my family. Without the love and education from my father, my mother, my elder brother, and my grandparents, nothing is possible. I am so grateful to my two clever and young nieces who are always willing to hear me about my experiences. There is so much I am deeply indebted to … but I would close it by presenting my thesis to my beloved wife, Aili, with her love, support, and great sacrifice, these words get their chances to flow.

Shurun Tan

November 11, 2016

Ann Arbor

TABLE OF CONTENTS

LIST OF TABLES

LIST OF FIGURES

ABSTRACT

The objective of my research is two-fold: to study wave scattering phenomena in dense volumetric random media and in periodic structures. For the first part, the goal is to use the microwave remote sensing technique to monitor the environmental status of our Earth including water sources and global climate change. Towards this goal, I study the microwave scattering behavior of snow and ice sheet. For snowpack scattering, I have extended the traditional dense media radiative transfer (DMRT) approach to include the cyclical terms in the Feynman diagram. The cyclical correction gives rise to backscattering enhancement. This extension enables the theory to model combined active and passive observations of snowpack using the same set of physical parameters.

The DMRT is called a partially coherent approach in which the coherent component of the model consists of calculating the phase matrix by using Maxwell equation for several cubic wavelengths of snow. The incoherent part consists of using this phase matrix in the radiative transfer theory which is incoherent. In my thesis, we developed a fully coherent approach for snowpack scattering by solving Maxwell's equations directly over the entire snowpack including a bottom half space. The task is considered to be computationally forbidden historically. Taking advantage of recent development in high performance computing and FFT-based fast algorithm, we have composed a volumetric integral equation (VIE) solver incorporating half space Green's function and periodic boundary conditions. The revolutionary new approach produces consistent scattering and emission results, and includes all the fully coherent wave interactions. We have also

developed an approach to model the uniaxial effective permittivities of an anisotropic snow layer by numerically solving Maxwell's equation directly and comparing the mean scattering field with Mie scattering of spheres.

For polar ice sheet emission, I have examined the effects of rapid density fluctuations in affecting brightness temperatures over the 0.5~2.0 GHz spectrum. The density fluctuation creates thousands of thin layers and these weak reflections accumulate to produce distinct emission spectrums. We have developed both fully coherent and partially coherent layered media emission theories that agree with each other and distinct from incoherent approaches.

For the second part, the goal is to develop integral equation based methods to solve wave scattering in periodic structures that can be used for broadband simulations. Set upon the concept of modal expansion of the periodic Green's function, we have developed the method of broadband Green's function with low wavenumber extraction (BBGFL), where a low wavenumber component is extracted from the Green's function, resulting a non-singular and fast-converging remaining part that has separable wavenumber dependence. We've applied the BBGFL to simulate band diagrams of periodic structures, applicable to both PEC and dielectric scatterers with arbitrary shapes and volume fractions. Using the BBGFL to formulate surface integral equations, the determination of band modal solution becomes a linear eigenvalue problem, producing all the modes in one shot. This is in contrast to using the usual free space Green's function or the KKR (Korringa Kohn Rostoker) method in which the eigenvalue problem is nonlinear. The modal field solutions are wavenumber independent. The modal analysis of the band structure can be further utilized to construct the Green's function including the periodic structure, where the technique of low wavenumber extraction can be again applied to generate the broadband Green's function. The methodology of modal expansion with low wavenumber extractions can be used to construct

Green's function satisfying all the prescribed boundary conditions, greatly reducing the number of unknowns in the method of moments (MoM) when applied to perturbations to the original problem. The method of BBGFL is a new approach that provides an effective and alternative approach to study wave behaviors in periodic wave functional materials.

CHAPTER I

Introduction

The objective of my research is two-fold: to study wave scattering phenomena in dense volumetric random media and in periodic structures. For the first part, the goal is to use the microwave remote sensing technique to monitor the environmental status of our Earth including water sources and global climate change. Towards this goal, I study the microwave scattering behavior of snow and ice sheet, and develop partially coherent and fully coherent scattering models of densely packed volumetric scatterers and layered media. For the second part, the goal is to develop integral equation based methods to solve wave scattering in periodic structures that can be used for broadband simulations. Set upon the concept of modal expansion of the periodic Green's function, we have developed the method of broadband Green's function with low wavenumber extraction (BBGFL), and applied the method effectively to simulate the band diagrams of the periodic wave functional materials and to construct the broadband Green's function including periodic scatterers.

1.1 Volumetric scattering of snowpack

Snow has vast coverage of the earth especially in high latitude. According to National Snow and Ice Data Center (NSIDC), there are 57 million square kilometers of land in the northern hemisphere that may be seasonally covered with snow (that is about 38% of the total land area on earth, or 42% of the land area excluding Antarctica), and adding ocean surfaces would increase

the number to 90 million square kilometers. And land where at least 40 percent of precipitation falls as snow is about 15 million square kilometers in area [1]. The snow cover on the earth would affect the energy balance by changing the surface reflection rate to the sun radiation and the long wave thermal emission rate from the earth and thus is highly related to climate change [2]. The climate change would also significantly change the snow accumulation pattern and affect the snow-melt fresh water supply [3]. The human society is highly related to snow: snow provides the water we drink and the food we eat; 50% of the Indus River flow depends on Himalayan glacier melt [4]; hydropower generates 20% of the world's electricity; the California snowmelt supports a $15 billion agriculture industry [1]. Snow is a natural reservoir of fresh water and river runoff. The timing of the melt is highly related to natural hazards such as spring flood and summer drought [5].

Our knowledge about the spatial distribution and temporal dynamics of snow across the prairies, tundra, mountains, on sea ice, and in the forest remains quite limited [1]. Remote sensing provides a method to measure these information from airborne or spaceborne platforms, with promising wide spatial coverage and high resolution. Microwave remote sensing offers a space perspective of the land that can be operated continuously irrespective of weather conditions and day and night. Developing microwave remote sensing techniques and to derive useful information of the snowpack from microwave observation requires a solid understanding of the physics of microwave-snowpack interaction.

Dry snow is densely packed ice grains in the air background. These ice grains creates strong volumetric scattering at the wavelengths comparable to the grain size. It has long been established that the volumetric scattering from snow in microwave is correlated with snow volume. In the simplest scenario, the active radar backscatter would increase as snow accumulates, while the

passive brightness temperature, with the major contribution from the thermal emission from the ground beneath the snowpack, would decrease as snow accumulates. Thus by measuring these microwave observables, the radar backscatter and the brightness temperature, it is possible to retrieve the snowpack parameters, provided that we have a forward microwave scattering / emission model that relates the snowpack parameters to the microwave signatures, Figure I.1.

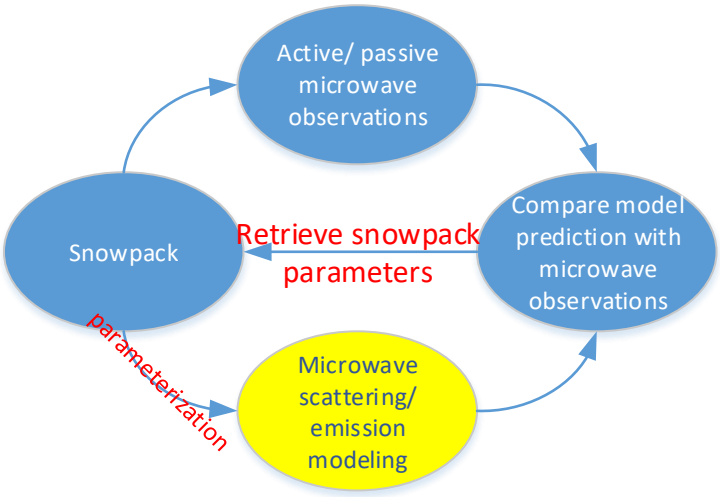

Figure I.1. Electromagnetic scattering of dense random media in snow microwave remote sensing.

The snow remote sensing community has been working on to develop and validate techniques to use X- and Ku-band radar backscatters and Ku- and Ka- band brightness temperatures to retrieve the snow water equivalent (SWE) information globally. There are satellite missions being proposed and actively developed worldwide, including the Cold Regions Hydrology High-Resolution Observatory (CoReH2O) of the European Space Agency (ESA) [6], the Snow and Cold Land Processes (SCLP) of the national aeronautics and space administration (NASA) [5, 7], and the Global Water Cycle Observation Mission (WCOM) of China [8, 9], etc., all targeting at a better snow mapping approach using microwave, combining both active and

passive observations. The understanding, interpretation and usage of the microwave signatures of the snowpack requires the development of microwave scattering and emission models of the snowpack.

The snowpack scattering models can be divided into empirical models [10, 11], semi-empirical models [12, 13] and physical based scattering models [14-22]. The empirical models, being simple, usually has strong limitations to snow conditions, and cannot be easily generalized. On the other hand, the physical based models try to relate directly the microwave signatures with the geometric parameters of the snowpack observed in the field measurements, such as snow depth, snow density, snow grain size, and snowpack stratigraphy, which apply to a much wider range of snow conditions, and provide various frequency, polarization, and snow depth dependences subject to local parameters. The physical based models offer much deep insight into the microwave scattering behavior. Our work aims to develop and improve the physical based scattering models.

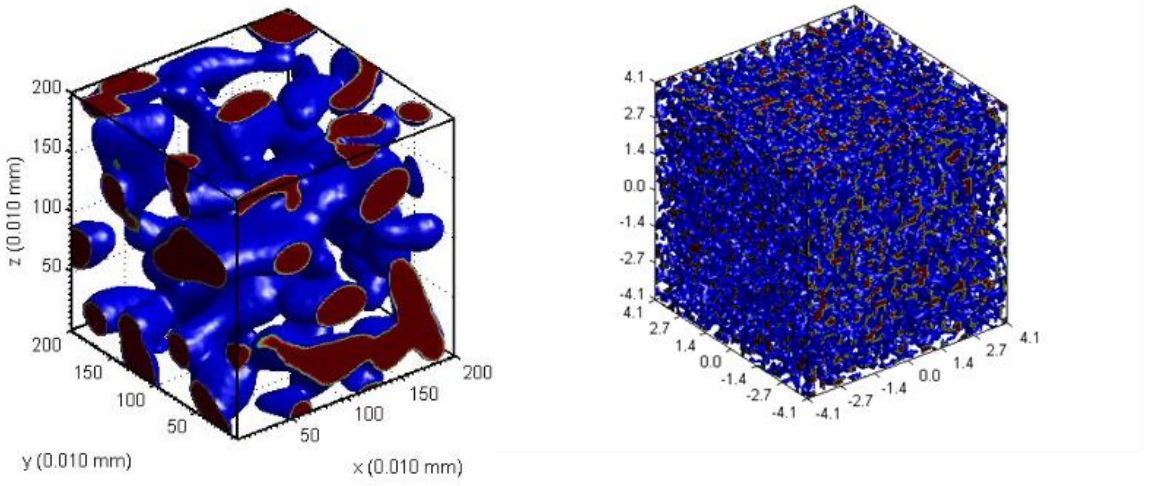

(a) MicroCT snow grain microstructure

(b) bicontinuous media

Figure I.2. Microstructure of natural snowpack and computer generated bicontinuous media. (a) 3D snow grain microstructure obtained from X-ray computer tomography, data source courtesy of H.-P. Marshall; (b) computer generated bicontinuous media.

Snow consists of ice grains on the scale of millimeters, Figure I.2 (a). These ice grains are densely packed in the wavelength scale at microwave frequencies so that the coherent microwave interactions among ice grains are important [15, 16]. Should these ice grains be too small, then the volumetric scattering drops to negligible in microwave; should theses ice grains be too large, then the volumetric scattering will be too large for the microwave to effectively penetrate into the snowpack to provide information proportional to snow volume. Thus the microwave signature of the snowpack is highly related to the snow grain size.

Although it is easy to deal with the scattering from one particle, it is in general hard to model the collective scattering behavior among large number of ice grains densely packed together. In order to attack this problem, people have developed the idea of radiative transfer (RT) [23] to propagate the intensity inside the snowpack, where homogenization is assumed in the scattering volume to develop the concept of effective permittivity, effective extinction coefficient, and the effective scattering phase matrix [15, 16, 18]. The radiative transfer theory is incoherent in the sense that it ignores the absolute phase information of the electric field as it propagates in the snow volume.

There are different approaches in approximating the effective permittivity, and effective extinction coefficient, and the effective scattering phase matrix in the radiative transfer theory. Rayleigh scattering [15, 24] is the simplest one which completely ignores the collective scattering among multiple scatters and assumes independent scattering. These assumptions lead to 4^{th} power dependence in scattering to the microwave frequency, and 3^{rd} power to the grain size for a fixed snow density (i.e. volume fraction of the scatterer), and linear dependence to volume fraction. All these results are either non-physical or much stronger than and failed to reproduce the dependence observed in the laboratory [25]. There is also strong permittivity fluctuations theory (SFT) of the

random media being developed in parallel with the discrete scatterer approach [26, 27]. SFT characterized the random media using its correlation function.

In the theory of dense media radiative transfer (DMRT), the locally coherent collective scattering effects are rigorously considered in calculating these effective quantities. The methods include the analytical approach of quasi-crystalline approximation (QCA) [16-18, 21, 22, 28], and the numerical approach of discrete dipole approximation (DDA) over bicontinuous media [19-21, 28]. In QCA [15, 16, 18], the snow media is approximated using densely packed sticky spheres, where the correlation in position of the spheres are analytically described by 2^{nd} order joint probability, the Percus-Yevick pair distribution function. Correlation functions can be derived from the pair distribution function [28]. The Dyson's equation of the coherent field is approximated by QCA, while the Bethe-Salpeter equation of the incoherent field is approximated by the correlated ladder approximation. The results of QCA are verified by numerical simulation of scattering from densely packed spheres using Foldy-Lax multiple scattering equations, and agree with measurements [29, 30]. In the DDA of bicontinuous media [19], the snow is approximated by a statistical bicontinuous random media, Figure I.2 (b), which is generated by level cutting a random field that is sum of a large number of stochastic waves. The bicontinuous media resembles snow visually and can be compared with snow quantitatively using correlation functions [28]. The discretized dipole approximation (DDA) is then used to solve the volume integral equations over samples of bicontinuous media of several wavelengths. Statistical average is performed explicitly using Monte Carlo simulation to derive the phase matrix [19, 20]. The bicontinuous media exhibits similar scattering behavior with QCA that compares well with experiments, and also shows much stronger cross-pol due to irregularities in geometry. The

scattering phase matrix can be more forward scattering than the QCA phase matrix with similar scattering coefficients [28].

The DMRT is thus a partially coherent approach, as illustrated in Figure I.3, in which the coherent component of the model consists of calculating the phase matrix by solving Maxwell equations either analytically or numerically for several cubic wavelengths of snow. The incoherent part consists of using this phase matrix in the radiative transfer theory which is incoherent.

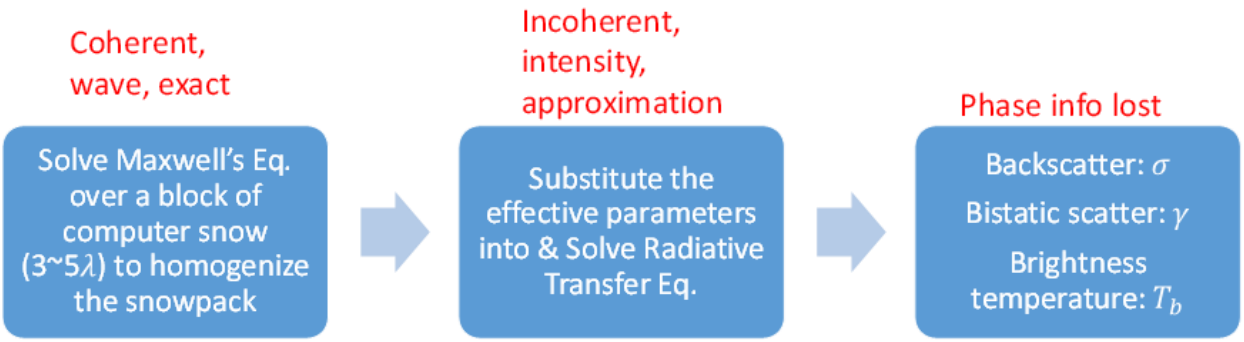

Figure I.3. DMRT as a partially coherent approach.

The framework of DMRT has been applied to snowpack scattering both for active [18, 20, 21] and for passive [17, 22, 30] microwave remote sensing separately. Because of its incoherent nature in dealing with far field interactions through radiative transfer, it cannot produce the feature of backscattering enhancement [31, 32], which is a natural outcome of constructive wave interferences in the backward scattering direction from dual and opposite scattering paths in the multiple volume scattering and volume-surface scattering scenario. This becomes an issue if one wants to model the scattering and emission of the snowpack simultaneously using the same set of physical parameters, as required in the combined active and passive remote sensing of snowpack.

The DMRT equations can actually be derived from Maxwell's equations. The reason it fails to include coherent far field interaction is due to that it stops at the ladder terms in the

Feynman diagram [15, 16]. The cyclical terms must be included to account for backscattering enhancement. By solving the DMRT equation using an iterative approach, one can readily identify the cyclical scattering mechanisms and apply cyclical correction. The iterative approach can be carried out numerically to any order to account for multiple scattering effects. In Chapter 2, I will discuss the extension to the traditional dense media radiative transfer (DMRT) approach to include the cyclical terms in the Feynman diagram. The cyclical correction gives rise to backscattering enhancement. This extension enables the theory to model combined active and passive observations of snowpack using the same set of physical parameters [33].

The cyclical correction to the DMRT equation is ad-hoc that it only applies to the backscattering direction. It is based on the methodology of the partially coherent approach of DMRT to use homogenization and effective propagation and scattering properties such as the effective permittivity and phase matrix. One may question the validity of such an approach when there are electrically thin layers, which is pervasive due to melt and refreeze and successive snow falls, in the snowpack [12]. In my thesis, we have also developed a fully coherent approach for snowpack scattering and emission by solving Maxwell's equations directly over the entire snowpack including a bottom half space, Figure I.4. Again, we use bicontinuous media to represent the snowpack, and we use a half-space Green's function to represent the effects of the underlying ground. We then apply method of moments (MoM) with discrete dipole approximation (DDA) to solve the volume integral equation (VIE). The task is considered to be computationally forbidden historically. Taking advantage of recent development in high performance computing and FFT-based fast algorithm [34], we have composed a volumetric integral equation (VIE) solver incorporating half space Green's function and periodic boundary conditions. The revolutionary

new approach produces consistent scattering and emission results, and includes all the fully coherent wave interactions. This part will be discussed in Chapter 3 [35, 36].

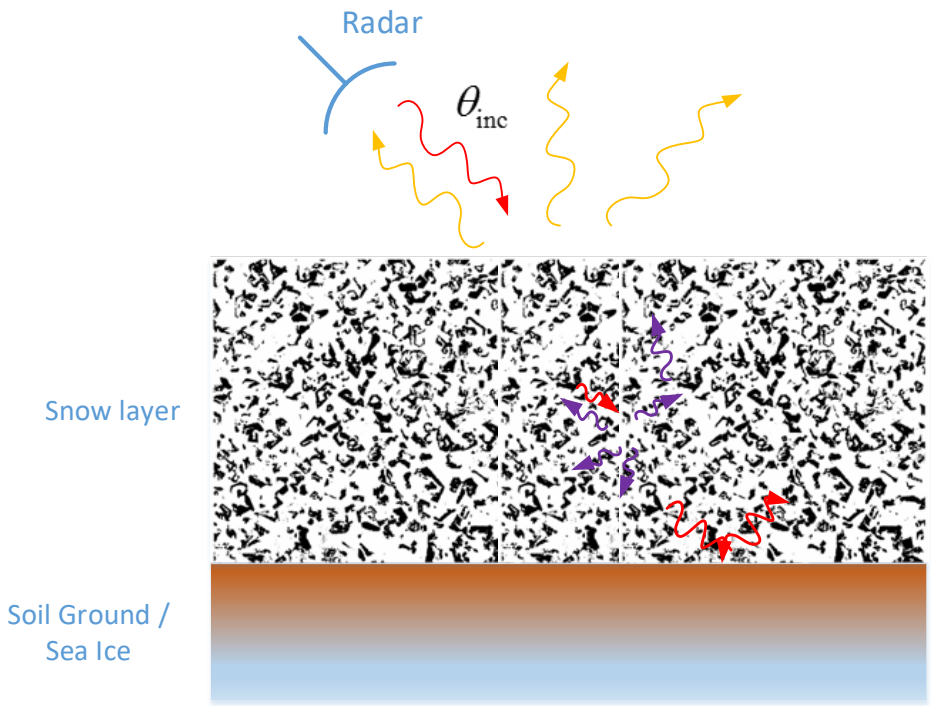

Figure I.4. The fully coherent approach: Solve Maxwell's equations over the entire snowpack.

The fully coherent approach as discussed in Chapter 3 will not only prove to be useful in checking against and validating the DMRT theory, it is also unique in that it produces the fully coherent scattering matrix of the snowpack directly, including both the magnitude and phase. The phase information is of critical importance, and it opens new possibility in studying the interferometric, polarimetric, and tomographic signatures of snowpack [37, 38].

1.2 Phase shift from an anisotropic snow layer

Besides the volumetric scattering approach, recent field measurements also revealed the correlation between the thickness of the snowpack and the microwave co-polarization phase

differences (CPD) of backscatters, Figure I.5. The CPD is the phase difference between vertically co-polarized backscatter and horizontally co-polarized backscatter, and it is affected by the snowpack anisotropy. The anisotropy of the snowpack arises from snow settlement and the temperature gradient driven snow metamorphism. The anisotropy in microstructure induces effective uniaxial permittivity of the snowpack and causes birefringence giving rise to CPD, Figure I.5 (a). The co-polarization phase differences are observed in both tower mounted scatterometer measurements at X- and Ku- bands and in space-borne radar measurements at X-band [39-42]. The Spaceborne TerraSAR-X and ground based SnowScat (an X- and Ku- band scatterometer) measurements of CPD are compared to in-situ measurements of snow depth in Figure I.5 (b). Studies show that the co-polarization phase difference can be used to retrieve the new fallen snow depth and snow water equivalent (SWE) and be used to monitor the change in snowpack microstructure evolution. The sensitivity to new fallen snow fall will prove to be especially useful since they have fine snow grains that yields very little volume scattering.

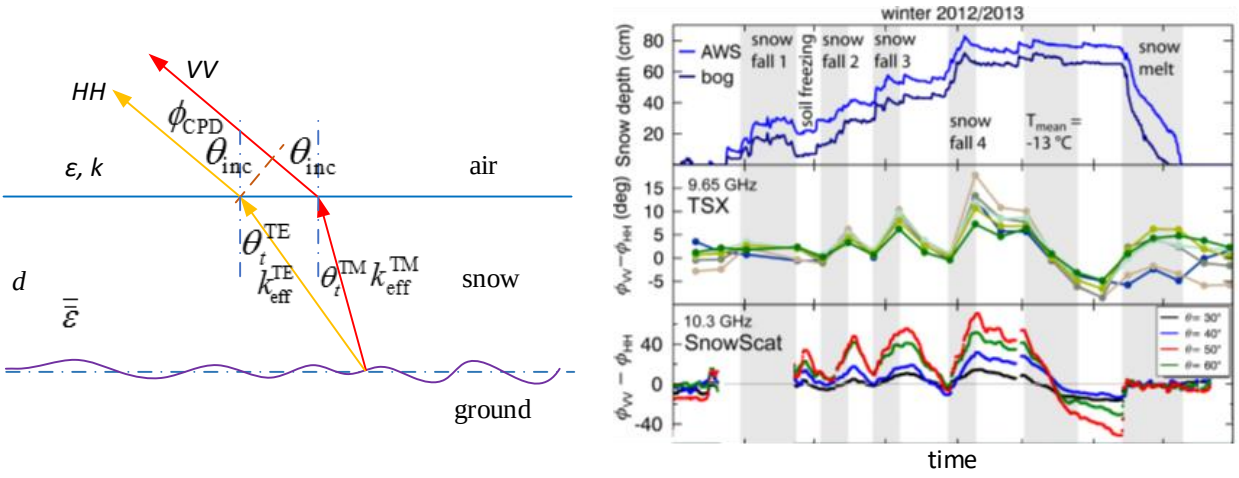

(a) Birefringence from an anisotropic snow layer causes co-polarization phase difference

(b) TerraSAR-X and SnowScat measurements of CPD

Figure I.5. Correlation between snow depth and co-polarization phase difference. (b) is reproduced from Fig. 4 of [41].

Previous studies have been using the low frequency Maxwell-Garnett mixing formulas of spheroids to model the uniaxial effectivity induced from the anisotropic snowpack with statistical azimuthal symmetry [42, 43]. This approach has several limitations. It is limited to low to moderate volume fraction of ice concentration and it ignores the collective scattering effects among scatterers. There is no size / frequency dependence of the effective permittivity. It does not consider scattering loss. Furthermore, it discards the complexities in the correlation function of the snow microstructure when approximating it through the correlation function of vertically oriented spheroids.

In Chapter 4, we will report a new approach of modeling snowpack anisotropy using anisotropic bicontinuous media [44]. We then extract the uniaxial effective permittivity of the anisotropic bicontinuous media by numerical solving Maxwell's equation in 3D (NMM3D) over spherical samples of the media extending a few wavelengths. The effective permittivity is then extracted by comparing the coherent scattering field from the spherical samples with the Mie scattering fields from a homogeneous sphere of the same size. Such concept of comparing mean scattering field has been used to derive low frequency effective permittivity of a mixture of sphere [45], and has been used to validate the effective permittivity of densely packed cylinders and spheres as predicted by the QCA theory [46, 47]. The approach takes into consideration of the exact geometry of the random media. We also extract the effective permittivity using the strong permittivity fluctuations (SPF) theory [26], which uses the correlation function derived directly from the anisotropic bicontinuous media. These results are then compared with the quasi-static Maxwell-Garnett dielectric mixing from oriented spheroids [42, 43]. These results of effective permittivity are also used to derive the co-polarization phase difference (CPD) of the backscatter from a layer of snowpack comprised of anisotropic microstructures.

The proposed new approach [44] goes beyond many limitations over the Maxwell-Garnett dielectric mixing. NMM3D takes the microstructure as input and SPF utilizes its correlation function directly, and both apply to a wide range of volume fraction and frequency. The scattering loss is included. The NMM3D approach, based on solving Maxwell's equations over the ground truth geometry, can be viewed as benchmarks to other models.

1.3 Wideband emission from polar ice sheet as a probe for ice sheet internal temperature profile sensing

Recent L-band radiometry from the SMOS [48], Aquarius [49] and SMAP [50] satellite missions has sparked interest in studying low-frequency microwave-emission from the polar ice sheets. Low frequency microwaves have less extinction and extremely long penetration depths in glacier ice (several hundreds to one thousand meters), and thus can provide sensitivity to the subsurface temperature profile, Figure I.6 (a). The Ultra-Wide Band Software Defined Radiometer (UWBRAD) [51-53] operating from 0.5 to 2.0 GHz is a new instrument to retrieve subsurface temperature profiles from a wide bandwidth radiation spectrum. The physical basis for the measurement is to retrieve the shallower subsurface temperature at higher frequency and the deeper subsurface temperature at lower frequency.

The scattering from ice grains can be ignored at these low frequencies because the size of the ice grains (mm or less) is much smaller than the wavelengths. On the other hand, the surface of the polar ice sheet is characterized by rapid density variations on centimeter scales due to the accumulation process [54-57], Figure I.6 (b). The density variation induces permittivity fluctuations and cause reflections. These reflections, although small at each interface, accumulate from the large number of layers and decrease the overall emissivity. When the scale of density

fluctuations is within a wavelength in the ice sheet, the coherent interference from reflections at multiple interfaces cannot be ignored [56-58]. These coherent wave effects remains even after statistical averages over density profiles. We have studied the density fluctuation effects using both incoherent and coherent models. The coherent model agrees with the incoherent model for large correlation lengths of density fluctuation but differs from the incoherent model when the correlation length is less than half a wavelength [58].

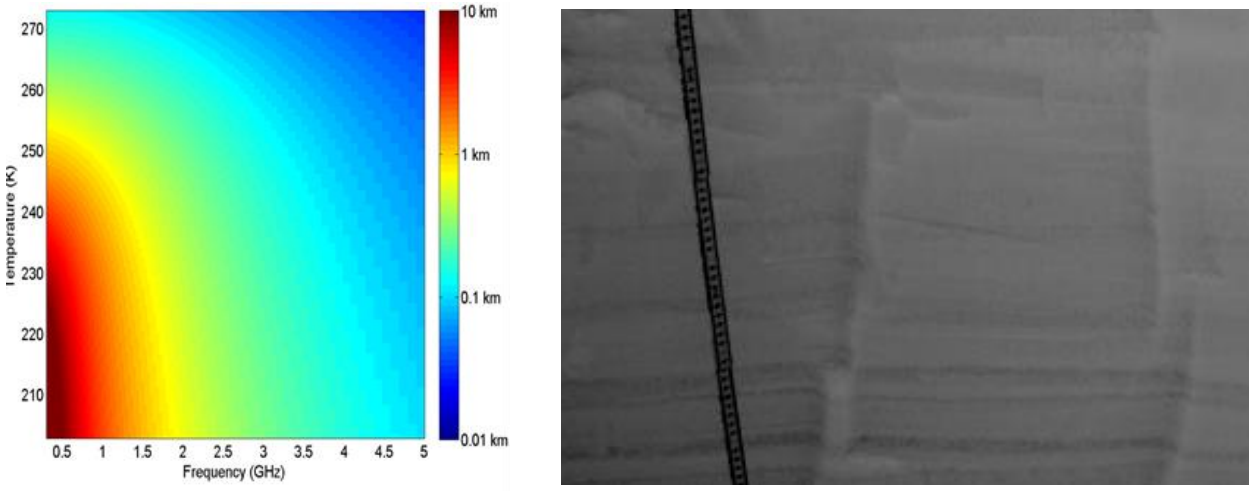

(a) Pure ice penetration depth vs. frequency and temperature

(b) NIR photos showing layers at centimeter scales in Greenland ice sheet near surface

Figure I.6. Factors affecting ice sheet emission spectrum (a) Penetration depth of pure ice, figure courtesy of [52], (b) Near infrared (NIR) images showing sun and wind crust layers at centimeter scales in the Greenland ice sheet near surface, photo courtesy of Michael Durand.

Since coherent wave effects are "localized" in random layered media to spatial scales within a few wavelengths, we can divide the entire ice sheet into blocks, with each block on the order of a few wavelengths, and apply fully coherent scattering models within a single block. We then incoherently cascade the intensities among different blocks. A smaller number of realizations is then required in the Monte Carlo averaging process for each block due to the smaller number of

interfaces. This partially coherent approach has proved to be much more efficient than applying the fully coherent model to the entire ice sheet, and to produce results in agreement with the fully coherent approach [59, 60].

The density variations near the top of the ice sheet form layers as well as introducing interface roughness, Figure I.6 (b). The layering causes reflections and modulates the ice sheet emission. The interface roughness, on the other hand, causes angular and polarization coupling [59, 60]. Besides being efficient and stable, the partially coherent approach also enables us to examine interface roughness effects by applying a full wave small perturbation method up to second order (SPM2) to the multi-layered roughness scattering problem within the same block. The SPM2 has the advantage of conserving energy [61, 62].

In Chapter 5, I will discuss the fully coherent and partially coherent layered media emission theories that we developed for polar ice sheet emission at the UWBRAD spectrum that agree with each other and distinct from incoherent approaches.

1.4 Broadband Green's function with low wavenumber extraction applied to periodic structure simulation

The Green's function is a fundamental concept in understanding and characterizing the wave propagation and scattering. Not only is it the kernel in integral equation based methods, it also offers physical insight into the electromagnetic / optics / quantum system.

Waves in periodic structures are important in physics and engineering and in the design of photonic, electronic, acoustic, microwave and millimeter devices such as that in photonic crystals, phononic crystals and metamaterials [63-67]. In such problems of wave functional materials, there exists a lattice with scatterers embedded periodically in the lattice. The design of the lattice

periodicity and the inclusions in a unit cell creates unique band structures with new wave phenomena such as edge states and topological insulators [68-70]. Besides the band structure, the band field solutions and the Green's functions are also important physical quantities. The Green's functions are physical responses of a point source. It offers physical insights into the wave behavior in the passband and stopband of the photonic crystals and metamaterials. The Green's function represents the response of sources and also impurities and defects. It can be used to formulate surface integral equations to deal with finite size, defects, imperfection and impurities in the periodic lattice. The periodic Green's function in an integral equation formulation has been used to derive the effective material parameters of the periodic structures [71-73]. The Green's function including periodic scatterers has been constructed to study the dipole near field and radiation field inside a bandgap material [74-77]. The field excited by a dipole near a periodic structure has also been examined [78, 79] using periodic Green's function.

The goal of this second part of my thesis is to develop integral equation based methods to solve wave scattering in periodic structures that can be used for broadband simulations. We also calculate the Green's functions of a periodic structure including the scatterers which can be of arbitrary shape. Set upon the concept of modal expansion of the periodic Green's function, we have developed the method of broadband Green's function with low wavenumber extraction (BBGFL) [80-83], where a low wavenumber component is extracted from the Green's function, resulting a non-singular and fast-converging remaining part that has separable wavenumber dependence. We have then applied the method for band diagram simulation and Green's function construction in the periodic structures.

The band diagrams and modal field distributions are fundamental in explaining the wave phenomena inside periodic structures and their computation are among the first steps in periodic

structure designs such as in photonic crystals and metamaterials. The frequency domain plane wave method [84-91] and the time domain finite difference method (FDTD) [92, 93] are among the most frequently used method in numerical simulation of periodic structures. However, in both methods, one suffers from the inaccuracy of representing the scatterer geometry using a coarse grid and needs specially designed interpolating functions [88, 91]. The plane wave method is also found to be of poor convergence when the dielectric contrast and occupying ratio are large [87]. The finite element method (FEM) [94, 95] is accurate in representing the geometry, but still one needs to discretize the whole lattice domain, converting to matrix equations of large dimensionality. The Korringa Kohn and Rostoker (KKR) method [96-99] on the other hand explicitly represents the multiple scattering in a surface integral formulation using the periodic Green's function of the host medium and solves it by modal expansion, suitable for special geometries of cylinders and spheres. The eigenvalue problem based on KKR is nonlinear as the impedance matrix is dependent on the wavenumber. A nonlinear root search is then needed in locating multiple bands, making the approach computing demanding.

The difficulty that halts the development of integral equation method is the poor convergence of the periodic Green's function. Realizing the similarity between the periodic Green's function and the waveguide Green's function, it is found that by subtracting out a low wave number component, the remaining part of the Green's function converges fast in terms of Bloch waves. The wavenumber dependence of the remaining part is simple and separable, giving it the name of the broadband Green's function. The broadband periodic Green's function with low wavenumber extraction (BBGFL) has been applied to the surface integral equations in two dimensions (2D) for both perfect electrical conductor (PEC) [80] and dielectric [81] scatterers. The application of MoM with boundary element representation greatly reduces the number of

unknowns and applies to arbitrary geometries of various shapes and volume filling ratios with high fidelity. The separable wavenumber dependence in the broadband Green's function converts the resulting matrix equations into a linear eigenvalue problem that has impedance matrix independent of wavenumber with all the eigenvalues and eigenvectors solvable simultaneously, giving all the band solutions and modal field solutions. The modal field solutions are wavenumber independent.

The modal analysis of the band structure can be further utilized to construct the Green's function including the periodic structure, where the technique of low wavenumber extraction can again be applied to generate the broadband Green's function at a fixed wave vector in the reciprocal space. In this process, two of the key steps are 1) to calculate the Green's function at a single low wavenumber, and 2) to solve for the modal fields and efficiently normalize the modal fields. The Green's function resulting from a single point source is then obtained by integrating the periodic Green's function over the first Brillouin zone [100].

The methodology of modal expansion with low wavenumber extractions can be used to construct Green's function satisfying all the prescribed boundary conditions, greatly reducing the number of unknowns in the method of moments (MoM) when applied to perturbations to the original problem [75, 100]. The method of BBGFL is a new approach that provides an effective and alternative approach to study wave behaviors in periodic wave functional materials.

The application of BBGFL to simulate band diagrams of periodic structure is discussed in Chapter 6, while the further application of BBGFL with the modal solution to construct Green's functions including periodic scatterers is discussed in Chapter 7.

1.5 Overview of the thesis

Figure I.7 depicts the scope of my thesis.

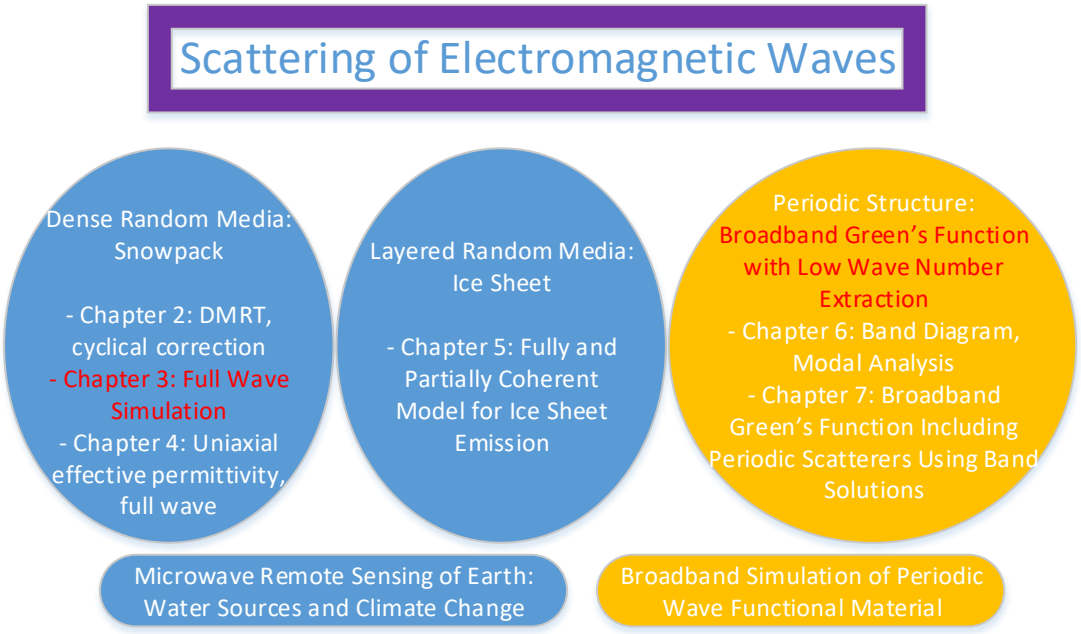

Figure I.7. Overview of the thesis.

CHAPTER II

Dense Media Radiative Transfer Theory with Multiple Scattering and Backscattering Enhancement

In this chapter we incorporate the cyclical terms in dense media radiative transfer (DMRT) theory to model combined active and passive microwave remote sensing of snow over the same scene. The inclusion of cyclical terms is crucial if the DMRT is used to model both the active and passive contributions with the same model parameters. This is a necessity when setting out on a joint active/ passive retrieval. Previously the DMRT model has been applied to active and passive separately, and in each case with a separate set of model parameters. The traditional DMRT theory only includes the ladder terms of the Feynman diagrams. The cyclical terms are important in multiple volume scattering and volume-surface interactions. This leads to backscattering enhancement which represents itself as a narrow peak centered at backward direction. This effect is of less significance in passive remote sensing since emissivity is relating to the angular integral of bistatic scattering coefficients. The inclusion of cyclical terms in first order radiative transfer (RT) accounts for the enhancement of the double bounce contribution and makes the results the same as that of distorted Born approximation in volume-surface interactions. In this chapter, we develop the methodology of cyclical corrections within the framework of DMRT beyond first order to all orders of multiple scattering. The active DMRT equation is solved using a numerical iterative approach followed by cyclical corrections. Both Quasi-crystalline Approximation (QCA)-

Mie theory with sticky spheres and bicontinuous media scattering model are used to illustrate the results. The cyclical correlation introduces around 1dB increase in backscatter with a moderate snowpack optical thickness of ~0.2. The bicontinuous / DMRT model is next applied to compare with data acquired in the Nordic Snow Radar Experiment (NoSREx) campaign in the snow season of 2010 to 2011. The model results are validated against coincidental active and passive measurements using the same set of physical parameters of snow in all frequency and polarization channels. Results show good agreement in multiple active and passive channels. The work reported here has been published in [33]. The same approach has also been used to study multiple scattering effects in vegetated surface, such as corn crop land, when the multiple scattering effects become non-negligible [101].

2.1 Introduction

Snow remote sensing community has demonstrated strong interests in combining active and passive observation to effectively retrieve snowpack information. The combined active and passive remote sensing of snowpack takes advantage of the high resolution polarimetric synthetic aperture radar (SAR) while providing a link back to the pervasive passive data archives. In Europe, the Cold Regions Hydrology High resolution Observatory (CoReH2O) satellite mission was proposed to the European Space Agency (ESA) and went through 4 years of assessment studies (Phase-0, 2005-2009) and 4 years of feasibility studies (Phase-A, 2009-2013) [102, 6]. Both scatterometer and radiometer systems were deployed in the validation campaign of Nordic Snow Radar Experiment (NoSREx) validation campaign, aiming to collect a common database of backscattering and emission properties of snow covered terrain [103, 104]. In the United States, the Snow and Cold Land Processes (SCLP) satellite mission was recommended to National

Aeronautics and Space Administration (NASA) for implementation in the Earth Science Decadal Study report in 2007 [5], and has undergone extensive ground-based and airborne field measurement campaign [7]. The SCLP is a combined active and passive mission. Within SCLP, the microwave instruments include both X- and Ku-band SARs (with VV- and VH- polarizations) and K- and Ka- band radiometers. Studies were taken to integrate all antennas on the same platform [105]. In China, the Global Water Cycle Observation Mission (WCOM) [8, 9] is being considered to provide synergetic observations of the global water cycle and in particular the properties of snow cover. WCOM is also a combined active and passive mission, with scatterometers operating at X- and Ku- band and radiometers operating at Ku- and Ka- band.

The analysis and retrieval of snowpack using active and passive microwave measurements would benefit from a physical scattering model that could accurately predict both backscatter and brightness temperature measured from the same set of snowpack physical parameters. There are models applicable to passive remote sensing such as the empirical model developed by Helsinki University of Technology (HUT) [10, 11], the semi-empirical Microwave Emission Model of Layered Snowpacks (MEMLS) based on six-flux theory [12], and the Dense Media Radiative Transfer (DMRT) models using any of several physical scattering models. These models include 1) Quasi-crystalline Approximation with Coherent Potential (QCA-CP) [14, 15, 16], 2) QCA Mie theory with sticky spheres [16-18], or 3) the bicontinuous media / Discrete Dipole Approximation (DDA) scattering model [19-21]. The DMRT theory has been applied to both passive [17, 22] and active [18, 20, 21] remote sensing by solving DMRT equations using the eigen-quadrature method [18], and the MEMLS model has also been extended to a bistatic-scattering model using Chandrasekhar's H-Functions recently [13]. Models differ in the approaches to model the collective scattering effects and multiple scattering effects inside a dense random media. MEMLS

and HUT are more empirical using measured data to adjust the scattering coefficients as a function of frequency and correlation length/ grain size, while the DMRT models are physically based and use parameters physically measurable [111]. However, none of the above models have included important physics related to backscattering enhancements, and as a result, different parameterization is required in order to match the active and passive model results to their respective measured quantities.

Without including backscattering enhancement, there is often the case of finding good agreement with the active measurements while the model predicted brightness temperatures are lower than the measured brightness. One could describe the multiple scattering process inside a dense media using Feynman diagram which diagrammatically symbolizes the integral equations recursively. The constructive interference in the backscattering direction are rigorously based on the cyclical terms of the Feynman diagrams [31, 32] and could not be modeled by the traditional radiative transfer theory [15, 16, 31, 32]. The radiative transfer theory only includes the ladder terms of the Feynman diagrams. Such constructive interference does not occur in other directions. Backscattering enhancement is also exhibited in the double bounce term in the distorted Born approximation [106].

In this chapter, we model both the backscattering enhancement effects and the multiple scattering effects under the framework of the DMRT theory. Specifically, the DMRT equations are cast into two coupled integral equations and solved iteratively. In the iterative solver, each term corresponds to a physical scattering path. A numerical iterative approach is adopted to keep track of all the scattering paths. The iteration is carried out numerically to higher order until convergence is achieved. In each order, we do not sum the terms but keep them separate so that we can keep track of the scattering process in each term. Using the iterative approach, the cyclical terms are

identified and their contributions are included in the total radar backscattering. In the iterative approach, the contribution from each term is computed straightforward by an angular integral of the product of phase matrix and one term in the lower order, followed by a z- integral, and thus the computation is robust to the phase matrix pattern, making it more stable than the eigen-quadrature method [18].

In this chapter, the DMRT equation is solved with two reflective boundaries as in the case of terrestrial snowpack scattering. Thus there are multiple interactions between volume scattering and surface scattering. In Section 2, we review the enhancement caused by coherent interference of cyclical paths in the context of double bounce scattering by comparing the results of radiative transfer and distorted Born approximation. In Section 3, we describe the iterative procedure of solving radiative transfer equation with cyclical corrections. Both QCA with sticky spheres and bicontinuous / DDA scattering model are used to account for the dense medium scattering effects. The two models show weaker dependence of scattering coefficients on grain size and frequency than the classical theory of 3^{rd} power and 4^{th} power, respectively. The sticky QCA model is applied in section 4 where we compare the results of the iterative approach to the eigen-quadrature approach. Cases are illustrated when the inclusion of cyclical terms is important. The bicontinuous /DDA model is then applied in section 5 to the ground data acquired in the NoSREx campaign in the snow season of 2010 to 2011 by the Finnish Meteorological Institute (FMI) [103, 104]. The same sets of snowpack parameters are applied to the active and passive models. Results show good agreement with multiple channel observations of both scatterometer (X- to Ku- band) and radiometer (X- to Ka- band) data. This is the first study that compares model predictions with active and passive measurements over the same scene. In previous modelling studies active and passive data were neither coincidental nor concurrent.

2.2 Double bounce scattering: radiative transfer and distorted Born approximation

We consider the double bounce backscattering from one scatterer inside a layer of random particles with thickness d above ground. The double bounce backscattering comprises scattering by a particle and scattering by the ground. The scattering by the particle can occur before ground scattering or after ground scattering. Thus it can be from a forward path (scattering by the particle before reflection of the ground) and a reverse path (scattering by the particle after reflection of the ground) as depicted in Figure II.1. The scattered fields of the two paths are exactly in phase in the backscattering direction. Radiative transfer theory sums the contribution from the two paths in an incoherent manner. Considering the co-polarized backscatter and ignoring the top boundary reflection, the power of each path is proportional to $e^{-2\tau}r(\theta_i)|f|^2$, yielding a total of $2e^{-2\tau}r(\theta_i)|f|^2$, where f is the scattering amplitude of the scatterer in the double bounce direction, $r(\theta_i)$ is the reflectivity at the bottom boundary in the angle of incidence, and τ is the optical thickness of the layer in the direction of wave propagation. On the other hand, if one applies the distorted Born approximation [106], the two scattered fields are added coherently, resulting to a total power of $\left|R(\theta_i)fe^{2ik_zd} + R(\theta_i)fe^{2ik_zd}\right|^2 = e^{-2\tau}|R(\theta_i)f + R(\theta_i)f|^2$, where $R(\theta_i)$ is the Fresnel reflection coefficient at the bottom boundary, and k_z is the z-component of the effective wavenumber in the random media. Note that $|R(\theta_i)|^2 = r(\theta_i)$, and $\tau = 2\mathrm{Im}\{k_z\}d$. The in-phase condition leads to the total power of $4e^{-2\tau}r(\theta_i)|f|^2$ in backscatter, which is twice as much as the radiative transfer results. The difference of a factor of 2 between radiative transfer theory and distorted Born approximation is well known and leads to backscattering enhancement [106]. However, one can still use radiative transfer theory by inserting a factor of 2 in the cyclical terms. The backscatter doubling associated with cyclical paths is the cyclical correction to radiative transfer theory.

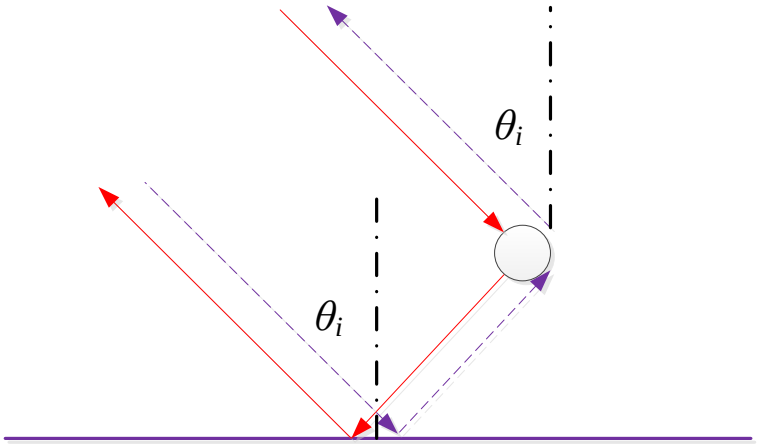

Figure II.1. Cyclical paths associated with double bounce scattering. In the solid path volume scattering occurs before surface scattering. In the dashed path, surface scattering occurs before volume scattering.

2.3 Numerical Iterative Approach with Cyclical Correction

In this section, we develop the methodology of cyclical correction beyond the first order to all orders of multiple scattering. We confine our analysis to a standard two layer configuration, i.e. a snow layer with thickness d above ground, as shown in Figure II.2. Solving the active DMRT equation using an iterative approach is a standard procedure performed by casting the differential equations into integral form and treating phase matrix as small arguments [24]. Here we only focus on the cyclical correction to the cyclical terms and the resulting backscattering enhancement. The key results of the iterative approach are given in Appendix A for completeness.

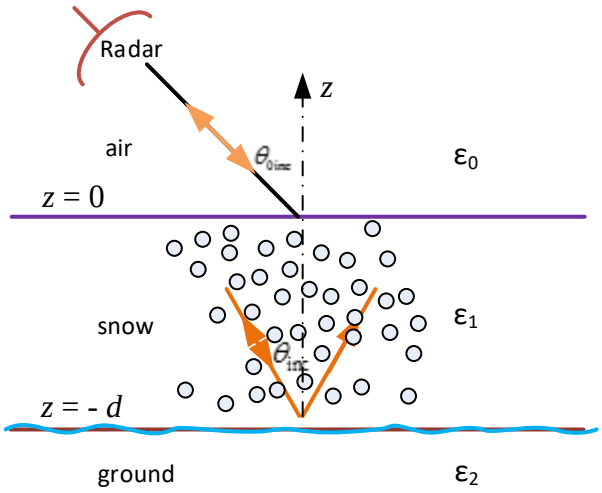

Figure II.2. Active remote sensing of a snow layer.

The advantage of the iterative approach is that each term in the expression corresponds to a physical interpretable scattering path and their contributions are separable. In each order of iteration, we do not sum the terms but keep them separate so that we can keep track of the scattering mechanism for each term. A scattering path describes the intensity flow in terms of scattering and reflection. The direction of energy flow is naturally grouped into upwelling and downwelling, as implied by equation (A.2a, A.2b) or its explicit form of 1st order in equation (A.6a, A.6b). We separate $\bar{S}^{(n)}(\theta,\phi,z)$ and $\bar{W}^{(n)}(\theta,\phi,z)$ into upward and downward component depending on the direction of the lower order specific intensity flow being collected,

$$\bar{S}_u^{(n)}(\theta,\phi,z) = \int_0^{2\pi} d\phi' \int_0^{\pi/2} d\theta' \sin\theta' \, \bar{\bar{P}}(\theta,\phi;\theta',\phi') \cdot \bar{I}^{(n-1)}(\theta',\phi',z) \tag{2.1a}$$

$$\bar{S}_d^{(n)}(\theta,\phi,z) = \int_0^{2\pi} d\phi' \int_0^{\pi/2} d\theta' \sin\theta' \, \bar{\bar{P}}(\theta,\phi;\pi-\theta',\phi') \cdot \bar{I}^{(n-1)}(\pi-\theta',\phi',z) \tag{2.1b}$$

$$\bar{W}_u^{(n)}(\theta,\phi,z) = \int_0^{2\pi} d\phi' \int_0^{\pi/2} d\theta' \sin\theta' \, \bar{\bar{P}}(\pi-\theta,\phi;\theta',\phi') \cdot \bar{I}^{(n-1)}(\theta',\phi',z) \tag{2.1c}$$

$$\bar{W}_d^{(n)}(\theta,\phi,z) = \int_0^{2\pi} d\phi' \int_0^{\pi/2} d\theta' \sin\theta' \, \bar{\bar{P}}(\pi-\theta,\phi;\pi-\theta',\phi') \cdot \bar{I}^{(n-1)}(\pi-\theta',\phi',z) \tag{2.1d}$$

Note $\bar{S}_u^{(n)}$, $\bar{S}_d^{(n)}$, $\bar{W}_u^{(n)}$ and $\bar{W}_d^{(n)}$ denotes all four possibilities of transition in energy flow direction due to scattering by particle once. Substituting the decomposition of $\bar{S}^{(n)}(\theta,\phi,z) = \bar{S}_u^{(n)}(\theta,\phi,z) + \bar{S}_d^{(n)}(\theta,\phi,z)$ and $\bar{W}^{(n)}(\theta,\phi,z) = \bar{W}_u^{(n)}(\theta,\phi,z) + \bar{W}_d^{(n)}(\theta,\phi,z)$ into equation (A.5a, A.5b), equation (A.5a) and (A.5b) are naturally grouped into four parts, respectively. $\bar{I}^{(n)}(\theta,\phi,z) = \bar{I}_{Su}^{(n)}(\theta,\phi,z) + \bar{I}_{Sd}^{(n)}(\theta,\phi,z) + \bar{I}_{Wu}^{(n)}(\theta,\phi,z) + \bar{I}_{Wd}^{(n)}(\theta,\phi,z)$, and $\bar{I}^{(n)}(\pi-\theta,\phi,z) = \bar{I}_{Su}^{(n)}(\pi-\theta,\phi,z) + \bar{I}_{Sd}^{(n)}(\pi-\theta,\phi,z) + \bar{I}_{Wu}^{(n)}(\pi-\theta,\phi,z) + \bar{I}_{Wd}^{(n)}(\pi-\theta,\phi,z)$, where the second subscript of 'u' (upward) and 'd' (downward) denotes the direction of energy flow before scattering, and the first subscript of 'S' (upward) and 'W' (downward) denotes the direction of energy flow after scattering, respectively. The terms in the right hand side are defined as follows,

$$\bar{I}_{Su}^{(n)}(\theta,\phi,z) = \exp(-\kappa_e(z+2d)\sec\theta)\,\bar{\bar{R}}_{12}(\theta)\bar{\bar{Z}}^{-1}(\theta)\bar{\bar{R}}_{10}(\theta)\bar{S}_{cu}^{(n)}(\theta,\phi) + \bar{S}_{zu}^{(n)}(\theta,\phi,z) \tag{2.2a}$$

$$\bar{I}_{Sd}^{(n)}(\theta,\phi,z) = \exp(-\kappa_e(z+2d)\sec\theta)\,\bar{\bar{R}}_{12}(\theta)\bar{\bar{Z}}^{-1}(\theta)\bar{\bar{R}}_{10}(\theta)\bar{S}_{cd}^{(n)}(\theta,\phi) + \bar{S}_{zd}^{(n)}(\theta,\phi,z) \tag{2.2b}$$

$$\bar{I}_{Wu}^{(n)}(\theta,\phi,z) = \exp(-\kappa_e(z+d)\sec\theta)\,\bar{\bar{R}}_{12}(\theta)\bar{\bar{Z}}^{-1}(\theta)\bar{W}_{cu}^{(n)}(\theta,\phi) \tag{2.2c}$$

$$\bar{I}_{Wd}^{(n)}(\theta,\phi,z) = \exp(-\kappa_e(z+d)\sec\theta)\,\bar{\bar{R}}_{12}(\theta)\bar{\bar{Z}}^{-1}(\theta)\bar{W}_{cd}^{(n)}(\theta,\phi) \tag{2.2d}$$

$$\bar{I}_{Su}^{(n)}(\pi-\theta,\phi,z) = \exp(\kappa_e z\sec\theta)\,\bar{\bar{Z}}^{-1}(\theta)\bar{\bar{R}}_{10}(\theta)\bar{S}_{cu}^{(n)}(\theta,\phi) \tag{2.2e}$$

$$\bar{I}_{Sd}^{(n)}(\pi-\theta,\phi,z) = \exp(\kappa_e z\sec\theta)\,\bar{\bar{Z}}^{-1}(\theta)\bar{\bar{R}}_{10}(\theta)\bar{S}_{cd}^{(n)}(\theta,\phi) \tag{2.2f}$$

$$\bar{I}_{Wu}^{(n)}(\pi-\theta,\phi,z)$$

$$= \exp(\kappa_e(z-d)\sec\theta)\,\bar{\bar{Z}}^{-1}(\theta)\bar{\bar{R}}_{10}(\theta)\bar{\bar{R}}_{12}(\theta)\bar{W}_{cu}^{(n)}(\theta,\phi) \tag{2.2g}$$

$$+ \bar{W}_{zu}^{(n)}(\theta,\phi,z)$$

$$\bar{I}_{Wd}^{(n)}(\pi-\theta,\phi,z)$$

$$= \exp(\kappa_e(z-d)\sec\theta)\,\bar{\bar{Z}}^{-1}(\theta)\bar{\bar{R}}_{10}(\theta)\bar{\bar{R}}_{12}(\theta)\bar{W}_{cd}^{(n)}(\theta,\phi) \tag{2.2h}$$

$$+ \bar{W}_{zd}^{(n)}(\theta,\phi,z)$$

where $\bar{S}_{cu}^{(n)}$, $\bar{S}_{cd}^{(n)}$, $\bar{S}_{zu}^{(n)}$, $\bar{S}_{zd}^{(n)}$, $\bar{W}_{cu}^{(n)}$, $\bar{W}_{cd}^{(n)}$, $\bar{W}_{zu}^{(n)}$, and $\bar{W}_{zd}^{(n)}$ are defined similar to $\bar{S}_{c}^{(n)}$, $\bar{S}_{z}^{(n)}$, $\bar{W}_{c}^{(n)}$, and $\bar{W}_{z}^{(n)}$ in equation (A.5a, A.5b) by introducing a new subscript u/d in $\bar{S}^{(n)}$ and $\bar{W}^{(n)}$. It immediately follows that each term in $\bar{I}^{(n-1)}(\theta,\phi,z)$ contributes to two terms in $\bar{I}^{(n)}(\theta,\phi,z)$ and two terms in $\bar{I}^{(n)}(\pi-\theta,\phi,z)$ through $\bar{S}_{u}^{(n)}$ and $\bar{W}_{u}^{(n)}$, and each term in $\bar{I}^{(n-1)}(\pi-\theta,\phi,z)$ contributes to another two terms in $\bar{I}^{(n)}(\theta,\phi,z)$ and two terms in $\bar{I}^{(n)}(\pi-\theta,\phi,z)$ through $\bar{S}_{d}^{(n)}$ and $\bar{W}_{d}^{(n)}$. A simple deduction results in a total of 4^n separated terms in $\bar{I}^{(n)}(\theta,\phi,z)$ as a result of two reflective boundaries, which greatly increases the number of scattering paths. All these terms could be separated through the bridging connection of $\bar{S}_{u}^{(n)}$, $\bar{S}_{d}^{(n)}$, $\bar{W}_{u}^{(n)}$ and $\bar{W}_{d}^{(n)}$.

In Figure II.3, several scattering terms are illustrated for example. Each term is depicted by a scattering path in backscattering direction. In general, for each of these paths, if the energy flow direction is reversed, it corresponds to another distinct scattering and reflection process. In the backscattering direction, if this also holds, it is a cyclical term, as shown in Figure II.3 (c, d). A cyclical term is special that in the backscattering direction, the two scattering fields of the two reverse scattering processes are identical for co-polarization, both in magnitude and phase. The coherent addition of fields gains a factor of two comparing to the incoherent addition of intensity. However, there are also non-cyclical terms, as shown in Figure II.3 (a, b). If the non-cyclical path

is reversed, it is still itself, representing the same physical scattering process in backscattering direction. It is possible to determine whether a term is cyclical by examining the scattering paths of propagation. A close examination reveals that only two non-cyclical terms exist, as illustrated in Figure II.3 (a, b). These two terms are the direct volume backscattering illustrated in Figure II.3 (a) and the reflection followed by the backward scattering followed by reflection illustrated in Figure II.3 (b) in first order scattering. Both these terms involve the backward volume scattering in first order. This is true because for any higher order scattering, the scattering events of the succeeding scatterers could always reverse the sequence to form a physically unique dual scattering path even in the backscattering direction.

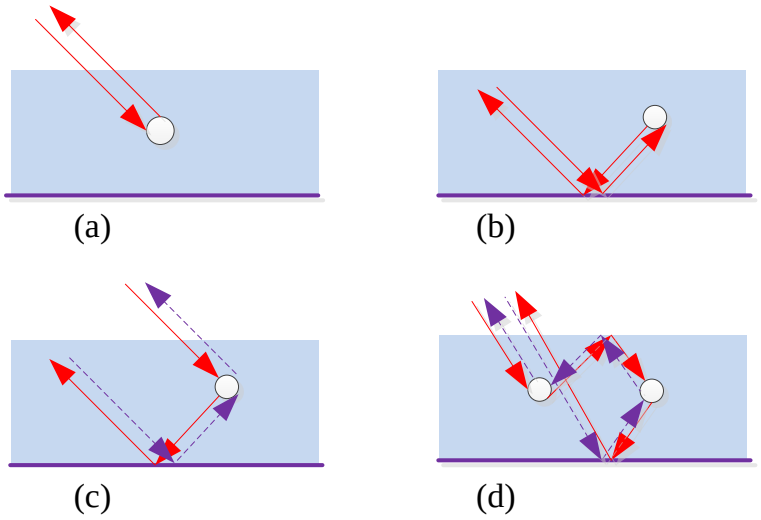

Figure II.3. Illustration of scattering terms (a) non-cyclical term in 1st order backward volume scattering (b) non-cyclical term in 1st order volume scattering with two bounces from the bottom surface before and after the volume scattering (c) dual cyclical terms in 1st order volume-surface double bounce scattering (d) dual cyclical terms in 2nd order volume scattering with one bounce from the top surface in connection of the two volume scattering and another bounce from the bottom surface before or after the volume scattering.

The cyclical correction of the radiative transfer results involves the identification of cyclical terms and the inclusion of a factor of two for the contribution from these terms. Let us use $\sigma_{\rm cyc}$ to denote contribution to backscattering from cyclical terms, and use $\sigma_{\rm noncyc}$ to denote contribution from non-cyclical terms, then

$$\sigma = \sigma_{\rm cyc} + \sigma_{\rm noncyc} \tag{2.3a}$$

$$\sigma_{\rm cor} = 2\sigma_{\rm cyc} + \sigma_{\rm noncyc} = 2\sigma - \sigma_{\rm noncyc} \tag{2.3b}$$

where σ is the total volume backscattering without the cyclical correction, and $\sigma_{\rm cor}$ is the corrected total volume backscattering. This cyclical correction only applies to co-polarization volume backscattering.

The numerical procedure to evaluate the angular integrals in equation (A.2a, A.2b) and z-integrals in equation (A.4a, A.4b) are detailed in Appendix B, as well as the criterion to the choice of numerical parameters.

2.4 Significance of Cyclical Correction in Prediction of Backscattering Coefficients

In this section, we illustrate the results of the iterative approach with the scattering model of QCA for sticky spheres. We first show that the results of the iterative approach of DMRT agree with the results of the eigen-quadrature approach [18] without the cyclical correction, and then discuss the importance of the inclusion of cyclical terms under various snow conditions.

We consider a snowpack with thickness $d = 100cm$, snow fractional volume 25%, and ice particle grain diameter 1.4mm. The radar incidence angle is 54˚, and frequency 17.5GHz. The ice permittivity is set to be 3.15 + 0.001i, and flat ground permittivity 3.2 + 0.002i. The QCA stickiness parameter is 0.1. The resulting optical thickness τ is1.98, and scattering albedo ϖ is 0.98. We carry out the numerical iteration up to the 20$^{\rm th}$ order. There are good agreements in the bistatic

scattering pattern of the two approaches as shown in Figure II.4. Cyclical correction is not included in the bistatic scattering coefficient. The contribution to backscattering from different orders with and without cyclical correction is shown in Figure II.5. Note that with QCA phase matrix there is no cross-pol in 1st order backscattering. So the accumulation bar diagram for cross-pol starts from the 2nd order. We only apply cyclical correction to copolarized components. The rate that the scattering order converges depends on the optical thickness and scattering albedo. In this case, contributions from the first ten orders are sufficient. The cyclical correction to 1st order scattering is minor, since the two double bounce terms are small compared to volume scattering term. The cyclical correction to all the other orders doubles their contribution. Calculations were repeated for X band (9.6GHz) with similar conclusions. X band results show less effects of multiple scattering and enhancement.

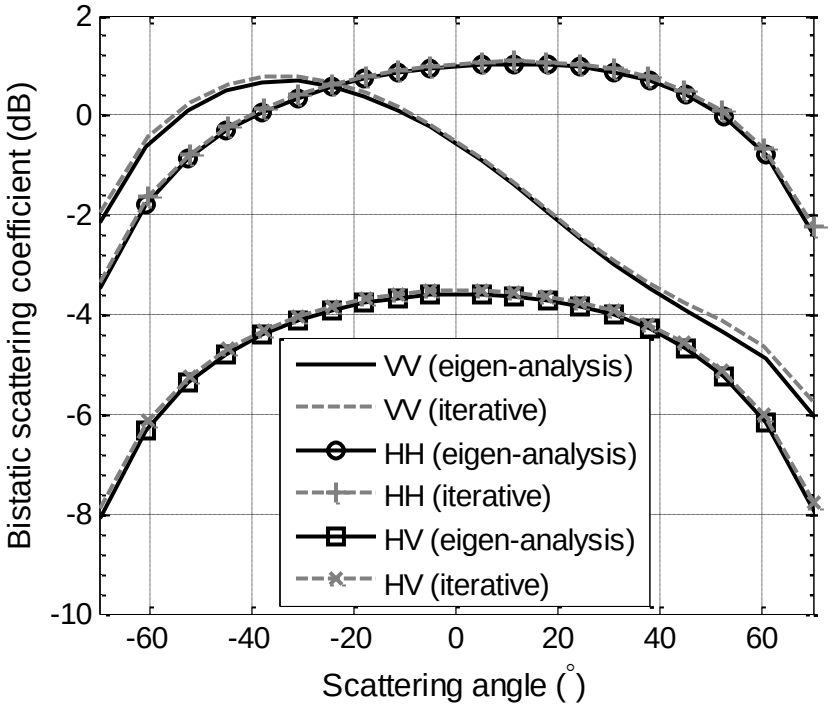

Figure II.4. Comparison of bistatic scattering coefficient between the eigen-analysis approach and iterative approach with grain size 1.4mm, frequency 17.5GHz, incidence angle 54°, and snow depth 100cm. The iterative approach has been computed up to 20th order. HV means v-pol transmission and h-pol receiving.

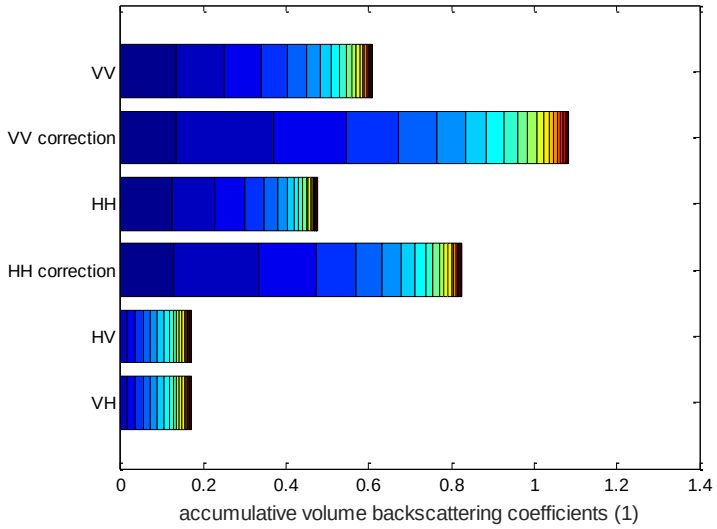

Figure II.5. Contribution to volume backscattering with / without cyclical correction from each scattering order at 17.5 GHz. Sections of bars depict the relative effect of scattering orders from left (1st order for co-pol and 2nd order for cross-pol) to right (20th order). HV means v-pol transmission and h-pol receiving.

Backscatter at 54° incidence angle with the snow grain diameter 1.0 mm, volume fraction 25%, stickiness parameter of 0.1, and snow-ground roughness with rms height of 3mm and correlation length of 21mm (the frozen ground permittivity is set as 5 + i1.5) is calculated for a shallow snowpack of depth 50cm and a thick snow pack of 100cm at X band (9.6GHz) and Ku (17.25GHz) band, respectively. The surface scattering from the snow-ground interface is interpolated from a pre-computed NMM3D lookup table [107, 108] including attenuation by the snow layer. The backscatter results are decomposed into surface scattering and volume scattering and compared in Table II-1. It is shown that at X band with shallow snowpack, the surface scattering is of the same order as volume scattering, and the backscattering enhancement is of less importance. At Ku band with thick snowpack, the volume scattering dominates, and the cyclical correction brings significant increase in the total backscatter. The conclusion is that backscattering

enhancement with significant optical thickness will cause a difference of 3dB enhancement. For a moderate optical thickness of 0.2, there will be ~1dB increase in backscatter.

Table II-1. Comparison of contribution to backscatter σ_{vv} (dB). The last column shows the optical thickness of the snow layer in the direction of wave incidence inside the snow media.

Frequency	Depth	σ_{surf}	σ_{vol}	σ_{vol}^{cor}	σ_{tot}	σ_{tot}^{cor}	$\tau_d / \cos\theta$
9.6 GHz	50 cm	-16.22	-13.86	-13.05	-11.87	-11.34	0.0921
	100 cm	-17.02	-10.80	-9.74	-9.87	-8.99	0.1842
17.25 GHz	50 cm	-18.18	-6.06	-4.22	-5.80	-4.05	0.6724
	100 cm	-24.02	-3.74	-1.56	-3.70	-1.53	1.3449

2.5 Validation against The NoSREx Campaign of Coincidental Active and Passive Measurement over The Same Scene

The Finnish Meteorological Institute (FMI) has hosted the Nordic Snow Radar Experiment (NoSREx) campaign [103, 104] under an ESA contract for four successive winter seasons from November 2009 through May 2013. The NoSREx campaign was conducted near the town of Sodankylä in northern Finland, about 100km north of the Arctic Circle. The objective of the campaign was to provide a continuous time series of coincidental active and passive microwave observations of snow cover, as part of Phase A studies for the proposed ESA CoReH2O mission. The main site for NoSREx activities was located at FMI Arctic Research Centre (FMI-ARC), known as the Intensive Observation Area (IOA). The IOA hosted three experimental microwave instruments: SnowScat, Elbara-II and SodRad. SnowScat is a frequency scanning scatterometer operating from X- to Ku- band (10.2, 13.3 and 16.7GHz); Elbara-II is a radiometer operating at L band (1.4GHz); SodRad is another radiometer operating from X- to W- band (10.65, 18.7, 36.5 and 90 GHz). All these three microwave instruments are installed on tower platforms, providing backscatter and brightness temperatures measurements at four incidence angles (30˚, 40˚, 50˚ and

60˚). The consolidated backscatter dataset of SnowScat is averaged over the full azimuth scan range. In situ measurements at IOA consist of manual snowpit measurements as well as extensive automated measurements on snow ground and meteorological parameters. The measurement sectors of the microwave instruments are located in a forest clearing. The location of the instruments, the approximate field of view of the instruments, and the location of manual snowpit observations are depicted in Figure II.6.

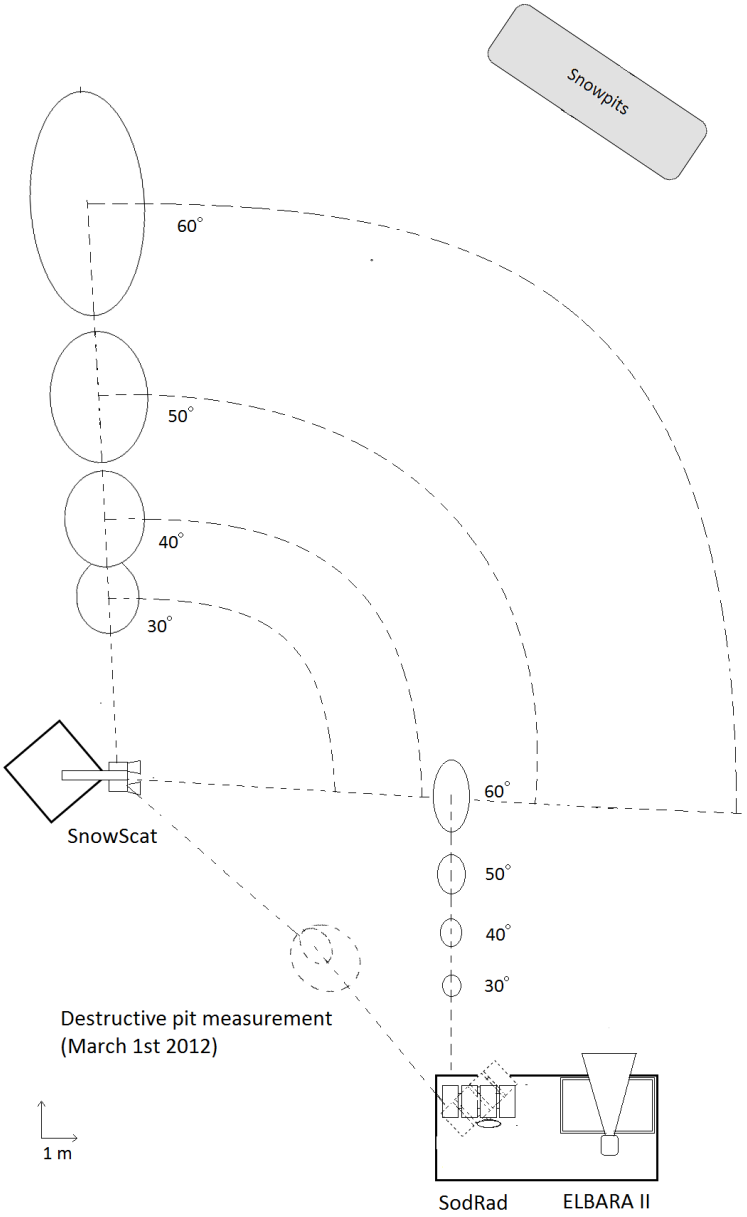

Figure II.6. Schematic of NoSREx measurement setup including SnowScat scatterometer and SodRad and ELBARA II radiometer systems. Approximate locations of SnowScat and SodRad 36.5 GHz receiver footprints at 30, 40, 50 and 60° incidence angles are depicted. At each incidence angle, SnowScat measured 17 discrete look directions over an arc spanning 96° over the test field. SnowScat was mounted at the height of 9.1 m, while SodRad receivers were at a height of approximately 4.5 m from the ground surface. Approximate location of snowpit measurements is also indicated. A destructive snowpit measurement was made on March 1st, 2012, with both SnowScat and SodRad measuring the same spot on the test field; the location of the pit coincided with SodRad measurements at 50° incidence angle.

Weekly snowpit measurements included the measurement of the snow temperature profile, measured using a digital thermometer at 10 cm vertical resolution, the snow density profile, measured using a manual scale at a 5 cm vertical resolution, as well as bulk snow density and snow water equivalent (SWE), using a large manual scale. Snow stratigraphy (layering) was identified visually and by use of a manual aid based of changes in snow hardness. The snow grain size and type were identified following Fierz et al. [109]. However, snow grain size was also analyzed in post-processing from macro photography, giving an approximate grain size for each layer at the precision of ¼ mm. A total of 31 snowpit measurements were made during the season of 2010-2011; 20 of these were made in dry snow conditions, between November 10th 2010, and March 29th, 2011. Figure II.7 depicts the manually measured SWE, bulk snow density, and snow grain size. The grain size values represent the average of measured grain size values over the snowpack, weighted by the respective depth of each layer. The average grain size (of depth-weight values) in the dry snow period was 1.4 mm, with a standard deviation of 0.2 mm. The large standard deviation reflects observer errors which originate from the highly subjective measurement methodology. Nevertheless, the mean grain size reflects snowpack metamorphism and average conditions: the initial rise in mean grain size between November 2010 and January 2011 reflects an increase in snow grain size due to snow faceting and rounding depending on the temperature gradient inside the snowpack. On the other hand, the slightly decreasing trend between January and March, 2011, reflects the increase of fine-grained snow through precipitation, decreasing the average grain size. Snow metamorphism continued in older snow layers also during this period.

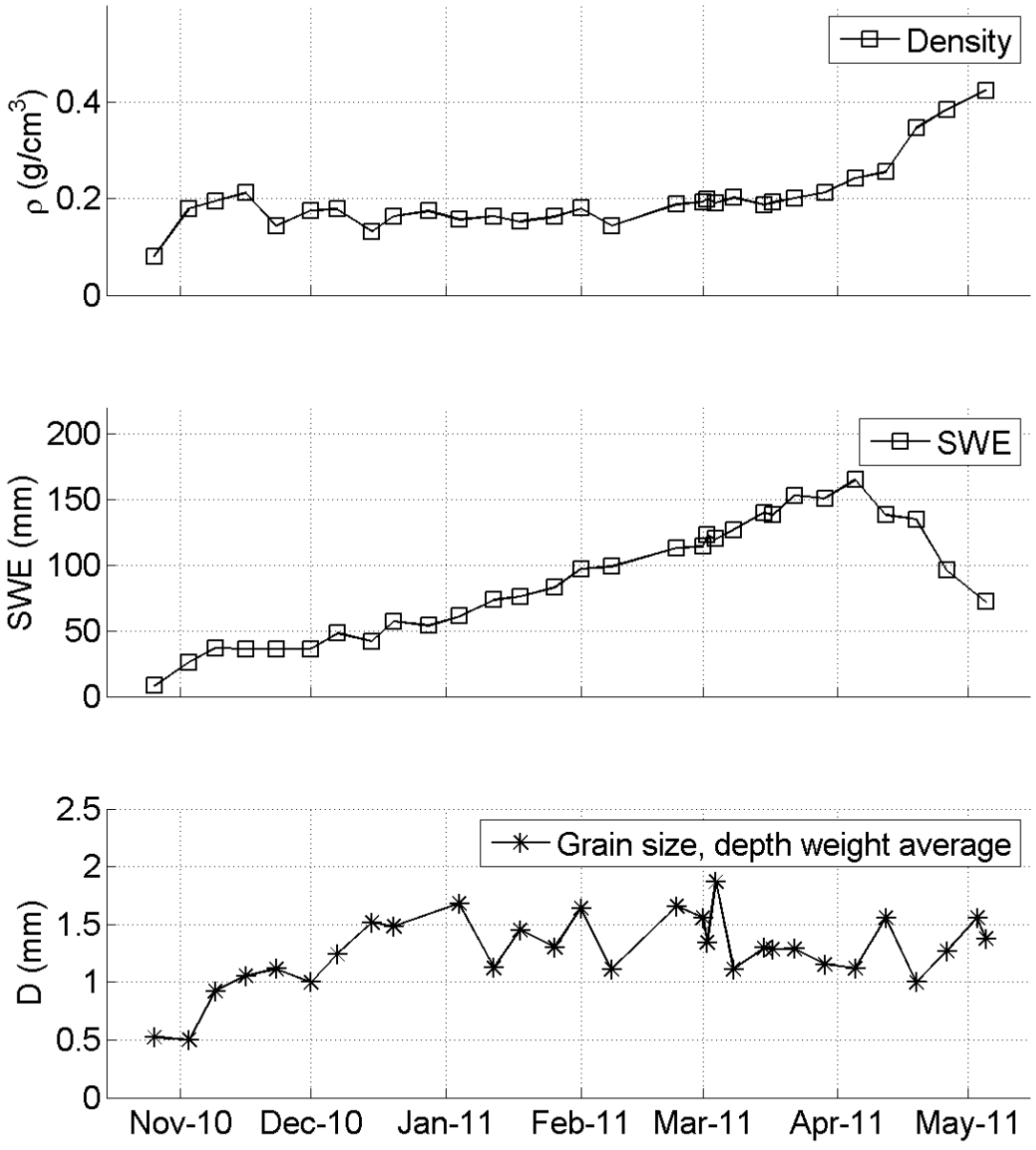

Figure II.7. Manually measured bulk snow density (a), SWE (b), and snow grain size (c) at the IOA site during 2010-2011. The grain size values represent the average of measured grain size values over the snowpack, weighted by the respective depth of each layer.

Automated data from the site include measurements of air temperature, soil temperature at 2 cm depth, soil moisture at 2 and 10 cm depths, as well as snow depth. All automated data was

recorded every ten minutes. Figure II.8 shows the measured snow depth (a), air and soil temperature (b) and soil moisture (c) at the site during 2010-2011. The first snowfall of the season occurred on October 29th, 2010. Temperatures on the following days remained above freezing point (up to +3°C) causing some initial melt of the fresh snowpack. However, from November 10th onwards, temperatures remained below zero until March 2nd, 2011, when temperatures rose to +1.7°C. Similar short periods of above-zero temperatures were experienced on several occasions in March. Initial cold temperatures in November, combined with a relatively shallow snowpack of < 20 cm resulted in a rapid freezing of the soil. Low values of measured volumetric soil moisture (< 0.05 m^3/m^3), after mid-November in Figure II.8 (c) reflect the low permittivity of frozen soil measured by the soil moisture probes. Major precipitation events (10 cm or over increase in snow depth) were experienced on December 8th, January 17th, and March 14th. Sustained periods of snowfall lasting several days occurred between 30 December, 2010 and January 8th, 2011 as well as between January 31st and February 8th, 2011. A maximum snow depth of 80 cm (ca. 170 mm in SWE) was reached in March.

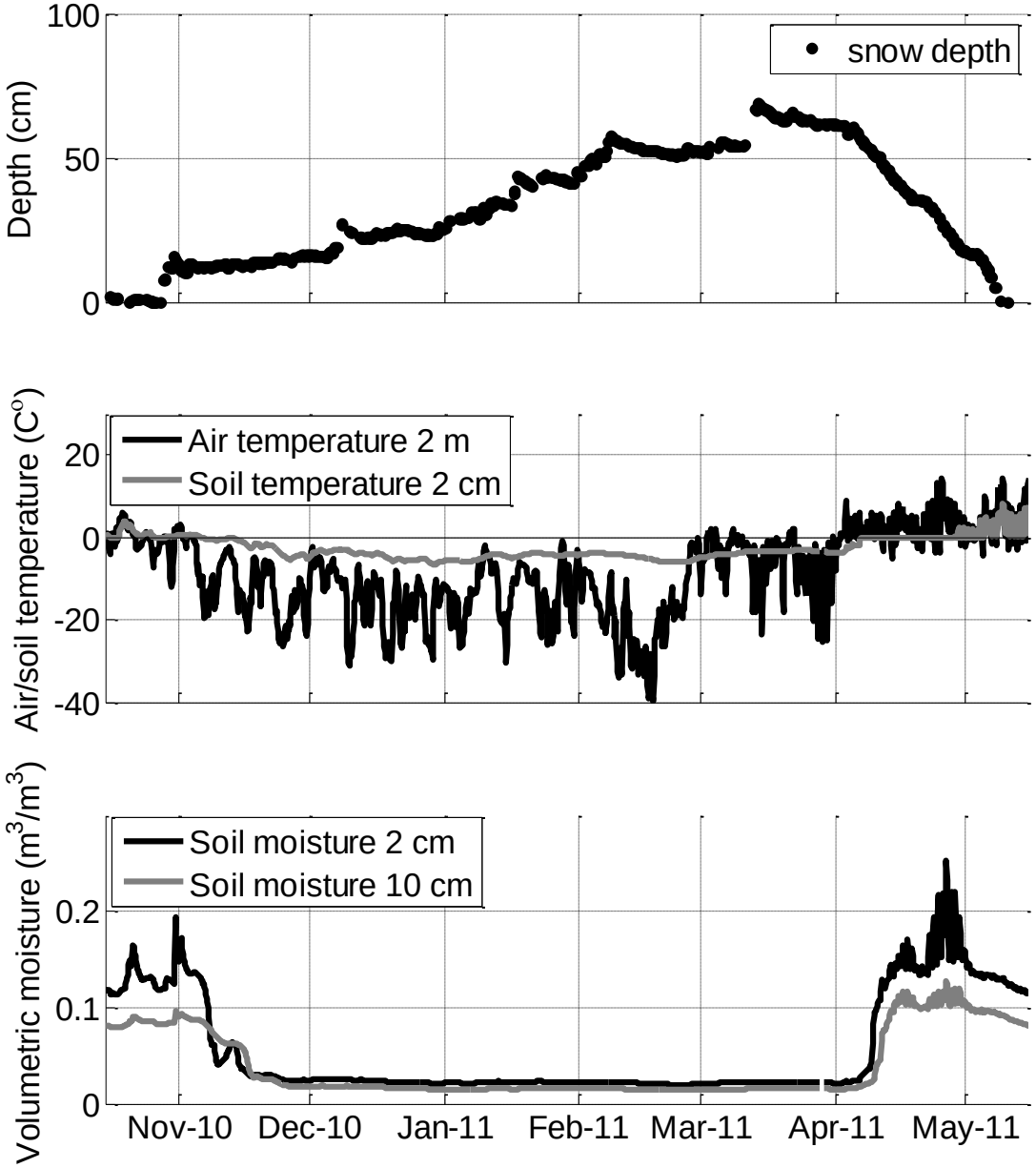

Figure II.8. Automated measurement of snow depth (a), air and soil temperature (b) and soil moisture (c) at the IOA site during 2010-2011.

In this section, the SnowScat backscatter observation at three frequencies ranging from X- to Ku- band (10.2, 13.3 and 16.7GHz) and the SodRad brightness temperature observation at three

frequencies ranging from X- to Ka- band (10.65, 18.7 and 36.5GHz) are selected to compare with model predictions. Five representative dates (Jan. 12, Jan. 18, Feb. 1, Feb. 8, and Mar. 1) with backscatter, brightness temperature observations and snowpit measurements collected during the winter season of 2010 to 2011 are chosen. It is noted from Figure II.7 and Figure II.8 that during this period, the snow density remain stable, the SWE keeps increasing, and the air temperature remains below 0°C. Thus the main uncertainty inside the snowpack is the stratigraphy and snow grain morphology. Brightness temperature and backscatter collected at 40° incidence angle are used. The microwave observation data as plotted in Figure II.9 through Figure II.11 shows positive correlation of backscatter with SWE at the two Ku band channels of 13.3GHz and 16.7GHz in both co-pol and cross-pol. There is around 2dB dynamic range in radar backscatter at 16.7GHz for SWE increasing from 73.5 to 114mm. Data also imply that there is a general negative correlation of brightness temperature (T_b) with SWE except for the abnormal increase of T_b at 10.65GHz with the largest SWE as shown in Figure II.10. The sensitivity of brightness temperature to SWE is best at 36.5GHz with ~10K decrease in V-pol and ~15K decrease in H-pol, for the same change in SWE.

The same bicontinuous media parameter is chosen to represent snow and applied to both active and passive models for all the six microwave channels. The bulk density, snowpack thickness and the ground temperature are taken directly from measurements. The snow temperature are taken as the temperature at 10cm above ground. The ground is assumed to be rough with rms height of 1mm and exponential correlation length of 4mm. The ground relative permittivity is set to be $3.0 + 0.001i$ relative to the effective permittivity of snow. The surface backscattering of co-polarization and cross polarization is taken from a pre-built lookup table based on numerical solution of Maxwell equations in 3D (NMM3D) [107, 108]. The rough surface

backscattering is next attenuated by the snow layer. In the passive DMRT code [22], the ground is assumed to be smooth. The vertical co-polarization backscatter is plotted versus SWE and compared against measurements in Figure II.9. The brightness temperature is plotted against SWE in Figure II.10 (a-c) for three different passive frequencies, respectively. The single set of physical parameters used in data matching is shown in Table II-2.

The results show that one set of physical parameters when put in the physical bicontinuous DMRT model with cyclical corrections can match microwave measurements in all six channels, for both active and passive. Without the cyclical corrections to DMRT, matching the backscatter would have the model predictions of brightness temperature lower than measurements. The statistics of the comparison between model and data are shown in Table II-3 and Table II-4 for backscatter and brightness temperature, respectively. The co-pol backscatter has an RMS error less than 0.5dB in all frequency channels. Without cyclical correction, the model prediction of backscatter will be further lower by ~0.5dB at 13.3GHz, and by ~1dB at 16.7GHz. It is also noted that the V pol brightness temperature has a better comparison than H-pol in terms of RMS error, which is possibly due to the sensitivity to reflections in H-polarization between snow layers. Note in Figure II.10 (a), the H-pol brightness temperature measurement at X band of 10.65 GHz seems unstable with respect to the increase in SWE, partially responsible for the worsened RMSE. The abnormal behavior of high T_{bh} with the largest SWE is still under investigation. A possible reason includes undetected changes in snow stratigraphy of the lowest snow layers, which are not apparent in the available in situ information. These would affect the horizontally polarized brightness temperature due to changes in the effective incidence angle at the snow-ground interface. These changes would be more apparent at low frequencies due to the low extinction of snow; similar variations in H-pol behavior were apparent also at L-band.

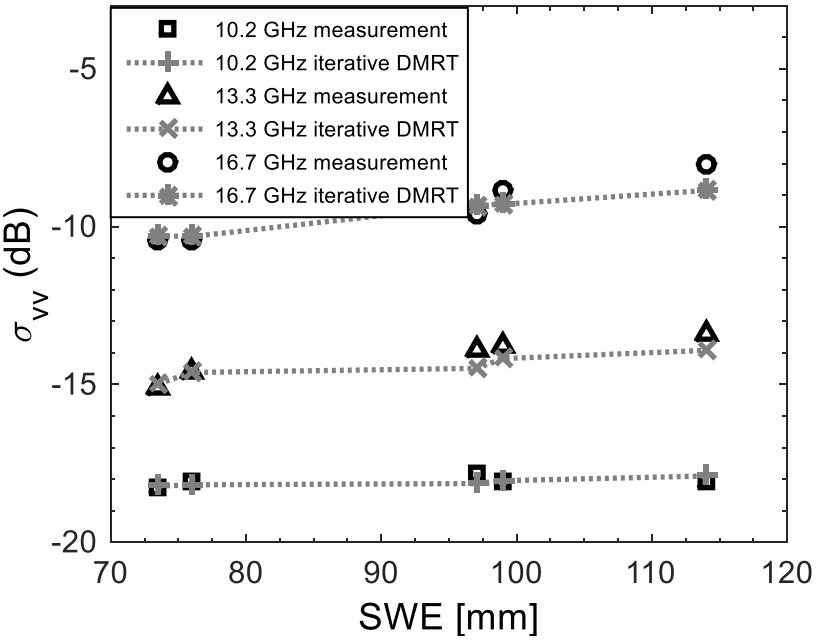

Figure II.9. Backscatter against SWE for vertical co-pol at 10.2GHz, 13.3GHz, and 16.7GHz. The DMRT results include cyclical correction.

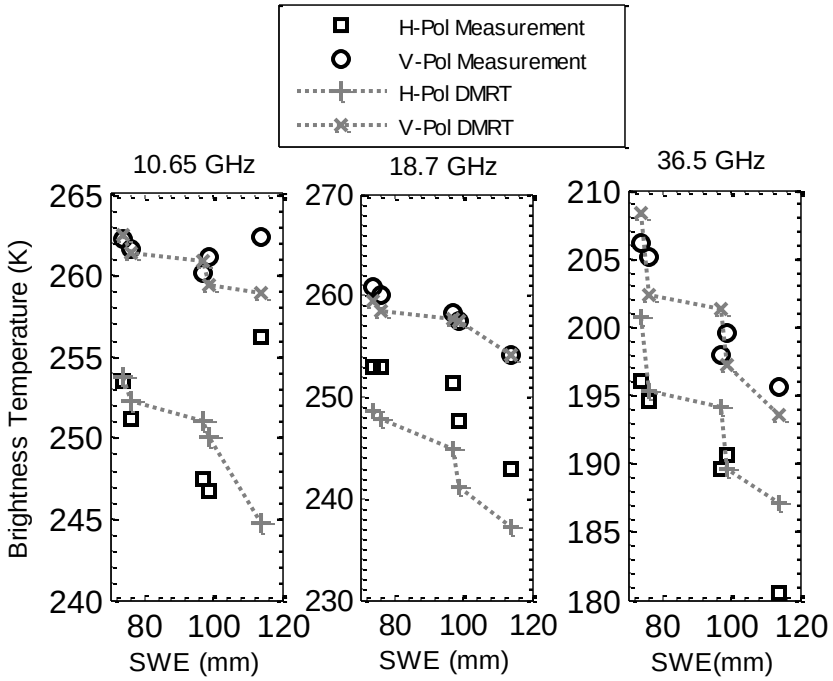

Figure II.10. Brightness temperature against SWE at (a) 10.65GHz, (b) 18.7GHz and (c) 36.5GHz.

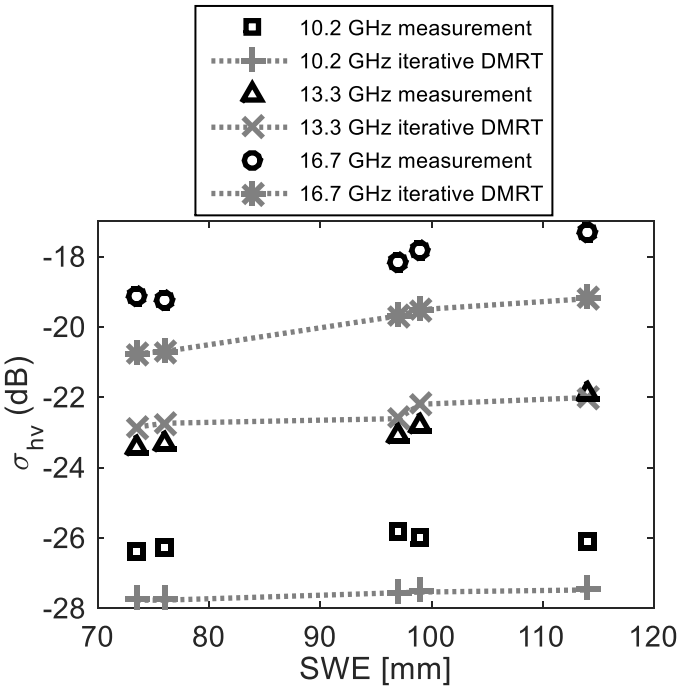

Figure II.11. Backscatter against SWE for cross-pol σ_{hv} at 10.2GHz, 13.3GHz, and 16.7GHz. See text for cyclical corrections to DMRT results.

Table II-2. Snowpack properties and bicontinuous media parameters

	Snow Depth [cm]	Density [g / cc]	$\langle\zeta\rangle$ [m^{-1}]	b	Snow temperature [ºC]	Ground temperature [ºC]
Jan. 12	44.3	0.163	10000	2.0	-4.0	-3.5
Jan. 18	51.7	0.152	10000	1.2	-5.0	-4.3
Feb. 01	54.3	0.180	9000	1.5	-5.2	-4.6
Feb. 08	68.7	0.143	11000	1.0	-8.2	-6.4
Mar. 01	60.7	0.193	11000	2.0	-4.8	-4.5

In Figure II.11, the corresponding cross-pol backscatter σ_{hv} is also plotted versus SWE and compared against measurements for the sake of completeness. The cross-pol enhancement mechanism is complicated and can be modeled using the wave approach. However, here an intuitive correction to cross-pol by adding a factor of two to all the higher order backscattering contributions above the 1st order is applied. Since the cross-pol phase matrix of bicontinuous media fluctuates around a certain level with respect to the angle Θ between the incidence direction and

scattering direction [18-20], we use the cross polarized phase matrix that is an average over the angle Θ. The modified phase matrix is then put into the active iterative DMRT code to estimate the cross-pol. The results of cross-pol are within 2 dB of the measurement and follow the increasing trend against SWE for all three frequencies. The statistics for comparison of cross-pol backscatter is also given in Table II-3. It should be noted that the model simulations are in good agreement with experimental data at 13.3 GHz but underestimate the measurements at 10.2 GHz and 16.7 GHz. The discrepancy between model and data may be due to the inaccuracy in cross-pol phase matrix calculation. The comparison of cross-pol is to illustrate that bicontinuous media / DDA approach has the potential capability to predict cross-pol correctly. The cross-pol is presently studied using the wave approach.

Table II-3. Statistics of comparison between model prediction and measurement for co-pol and cross-pol backscatter

σ^0 (dB)	VV			HV		
Frequency	10.2 GHz	13.3 GHz	16.7 GHz	10.2 GHz	13.3 GHz	16.7 GHz
Bias	-0.034	-0.278	-0.154	-1.514	0.426	1.634
RMS	0.1807	0.397	0.4493	1.5206	0.4978	1.6402

Table II-4. Statistics of comparison between model prediction and measurement for v-pol and h-pol brightness temperature

Tb (K)	V			H		
Frequency	10.65 GHz	18.7 GHz	36.5 GHz	10.65 GHz	18.7 GHz	36.5 GHz
Bias	-0.9	-0.66	-0.32	-0.58	-5.7	3.14
RMS	1.7782	0.9788	2.6054	5.5859	5.7621	4.1797

The parameterization of the bicontinuous media to represent snow is a problem of continual investigation. The bicontinuous media uses two parameters, the mean wavenumber $\langle\zeta\rangle$ and the parameter b. A larger $\langle\zeta\rangle$ leads to a smaller mean grain size, and a larger b leads to more uniform

distribution in grain size. Both parameters control the correlation function. Thus if the correlation function of snow is measured accurately, then the bicontinuous parameters can be determined [28, 110, 111]. In the present work, $\langle \zeta \rangle$ and b are manually tuned to match both the backscatter and brightness temperature in multiple channels, with the model derived correlation length and specific surface area (SSA) falling within the range of measurements [21, 28, 110, 111].

2.6 Conclusions

The classical radiative transfer theory does not include the cyclical terms in the Feynman diagram. When DMRT is applied to active or passive remote sensing of snowpack separately, this omission does not cause serious problems as model parameters can always be adjusted to fit observational active and passive data separately. However, when both active and passive remote sensing of snowpack are being modeled simultaneously over the same scene, one must take into account backscattering enhancement effects originating from these cyclical terms. With this new approach, we show in this chapter that backscattering enhancement effects are important for moderate snowpack optical thickness, and could increase backscatter up to approximately 3dB without decreasing brightness temperature. For a moderate optical thickness of 0.2, there will be a ~1dB increase in backscatter due to the cyclical correction. The bicontinuous media scattering model, when combined with DMRT with cyclical correction, are in good agreement with both passive and active observations from the NoSREx campaign for multiple channels.

Appendix A DMRT and iterative approach

In this appendix, we formulate the iterative approach to solve DMRT equations.

Consider the active remote sensing of a snow layer with thickness d above ground, as shown in Figure II.2. Region 0 is air, region 1 is snow and region 2 is ground. The vector dense media radiative transfer (DMRT) equations governing the specific intensity $\bar{I}(\theta,\phi,z)$ are [24]

$$\cos\theta\frac{d\bar{I}(\theta,\phi,z)}{dz}=-\kappa_e\cdot\bar{I}(\theta,\phi,z)+\bar{S}(\theta,\phi,z) \tag{2.A.1a}$$

$$-\cos\theta\frac{d\bar{I}(\pi-\theta,\phi,z)}{dz}=-\kappa_e\cdot\bar{I}(\pi-\theta,\phi,z)+\bar{W}(\theta,\phi,z) \tag{2.A.1b}$$

where κ_e is the extinction coefficient. The source terms $\bar{S}(\theta,\phi,z)$ and $\bar{W}(\theta,\phi,z)$ are related to the specific intensity by phase matrix $\bar{\bar{P}}$,

$$\begin{aligned}\bar{S}(\theta,\phi,z)=\int_0^{2\pi}d\phi'\int_0^{\pi/2}d\theta'\,\sin\theta'\,\big[&\bar{\bar{P}}(\theta,\phi;\theta',\phi')\cdot\bar{I}(\theta',\phi',z)\\&+\bar{\bar{P}}(\theta,\phi;\pi-\theta',\phi')\cdot\bar{I}(\pi-\theta',\phi',z)\big]\end{aligned} \tag{2.A.2a}$$

$$\begin{aligned}\bar{W}(\theta,\phi,z)=\int_0^{2\pi}d\phi'\int_0^{\pi/2}d\theta'\,\sin\theta'\,\big[&\bar{\bar{P}}(\pi-\theta,\phi;\theta',\phi')\\&\cdot\bar{I}(\theta',\phi',z)+\bar{\bar{P}}(\pi-\theta,\phi;\pi-\theta',\phi')\\&\cdot\bar{I}(\pi-\theta',\phi',z)\big]\end{aligned} \tag{2.A.2b}$$

The top reflective boundary condition at $z=0$,

$$\begin{aligned}\bar{I}(\pi-\theta,\phi,z=0)&\\=\bar{\bar{R}}_{10}(\theta)\bar{I}(\theta,\phi,z=0)&\\+\bar{\bar{T}}_{01}(\theta_0)\bar{I}_0\delta(\cos\theta_0-\cos\theta_{0\mathrm{inc}})\delta(\phi-\phi_{\mathrm{inc}})&\end{aligned} \tag{2.A.3a}$$

and the bottom reflective boundary condition at $z=-d$,

$$\bar{I}(\theta,\phi,z=-d)=\bar{\bar{R}}_{12}(\theta)\bar{I}(\pi-\theta,\phi,z=-d) \tag{2.A.3b}$$

The angle in air region θ_0 is related to the angle in snow region θ by Snell's law, $n_0 \sin\theta_0 = n_1 \sin\theta$, where $n_1=\sqrt{\varepsilon_1/\varepsilon_0}$, and ε_1 is the real part of the effective dielectric constant of snow. The incidence angle in air region $\theta_{0\mathrm{inc}}$ is also related to angle θ_{inc} in snow region by Snell's law. $\bar{\bar{R}}_{10}(\theta)$ and $\bar{\bar{R}}_{12}(\theta)$ are the reflective matrix on the snow-air boundary and the snow-ground boundary. $\bar{\bar{T}}_{01}(\theta_0)$ is the transmissivity matrix from air to snow [24].

When the bottom boundary is rough with rms height h, the coherent reflectivity $\bar{\bar{R}}_{12}(\theta)$ is multiplied by an attenuation factor K_F^2 following Kirchhoff approximation, where $K_F = \exp(-2(n_1 k\cos\theta\, h)^2)$. k is the wave number in free space.

To facilitate the iterative approach, the DMRT equations are cast into two coupled integral equations [24],

$$\begin{aligned}
&\bar{I}(\theta,\phi,z)\\
&=\exp\left(-\kappa_e(z+2d)\sec\theta\right)\bar{\bar{R}}_{12}(\theta)\bar{\bar{Z}}^{-1}(\theta)\bar{\bar{T}}_{01}(\theta_0)\\
&\times\bar{I}_0\delta(\cos\theta-\cos\theta_{\mathrm{inc}})\delta(\phi-\phi_{\mathrm{inc}})\\
&+\sec\theta\exp\left(-\kappa_e(z+2d)\sec\theta\right)\bar{\bar{R}}_{12}(\theta)\bar{\bar{Z}}^{-1}(\theta)\bar{\bar{R}}_{10}(\theta)\\
&\times\int_{-d}^{0}dz'\exp\left(\kappa_e z'\sec\theta\right)\bar{S}(\theta,\phi,z')\\
&+\sec\theta\exp\left(-\kappa_e(z+d)\sec\theta\right)\bar{\bar{R}}_{12}(\theta)\bar{\bar{Z}}^{-1}(\theta)\\
&\times\int_{-d}^{0}dz'\exp\left(-\kappa_e(z'+d)\sec\theta\right)\bar{W}(\theta,\phi,z')\\
&+\sec\theta\int_{-d}^{z}dz'\exp\left(\kappa_e(z'-z)\sec\theta\right)\bar{S}(\theta,\phi,z')
\end{aligned} \tag{2.A.4a}$$

$$
\begin{aligned}
&\bar{I}\left(\pi-\theta,\phi,z\right)\\
&=\exp\left(\kappa_e z\sec\theta\right)\bar{\bar{Z}}^{-1}\left(\theta\right)\bar{\bar{T}}_{01}\left(\theta_0\right)\bar{I}_0\delta\left(\cos\theta-\cos\theta_{\text{inc}}\right)\delta\left(\phi-\phi_{\text{inc}}\right)\\
&+\sec\theta\exp\left(\kappa_e z\sec\theta\right)\bar{\bar{Z}}^{-1}\left(\theta\right)\bar{\bar{R}}_{10}\left(\theta\right)\\
&\times\int_{-d}^{0}dz'\exp\left(\kappa_e z'\sec\theta\right)\bar{S}\left(\theta,\phi,z'\right)\\
&+\sec\theta\exp\left(\kappa_e\left(z-d\right)\sec\theta\right)\bar{\bar{Z}}^{-1}\left(\theta\right)\bar{\bar{R}}_{10}\left(\theta\right)\bar{\bar{R}}_{12}\left(\theta\right)\\
&\times\int_{-d}^{0}dz'\exp\left(-\kappa_e\left(z'+d\right)\sec\theta\right)\bar{W}\left(\theta,\phi,z'\right)\\
&+\sec\theta\int_{z}^{0}dz'\exp\left(\kappa_e\left(z'-z\right)\sec\theta\right)\bar{W}\left(\theta,\phi,z'\right)
\end{aligned}
\tag{2.A.4b}
$$

where $\bar{\bar{Z}}(\theta)=\bar{\bar{I}}-\bar{\bar{R}}_{10}(\theta)\bar{\bar{R}}_{12}(\theta)\exp(-\kappa_e 2d\sec\theta)$.

Equation (A.4a, A.4b) could be solved using iterative approach, $\bar{I}=\bar{I}^{(0)}+\bar{I}^{(1)}+\cdots$, by viewing $\bar{S}$ and $\bar{W}$ as small perturbations. The zero-th order solution $\bar{I}^{(0)}$, known as the reduced solution, is the first term in equation (A.4a, A.4b) and does not contribute to backscattering. The n-th order solution $\bar{I}^{(n)}$ $(n=1,2,\dots)$ could be updated from lower order solution $\bar{I}^{(n-1)}$ through source terms $\bar{S}^{(n)}$ and $\bar{W}^{(n)}$.

$$
\begin{aligned}
\bar{I}^{(n)}(\theta,\phi,z)=&\exp(-\kappa_e(z+2d)\sec\theta)\,\bar{\bar{R}}_{12}(\theta)\bar{\bar{Z}}^{-1}(\theta)\bar{\bar{R}}_{10}(\theta)\bar{S}_c^{(n)}(\theta,\phi)\\
&+\exp(-\kappa_e(z+d)\sec\theta)\,\bar{\bar{R}}_{12}(\theta)\bar{\bar{Z}}^{-1}(\theta)\bar{W}_c^{(n)}(\theta,\phi)\\
&+\bar{S}_z^{(n)}(\theta,\phi,z)
\end{aligned}
\tag{2.A.5a}
$$

$$
\begin{aligned}
&\bar{I}^{(n)}(\pi-\theta,\phi,z)\\
&\quad=\exp(\kappa_e z\sec\theta)\,\bar{\bar{Z}}^{-1}(\theta)\bar{\bar{R}}_{10}(\theta)\bar{S}_c^{(n)}(\theta,\phi)\\
&\quad+\exp(\kappa_e(z-d)\sec\theta)\,\bar{\bar{Z}}^{-1}(\theta)\bar{\bar{R}}_{10}(\theta)\bar{\bar{R}}_{12}(\theta)\bar{W}_c^{(n)}(\theta,\phi)\\
&\quad+\bar{W}_z^{(n)}(\theta,\phi,z)
\end{aligned}
\tag{2.A.5b}
$$

where $\bar{S}_c{}^{(n)}(\theta,\phi)$, $\bar{W}_c{}^{(n)}(\theta,\phi)$, $\bar{S}_z{}^{(n)}(\theta,\phi,z)$, and $\bar{W}_z{}^{(n)}(\theta,\phi,z)$ are defined as follows,

$$
\bar{S}_c{}^{(n)}(\theta,\phi)=\sec\theta\int_{-d}^{0}dz'\exp(\kappa_e z'\sec\theta)\,\bar{S}^{(n)}(\theta,\phi,z')
$$

$$\bar{W}_c^{(n)}(\theta,\phi) = \sec\theta \int_{-d}^{0} dz' \exp(-\kappa_e(z'+d)\sec\theta)\, \bar{W}^{(n)}(\theta,\phi,z')$$

$$\bar{S}_z^{(n)}(\theta,\phi,z) = \sec\theta \int_{-d}^{z} dz' \exp(\kappa_e(z'-z)\sec\theta)\, \bar{S}^{(n)}(\theta,\phi,z')$$

$$\bar{W}_z^{(n)}(\theta,\phi,z) = \sec\theta \int_{z}^{0} dz' \exp(\kappa_e(z'-z)\sec\theta)\, \bar{W}^{(n)}(\theta,\phi,z')$$

$\bar{S}^{(n)}$ and $\bar{W}^{(n)}$ are related to $\bar{I}^{(n-1)}$ by equation (A.2a, A.2b), with $\bar{S}^{(1)}$ and $\bar{W}^{(1)}$ given explicitly,

$$\begin{aligned}\bar{S}^{(1)}(\theta,\phi,z) = {} & \bar{\bar{P}}(\theta,\phi;\theta_{\text{inc}},\phi_{\text{inc}})\bar{M}^{(0)}(\theta_{\text{inc}})\exp(-\kappa_e(z+2d)\sec\theta_{\text{inc}}) \\ & + \bar{\bar{P}}(\theta,\phi;\pi-\theta_{\text{inc}},\phi_{\text{inc}})\bar{N}^{(0)}(\theta_{\text{inc}})\exp(\kappa_e z\sec\theta_{\text{inc}})\end{aligned} \tag{2.A.6a}$$

$$\begin{aligned}\bar{W}^{(1)}(\theta,\phi,z) = {} & \bar{\bar{P}}(\pi-\theta,\phi;\theta_{\text{inc}},\phi_{\text{inc}})\bar{M}^{(0)}(\theta_{\text{inc}})\exp(-\kappa_e(z+2d)\sec\theta_{\text{inc}}) \\ & + \bar{\bar{P}}(\pi-\theta,\phi;\pi-\theta_{\text{inc}},\phi_{\text{inc}})\bar{N}^{(0)}(\theta_{\text{inc}})\exp(\kappa_e z\sec\theta_{\text{inc}})\end{aligned} \tag{2.A.6b}$$

where

$$\bar{M}^{(0)}(\theta_{\text{inc}}) = \bar{\bar{R}}_{12}(\theta_{\text{inc}})\bar{\bar{Z}}^{-1}(\theta_{\text{inc}})\bar{\bar{T}}_{01}(\theta_{0\text{inc}})\bar{I}_0\frac{\varepsilon_0\cos\theta_{0\text{inc}}}{\varepsilon_1\cos\theta_{\text{inc}}}$$

$$\bar{N}^{(0)}(\theta_{\text{inc}}) = \bar{\bar{Z}}^{-1}(\theta_{\text{inc}})\bar{\bar{T}}_{01}(\theta_{0\text{inc}})\bar{I}_0\frac{\varepsilon_0\cos\theta_{0\text{inc}}}{\varepsilon_1\cos\theta_{\text{inc}}}$$

The contribution to bistatic scattering coefficient $\gamma_{\beta\alpha}^{(n)}(\theta_0,\phi;\theta_{0\text{inc}},\phi_{\text{inc}})$ and backscattering coefficient $\sigma_{\beta\alpha}^{(n)}(\theta_{0\text{inc}},\phi_{\text{inc}})$ from the n-th order specific intensity $\bar{I}^{(n)}(\theta,\phi,z)$ is [24]

$$\gamma_{\beta\alpha}^{(n)}(\theta_0,\phi;\theta_{0\text{inc}},\phi_{\text{inc}}) = 4\pi\frac{\cos\theta_0\, I_{0\beta}^{(n)}(\theta_0,\phi)}{\cos\theta_{0\text{inc}}\, I_{0\text{inc}\alpha}} \tag{2.A.7}$$

$$\sigma_{\beta\alpha}^{(n)}(\theta_{0\text{inc}},\phi_{\text{inc}}) = \cos\theta_{0\text{inc}}\,\gamma_{\beta\alpha}^{(n)}(\theta_{0\text{inc}},\pi+\phi_{\text{inc}};\theta_{0\text{inc}},\phi_{\text{inc}}) \tag{2.A.8}$$

where the n-th order specific intensity in the air region $\bar{I}_0^{(n)}(\theta,\phi)$ is related to $\bar{I}^{(n)}(\theta,\phi,z)$ by the transmissivity matrix from snow to air $\bar{\bar{T}}_{10}(\theta)$, $\bar{I}_0^{(n)}(\theta,\phi)=\bar{\bar{T}}_{10}(\theta)\cdot\bar{I}^{(n)}(\theta,\phi,z=0)$. The overall bistatic scattering and backscattering is the sum of contribution from each order.

When the underlying boundary is rough, surface scattering also contributes to backscattering by $\sigma_s=\sigma_{s0}(\theta_{\rm inc})\exp(-2\kappa_e d\sec\theta_{\rm inc})$, where $\sigma_{s0}(\theta_{\rm inc})$ is the bare surface backscattering coefficient at the incidence angle inside the snow medium. The bistatic scattering effects of rough surface are ignored.

Appendix B Numerical Recipes

In this appendix, we describe the numerical recipes, in particular how to evaluate the angular integral in Eq. (A.2a, A.2b) or in main text Eq. (1a-1d), and the z- integral in equation (A.4a, A.4b) or the definition of $\bar{S}_c^{(n)}$, $\bar{S}_z^{(n)}$, $\bar{W}_c^{(n)}$, and $\bar{W}_z^{(n)}$, and give criteria for parameter selection.

Let us first consider the typical angular integral of main text Eq. (1a). We apply Gaussian-Legendre quadrature for θ-integral and trapezoidal quadrature for ϕ- integral. Considering the azimuthal symmetry of phase matrix $\bar{\bar{P}}(\theta,\phi;\theta',\phi')$ with respect to $\phi-\phi'$, the discretized version of main text Eq. (1a) reads

$$\bar{S}_u^{(n)}(\theta_k,\phi_p,z)=\Delta\phi\sum_{p'=1}^{N_p}\sum_{k'=1}^{N_k}a_{k'}\left[\bar{\bar{P}}\left(\theta_k,\phi_p-\phi_{p'};\theta_{k'},0\right)\cdot\bar{I}^{(n-1)}\left(\theta_{k'},\phi_{p'},z\right)\right] \tag{2.B.1}$$

where θ_k $(k=1,\ldots,N_k)$ are the Gaussian-Legendre quadrature points, with $\mu_k=\cos(\theta_k)$ the positive half of the $2N_k$ roots of Legendre polynomial of $2N_k$-th order and a_k the corresponding Gaussian-Legendre quadrature weights at θ_k; $\phi_p=p\Delta\phi$ $(p=0,1,\ldots,N_p-1)$ are the uniformly

spaced trapezoidal quadrature points, with $\Delta\phi = 2\pi/N_p$. Note phase matrix $\bar{\bar{P}}(\theta,\phi;\theta',\phi')$ is only required at the grid points $\bar{\bar{P}}(\theta_k,\phi_p;\theta_{k'},0)$, and the summation over $\phi_{p'}$ in Eq. (B.1) forms a cyclical convolution, and could be accelerated by FFT.

Three kind of z-integrals are encountered in the form of $\int_{-d}^{0} dz' f(z')$ as in $\bar{S}_c^{(n)}$ and $\bar{W}_c^{(n)}$, $\int_{-d}^{z} dz' f(z')$ in $\bar{S}_z^{(n)}$ and $\int_{z}^{0} dz' f(z')$ in $\bar{W}_z^{(n)}$. We sample z uniformly at $z_q = -d + q\Delta z$, $\Delta z = d/N_q$, $q = 0,1,\ldots,N_q$, and denote $f(z_q)$ with f_q. Then $\int_{-d}^{0} dz' f(z')$ could be evaluated with trapezoidal quadrature rule directly,

$$\int_{-d}^{0} dz' f(z') = \Delta z\left(\frac{1}{2}f_0 + \sum_{q'=1}^{N_q-1} f_{q'} + \frac{1}{2}f_{N_q}\right) \tag{2.B.2}$$

And $\int_{-d}^{z_q} dz' f(z')$ and $\int_{z_q}^{0} dz' f(z')$ could be evaluated recursively,

$$\int_{-d}^{z_q} dz' f(z') = \int_{-d}^{z_{q-1}} dz' f(z') + \frac{\Delta z}{2}(f_{q-1} + f_q), q = 1,\ldots,N_q \tag{2.B.3}$$

$$\int_{z_q}^{0} dz' f(z') = \frac{\Delta z}{2}(f_q + f_{q+1}) + \int_{z_{q+1}}^{0} dz' f(z'), q = N_q - 1,\ldots,0 \tag{2.B.4}$$

with $\int_{-d}^{z_0} dz' f(z') = 0$ and $\int_{z_{N_q}}^{0} dz' f(z') = 0$.

Note the angular integral as illustrated in Eq. (B.1) is to be applied for any sampling point of z_q. An estimation criterion of typical numerical parameters is provided. The discretization number of θ_k, ϕ_p can be set as $N_k = 16$ and $N_p = 32$ for a relatively smoothly changing phase matrix; the discretization number of z_q could be related to the optical thickness of snow layer $\tau = \kappa_e d$ by $N_q = \max(\tau/0.05, 8)$; the sufficient scattering order for the convergence of backscattering could be related to the optical thickness τ and the scattering albedo $\varpi = \kappa_s/\kappa_e$ as $\max(\varpi\tau/0.1, 5)$.

CHAPTER III

Numerical Solution of Maxwell's Equation of a Dense Random Media Layer above a Half Space

The traditional approach in dealing with dense media volume scattering is to invoke a partially coherent approach of dense media radiative transfer (DMRT) as discussed in the previous chapter. In this approach, homogeneity is assumed and homogenization is used to describe the random media.

The partially coherent approach of dense media radiative transfer (DMRT) has been extensively applied to study the wave propagation and scattering inside dense media such as terrestrial snow [20, 21, 28, 33, 111]. In the DMRT partially coherent approach, the coherent part is obtained by solving Maxwell's equations over several cubic wavelengths of statistically homogeneous snow volume to compute the phase matrix, the extinction coefficient, the effective propagation constants and the effective permittivity. These parameters homogenize the snowpack. Solving Maxwell's equations accounts for the coherent near field and intermediate field interactions within several cubic wavelengths. The phase matrix is then substituted into the radiative transfer equation which constitutes the incoherent part of DMRT. The DMRT equation is then solved to include incoherent far field interactions and volume / surface interactions. This approach is appropriate when the snow layers are electrically thick such that the coherent far field interaction cancels out over statistical average. This is true for many applications in terrestrial

snow remote sensing where the wavelength is 1~3cm and the snow depth can be several decimeters to meters.

On the other hand, snow on sea ice is typically thin of 10~20cm with a decreasing trend over the western Arctic [112]. The local wave interaction arising from these thin layers are largely coherent. And in the backscattering direction of the active remote sensing, the coherent wave interaction can extend to far field giving rise to backscattering enhancement phenomena [33]. These short-range and long-range coherent wave effects are not captured by DMRT. In this chapter [35, 36, 113-117], we have developed a fully coherent snowpack scattering model by solving the Maxwell's equation directly over the entire domain of snowpack on top of a dielectric half-space. The half-space represents the soil ground under the terrestrial snow or the sea ice below the snow cover across the Arctic Ocean. This is applicable when the sea ice thickness is larger than the penetration depth, depending on the wave frequency of the incidence waves. Effects of the half-space are included in the volume integral equation by the half-space dyadic Green's function. The snow volume is represented by bicontinuous media [19] and discretized into cubes. The method of moments (MoM) is then used to solve the volume integral equation with a pulse basis function and point matching, leading to discrete dipole approximation (DDA). The fast Fourier transform (FFT) is adapted for the kernel of the half-space dyadic Green's function to accelerate the matrix-vector multiplication in the iterative linear system solver [119]. For the first time, the scattering matrix of the snowpack is computed using this fully coherent approach of numerical solution of Maxwell's equation in 3 dimension (NMM3D), including both magnitude and phase. This allows the modeling of the coherence matrix and speckle statistics [37]. Backscattering enhancement effects are also exhibited, and for a homogeneous snowpack of moderate optical thickness, the

overall trend of the bistatic scattering pattern from the fully coherent approach agrees with the results of DMRT.

In this chapter, the fully coherent approach is further improved by implementing the periodic boundary condition. The periodic Green's function in half space is used. The incorporation of the periodic boundary condition removes the edge diffraction artifacts from the finite computational domain and produces more physically plausible results. We also extend the fully coherent approach to compute the brightness temperatures of the snowpack following the reciprocity principle. This approach accounts for an arbitrary temperature profile of the snowpack and includes coherent effects in the thin layer together with fully coherent volume-surface interactions. This new method circumvents the unrealistic isothermal condition incorrectly assumed in the Kirchhoff approximation approach. The brightness temperatures and backscatters from the fully coherent model are compared with the results of DMRT for various snowpack configurations to understand and to determine the applicability regime of DMRT.

We also illustrate results of SAR-tomograms making use of the scattering matrix out of the full wave simulations to demonstrate the possibility of using tomographic SAR to reveal the vertical structures of the layered snowpack [38, 120].

3.1 Plane wave excitation of a truncated 2D snow layer

In our mind is the scattering of wave from an infinite layer of snowpack on top of a half space (ground), but our computation domain must be finite to fit into our finite computing resources. So the first problem is how to truncate the snow volume. One can apply periodic boundary condition to emulate an infinite snow layer, as we are going to discuss later, but before going into that complexity, which also brings in limitations, the natural choice is to simply simulate

the scattering from a finite snow volume due to an impinging plane wave, Figure III.1, and see how the scattering results converges with respect to the number of realizations and behaves as the truncation domain in the horizontal direction increases.

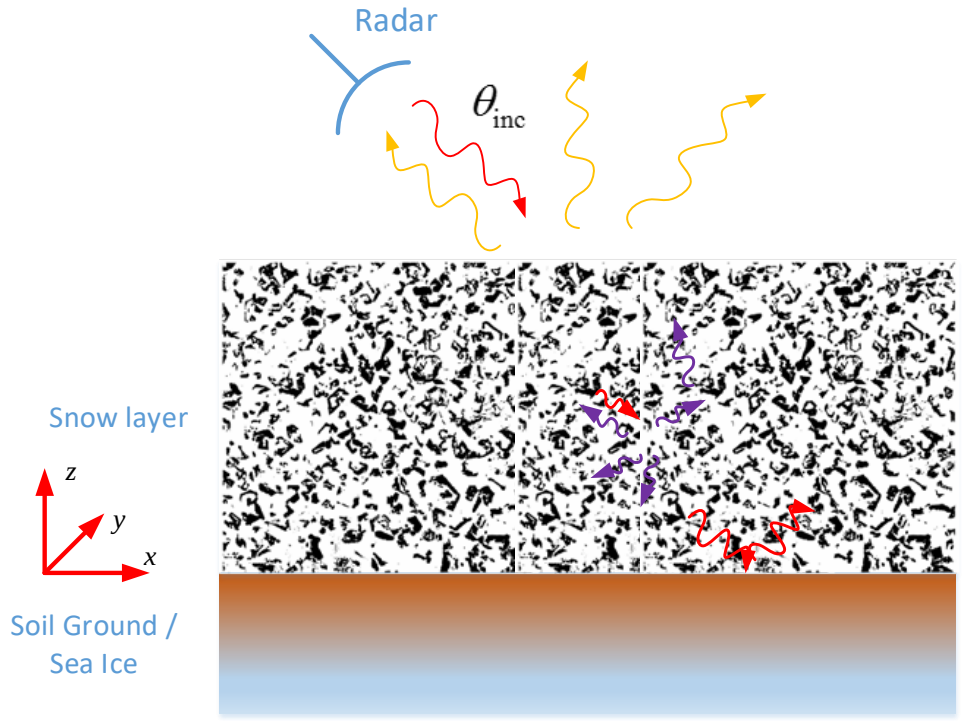

Figure III.1 Plane wave impinging upon a layer of snow above a dielectric half-space. The computational domain in the horizontal directions are finite.

On the other hand, two-dimension (2D) simulation is always simpler than three-dimension (3D) simulation, but it can demonstrate most of the physics, such as the edge diffraction, the energy conservation, the separation of incoherent scattering field and coherent scattering field through Monte Carlo simulation, the effective media effects causing coherent multiple wave reflections, etc. Thus in this first section, we consider the plane wave excitation of a truncated 2D snow layer.

3.1.1 The volume integral equation in 2D

To suppress the y dependence, we let the excitation to be in the xOz plane. We use wave function $\psi(\bar{\rho})$ to represent E_y for the TE or horizontally polarized wave, and use $\psi(\bar{\rho})$ to represent H_y for the TM or vertically polarized wave. We limit ourselves to electric media. The wave function $\psi(\bar{\rho})$ satisfies the 2D scalar wave equation (one can easily derive it from the 3D vector wave equation), where $\nabla_\perp^2 = \frac{\partial^2}{\partial x^2} + \frac{\partial^2}{\partial z^2}$,

$$\nabla_\perp^2 \psi(\bar{\rho}) + k^2 \varepsilon_r(\bar{\rho}) \psi(\bar{\rho}) = 0 \tag{3.1}$$

To formulate the integral equation, we put it in the form

$$\nabla_\perp^2 \psi(\bar{\rho}) + k^2 \psi(\bar{\rho}) = -k^2 \left(\varepsilon_r(\bar{\rho}) - 1\right) \psi(\bar{\rho}) \tag{3.2}$$

On the other hand the incidence wave function $\psi^{\text{inc}}(\bar{\rho})$ satisfies

$$\nabla_\perp^2 \psi^{\text{inc}}(\bar{\rho}) + k^2 \psi^{\text{inc}}(\bar{\rho}) = 0 \tag{3.3}$$

Considering

$$\psi(\bar{\rho}) = \psi^{\text{inc}}(\bar{\rho}) + \psi^s(\bar{\rho}) \tag{3.4}$$

Subtracting (3.3) from (3.1), we get the equation for the scattering field $\psi^s(\bar{\rho})$,

$$\nabla_\perp^2 \psi^s(\bar{\rho}) + k^2 \psi^s(\bar{\rho}) = -k^2 \left(\varepsilon_r(\bar{\rho}) - 1\right) \psi(\bar{\rho}) \tag{3.5}$$

Using Green's function $g(\bar{\rho}, \bar{\rho}')$, satisfying

$$\nabla_\perp^2 g(\bar{\rho}, \bar{\rho}') + k^2 g(\bar{\rho}, \bar{\rho}') = -\delta(\bar{\rho} - \bar{\rho}') \tag{3.6}$$

The scattering field can be expressed as

$$\psi^s(\bar{\rho}) = k^2 \int_S d\bar{\rho}' \, g(\bar{\rho}, \bar{\rho}') \left(\varepsilon_r(\bar{\rho}') - 1\right) \psi(\bar{\rho}') \tag{3.7}$$

Using (3.4) to eliminate $\psi^s(\bar{\rho})$, we get the integral equation for total field $\psi(\bar{\rho})$

$$\psi(\bar{\rho}) = \psi^{\text{inc}}(\bar{\rho}) + k^2 \int_S d\bar{\rho}' \, g(\bar{\rho}, \bar{\rho}') \left(\varepsilon_r(\bar{\rho}') - 1\right) \psi(\bar{\rho}') \tag{3.8}$$

To include the bottom half space, representing the ground, into the volume integral equation, we use the half space Green's function $g_{00}(\bar{\rho},\bar{\rho}')$ in (3.8), including both the primary contribution $g_0(\bar{\rho},\bar{\rho}')$, which is the free space Green's function, and the response contribution, $g_R(\bar{\rho},\bar{\rho}')$, which is the reflection components.

$$g(\bar{\rho},\bar{\rho}') = g_{00}(\bar{\rho},\bar{\rho}') = g_0(\bar{\rho},\bar{\rho}') + g_R(\bar{\rho},\bar{\rho}') \tag{3.9}$$

With (3.9), the integral equation (3.8) takes its final form

$$\begin{aligned}\psi(\bar{\rho}) = \psi^{\text{inc}}(\bar{\rho}) + k^2\int_S d\bar{\rho}'\, g_0(\bar{\rho},\bar{\rho}')\left(\varepsilon_r(\bar{\rho}')-1\right)\psi(\bar{\rho}') \\ + k^2\int_S d\bar{\rho}'\, g_R(\bar{\rho},\bar{\rho}')\left(\varepsilon_r(\bar{\rho}')-1\right)\psi(\bar{\rho}')\end{aligned} \tag{3.10}$$

We're going to solve (3.10) using discrete dipole approximation, i.e., method of moments (MoM) with pulse basis and point matching.

3.1.2 Discretization and the Discrete Dipole Approximation

Let us divide the integral domain into squares (2D cross section of cubes) with area ΔS. We discretize (3.10) putting $\bar{\rho}$ at the center of the i-th square $\bar{\rho}_i$. Note that the integral of $g_R(\bar{\rho},\bar{\rho}')$ has no singularity, thus with pulse basis,

$$\int_S d\bar{\rho}'\, g_R(\bar{\rho}_i,\bar{\rho}')\left(\varepsilon_r(\bar{\rho}')-1\right)\psi(\bar{\rho}') = \sum_j g_R(\bar{\rho}_i,\bar{\rho}_j)\left(\varepsilon_r(\bar{\rho}_j)-1\right)\psi(\bar{\rho}_j)\Delta S \tag{3.11}$$

We then consider the integral of $g_0(\bar{\rho},\bar{\rho}')$. We first separate out the singularity which is located in the self-square $S_C^{(i)}$,

$$\begin{aligned}\int_S d\bar{\rho}'\, g_0(\bar{\rho}_i,\bar{\rho}')\left(\varepsilon_r(\bar{\rho}')-1\right)\psi(\bar{\rho}') = \int_{S_C^{(i)}} d\bar{\rho}'\, g_0(\bar{\rho}_i,\bar{\rho}')\left(\varepsilon_r(\bar{\rho}')-1\right)\psi(\bar{\rho}') \\ + \int_{S-S_C^{(i)}} d\bar{\rho}'\, g_0(\bar{\rho}_i,\bar{\rho}')\left(\varepsilon_r(\bar{\rho}')-1\right)\psi(\bar{\rho}')\end{aligned} \tag{3.12}$$

Note the second term has no singularity, thus

$$\int_{S-S_C^{(i)}} d\bar{\rho}'\, g_0(\bar{\rho}_i,\bar{\rho}')\left(\varepsilon_r(\bar{\rho}')-1\right)\psi(\bar{\rho}') = \sum_{j\neq i} g_0(\bar{\rho}_i,\bar{\rho}_j)\left(\varepsilon_r(\bar{\rho}_j)-1\right)\psi(\bar{\rho}_j)\Delta S \tag{3.13}$$

For the first term, the singularity is in $g_0(\bar{\rho},\bar{\rho}')$, thus

$$\int_{S_C^{(i)}} d\bar{\rho}'\, g_0\left(\bar{\rho}_i,\bar{\rho}'\right)\left(\varepsilon_r\left(\bar{\rho}'\right)-1\right)\psi\left(\bar{\rho}'\right)=\left(\varepsilon_r\left(\bar{\rho}_i\right)-1\right)\psi\left(\bar{\rho}_i\right)\int_{S_C^{(i)}} d\bar{\rho}'\, g_0\left(\bar{\rho}_i,\bar{\rho}'\right) \tag{3.14}$$

Let us denote

$$\int_{S_C} d\bar{\rho}'\, g_0\left(\bar{\rho}_C,\bar{\rho}'\right)=s_0 \tag{3.15}$$

where $\bar{\rho}_C$ is located at the center of the self-square S_C.

Putting everything together, the discretized integral equations becomes

$$\begin{aligned}\psi\left(\bar{\rho}_i\right)=\psi^{\text{inc}}\left(\bar{\rho}_i\right)+k^2\left[\left(\varepsilon_r\left(\bar{\rho}_i\right)-1\right)\psi\left(\bar{\rho}_i\right)s_0+\sum_{j\neq i} g_0\left(\bar{\rho}_i,\bar{\rho}_j\right)\left(\varepsilon_r\left(\bar{\rho}_j\right)-1\right)\psi\left(\bar{\rho}_j\right)\Delta S\right]\\ +k^2\sum_j g_R\left(\bar{\rho}_i,\bar{\rho}_j\right)\left(\varepsilon_r\left(\bar{\rho}_j\right)-1\right)\psi\left(\bar{\rho}_j\right)\Delta S\end{aligned} \tag{3.16}$$

We then reorganize (3.16)

$$\begin{aligned}&\frac{1-k^2\left(\varepsilon_r\left(\bar{\rho}_i\right)-1\right)s_0}{\Delta S\varepsilon\left(\varepsilon_r\left(\bar{\rho}_j\right)-1\right)}\Delta S\varepsilon\left(\varepsilon_r\left(\bar{\rho}_j\right)-1\right)\psi\left(\bar{\rho}_i\right)\\ &=\psi^{\text{inc}}\left(\bar{\rho}_i\right)+\frac{k^2}{\varepsilon}\left[\sum_{j\neq i} g_0\left(\bar{\rho}_i,\bar{\rho}_j\right)\varepsilon\left(\varepsilon_r\left(\bar{\rho}_j\right)-1\right)\psi\left(\bar{\rho}_j\right)\Delta S\right]\\ &+\frac{k^2}{\varepsilon}\sum_j g_R\left(\bar{\rho}_i,\bar{\rho}_j\right)\varepsilon\left(\varepsilon_r\left(\bar{\rho}_j\right)-1\right)\psi\left(\bar{\rho}_j\right)\Delta S\end{aligned} \tag{3.17}$$

Now define the dipole moment p_i and the free space polarizability α_i for the i-th cell,

$$p_i=\Delta S\varepsilon\left(\varepsilon_r\left(\bar{\rho}_j\right)-1\right)\psi\left(\bar{\rho}_i\right) \tag{3.18}$$

$$\alpha_i=\frac{\Delta S\varepsilon\left(\varepsilon_r\left(\bar{\rho}_j\right)-1\right)}{1-k^2\left(\varepsilon_r\left(\bar{\rho}_i\right)-1\right)s_0} \tag{3.19}$$

Then (3.16) is cast into a much concise form,

$$p_i=\alpha_i\left[\psi^{\text{inc}}\left(\bar{\rho}_i\right)+\frac{k^2}{\varepsilon}\sum_{j\neq i} g_0\left(\bar{\rho}_i,\bar{\rho}_j\right)p_j+\frac{k^2}{\varepsilon}\sum_j g_R\left(\bar{\rho}_i,\bar{\rho}_j\right)p_j\right] \tag{3.20}$$

Equation (3.20) is the discrete dipole approximation (DDA) of the volume integral equation of (3.10).

3.1.3 Free space Green's function and the self-patch integral

In this subsection, we deal with the self-patch integral of (3.15), where $g_0(\bar{\rho},\bar{\rho}')$ is the free space Green's function. We follow the $\exp(-i\omega t)$ time convention throughout the text.

$$g_0\left(\bar{\rho},\bar{\rho}'\right)=\frac{i}{4}H_0^{(1)}\left(k\left|\bar{\rho}-\bar{\rho}'\right|\right) \tag{3.21}$$

We show that s_0 can be approximated by

$$s_0=\frac{i}{4}d^2-\frac{d^2}{2\pi}\left[\ln\left(\gamma kd\right)-\frac{3}{2}\ln 2-\frac{3}{2}+\frac{\pi}{4}\right] \tag{3.22}$$

where d is the edge length of the square, and $\gamma = 1.7810724180$ is the Euler's constant.

Proof:

$$\begin{aligned}
s_0 &= \int_{\sigma_m} dx'dz' g_0\left(x_m, z_m; x', z'\right) \\
&= \frac{i}{4}\int_{-\Delta/2}^{\Delta/2} dx' \int_{-\Delta/2}^{\Delta/2} dz' H_0^{(1)}\left(k\sqrt{x'^2+z'^2}\right) \\
&= \frac{i}{4}\times 4\int_{0}^{\Delta/2} dx' \int_{0}^{\Delta/2} dz' H_0^{(1)}\left(k\sqrt{x'^2+z'^2}\right)
\end{aligned}$$

where Δ is the size of discretization.

We first convert the integral into cylindrical coordinate,

$$s_0=\frac{i}{4}\times 8\int_0^{\pi/4} d\phi \int_0^{(\Delta/2)\sec\phi} d\rho\rho H_0^{(1)}\left(k\rho\right)$$

We then apply the small argument approximation of the Hankel function,

$$
\begin{aligned}
s_0 &\approx 2i\int_0^{\pi/4} d\phi \int_0^{(\Delta/2)\sec\phi} d\rho\rho \left[1 + i\frac{2}{\pi}\ln\frac{\gamma k\rho}{2}\right] \\
&= 2i\int_0^{\pi/4} d\phi \int_0^{(\Delta/2)\sec\phi} d\rho\rho \left[1 + i\frac{2}{\pi}\ln\frac{\gamma k}{2}\right] \\
&+2i\int_0^{\pi/4} d\phi \int_0^{(\Delta/2)\sec\phi} d\rho\rho \left[i\frac{2}{\pi}\ln\rho\right]
\end{aligned}
$$

One can show that the first term

$$
\text{self}_c = \frac{i}{4}\Delta^2\left[1 + i\frac{2}{\pi}\ln\frac{\gamma k}{2}\right]
$$

And the second term

$$
\text{self}_{\ln} = -\frac{1}{\pi}\frac{\Delta^2}{2}\left[\ln\Delta - \frac{1}{2}\ln 2 - \frac{3}{2} + \frac{\pi}{4}\right]
$$

Adding up results (3.22).

■

3.1.4 Half-space Green's function

The half space Green's function, as given in (3.9), contains two parts. In order to derive the expression for $g_R(\bar{\rho},\bar{\rho}')$, we put $g_0(\bar{\rho},\bar{\rho}')$ in the form of spectral domain integration,

$$
g_0\left(x,z;x',z'\right) = \frac{i}{4\pi}\int_{-\infty}^{\infty} dk_x e^{ik_x(x-x')}\frac{1}{k_z}e^{ik_z|z-z'|} \tag{3.23}
$$

Assuming the boundary is at $z = 0$, and the source is in the top region 0, i.e., $z' > 0$, then the reflection field in region 0, denoted by g_R, and the transmission field in the bottom region 1, denoted by g_T, can be put down as follows,

$$
g_R\left(x,z;x',z'\right) = \frac{i}{4\pi}\int_{-\infty}^{\infty} dk_x e^{ik_x(x-x')}\frac{R\left(k_x\right)}{k_z}e^{ik_z(z+z')}, z > 0 \tag{3.24}
$$

$$g_T\left(x,z;x',z'\right)=\frac{i}{4\pi}\int_{-\infty}^{\infty}dk_x e^{ik_x(x-x')}\frac{T\left(k_x\right)}{k_z}e^{-ik_{1z}z+ik_z z'},\ z<0 \tag{3.25}$$

where

$$k_z=\sqrt{k^2-k_x^2} \tag{3.26}$$

$$k_{1z}=\sqrt{k_1^2-k_x^2} \tag{3.27}$$

The coefficient $R(k_x)$ and $T(k_x)$ can be determined by matching the boundary conditions at $z=0$,

$$g_T=g_0+g_R \tag{3.28}$$

$$\frac{\partial g_T}{\partial z}=\frac{1}{\rho}\left(\frac{\partial g_0}{\partial z}+\frac{\partial g_R}{\partial z}\right) \tag{3.29}$$

where $\rho=\varepsilon/\varepsilon_1$ for TM polarization and $\rho=\mu/\mu_1=1$ for TE polarization.

The coefficients $R(k_x)$ and $T(k_x)$ are found to be identical to the Fresnel reflection and transmission coefficients,

$$R=\frac{k_z-\rho k_{1z}}{k_z+\rho k_{1z}} \tag{3.30}$$

$$T=\frac{2k_z}{k_z+\rho k_{1z}} \tag{3.31}$$

Explicitly,

$$R^{\mathrm{TE}}=\frac{k_z-k_{1z}}{k_z+k_{1z}},\qquad T^{\mathrm{TE}}=\frac{2k_z}{k_z+k_{1z}}$$
$$R^{\mathrm{TM}}=\frac{\varepsilon_1 k_z-\varepsilon k_{1z}}{\varepsilon_1 k_z+\varepsilon k_{1z}},\quad T^{\mathrm{TM}}=\frac{2\varepsilon_1 k_z}{\varepsilon_1 k_z+\varepsilon k_{1z}}$$

We need to numerically carry out the integral in (3.24) to get $g_R(\bar{\rho},\bar{\rho}')$ for both $z>0$ and $z'>0$ in the DDA formulation. In doing so, we combine the positive and negative part of the integration,

$$g_R\left(x,z;x',z'\right)=\frac{i}{2\pi}\int_0^\infty dk_x\cos\left(k_x\left(x-x'\right)\right)\frac{R\left(k_x\right)}{k_z}e^{ik_z\left(z+z'\right)},\ z>0 \tag{3.32}$$

Note that the $1/k_z$ weak singularity is integrable. Thus numerically,

$$\begin{aligned} g_R\left(x,z;x',z'\right)=&\frac{i}{2\pi}\lim_{\epsilon\to 0}\int_0^{k-\epsilon} dk_x\cos\left(k_x\left(x-x'\right)\right)\frac{R\left(k_x\right)}{k_z}e^{ik_z\left(z+z'\right)}\\ &+\frac{i}{2\pi}\lim_{\epsilon\to 0}\int_{k+\epsilon}^\infty dk_x\cos\left(k_x\left(x-x'\right)\right)\frac{R\left(k_x\right)}{k_z}e^{ik_z\left(z+z'\right)}\end{aligned} \tag{3.33}$$

where ϵ is a positive and arbitrarily small number.

The special case of $z=z'=0$, where the integration converges slowly, can be calculated by using path deformation techniques, if necessary.

From (3.23) and (3.24), we also notice the translational invariance of the Green's function,

$$g_0\left(x,z;x',z'\right)=g_0\left(x-x';z-z'\right) \tag{3.34}$$

$$g_R\left(x,z;x',z'\right)=g_R\left(x-x';z+z'\right) \tag{3.35}$$

This symmetry in Green's function not only reduces the number of independent arguments from 4 to 2, and it also turns out to be of critical significance in accelerating the matrix-vector multiplication and in lowering the memory requirements.

3.1.5 Efficient evaluation of the matrix-vector multiplication using FFT

Note that in solving the DDA equation (3.20) using an iterative approach such as generalized minimal residual method (GMRES) or conjugate-gradient (CG), the most time consuming part is the matrix-vector multiplication. The translational invariance of the Green's function as shown in (3.34) and (3.35) makes the matrix Toeplitz-like. Thus it is possible to apply fast Fourier transform (FFT) techniques in accelerating the matrix-vector multiplications.

(a) $\sum_{j\neq i} \boldsymbol{g_0}\left(\bar{\boldsymbol{\rho}}_i, \bar{\boldsymbol{\rho}}_j\right)\bar{\boldsymbol{p}}_j$

Let us write out the summation explicitly. Let

$$\begin{aligned} i &\to (n,l) \\ j &\to (n',l') \\ p_j &\to p\left(x_{n'}, z_{l'}\right) \\ x_n &= x_0 + n\Delta x, 0 \le n \le N_x - 1 \\ z_l &= z_0 + l\Delta z, 0 \le l \le N_z - 1 \end{aligned}$$

where (x_0, z_0) is the coordinate of the $(0,0)$-th cell. Then

$$\begin{aligned} \sum_{j\neq i} g_0\left(\bar{\rho}_i, \bar{\rho}_j\right) p_j &= \sum_{(n',l')\neq(n,l)} g_0\left(x_n - x_{n'}, z_l - z_{l'}\right) p\left(x_{n'}, z_{l'}\right) \\ &= \sum_{(n',l')\neq(n,l)} g_0\left(\left(n-n'\right)\Delta x, \left(l-l'\right)\Delta z\right) p\left(x_{n'}, z_{l'}\right) \end{aligned} \tag{3.36}$$

Let us simplify our notation,

$$\begin{aligned} p\left(x_{n'}, z_{l'}\right) &\to p\left(n',l'\right) \\ g_0\left(\left(n-n'\right)\Delta x, \left(l-l'\right)\Delta z\right) &\to g_0\left(n-n', l-l'\right) \\ \sum_{j\neq i} g_0\left(\bar{\rho}_i, \bar{\rho}_j\right) p_j &\to y(n,l) \end{aligned}$$

And we also set

$$g_0(0,0) = 0$$

Then

$$y(n,l) = \sum_{n'=0}^{N_x-1} \sum_{l'=0}^{N_y-1} g_0\left(n-n', l-l'\right) p\left(n',l'\right), 0 \le n \le N_x, 0 \le l \le N_z \tag{3.37}$$

Note that (3.37) is in the form of linear convolution, where

$$\begin{aligned} -\left(N_x - 1\right) \le n - n' \le \left(N_x - 1\right) &: \text{of length } 2N_x - 1 \\ -\left(N_z - 1\right) \le l - l' \le \left(N_z - 1\right) &: \text{of length } 2N_z - 1 \\ 0 \le n \le \left(N_x - 1\right) &: \text{of length } N_x \\ 0 \le l \le \left(N_z - 1\right) &: \text{of length } N_z \end{aligned}$$

in order to convert it into circular convolution to use FFT, we extend the length of both arrays to be $2N_x \times 2N_z$ by padding zeros and periodic folding,

$$p \to \tilde{p} : \tilde{p}(n,l) = \begin{cases} p(n,l) & 0 \le n < N_x, \text{ and } 0 \le l < N_z \\ 0 & \text{otherwise} \end{cases}$$

$$g_0 \to \tilde{g}_0 : \tilde{g}_0(n,l) = \begin{cases} 0 & n = N_x, \text{ or } l = N_z \text{ or } (n,l) = (0,0) \\ g_0(n',l') & \text{otherwise} \end{cases}$$

where

$$n' = \begin{cases} n & 0 \le n < N_x \\ n - 2N_x & N_x < n < 2N_x \end{cases}$$

$$l' = \begin{cases} l & 0 \le l < N_z \\ l - 2N_z & N_z < l < 2N_z \end{cases}$$

then

$$\begin{aligned} \tilde{y}(n,l) &= \mathrm{FT}^{-1}_{2N_x \times 2N_z} \left\{ G_0(i,k) \cdot P(i,k) \right\} \\ G_0(i,k) &= \mathrm{FT}_{2N_x \times 2N_z} \left\{ \tilde{g}_0(n,l) \right\} \\ P(i,k) &= \mathrm{FT}_{2N_x \times 2N_z} \left\{ \tilde{p}_0(n,l) \right\} \end{aligned} \tag{3.38}$$

where $G_0(i,k)$ and $P(i,k)$ are the $2N_x \times 2N_z$ Fourier transforms of $\tilde{g}_0(n,l)$ and $\tilde{p}(n,l)$, respectively. $G_0(i,k) \cdot P(i,k)$ denotes the pointwise product of G_0 and P in spectral domain, whose inverse $2N_x \times 2N_z$ Fourier transforms gives $\tilde{y}(n,l)$.

Finally, the results of matrix-vector multiplication are obtained by keeping the first quadrant of the 2D circular convolution.

$$y(n,l) = \tilde{y}(n,l), 0 \le n < N_x, 0 \le l < N_z \tag{3.39}$$

Thus the matrix vector multiplication is implemented by 3 successive Fourier transforms, with computing complexity of $O(N \lg N)$, which is much faster than the direct computation with $O(N^2)$. Meanwhile, the memory requirements improves from $O(N^2)$ in the direct computation,

where all the matrix elements must be stored, to $O(N)$ in the FFT, where only one row of the extended Toeplitz matrix needs to be stored. These benefits will be revisited in dealing with $\sum_j g_R(\bar{\rho}_i, \bar{\rho}_j)\bar{p}_j$.

(b) $\sum_j g_R(\bar{\rho}_i, \bar{\rho}_j)\bar{p}_j$

$$g_R\left(\bar{\rho}_i, \bar{\rho}_j\right) = g_R\left(x_n - x_{n'}, z_l + z_{l'}\right) = g_R\left(\left(n-n'\right)\Delta \mathrm{x}, 2z_0 + \left(l+l'\right)\Delta z\right) \tag{3.40}$$

Let us denote

$$g_R\left(\left(n-n'\right)\Delta x, 2z_0 + \left(l+l'\right)\Delta z\right) \to g_R\left(n-n', l+l'\right)$$
$$\sum_{j\neq i} g_R\left(\bar{\rho}_i, \bar{\rho}_j\right) p_j \to y(n,l), 0 \le n \le N_x, 0 \le l < N_z$$

then

$$y(n,l) = \sum_{n'=0}^{N_x-1}\sum_{l'=0}^{N_z-1} g_R\left(n-n', l+l'\right) p\left(n', l'\right) \tag{3.41}$$

Note this is in the form of linear convolution along x-direction and linear correlation along z-direction.

$$-\left(N_x-1\right) \le n-n' \le \left(N_x-1\right) : \text{of length } 2N_x-1$$
$$0 \le l+l' \le 2\left(N_z-1\right) : \text{of length } 2N_z-1$$
$$0 \le n \le \left(N_x-1\right) : \text{of length } N_x$$
$$0 \le l \le \left(N_z-1\right) : \text{of length } N_z$$

Let us extend the length of both arrays to be $2N_x \times 2N_z$ by pending zeros,

$$p \to \tilde{p} : \tilde{p}(n,l) = \begin{cases} p(n,l) & 0 \le n < N_x, \text{ and } 0 \le l < N_z \\ 0 & \text{otherwise} \end{cases}$$

$$g_R \to \tilde{g}_R : \tilde{g}_R(n,l) = \begin{cases} 0 & n = N_x, \text{ or } l = 2N_z\text{-}1 \\ g_R\left(n', l\right) & \text{otherwise} \end{cases}$$

where

$$n' = \begin{cases} n & 0 \le n < N_x \\ n - 2N_x & N_x < n < 2N_x \end{cases}$$

Then

$$\begin{aligned} \tilde{y}(n,l) &= \mathrm{FT}^{-1}_{2N_x \times 2N_z} \left\{ G_R(i,k) \bullet P(i,-k) \right\} \\ G_R(i,k) &= \mathrm{FT}_{2N_x \times 2N_z} \left\{ \tilde{g}_R(n,l) \right\} \\ P(i,k) &= \mathrm{FT}_{2N_x \times 2N_z} \left\{ \tilde{p}_0(n,l) \right\} \\ P(i,-k) &= P(i,2N_z - k), 1 \le k < 2N_z \end{aligned} \tag{3.42}$$

And

$$y(n,l) = \tilde{y}(n,l), 0 \le n < N_x, 0 \le l < N_z \tag{3.43}$$

So again, the matrix vector multiplication is implemented by 3 successive Fourier transforms, reducing significantly the computation complexity and memory requirements.

3.1.6 The incident wave

For TE polarized wave, the incidence field is E_y, while for TM polarized wave, the incidence field is H_y. Since the half space effects is included in the Green's function, the incidence field comprises of both the direct impinging field and the reflection field.

$$\psi_{\mathrm{inc}} = \psi_0 e^{ik_{ix}x} \left(e^{-ik_{iz}z} + e^{ik_{iz}z} R \right) \tag{3.44}$$

where

$$\begin{aligned} k_{ix} &= k \sin\theta_i \\ k_{iz} &= k \cos\theta_i \end{aligned}$$

Note the convention for incidence angle θ_i is different from that of the scattering angle θ_s. We assume θ_i is the angle between $-\hat{k}_i$ and $\hat{z}$, and positive θ_i indicates that the incidence wave is propagating towards the positive $\hat{x}$ axis.

3.1.7 The scattering field and the scattering amplitude

The scattering field at any $\bar{\rho}$

$$\begin{aligned}\psi_s(\bar{\rho}) &= k^2\int_S d\bar{\rho}'\, g_0(\bar{\rho},\bar{\rho}')\left(\varepsilon_r(\bar{\rho}')-1\right)\psi(\bar{\rho}') \\ &\quad + k^2\int_S d\bar{\rho}'\, g_R(\bar{\rho},\bar{\rho}')\left(\varepsilon_r(\bar{\rho}')-1\right)\psi(\bar{\rho}') \\ &= \frac{k^2}{\varepsilon}\sum_j g_0(\bar{\rho}_i,\bar{\rho}_j)p_j + \frac{k^2}{\varepsilon}\sum_j g_R(\bar{\rho}_i,\bar{\rho}_j)p_j\end{aligned} \tag{3.45}$$

To consider the scattering amplitude, we need to know ψ_s in the far field.

(a) Far field approximation of $g_0(\bar{\rho},\bar{\rho}')$

We put down again (3.21)

$$g_0(\bar{\rho},\bar{\rho}') = \frac{i}{4}H_0^{(1)}\left(k|\bar{\rho}-\bar{\rho}'|\right)$$

Using the asymptotic expansions of Hankel function for large arguments [121] (Abramowitz and Stegun, pp. 364, Section 9.2.3),

$$H_0^{(1)}(z) \sim \sqrt{\frac{2}{\pi z}}e^{i\left(z-\frac{\pi}{4}\right)} \tag{3.46}$$

Thus

$$g_0(\bar{\rho},\bar{\rho}') \sim \frac{i}{4}\sqrt{\frac{2}{\pi k|\bar{\rho}-\bar{\rho}'|}}e^{i\left(k|\bar{\rho}-\bar{\rho}'|-\frac{\pi}{4}\right)} \tag{3.47}$$

In far field,

$$\begin{aligned}\hat{k} &= (\sin\theta,\cos\theta), -\frac{\pi}{2}<\theta<\frac{\pi}{2} \\ |\bar{\rho}-\bar{\rho}'| &\sim \rho-\bar{\rho}'\cdot\hat{k} = \rho-\left(x'\sin\theta+z'\cos\theta\right) \\ \frac{1}{|\bar{\rho}-\bar{\rho}'|} &\sim \frac{1}{\rho} \\ e^{ik|\bar{\rho}-\bar{\rho}'|} &\sim e^{ik\rho}e^{-ik\left(x'\sin\theta+z'\cos\theta\right)}\end{aligned}$$

Thus

$$g_0\left(\bar{\rho},\bar{\rho}'\right)\sim\frac{i}{4}\sqrt{\frac{2}{\pi k\rho}}e^{-i\frac{\pi}{4}}e^{ik\rho}e^{-ik\left(x'\sin\theta+z'\cos\theta\right)} \tag{3.48}$$

(b) Far field approximation of $g_R(\bar{\rho},\bar{\rho}')$

We put down again (3.24)

$$g_R\left(x,z;x',z'\right)=\frac{i}{4\pi}\int_{-\infty}^{\infty}dk_x e^{ik_x\left(x-x'\right)}\frac{R\left(k_x\right)}{k_z}e^{ik_z\left(z+z'\right)},z>0$$

Let us apply the stationary phase method to evaluate g_R at far field,

$$I\left(\lambda\right)=\int_a^b f\left(t\right)e^{i\lambda g(t)}dt$$
$$\lambda\gg 1,\lambda g\left(t\right)\text{ fast varying}$$
$$g\left(t\right):\text{ smooth real value function}$$
$$f\left(t\right):\text{ slow varying compared to }\lambda\mathrm{g}\left(t\right)$$

Then

$$I\left(\lambda\right)\sim\ f\left(c\right)e^{i\lambda g(c)}\left(\frac{2\pi}{\lambda\left|g"\left(c\right)\right|}\right)^{1/2}e^{i\frac{\pi}{4}\mu},\text{ as }\lambda\to\infty \tag{3.49}$$

where c is the stationary point of $g(t)$, where

$$g'\left(c\right)=0,\ c\text{ is the single root}$$
$$g''\left(c\right)\neq 0$$
$$\text{sign}\left(g''\left(c\right)\right)=\mu$$

Now

$$x=\rho\sin\theta$$
$$z=\rho\cos\theta$$

$$g_R\left(x,z;x',z'\right)=\frac{i}{4\pi}\int_{-\infty}^{\infty}dk_x e^{i\rho\left(k_x\sin\theta+k_z\cos\theta\right)}e^{-ik_x x'+ik_z z'}\frac{R}{k_z} \tag{3.50}$$

Thus

$$\lambda = \rho = \sqrt{x^2 + z^2}$$
$$g\left(k_x\right) = k_x \sin\theta + k_z \cos\theta$$
$$f\left(k_x\right) = e^{-ik_x x' + ik_z z'} \frac{R}{k_z}$$

It is easy to show that

$$c = k \sin\theta$$
$$\mu = -1$$

And

$$g_R\left(\bar{\rho}, \bar{\rho}'\right) \sim \frac{i}{4}\sqrt{\frac{2}{\pi k \rho}} e^{-i\frac{\pi}{4}} e^{ik\rho} e^{-ik\left(x'\sin\theta - z'\cos\theta\right)} R \tag{3.51}$$

Note the similarity to (3.48).

(c) Scattering field and scattering amplitude

Thus the scattering far field

$$\psi_s\left(\bar{\rho}\right) \sim \frac{k^2}{\varepsilon}\frac{i}{4}\sqrt{\frac{2}{\pi k \rho}} e^{-i\frac{\pi}{4}} e^{ik\rho} \sum_j \left[e^{-ik\left(x'\sin\theta + z'\cos\theta\right)} + e^{-ik\left(x'\sin\theta - z'\cos\theta\right)} R \right] p_j \tag{3.52}$$

The scattering amplitude f is defined by

$$\psi^s = \psi_0 \frac{1}{\sqrt{\rho}} e^{ik\rho} f \tag{3.53}$$

Assuming $\psi_0 = 1$

We have

$$f = \frac{k^2}{\varepsilon}\frac{i}{4}\sqrt{\frac{2}{\pi k}} e^{-i\frac{\pi}{4}} \sum_j \left[e^{-ik\left(x'\sin\theta + z'\cos\theta\right)} + e^{-ik\left(x'\sin\theta - z'\cos\theta\right)} R \right] p_j \tag{3.54}$$

3.1.8 The bistatic scattering coefficient

The bistatic scattering coefficient $\sigma(\theta_s)$ is related to the scattered power ratio ([34], pp. 68, eq. (3.1.42))

$$\frac{P_s}{P_{\text{inc}}} = \int_{-\pi/2}^{\pi/2} d\theta_s \sigma(\theta_s) \tag{3.55}$$

Let us first consider the incidence power P_{inc},

$$P_{\text{inc}} = -\int_{-L_x/2}^{L_x/2} ds\hat{s} \cdot \bar{S} \tag{3.56}$$

where L_x is the truncation length in the horizontal direction.

$\bar{S}$ is the Poynting vector,

$$\bar{S} = \frac{1}{2}\text{Re}\left[\bar{E} \times \bar{H}^*\right] \tag{3.57}$$

Using TE wave for example,

$$\bar{E} = \hat{y}E_y = \hat{y}\psi$$

It can be shown that

$$\bar{S} = -\frac{1}{2}\frac{1}{\omega\mu}\text{Im}\left[\psi\nabla\psi^*\right]$$

Note that in defining the bistatic scattering coefficient, P_{inc} only accounts for the direct incidence wave.

Let

$$\psi_i = \psi_0 e^{i\hat{k}_i \cdot \bar{\rho}} \tag{3.58}$$

Then

$$\bar{S} = \frac{1}{2}\frac{1}{\omega\mu}\bar{k}_i \left|\psi_0\right|^2$$

Thus

$$P_{\text{inc}} = -\int_{-L_x/2}^{L_x/2} ds\hat{s}\cdot\bar{S} = L_x \frac{1}{2}\frac{1}{\eta}|\psi_0|^2 \cos\theta_i$$

Note this result is in agreement with physical interpretation.

Next we consider the scattering power P_s,

$$P_s = \int_{-\pi/2}^{\pi/2} d\theta_s \rho\hat{\rho}\cdot\bar{S} \tag{3.59}$$

Now

$$\psi_s = \psi_0 \frac{1}{\sqrt{\rho}} e^{ik\rho} f$$
$$\nabla\psi_s \sim \psi_0 \frac{1}{\sqrt{\rho}} ik\hat{\rho} e^{ik\rho} f$$

where we only keep the term with $1/\sqrt{\rho}$ decay rate in $\nabla\psi_s$.

Thus

$$\bar{S} = \frac{1}{2}\frac{1}{\eta}|\psi_0|^2 \frac{1}{\rho}\hat{\rho}|f|^2$$

And

$$P_s = \int_{-\pi/2}^{\pi/2} d\theta_s \rho\hat{\rho}\cdot\bar{S} = \frac{1}{2}\frac{1}{\eta}|\psi_0|^2 \int_{-\pi/2}^{\pi/2} d\theta_s |f|^2$$

And the bistatic scattering coefficient $\sigma(\theta_s)$ is obtained by balancing

$$\int_{-\pi/2}^{\pi/2} d\theta_s \sigma(\theta_s) = \frac{P_s}{P_{\text{inc}}} = \frac{1}{L_x \cos\theta_i} \int_{-\pi/2}^{\pi/2} d\theta_s |f|^2$$

Thus

$$\sigma(\theta_s) = \frac{|f|^2}{L_x \cos\theta_i} \tag{3.60}$$

We will get the same expression for TM polarization.

3.1.9 The Coherent and Incoherent Scattering Field

In volumetric random media scattering, the coherent scattering field shows behavior of the effective media, while the incoherent scattering field represents the fluctuation due to random phase. Coherent field ideally only exists in the specular direction, but would spread out due to the finite simulation volume effect. In order to eliminate this truncation effects, we separate the computed scattering field into coherent scattering field and incoherent scattering field using Monte Carlo simulation. The incoherent scattering field will then converge as the truncation domain increases. It would resemble the observed radar backscatters, and in general the bistatic scattering other than in the specular direction.

We take the coherent scattering field as the average scattering field out of N_r realization,

$$\psi_s^{\text{coh}} = \langle \psi_s \rangle = \frac{1}{N_r} \sum_{i=1}^{N_r} \psi_s^i \tag{3.61}$$

And the incoherent scattering field as the fluctuation around the mean scattering field,

$$\tilde{\psi}_s^i = \psi_s^i - \langle \psi_s \rangle \tag{3.62}$$

Following (3.61) and (3.62), we also define the coherent bistatic scattering coefficients $\sigma^{\text{coh}}(\theta_s)$ and incoherent bistatic scattering coefficients $\sigma^{\text{inc}}(\theta_s)$ after (3.60),

$$\sigma^{\text{coh}}(\theta_s) = \frac{|\langle f \rangle|^2}{L_x \cos\theta_i} \tag{3.63}$$

$$\sigma^{\text{inc}}(\theta_s) = \frac{\left\langle |f - \langle f \rangle|^2 \right\rangle}{L_x \cos\theta_i} \tag{3.64}$$

It then follows

$$\sigma^{\text{coh}}(\theta_s) + \sigma^{\text{inc}}(\theta_s) = \sigma^{\text{tot}}(\theta_s) = \frac{\left\langle |f|^2 \right\rangle}{L_x \cos\theta_i} \tag{3.65}$$

Thus the total bistatic scattering coefficients $\sigma^{\mathrm{tot}}(\theta_s)$ has the meaning of second order moments, while the incoherent bistatic scattering coefficients $\sigma^{\mathrm{inc}}(\theta_s)$ has the meaning of variance.

3.1.10 Simulation results

We consider the backscattering from a layer of snow with 10cm thickness sitting on top of a dielectric ground with permittivity of $\varepsilon = (5 + 0.5i)\varepsilon_0$ at Ku band of 17.2GHz. The ice permittivity is taken as $(3.2 + 0.001i)\varepsilon_0$. The horizontal extent of the snow layer is truncated at 100cm. The incidence angle is at 40° and the wave is propagating in the xOz plane. The snow layer is represented by bicontinuous media with $\langle\zeta\rangle = 5000$, $b = 1$, and volume fraction $f_v = 0.3$. Such bicontinuous media has an equivalent exponential correlation length $p_{ex} = 0.36$mm. The 2D random media is generated by taking one cross section of the 3D bicontinuous media samples. The cylindrical 2D random media extends to infinity in the $\hat{y}$ direction. The computational domain configurations are illustrated in Figure III.2.

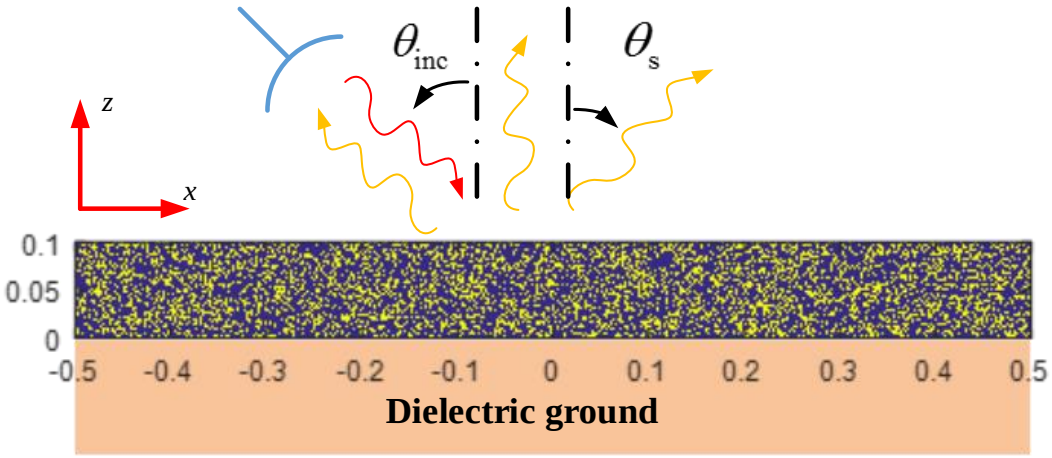

Figure III.2. Illustration of the computational domain configuration in 2D simulation.

The bistatic scattering coefficients γ (same as σ defined in Eq. (3.63-3.65)) are illustrated in Figure III.3 as a function of observation angle. The TE-polarized incidence wave is fixed at 40°. The results are averaged out of 1000 Monte Carlo simulations, and separated into coherent and incoherent scattering components. The coherent wave is concentrated into the specular scattering direction, containing information about the effective random media and influenced by the computational domain, while the incoherent wave dominates the other scattering directions and is more uniform as a function of angle, and is an approximation of the quantity measured by radar. The backscatter is shown to converge with ~500 realizations, and it converges as the horizontal extent of the computational domain increases.

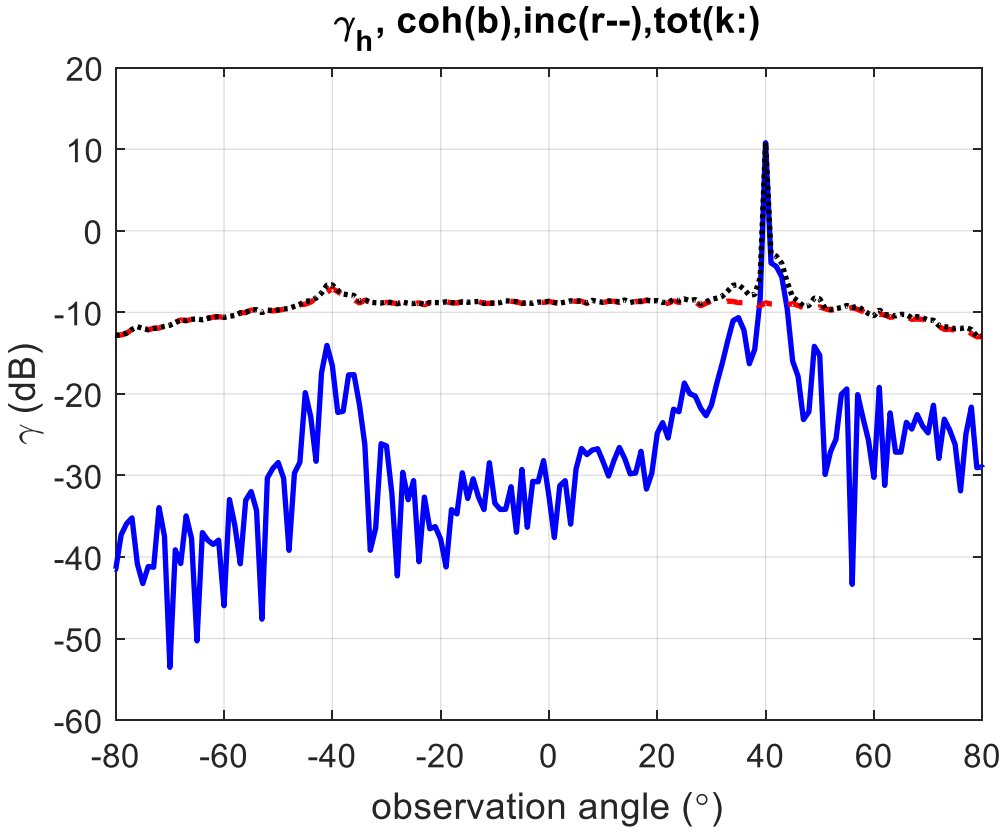

Figure III.3. Separation of bistatic scattering coefficients γ into coherent and incoherent components.

The incoherent scattering coefficients are again plotted in Figure III.4. There is a noticeable peak exceeding its neighbors by ~2dB with angular spread of ~10 degrees near the backward scattering direction, demonstrating the backscattering enhancement effects. The backscattering enhancement is a natural outcome of constructive wave interferences in the backward scattering direction due to possible dual opposite scattering paths arising from multiple volume scattering and volume-surface interactions, as explained in the previous chapter. The full wave simulation verifies this effect.

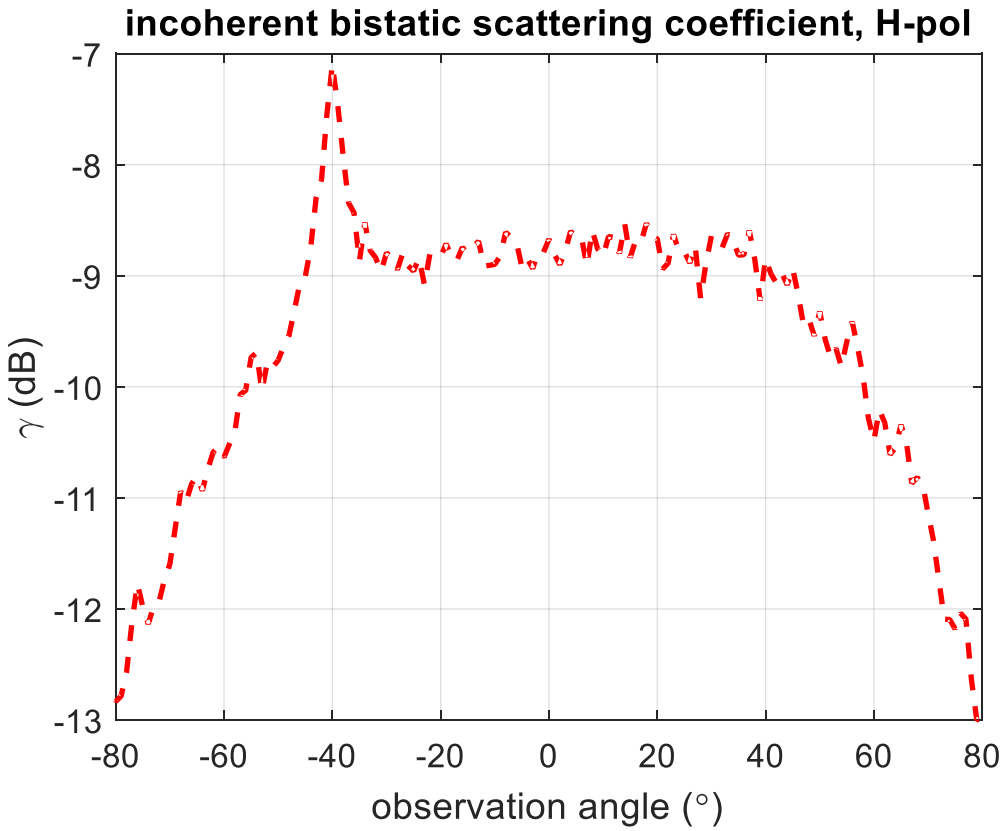

Figure III.4. Incoherent bistatic scattering coefficients

3.2 SAR Tomogram simulation to resolve snowpack vertical structure

In this section, we diverge from the electromagnetic scattering model of the snowpack itself, and instead we make use of the unique advantage of the full wave simulation, in that it is capable to calculate coherent scattering matrices of the scene with both amplitude and phase, to form a coherent synthetic aperture radar (SAR) tomogram of the snowpack. The SAR tomogram is a vertical cut of the 3D SAR image, which is formed by introducing multiple baseline in the traditional SAR configuration. The tomographic SAR (tomo-SAR) is an extension of the interferometric SAR (InSAR). The InSAR forms two SAR images of the same scene at slightly different observation angles, and obtain the surface topology from the slightly different phase of the two SAR images. The tomo-SAR uses multiple baselines, and combines the signal to obtain resolution over a third dimension, thus capable to compute 3D tomographic image. In a tomographic SAR, the bandwidth of the chirp signal generates the resolution along the range direction, the movement of the platform along track introducing Doppler shift creates the resolution in the cross-range direction, while the multiple baseline, bringing in multiple elevation angles, forms the resolution perpendicular to the plane spanned by the light of sight and the direction of platform motion. This third freedom introduced by multiple baseline has provided opportunity to resolve the vertical structure of volumetric random media, as demonstrated in the L-band [122] and P-band [123] tomographic SAR for forest mapping, and has brought forth tentative and experimental applications in multi-layer sea-ice/ lake-ice and snowpack stratigraphy observations [38, 120, 124-127] using tomo-SAR system scaled to X- and Ku-band. The traditional image focusing algorithms are derived from the single scattering process. Snow, however, as a densely packed random media, has strong multiple scattering effects within wavelengths. The multiple volume scattering will lead to defocusing of the obtained tomogram. It remains

questionable how the existence of multiple scattering affects the obtained 3D SAR image. Being able to simulate a SAR tomogram will help to tune the system operating parameters, to improve the image focusing algorithms, and to quantitatively interpret the tomogram and derive useful information.

In this section, we use the full-wave simulation techniques developed in section 3.1, to formulate a tomogram of a 2D snowpack. In a monostatic configuration, the 2D tomogram is constructed from the backward scattering matrices collected by scanning the incidence angles and the incidence wave frequencies, Figure III.5. We will apply two image focusing techniques, the field imaging using backward projection [124-129], and the imaging using frequency angular correlation functions (FACFs) [130], respectively. We will illustrate the tomograms for a synthesized two-layer snowpack.

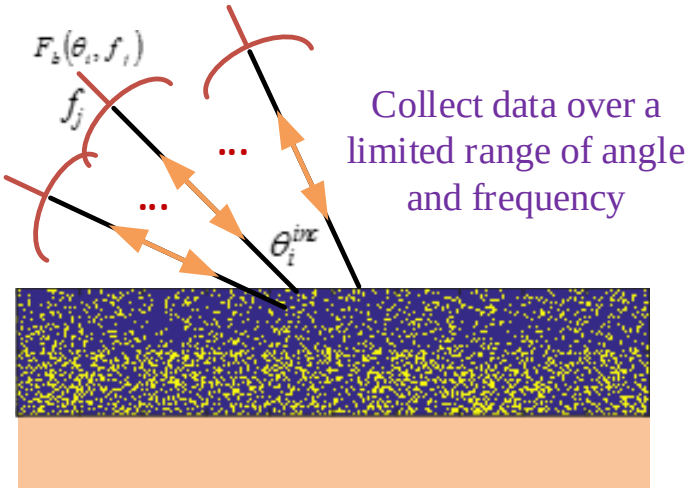

Figure III.5. Tomogram simulation configuration for 2D snowpack

3.2.1 The field imaging using backward projection

We have from (3.45) that, the scattering field

$$\begin{aligned}\psi_s(\bar{\rho}) &= k^2 \int_S d\bar{\rho}' g_0(\bar{\rho},\bar{\rho}')\left(\varepsilon_r(\bar{\rho}')-1\right)\psi(\bar{\rho}') \\ &+k^2 \int_S d\bar{\rho}' g_R(\bar{\rho},\bar{\rho}')\left(\varepsilon_r(\bar{\rho}')-1\right)\psi(\bar{\rho}')\end{aligned} \tag{3.66}$$

Ignoring the reflection term and making use of the far field approximation of g_0 as given in (3.48), we have

$$\psi_s(\bar{\rho}) \sim k^2 \frac{i}{4}\sqrt{\frac{2}{\pi k\rho}} e^{-i\frac{\pi}{4}} e^{ik\rho} \int_S d\bar{\rho}' e^{-i\bar{k}_s\cdot\bar{\rho}'}\left(\varepsilon_r(\bar{\rho}')-1\right)\psi(\bar{\rho}') \tag{3.67}$$

We further make use of the Born approximation, i.e., keeping the first order in the Born series,

$$\psi(\bar{\rho}) = \psi_0 e^{i\bar{k}_i\cdot\bar{\rho}} \tag{3.68}$$

then

$$\psi_s(\bar{\rho}) \sim k^2 \frac{i}{4}\sqrt{\frac{2}{\pi k\rho}} e^{-i\frac{\pi}{4}} e^{ik\rho} \int_S d\bar{\rho}' e^{i\left(\bar{k}_i-\bar{k}_s\right)\cdot\bar{\rho}'}\left(\varepsilon_r(\bar{\rho}')-1\right)\psi_0 \tag{3.69}$$

Considering the scattering amplitude f as defined in (3.53), we have

$$f(\bar{k}_s,\bar{k}_i) \sim k^2 \frac{i}{4}\sqrt{\frac{2}{\pi k}} e^{-i\frac{\pi}{4}} \int_S d\bar{\rho}' e^{i\left(\bar{k}_i-\bar{k}_s\right)\cdot\bar{\rho}'}\left(\varepsilon_r(\bar{\rho}')-1\right) \tag{3.70}$$

Let

$$\bar{k}_d = \bar{k}_i - \bar{k}_s \tag{3.71}$$

And define the object function $O(\bar{\rho})$ as

$$O(\bar{\rho}) = \varepsilon_r(\bar{\rho})-1 \tag{3.72}$$

We have

$$f(\bar{k}_d,k) \sim k^2 \frac{i}{4}\sqrt{\frac{2}{\pi k}} e^{-i\frac{\pi}{4}} \int_S d\bar{\rho}' e^{i\bar{k}_d\cdot\bar{\rho}'} O(\bar{\rho}') \tag{3.73}$$

It immediately follows that $f(\bar{k}_d, k)$ is related to the Fourier transform of $O(\bar{\rho}')$, and the object function $O(\bar{\rho}')$ can be reconstructed from $f(\bar{k}_d, k)$ using a two-dimensional inverse Fourier transform.

$$\begin{aligned} O(\bar{\rho}) &= \mathrm{FT}_{2d}^{-1}\left\{ f(\bar{k}_d, k)\frac{1}{k^2}\frac{4}{i}\sqrt{\frac{\pi k}{2}}e^{i\frac{\pi}{4}} \right\} \\ &= \frac{1}{(2\pi)^2}\int d\bar{k}_d e^{-i\bar{k}_d\cdot\bar{\rho}} f(\bar{k}_d, k)\frac{1}{k^2}\frac{4}{i}\sqrt{\frac{\pi k}{2}}e^{i\frac{\pi}{4}} \end{aligned} \tag{3.74}$$

Note that the integration of $\bar{k}_d$ in (3.74) is over the entire space in spectral domain, and in practice we can only integrate over a finite sampling space over which we have collected measurement.

Assuming that $f(\bar{k}_d, k)$ is due to a single point scatterer located at origin, i.e., $O(\bar{\rho}) = \delta(\bar{\rho})$ in (3.74), yields the point spreading function $U(\bar{\rho})$ of the imaging system,

$$U(\bar{\rho}) = \frac{1}{(2\pi)^2}\int d\bar{k}_d e^{-i\bar{k}_d\cdot\bar{\rho}} \tag{3.75}$$

Fourier analysis of $U(\bar{\rho})$ on a finite sampling space will tell about the finite spatial resolution and the domain of unambiguity of the imaging system. To summarize, the range resolution is $\delta_{\text{range}} = \frac{1}{2}\frac{c}{\text{BW}}$, where c is the speed of light, BW is the frequency bandwidth; the cross-range resolution is $\delta_{\text{cross-range}} = \frac{\lambda}{2\theta_B}$, where λ is the wavelength of operation, and θ_B is the span of the incidence angles. The unambiguity region is limited by the sampling density of the frequency and angle: in range direction the maximum domain of unambiguity $L_{\text{range}} = \frac{c}{2\Delta f}$, where Δf is the frequency sampling resolution; in cross-range direction, the maximum domain of unambiguity is $L_{\text{cross-range}} = \frac{\lambda}{2\Delta\theta}$, where $\Delta\theta$ is the angular sampling resolution.

The back-projection algorithm is an approximation of (3.74) with finite discrete measurements of $f\left(\bar{k}_s^{(n)}, \bar{k}_i^{(n)}\right)$, where $\left(\bar{k}_s^{(n)}, \bar{k}_i^{(n)}\right)$ denotes a unique combination of angle and frequency, possibly non-uniformly sampled in the k-space. It simply sums up the contribution from each measurements by correcting the propagation phase delay between the image point and the antenna aperture. Such an approach is computational intensive.

Dropping the unnecessary constants, the object function can be reconstructed, in the back-projection algorithm [124-129], by

$$O_{\text{back-projection}}\left(\bar{\rho}\right) \triangleq \sum_n e^{-i\left(\bar{k}_i^{(n)} - \bar{k}_s^{(n)}\right)\cdot\bar{\rho}} f\left(\bar{k}_s^{(n)}, \bar{k}_i^{(n)}\right) \frac{1}{k_n^{3/2}} \tag{3.76}$$

3.2.2 Imaging using frequency angular correlation function (FACF)

The back-projection algorithm of (3.76) is designed for the reconstruction of a deterministic scatterer, as its object function, as given in (3.72), has a point-wisely correspondence to the permittivity. When applied to random media reconstruction, such as snow, the quantity of interest is actually not the point-wise permittivity variation, but the statistics of these fluctuations. Thus we seek to add up the inter-correlation of each term in (3.76), denoted by $O^{(n)}\left(\bar{\rho}\right)$, except the self-interactions. The correlation is expected to cancel out the fluctuation effects in the random media, but keep those statistics, such as the effective permittivities of each layer. We define $C(\bar{\rho})$ as the reconstructed target using the frequency angular correlation functions (FACF) [130], given as follows,

$$\begin{aligned} C\left(\bar{\rho}\right) &= \sum_n \sum_{m\neq n} O^{(n)}\left(\bar{\rho}\right) O^{(m)*}\left(\bar{\rho}\right) \\ &= \sum_n e^{-i\left(\bar{k}_i^{(n)} - \bar{k}_s^{(n)}\right)\cdot\bar{\rho}} f\left(\bar{k}_s^{(n)}, \bar{k}_i^{(n)}\right) \frac{1}{k_n^{3/2}} \sum_{m\neq n} e^{i\left(\bar{k}_i^{(m)} - \bar{k}_s^{(m)}\right)\cdot\bar{\rho}} f^*\left(\bar{k}_s^{(m)}, \bar{k}_i^{(m)}\right) \frac{1}{k_m^{3/2}} \end{aligned} \tag{3.77}$$

In implementation, the exclusion criterion of $m \neq n$ can be generalized to

$$\left|\bar{k}_i^{(m)} - \bar{k}_i^{(n)}\right| > K = qk_0 \tag{3.78}$$

where k_0 is the center wavenumber and q is some adjustable parameter with default value $q = 1/16$.

The FACF imaging approach of (3.77) is expected to suppress the noisy cluster scattering from snow grains, but retain statistical contrasts between layers, and possibly requires less number of acquisitions to derive the parameters of interest, such as the density and thickness of each layers. This is of particular interest in airborne and spaceborne applications, as the number of acquisitions, the angular span, and the bandwidth are quite limited.

3.2.3 Illustration of imaging results

We consider a synthesized two-layer snowpack as demonstrated in Figure III.5. The computation domain is of 100cm x 20 cm, with the top 10cm of $\langle\zeta\rangle = 10000m^{-1}$, $b = 2.0$, and volume fraction $f_v = 0.15$, and the bottom 10cm of $\langle\zeta\rangle = 5000m^{-1}$, $b = 1.0$, and $f_v = 0.3$, where $\langle\zeta\rangle$, b, and f_v are the defining parameters of the bicontinuous media. The ground underneath the snowpack has permittivity of $(1 + i0.5)\varepsilon_0$. The ice permittivity is taken as $(3.2 + 0.001i)\varepsilon_0$.

The reconstructed tomograms from 2D simulation of TE polarized wave impinging upon the layered 2D bicontinuous structures are shown in Figure III.6. The frequency scans from 9 to 11GHz with 100MHz stepping, and the incidence angle spans from 30 to 50 degree with 1 degree stepping. This corresponds to a range resolution of 7.5cm, and cross range resolution of 4.8cm. The results of field back-projection imaging $|O(\bar{\rho})|$ and the FACF imaging $\sqrt{|C(\bar{\rho})|}$ are calculated using the total backward scattering amplitude computed from one realization of the two-layer random media, and are shown in Figure III.6 (a) and (b), respectively. In both cases, the two-layer

structure are clearly revealed. The field imaging results shows more internal spatial variations within each layer; the FACF imaging helps to suppress scattering from ice grains which has little correlations, and reveal boundaries and layer interfaces that scattering has stronger correlations. The two strong peaks and leakages near the two truncating edges, as annotated by the circles, are possibly due to the reflected wave and multiple scattering that are not considered in the imaging algorithm in both the incident and scattered waves. Note that the interface separating the two layers in the reconstructed images is slightly tilting up around $z = 0.1m$ as annotated by the dashed line. The up-tilting interface is due to the slow-down of phase velocity inside the bicontinuous media than in the free space that is not considered in the Born approximation from which the imaging algorithms are derived [124, 125].

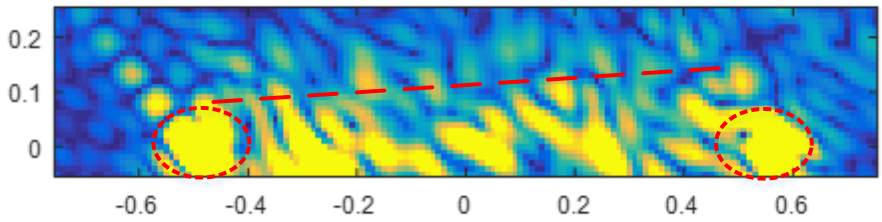

(a) field back-projection imaging

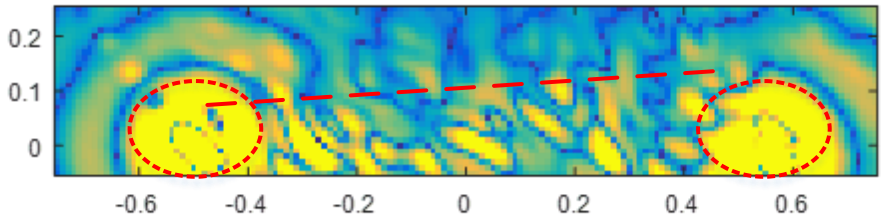

(b) FACF imaging

Figure III.6. Reconstructed tomogram of the two-layer 2D snowpack using TE polarization (a) field back-projection imaging (b) FACF imaging. The circles denote the leakage near the two truncating edges; the dashed lines illustrate the up-tilting interfaces separating the two layers in the reconstructed image. The tomogram is constructed from the scattering field calculated from one realization of the two-layer random media.

3.3 Plane wave excitation of a truncated 3D snow layer

In this section, we move on to the real scenario of 3D simulation, where the snow volume can be represented by 3D bicontinuous media. The formulation procedure is in direct parallel to the 2D case as described in section 3.1. Thus we only focus on the unique parts to 3D, including the formulation of half space dyadic Green's function and its rapid interpolation, and the parallelization scheme on high performance computing (HPC) clusters, etc. Comparing to the popular deployed DDA code, the uniqueness of our formulation is that it incorporates a half-space dyadic Green's function instead of the free-space counterpart, and its scalability to large scale parallel clusters. We also compare the full wave simulation results with the DMRT results.

3.3.1 The 3D volume integral equation (VIE) and the Discrete Dipole Approximation

We start from the 3D Helmholtz equation (the vector wave equation) where we readily separate out an equivalent source term due to polarization to the right hand side.

$$\nabla\times\nabla\times\bar{E}(\bar{r})-k^2\bar{E}(\bar{r})=k^2\left(\varepsilon_r(\bar{r})-1\right)\bar{E}(\bar{r}) \tag{3.79}$$

The incidence field, on the other hand, propagates in the background medium,

$$\nabla\times\nabla\times\bar{E}_{\text{inc}}(\bar{r})-k^2\bar{E}_{\text{inc}}(\bar{r})=0 \tag{3.80}$$

Subtracting (3.80) from (3.79), and considering

$$\bar{E}(\bar{r})=\bar{E}^{\text{inc}}(\bar{r})+\bar{E}^{\text{s}}(\bar{r}) \tag{3.81}$$

we get the equation governing the scattering field,

$$\nabla\times\nabla\times\bar{E}^{s}(\bar{r})-k^2\bar{E}^{s}(\bar{r})=k^2\left(\varepsilon_r(\bar{r})-1\right)\bar{E}(\bar{r}) \tag{3.82}$$

Considering the dyadic Green's function $\bar{\bar{G}}(\bar{r},\bar{r})$,

$$\nabla\times\nabla\times\bar{\bar{G}}(\bar{r},\bar{r}')-k^2\bar{\bar{G}}(\bar{r},\bar{r}')=\bar{\bar{I}}\,\delta(\bar{r}-\bar{r}') \tag{3.83}$$

where $\bar{\bar{I}}$ is the identity dyad.

We can represent the scattering field $\bar{E}^s(\bar{r})$ in an integral formulation,

$$\bar{E}^s(\bar{r}) = k^2 \int_V d\bar{r}\,' \bar{\bar{G}}(\bar{r},\bar{r}\,')\left[\left(\varepsilon_r(\bar{r}\,')-1\right)\right]\bar{E}(\bar{r}\,') \tag{3.84}$$

Using (3.81) to eliminate $\bar{E}^s(\bar{r})$, we get the volume integral equation for the total field $\bar{E}(\bar{r})$.

$$\bar{E}(\bar{r}) = \bar{E}^{\text{inc}}(\bar{r}) + k^2 \int_V d\bar{r}\,' \bar{\bar{G}}(\bar{r},\bar{r}\,')\left[\left(\varepsilon_r(\bar{r}\,')-1\right)\right]\bar{E}(\bar{r}\,') \tag{3.85}$$

Note that $\bar{\bar{G}}(\bar{r},\bar{r})$ is the dyadic Green's function including half-space $\bar{\bar{G}}_{00}(\bar{r},\bar{r})$, consisting the primary contribution from free-space dyadic Green's function $\bar{\bar{G}}_0(\bar{r},\bar{r})$ and the response contribution from reflection $\bar{\bar{G}}_R(\bar{r},\bar{r})$.

$$\bar{\bar{G}}(\bar{r},\bar{r}\,') = \bar{\bar{G}}_0(\bar{r},\bar{r}\,') + \bar{\bar{G}}_R(\bar{r},\bar{r}\,') \tag{3.86}$$

Then

$$\begin{aligned}\bar{E}(\bar{r}) = \bar{E}^{\text{inc}}(\bar{r}) &+ k^2 \int_V d\bar{r}\,' \bar{\bar{G}}_0(\bar{r},\bar{r}\,')\left[\left(\varepsilon_r(\bar{r}\,')-1\right)\right]\bar{E}(\bar{r}\,') \\ &+ k^2 \int_V d\bar{r}\,' \bar{\bar{G}}_R(\bar{r},\bar{r}\,')\left[\left(\varepsilon_r(\bar{r}\,')-1\right)\right]\bar{E}(\bar{r}\,')\end{aligned} \tag{3.87}$$

In discretizing (3.87), we follow the same scheme as in section 3.1.2 using pulse basis and point matching. After defining the singular integral over the self-cube V_c,

$$\bar{\bar{S}} = \int_{V_c} d\bar{r}\,' \bar{\bar{G}}_0(\bar{r},\bar{r}\,') \tag{3.88}$$

which can be evaluated out to be diagonal over cubes [34],

$$\bar{\bar{S}} = \bar{\bar{I}}s \tag{3.89}$$

$$s = -\frac{1}{3k^2} + \frac{1}{k^2}\frac{1}{4\pi}\left[\left(\frac{4\pi}{3}\right)^{1/3} k^2 d^2 + \frac{i2k^3 d^3}{3}\right] \tag{3.90}$$

where d is the edge length of the discretization cubes.

Then (3.87) becomes

$$\begin{aligned}\bar{E}\left(\bar{r}_i\right) = \bar{E}^{\text{inc}}\left(\bar{r}_i\right) + k^2\left(\varepsilon_r\left(\bar{r}_i\right)-1\right)s\bar{E}\left(\bar{r}_i\right) + \frac{k^2}{\varepsilon}\sum_{j\neq i}\bar{\bar{G}}_0\left(\bar{r}_i,\bar{r}_j\right)\left[\varepsilon\left(\varepsilon_r\left(\bar{r}_j\right)-1\right)\right]\bar{E}\left(\bar{r}_j\right)\Delta V \\ + \frac{k^2}{\varepsilon}\sum_{j}\bar{\bar{G}}_R\left(\bar{r}_i,\bar{r}_j\right)\left[\varepsilon\left(\varepsilon_r\left(\bar{r}_j\right)-1\right)\right]\bar{E}\left(\bar{r}_j\right)\Delta V\end{aligned} \tag{3.91}$$

where $\Delta V = d^3$ is the volume of each cube. In doing so, we have utilized the fact that all the singularities are within the self-term of $\bar{\bar{G}}_0(\bar{r},\bar{r})$.

We then define the dipole moment $\bar{p}_i$

$$\bar{p}_i = \Delta V\varepsilon\left(\varepsilon_r\left(\bar{r}_i\right)-1\right)\bar{E}_i \tag{3.92}$$

and the free-space polarizability α_i,

$$\alpha_i = \frac{\Delta V\varepsilon\left(\varepsilon_r\left(\bar{r}_i\right)-1\right)}{1-\left(\varepsilon_r\left(\bar{r}_i\right)-1\right)k^2 s} \tag{3.93}$$

Then (3.91) can be considerably simplified,

$$\bar{p}_i = \alpha_i\left[\bar{E}^{\text{inc}}\left(\bar{r}_i\right) + \frac{k^2}{\varepsilon}\sum_{j\neq i}\bar{\bar{G}}_0\left(\bar{r}_i,\bar{r}_j\right)\cdot\bar{p}_j + \frac{k^2}{\varepsilon}\sum_{j}\bar{\bar{G}}_R\left(\bar{r}_i,\bar{r}_j\right)\cdot\bar{p}_j\right] \tag{3.94}$$

Such is the DDA equation to be solved in 3D. It is quite similar to its 2D counterparts in (3.20). The only difference is that we are changing from scalar unknowns to vector unknowns. And the real complexity lies in the dyadic Green's function.

3.3.2 The half-space dyadic Green's function

The math is much more involved in 3D than 2D to evaluate the Green's function. As already given in (3.86), the half-space dyadic Green's function $\bar{\bar{G}}_{00}(\bar{r},\bar{r})$ comprises two parts: the free space component $\bar{\bar{G}}_0(\bar{r},\bar{r})$ and the reflection component $\bar{\bar{G}}_R(\bar{r},\bar{r})$.

$$\bar{\bar{G}}_{00}\left(\bar{r},\bar{r}'\right)=\bar{\bar{G}}_{0}\left(\bar{r},\bar{r}'\right)+\bar{\bar{G}}_{R}\left(\bar{r},\bar{r}'\right)$$

(a) The free-space dyadic Green's function

The free space dyadic Green's function $\bar{\bar{G}}_0(\bar{r},\bar{r})$ can be related to the 3D scalar Green's function $g_0(\bar{r},\bar{r})$ through the scalar and vector potential, given explicitly,

$$\bar{\bar{G}}_{0}\left(\bar{r},\bar{r}'\right)=\left(\bar{\bar{I}}+\frac{\nabla\nabla}{k^{2}}\right)g_{0}\left(\bar{r},\bar{r}'\right) \tag{3.95}$$

where

$$g_{0}\left(\bar{r},\bar{r}'\right)=\frac{\exp\left(ik\left|\bar{r}-\bar{r}'\right|\right)}{4\pi\left|\bar{r}-\bar{r}'\right|} \tag{3.96}$$

In calculation, it is much easier to put the dyadic Green's function in the spherical coordinate [34],

$$\bar{\bar{G}}_{0}\left(\bar{r},\bar{r}'\right)=G_{1}\left(R\right)\bar{\bar{I}}+G_{2}\left(R\right)\hat{R}\hat{R} \tag{3.97}$$

where

$$\begin{aligned}
&R=\left|\bar{r}-\bar{r}'\right|\\
&G_{1}\left(R\right)=\left(-1+ikR+k^{2}R^{2}\right)\frac{\exp\left(ikR\right)}{4\pi k^{2}R^{3}}\\
&G_{2}\left(R\right)=\left(3-3ikR-k^{2}R^{2}\right)\frac{\exp\left(ikR\right)}{4\pi k^{2}R^{3}}
\end{aligned} \tag{3.98}$$

One can also put the dyadic Green's function in spectral domain, derivable from the integral representation of $g_0(\bar{r},\bar{r})$ [24],

$$g_{0}\left(\bar{r},\bar{r}'\right)=\frac{i}{8\pi^{2}}\int_{-\infty}^{\infty}dk_{x}\int_{-\infty}^{\infty}dk_{y}\,\frac{\exp\left(ik_{x}\left(x-x'\right)+ik_{y}\left(y-y'\right)+ik_{z}\left|z-z'\right|\right)}{k_{z}} \tag{3.99}$$

where $k_z=\sqrt{k^2-k_x^2-k_y^2}$ with $\mathrm{Im}\{k_z\}\geq 0$. Then using (3.95),

$$\bar{\bar{G}}_0(\bar{r},\bar{r}') = -\frac{1}{k^2}\delta(x-x')\delta(y-y')\delta(z-z')\hat{z}\hat{z} + \begin{cases} \dfrac{i}{8\pi^2}\displaystyle\int_{-\infty}^{\infty}dk_x\int_{-\infty}^{\infty}dk_y\left[\hat{e}(k_z)\hat{e}(k_z)+\hat{h}(k_z)\hat{h}(k_z)\right]\dfrac{\exp\left(i\bar{k}\cdot(\bar{r}-\bar{r}')\right)}{k_z} & z>z' \\ \dfrac{i}{8\pi^2}\displaystyle\int_{-\infty}^{\infty}dk_x\int_{-\infty}^{\infty}dk_y\left[\hat{e}(-k_z)\hat{e}(-k_z)+\hat{h}(-k_z)\hat{h}(-k_z)\right]\dfrac{\exp\left(i\bar{K}\cdot(\bar{r}-\bar{r}')\right)}{k_z} & z<z' \end{cases} \tag{3.100}$$

where

$$\hat{e}(k_x,k_y,k_z) = \frac{1}{k_\rho}\left(-k_x\hat{y}+k_y\hat{x}\right) \tag{3.101}$$

$$\hat{h}(k_x,k_y,k_z) = -\frac{k_z}{kk_\rho}\left(k_x\hat{x}+k_y\hat{y}\right)+\frac{k_\rho}{k}\hat{z} \tag{3.102}$$

where $k_\rho = \sqrt{k_x^2+k_y^2}$.

$$\bar{k} = k_x\hat{x}+k_y\hat{y}+k_z\hat{z} \tag{3.103}$$

$$\bar{K} = k_x\hat{x}+k_y\hat{y}-k_z\hat{z} \tag{3.104}$$

Equation (3.100) is helpful in deriving the integral formulation of the half-space dyadic Green's function.

(b) The reflection component of the dyadic Green's function

It is straightforward to derive the spectral domain representation of the reflection component of the half-space dyadic Green's function $\bar{\bar{G}}_R(\bar{r},\bar{r})$ from (3.100) by matching the modes and boundary conditions [24]. Assuming the boundary is at $z=0$,

$$\bar{\bar{G}}_R(\bar{r},\bar{r}') = \frac{i}{8\pi^2}\int_{-\infty}^{\infty}dk_x\int_{-\infty}^{\infty}dk_y\left[R^{\mathrm{TE}}\hat{e}(k_z)\hat{e}(-k_z)+R^{\mathrm{TM}}\hat{h}(k_z)\hat{h}(-k_z)\right]\frac{\exp\left(i\bar{k}\cdot\bar{r}-i\bar{K}\cdot\bar{r}'\right)}{k_z} \tag{3.105}$$

where R^{TE} and R^{TM} are the Fresnel reflection coefficient for each plane wave component of the TE and TM polarization, respectively, as given in (3.30).

Although it is possible to evaluate the 2D integral directly in (3.105), it is more efficient to convert it into a 1D integral by invoking plane wave and cylindrical wave transformations. In doing so, it is more convenient to examine directly the scattering field due to a vertical electric dipole (VED) and a horizontal electric dipole (HED) above a half space, respectively [131, 132]. This corresponds to the physical meaning of each component of the dyadic Green's function.

(c) The VED and HED above a half space

Assume a point current source (Hertz dipole) above ground at $\bar{r}' = (0,0,z')$, $z' > 0$

$$\bar{J}(\bar{r}) = \hat{\alpha} Il\delta(\bar{r} - \bar{r}') \tag{3.106}$$

where $\hat{\alpha}$ is a unit vector representing the orientation of the Hertz dipole. $\hat{\alpha} = \hat{z}$ represents a vertical electric dipole (VED) and $\hat{\alpha} = \hat{x}$ represents a horizontal electric dipole (HED).

By applying the Sommerfeld identity,

$$\frac{e^{ikr}}{r} = \frac{i}{2}\int_{-\infty}^{\infty} dk_\rho \frac{k_\rho}{k_z} H_0^{(1)}(k_\rho \rho) e^{ik_z|z|} = i\int_0^{\infty} dk_\rho \frac{k_\rho}{k_z} J_0(k_\rho \rho) e^{ik_z|z|}$$

where the first equality is more suitable for analytical path deformation, and the second equality is more suitable for numerical evaluation.

We can represent the primary field in integral forms and then by matching boundary condition get the integral representation of the reflection field. We summarize the pilot z-component of the fields. We have assumed the boundary at $z = 0$.

For VED ($\hat{\alpha} = \hat{z}$)

$$E_z^0\left(\bar{r},\bar{r}'\right)=-\frac{Il}{8\pi\omega\varepsilon}\int_{-\infty}^{\infty}dk_\rho\,\frac{k_\rho^3}{k_z}H_0^{(1)}\left(k_\rho\rho\right)e^{ik_z|z-z'|}$$
$$-\frac{iIl}{4\pi\omega\varepsilon}\delta\left(z-z'\right)\int_{-\infty}^{\infty}dk_\rho k_\rho H_0^{(1)}\left(k_\rho\rho\right) \tag{3.107}$$

$$H_z^0\left(\bar{r},\bar{r}'\right)=0 \tag{3.108}$$

$$E_z^R\left(\bar{r},\bar{r}'\right)=-\frac{Il}{4\pi\omega\varepsilon}\int_0^{\infty}dk_\rho\,\frac{k_\rho^3}{k_z}J_0\left(k_\rho\rho\right)R^{\mathrm{TM}}e^{ik_z\left(z+z'\right)} \tag{3.109}$$

$$H_z^R\left(\bar{r},\bar{r}'\right)=0 \tag{3.110}$$

For HED ($\hat{\alpha}=\hat{x}$)

$$E_z^0\left(\bar{r},\bar{r}'\right)=\begin{cases}\dfrac{iIl}{8\pi\omega\varepsilon}\cos\phi\displaystyle\int_{-\infty}^{\infty}dk_\rho k_\rho^2H_1^{(1)}\left(k_\rho\rho\right)e^{ik_z\left(z-z'\right)},\ z>z'\\ -\dfrac{iIl}{8\pi\omega\varepsilon}\cos\phi\displaystyle\int_{-\infty}^{\infty}dk_\rho k_\rho^2H_1^{(1)}\left(k_\rho\rho\right)e^{-ik_z\left(z-z'\right)},\ z<z'\end{cases} \tag{3.111}$$

$$H_z^0\left(\bar{r},\bar{r}'\right)=\frac{iIl}{8\pi}\sin\phi\int_{-\infty}^{\infty}dk_\rho\,\frac{k_\rho^2}{k_z}H_1^{(1)}\left(k_\rho\rho\right)e^{ik_z|z-z'|} \tag{3.112}$$

$$E_z^R\left(\bar{r},\bar{r}'\right)=-\frac{iIl}{4\pi\omega\varepsilon}\cos\phi\int_0^{\infty}dk_\rho k_\rho^2J_1\left(k_\rho\rho\right)R^{\mathrm{TM}}e^{ik_z\left(z+z'\right)} \tag{3.113}$$

$$H_z^R\left(\bar{r},\bar{r}'\right)=\frac{iIl}{4\pi}\sin\phi\int_0^{\infty}dk_\rho\,\frac{k_\rho^2}{k_z}J_1\left(k_\rho\rho\right)R^{\mathrm{TE}}e^{ik_z\left(z+z'\right)} \tag{3.114}$$

where $\rho=\sqrt{x^2+y^2}$, $\sin\phi=y/\rho$, and $\cos\phi=x/\rho$.

We then express the tangential field components using the pilot z-components. For each k_ρ,

$$\tilde{E}\left(k_\rho,\bar{r}\right)=\frac{1}{k_\rho^2}\left[ik_z\nabla_s\tilde{E}_z-i\omega\mu\hat{z}\times\nabla_s\tilde{H}_z\right] \tag{3.115}$$

$$\tilde{H}\left(k_\rho,\bar{r}\right)=\frac{1}{k_\rho^2}\left[ik_z\nabla_s\tilde{H}_z+i\omega\varepsilon\hat{z}\times\nabla_s\tilde{E}_z\right] \tag{3.116}$$

where $\nabla_s = \hat{\rho}\frac{\partial}{\partial\rho} + \hat{\phi}\frac{1}{\rho}\frac{\partial}{\partial\phi}$.

Explicitly, for VED ($\hat{\alpha} = \hat{z}$)

$$E_\rho^R\left(\bar{r},\bar{r}'\right) = \frac{iIl}{4\pi\omega\varepsilon}\int_0^\infty dk_\rho k_\rho^2 J_1\left(k_\rho\rho\right)R^{\mathrm{TM}}e^{ik_z(z+z')} \tag{3.117}$$

$$E_\phi^R\left(\bar{r},\bar{r}'\right) = 0 \tag{3.118}$$

$$H_\rho^R\left(\bar{r},\bar{r}'\right) = 0 \tag{3.119}$$

$$H_\phi^R\left(\bar{r},\bar{r}'\right) = \frac{iIl}{4\pi}\int_0^\infty dk_\rho \frac{k_\rho^2}{k_z} J_1\left(k_\rho\rho\right)R^{\mathrm{TM}}e^{ik_z(z+z')} \tag{3.120}$$

And for HED ($\hat{\alpha} = \hat{x}$)

$$E_\rho^R\left(\bar{r},\bar{r}'\right) = \frac{Il}{4\pi\omega\varepsilon}\cos\phi\int_0^\infty dk_\rho k_\rho\left[k_z J_1'\left(k_\rho\rho\right)R^{\mathrm{TM}} - \frac{k^2}{k_z}\frac{J_1\left(k_\rho\rho\right)}{k_\rho\rho}R^{\mathrm{TE}}\right]e^{ik_z(z+z')} \tag{3.121}$$

$$E_\phi^R\left(\bar{r},\bar{r}'\right) = -\frac{Il}{4\pi\omega\varepsilon}\sin\phi\int_0^\infty dk_\rho k_\rho\left[k_z\frac{J_1\left(k_\rho\rho\right)}{k_\rho\rho}R^{\mathrm{TM}} - \frac{k^2}{k_z}J_1'\left(k_\rho\rho\right)R^{\mathrm{TE}}\right]e^{ik_z(z+z')} \tag{3.122}$$

$$H_\rho^R\left(\bar{r},\bar{r}'\right) = -\frac{Il}{4\pi}\sin\phi\int_0^\infty dk_\rho k_\rho\left[J_1'\left(k_\rho\rho\right)R^{\mathrm{TE}} - \frac{J_1\left(k_\rho\rho\right)}{k_\rho\rho}R^{\mathrm{TM}}\right]e^{ik_z(z+z')} \tag{3.123}$$

$$H_\phi^R\left(\bar{r},\bar{r}'\right) = \frac{Il}{4\pi}\cos\phi\int_0^\infty dk_\rho k_\rho\left[J_1'\left(k_\rho\rho\right)R^{\mathrm{TM}} - \frac{J_1\left(k_\rho\rho\right)}{k_\rho\rho}R^{\mathrm{TE}}\right]e^{ik_z(z+z')} \tag{3.124}$$

where $J_1'(x)$ denotes the derivative of the Bessel function with respect to its argument.

Defining the four kernel Sommerfeld integrals as follows,

$$g_z^{\mathrm{TM}}\left(\rho, z+z'\right) = \frac{i}{4\pi k^2}\int_0^\infty dk_\rho \frac{k_\rho^3}{k_z} J_0\left(k_\rho\rho\right)R^{\mathrm{TM}}e^{ik_z(z+z')} \tag{3.125}$$

$$g_\rho^{\mathrm{TM}}\left(\rho, z+z'\right) = \frac{1}{4\pi k^2}\int_0^\infty dk_\rho k_\rho^2 J_1\left(k_\rho\rho\right)R^{\mathrm{TM}}e^{ik_z(z+z')} \tag{3.126}$$

$$g_{\rho}^{\mathrm{EM}}\left(\rho, z+z'\right)=\frac{-i}{4\pi k^{2}}\int_{0}^{\infty}dk_{\rho}k_{\rho}\left[k_{z}J_{1}'\left(k_{\rho}\rho\right)R^{\mathrm{TM}}-\frac{k^{2}}{k_{z}}\frac{J_{1}\left(k_{\rho}\rho\right)}{k_{\rho}\rho}R^{\mathrm{TE}}\right]e^{ik_{z}\left(z+z'\right)} \tag{3.127}$$

$$g_{\phi}^{\mathrm{EM}}\left(\rho, z+z'\right)=\frac{i}{4\pi k^{2}}\int_{0}^{\infty}dk_{\rho}k_{\rho}\left[k_{z}\frac{J_{1}\left(k_{\rho}\rho\right)}{k_{\rho}\rho}R^{\mathrm{TM}}-\frac{k^{2}}{k_{z}}J_{1}'\left(k_{\rho}\rho\right)R^{\mathrm{TE}}\right]e^{ik_{z}\left(z+z'\right)} \tag{3.128}$$

Note that each of these four integral has only two independent arguments of ρ and $z+z'$. Then all the field components can be represented using these key integrals,

$$E_{z}^{R,\mathrm{VED}}\left(\rho, z+z'\right)=i\omega\mu Ilg_{z}^{\mathrm{TM}} \tag{3.129}$$

$$E_{\rho}^{R,\mathrm{VED}}\left(\rho, z+z'\right)=i\omega\mu Ilg_{\rho}^{\mathrm{TM}} \tag{3.130}$$

$$E_{\rho}^{R,\mathrm{HED}}\left(\rho, z+z', \phi\right)=i\omega\mu Il\cos\phi g_{\rho}^{\mathrm{EM}} \tag{3.131}$$

$$E_{\phi}^{R,\mathrm{HED}}\left(\rho, z+z', \phi\right)=i\omega\mu Il\sin\phi g_{\phi}^{\mathrm{EM}} \tag{3.132}$$

$$E_{z}^{R,\mathrm{HED}}\left(\rho, z+z', \phi\right)=-i\omega\mu Il\cos\phi g_{\rho}^{\mathrm{TM}} \tag{3.133}$$

And we further represent each of the field components in the Cartesian coordinates,

From VED ($\hat{\alpha}=\hat{z}$), we get E_{xz}^{R}, E_{yz}^{R}, and E_{zz}^{R},

$$E_{xz}^{R}=\hat{x}\cdot\hat{\rho}E_{\rho}^{R,\mathrm{VED}}=\cos\phi E_{\rho}^{R,\mathrm{VED}} \tag{3.134}$$

$$E_{yz}^{R}=\hat{y}\cdot\hat{\rho}E_{\rho}^{R,\mathrm{VED}}=\sin\phi E_{\rho}^{R,\mathrm{VED}} \tag{3.135}$$

$$E_{zz}^{R}=E_{z}^{R,\mathrm{VED}} \tag{3.136}$$

From HED ($\hat{\alpha}=\hat{x}$), we get E_{xx}^{R}, E_{yx}^{R}, and E_{zx}^{R},

$$E_{xx}^{R}=\hat{x}\cdot\hat{\rho}E_{\rho}^{R,\mathrm{HED}}+\hat{x}\cdot\hat{\phi}E_{\phi}^{R,\mathrm{HED}}=\cos\phi E_{\rho}^{R,\mathrm{HED}}\left(\phi\right)-\sin\phi E_{\phi}^{R,\mathrm{HED}}\left(\phi\right) \tag{3.137}$$

$$E_{yx}^{R}=\hat{y}\cdot\hat{\rho}E_{\rho}^{R,\mathrm{HED}}+\hat{y}\cdot\hat{\phi}E_{\phi}^{R,\mathrm{HED}}=\sin\phi E_{\rho}^{R,\mathrm{HED}}\left(\phi\right)+\cos\phi E_{\phi}^{R,\mathrm{HED}}\left(\phi\right) \tag{3.138}$$

$$E_{zx}^{R}=E_{z}^{R,\mathrm{HED}}\left(\phi\right) \tag{3.139}$$

And to get E_{xy}^R, E_{yy}^R, and E_{zy}^R due to J_y (HED ($\hat{\alpha} = \hat{y}$)), we can still express the results using HED oriented along $\hat{x}$ by introducing a localized azimuth angle $\varphi = \phi - \frac{\pi}{2}$, which is the angle between $\hat{\rho}$ and $\hat{y}$, thus

$$E_{xy}^R = \hat{x} \cdot \hat{\rho} E_{\rho}^{R,\mathrm{HED}} + \hat{x} \cdot \hat{\phi} E_{\phi}^{R,\mathrm{HED}} = \cos\phi E_{\rho}^{R,\mathrm{HED}}\left(\phi - \frac{\pi}{2}\right) - \sin\phi E_{\phi}^{R,\mathrm{HED}}\left(\phi - \frac{\pi}{2}\right) \tag{3.140}$$

$$E_{yy}^R = \hat{y} \cdot \hat{\rho} E_{\rho}^{R,\mathrm{HED}} + \hat{y} \cdot \hat{\phi} E_{\phi}^{R,\mathrm{HED}} = \sin\phi E_{\rho}^{R,\mathrm{HED}}\left(\phi - \frac{\pi}{2}\right) + \cos\phi E_{\phi}^{R,\mathrm{HED}}\left(\phi - \frac{\pi}{2}\right) \tag{3.141}$$

$$E_{zy}^R = E_z^{R,\mathrm{HED}}\left(\phi - \frac{\pi}{2}\right) \tag{3.142}$$

Thus we get all the field components in the Cartesian coordinates. We then relate the dyadic Green's function to these field components radiated from the Hertz dipoles.

Considering (3.106), and

$$\bar{E}^R(\bar{r}) = i\omega\mu \int d\bar{r}'' \bar{\bar{G}}_R(\bar{r}, \bar{r}'') \cdot \bar{J}(\bar{r}'') = i\omega\mu Il \bar{\bar{G}}_R(\bar{r}, \bar{r}') \cdot \hat{\alpha} \tag{3.143}$$

We have

$$\bar{\bar{G}}_R(\bar{r}, \bar{r}') = \frac{1}{i\omega\mu Il} \begin{bmatrix} E_{xx} & E_{xy} & E_{xz} \\ E_{yx} & E_{yy} & E_{yz} \\ E_{zx} & E_{zy} & E_{zz} \end{bmatrix} \tag{3.144}$$

Substituting (3.134)-(3.142) into (3.144), and making use of (3.129)-(3.133), we get the explicit expressions for each Cartesian component of $\bar{\bar{G}}_R(\bar{r}, \bar{r}')$.

In general for $\rho \neq 0$ (except for G_{zz}^R, which expression is valid at $\rho = 0$)

$$
\begin{aligned}
G_{xx}^{R}\left(x,y,z+z'\right) &= g_{\rho}^{\mathrm{EM}}\left(\rho,z+z'\right)\cos^{2}\phi - g_{\phi}^{\mathrm{EM}}\left(\rho,z+z'\right)\sin^{2}\phi \\
G_{yy}^{R}\left(x,y,z+z'\right) &= g_{\rho}^{\mathrm{EM}}\left(\rho,z+z'\right)\sin^{2}\phi - g_{\phi}^{\mathrm{EM}}\left(\rho,z+z'\right)\cos^{2}\phi \\
G_{zz}^{R}\left(x,y,z+z'\right) &= g_{z}^{\mathrm{TM}}\left(\rho,z+z'\right) \\
G_{xy}^{R}\left(x,y,z+z'\right) &= G_{yx}^{R}\left(x,y,z+z'\right) = \left[g_{\rho}^{\mathrm{EM}}\left(\rho,z+z'\right) + g_{\phi}^{\mathrm{EM}}\left(\rho,z+z'\right)\right]\sin\phi\cos\phi \\
G_{xz}^{R}\left(x,y,z+z'\right) &= -G_{zx}^{R}\left(x,y,z+z'\right) = g_{\rho}^{\mathrm{TM}}\left(\rho,z+z'\right)\cos\phi \\
G_{yz}^{R}\left(x,y,z+z'\right) &= -G_{zy}^{R}\left(x,y,z+z'\right) = g_{\rho}^{\mathrm{TM}}\left(\rho,z+z'\right)\sin\phi
\end{aligned}
\tag{3.145}
$$

And the special case for $\rho = 0$, all the off diagonal elements are zero,

$$
\begin{aligned}
G_{xx}^{R}\left(x=0,y=0,z+z'\right) &= G_{yy}^{R}\left(x=0,y=0,z+z'\right) = g_{\rho}^{\mathrm{EM}}\left(\rho=0,z+z'\right) \\
G_{xy}^{R}\left(x=0,y=0,z+z'\right) &= G_{yx}^{R}\left(x=0,y=0,z+z'\right) = 0 \\
G_{xz}^{R}\left(x=0,y=0,z+z'\right) &= G_{zx}^{R}\left(x=0,y=0,z+z'\right) = 0 \\
G_{yz}^{R}\left(x=0,y=0,z+z'\right) &= G_{zy}^{R}\left(x=0,y=0,z+z'\right) = 0
\end{aligned}
\tag{3.146}
$$

(d) Fast interpolation of Green's function

From the previous discussion, we notice that the dyadic Green's function $\bar{\bar{G}}_R(\bar{r},\bar{r}')$, satisfies the translation invariance relationship

$$
\bar{\bar{G}}_{R}\left(\bar{r},\bar{r}'\right) = \bar{\bar{G}}_{R}\left(x-x',y-y',z+z'\right) \tag{3.147}
$$

This not only reduces the independent arguments from 6 to 3, but also is the key to apply FFT based fast algorithm in solving the linear matrix equations.

And from (3.145), we can separate out 4 kernel integrals of g_{ρ}^{TM}, g_{z}^{TM}, g_{ρ}^{EM}, and g_{ϕ}^{EM}, which only involves two independent arguments of ρ and $z_s = z + z'$. Thus the dimensionality in computing the Green's function is greatly reduced.

The 4 kernel function are slowly converging and time consuming Sommerfeld integrals. However, we can precompute them and prepare four 2D look-up tables (LUTs) offline, and then use them to do fast interpolations of the Green's function.

Considering the asymptotic behavior of $\bar{\bar{G}}_R(\bar{r},\bar{r}') \propto \frac{\exp\left(ik\sqrt{\rho^2+z_s^2}\right)}{\sqrt{\rho^2+z_s^2}}$, we actually remove this oscillating and decaying factor in the interpolation. We apply a multiplicative factor of $\sqrt{\rho^2+z_s^2}\exp\left(-ik\sqrt{\rho^2+z_s^2}\right)$ in preparing the LUTs, and then divide the results by this factor after interpolation [133]. We have used linear interpolation with sampling density of more than 20 points in a wavelength.

3.3.3 The incident field

We consider a plane-wave impinging upon a truncated snow volume in the horizontal domain. The truncation generates spreading coherent scattering waves that depends on the truncation shape and the effective permittivity of the medium. This could be removed by separation of the results into coherent and incoherent components using statistical average in the Monte Carlo simulation.

We assume the reflective boundary is at $z = 0$. In general, let the incoming wave be polarized at direction $\hat{q}_i$, and propagating in the direction $\hat{K}_i$. Then

$$\bar{E}_{\text{inc}}(\bar{r}) = \bar{E}_{\text{inc}}^{\text{direct}}(\bar{r}) + \bar{E}_{\text{inc}}^{\text{reflected}}(\bar{r}) \tag{3.148}$$

$$\bar{E}_{\text{inc}}^{\text{direct}}(\bar{r}) = \exp\left(i\bar{K}_i \cdot \bar{r}\right)\left[\hat{e}(-k_{iz})\hat{e}(-k_{iz}) + \hat{h}(-k_{iz})\hat{h}(-k_{iz})\right]\cdot \hat{q}_i \tag{3.149}$$

$$\bar{E}_{\text{inc}}^{\text{reflected}}(\bar{r}) = \exp\left(i\bar{k}_i \cdot \bar{r}\right)\left[R^{\text{TE}}\hat{e}(k_{iz})\hat{e}(-k_{iz}) + R^{\text{TM}}\hat{h}(k_{iz})\hat{h}(-k_{iz})\right]\cdot \hat{q}_i \tag{3.150}$$

where

$$\hat{q}_i = \alpha\hat{e}(-k_{iz}) + \beta\hat{h}(-k_{iz}) \tag{3.151}$$

$$\bar{k}_i = k_{ix}\hat{x} + k_{iy}\hat{y} + k_{iz}\hat{z} \tag{3.152}$$

$$\bar{K}_i = k_{ix}\hat{x} + k_{iy}\hat{y} - k_{iz}\hat{z} \tag{3.153}$$

For TE polarization (horizontal), $\alpha = 1, \beta = 0$,

$$\bar{E}_{\text{inc}}^{\text{TE}}(\bar{r}) = E_0\left[\hat{e}(-k_{iz})\exp(i\bar{K}_i\cdot\bar{r}) + R^{\text{TE}}\hat{e}(k_{iz})\exp(i\bar{k}_i\cdot\bar{r})\right] \tag{3.154}$$

For TM polarization (vertical), $\alpha = 0, \beta = 1$,

$$\bar{E}_{\text{inc}}^{\text{TM}}(\bar{r}) = E_0\left[\hat{h}(-k_{iz})\exp(i\bar{K}_i\cdot\bar{r}) + R^{\text{TM}}\hat{h}(k_{iz})\exp(i\bar{k}_i\cdot\bar{r})\right] \tag{3.155}$$

Let $\phi_i = 0$ without loss of generality, and assume $\pi - \theta_i$ be the angle of propagation of $\hat{K}_i$, then $k_{ix} = k\sin\theta_i$, $k_{iy} = 0$, $k_{iz} = k\cos\theta_i$. By working out the expression of $\hat{e}$, $\hat{h}$, $\hat{k}$ and $\hat{K}$ directly, we have

$$\bar{E}_{\text{inc}}^{\text{TE}}(\bar{r}) = -\hat{y}E_0\exp(ik\sin\theta_i x)\left[\exp(-ik\cos\theta_i z) + R^{\text{TE}}\exp(ik\cos\theta_i z)\right] \tag{3.156}$$

$$\begin{aligned}\bar{E}_{\text{inc}}^{\text{TM}}(\bar{r}) = &-\hat{x}\cos\theta_i E_0\exp(ik\sin\theta_i x)\left[-\exp(-ik\cos\theta_i z) + R^{\text{TM}}\exp(ik\cos\theta_i z)\right]\\ &+\hat{x}\sin\theta_i E_0\exp(ik\sin\theta_i x)\left[\exp(-ik\cos\theta_i z) + R^{\text{TM}}\exp(ik\cos\theta_i z)\right]\end{aligned} \tag{3.157}$$

3.3.4 The scattering field and scattering coefficients

The scattering can be obtained from (3.84), represented as follows,

$$\begin{aligned}\bar{E}^s(\bar{r}) &= k^2\int_V d\bar{r}'\,\bar{\bar{G}}(\bar{r},\bar{r}')\left[\left(\varepsilon_r(\bar{r}')-1\right)\right]\bar{E}(\bar{r}')\\ &= \frac{k^2}{\varepsilon}\sum_j\left[\bar{\bar{G}}_0(\bar{r},\bar{r}_j) + \bar{\bar{G}}_R(\bar{r},\bar{r}_j)\right]\cdot\bar{p}(\bar{r}_j)\end{aligned} \tag{3.158}$$

We then apply the far field approximation to $\bar{\bar{G}}_0$ and $\bar{\bar{G}}_R$.

From (3.97), it is ready to show that in far field,

$$\bar{\bar{G}}_0(\bar{r},\bar{r}_j) \sim \frac{\exp(ikr)}{4\pi r}\exp(-i\bar{k}_s\cdot\bar{r}')\left(\hat{e}(k_{zs})\hat{e}(k_{zs}) + \hat{h}(k_{zs})\hat{h}(k_{zs})\right) \tag{3.159}$$

From (3.105), applying stationary phase method assuming $\bar{r}$ in far field leads to

$$\bar{\bar{G}}_R\left(\bar{r},\bar{r}_j\right) \sim \frac{\exp(ikr)}{4\pi r}\exp\left(-i\bar{K}_s\cdot\bar{r}'\right)\left(R^{\mathrm{TE}}\hat{e}\left(k_{zs}\right)\hat{e}\left(-k_{zs}\right)+R^{\mathrm{TM}}\hat{h}\left(k_{zs}\right)\hat{h}\left(-k_{zs}\right)\right) \quad (3.160)$$

Putting together, we get the scattering far field to be

$$\begin{aligned}\bar{E}^s\left(\bar{r}\right) = &\frac{k^2}{\varepsilon}\frac{\exp(ikr)}{4\pi r}\sum_j \exp\left(-i\bar{k}_s\cdot\bar{r}_j\right)\left(\hat{e}\left(k_{zs}\right)\hat{e}\left(k_{zs}\right)+\hat{h}\left(k_{zs}\right)\hat{h}\left(k_{zs}\right)\right)\cdot\bar{p}\left(\bar{r}_j\right)\\ &+\frac{k^2}{\varepsilon}\frac{\exp(ikr)}{4\pi r}\sum_j \exp\left(-i\bar{K}_s\cdot\bar{r}_j\right)\left(R^{\mathrm{TE}}\hat{e}\left(k_{zs}\right)\hat{e}\left(-k_{zs}\right)+R^{\mathrm{TM}}\hat{h}\left(k_{zs}\right)\hat{h}\left(-k_{zs}\right)\right)\cdot\bar{p}\left(\bar{r}_j\right)\end{aligned} \quad (3.161)$$

The scattering amplitude matrix $\bar{\bar{F}}$ is defined such that

$$\bar{E}^s = \begin{bmatrix}E_v^s\\ E_h^s\end{bmatrix} = \frac{\exp(ikr)}{r}\begin{bmatrix}f_{vv} & f_{vh}\\ f_{hv} & f_{hh}\end{bmatrix}\cdot\begin{bmatrix}E_v^i\\ E_h^i\end{bmatrix} \quad (3.162)$$

It then follows that,

$$f_v = \frac{k^2}{4\pi\varepsilon}\left[\hat{h}\left(k_{zs}\right)\cdot\sum_j \exp\left(-i\bar{k}_s\cdot\bar{r}_j\right)\bar{p}\left(\bar{r}_j\right)+R^{\mathrm{TM}}\hat{h}\left(-k_{zs}\right)\cdot\sum_j \exp\left(-i\bar{K}_s\cdot\bar{r}_j\right)\bar{p}\left(\bar{r}_j\right)\right] \quad (3.163)$$

$$f_h = \frac{k^2}{4\pi\varepsilon}\left[\hat{e}\left(k_{zs}\right)\cdot\sum_j \exp\left(-i\bar{k}_s\cdot\bar{r}_j\right)\bar{p}\left(\bar{r}_j\right)+R^{\mathrm{TE}}\hat{e}\left(-k_{zs}\right)\cdot\sum_j \exp\left(-i\bar{K}_s\cdot\bar{r}_j\right)\bar{p}\left(\bar{r}_j\right)\right] \quad (3.164)$$

And

$$\begin{aligned} f_{vv} &= f_v, \text{ with } \hat{q}_i = \hat{h}\\ f_{hv} &= f_h, \text{ with } \hat{q}_i = \hat{h}\\ f_{vh} &= f_v, \text{ with } \hat{q}_i = \hat{e}\\ f_{hh} &= f_h, \text{ with } \hat{q}_i = \hat{e}\end{aligned} \quad (3.165)$$

with $E_0 = 1$.

The bistatic scattering coefficient is then

$$\gamma_{\beta\alpha}\left(\theta_s,\phi_s;\theta_{\text{inc}},\phi_{\text{inc}}\right)=\lim_{\vec{r}\to\infty}\frac{4\pi r^2\left|E_\beta^s\right|^2}{\left|E_\alpha^{\text{inc}}\right|^2 A\cos\theta_{\text{inc}}}$$
$$=\frac{4\pi}{A\cos\theta_{\text{inc}}}\left|f_{\beta\alpha}\left(\theta_s,\phi_s;\pi-\theta_{\text{inc}},\phi_{\text{inc}}\right)\right|^2 \tag{3.166}$$

And the backscattering coefficients,

$$\sigma_{\beta\alpha}\left(\theta_{\text{inc}},\phi_{\text{inc}}\right)=\cos\theta_{\text{inc}}\gamma_{\beta\alpha}\left(\theta_{\text{inc}},\pi+\phi_{\text{inc}};\theta_{\text{inc}},\phi_{\text{inc}}\right)$$
$$=\frac{4\pi}{A}\left|f_{\beta\alpha}\left(\theta_{\text{inc}},\pi+\phi_{\text{inc}};\pi-\theta_{\text{inc}},\phi_{\text{inc}}\right)\right|^2 \tag{3.167}$$

The bistatic scattering coefficient is related to the reflectivity by

$$r_\alpha\left(\theta_{\text{inc}},\phi_{\text{inc}}\right)=\int_0^{2\pi}d\phi_s\int_0^{\pi/2}d\theta_s\sin\theta_s\left[\sum_{\beta=v,h}\gamma_{\beta\alpha}\left(\theta_s,\phi_s;\theta_{\text{inc}},\phi_{\text{inc}}\right)\right] \tag{3.168}$$

Equation (3.166) is for total bistatic scattering coefficients from a single realization of the random media. Using Monte Carlo simulation, we can separate the coherent and incoherent components,

$$\gamma_{\beta\alpha}^{\text{coh}}=\frac{4\pi}{A\cos\theta_{\text{inc}}}\left|\left\langle f_{\beta\alpha}\right\rangle\right|^2 \tag{3.169}$$

$$\gamma_{\beta\alpha}^{\text{tot}}=\frac{4\pi}{A\cos\theta_{\text{inc}}}\left\langle\left|f_{\beta\alpha}\right|^2\right\rangle \tag{3.170}$$

$$\gamma_{\beta\alpha}^{\text{incoh}}=\gamma_{\beta\alpha}^{\text{tot}}-\gamma_{\beta\alpha}^{\text{coh}} \tag{3.171}$$

3.3.5 The iterative GMRES linear system solver

By now, we are well set in a position to solve a linear system of (3.94), putting in a more general form

$$\bar{\bar{A}}\bar{x}=\bar{b}$$

The direct solution using Gaussian elimination takes $\Theta(N^3)$ arithmetic operations, which is unbearable for extremely large N. Thus we alternatively seek an iterative approach. The generalized minimum residuals (GMRES) method, as suggested by Saad and Schultz in 1986 [134], is an iterative method with fast convergence rate seeking approximate solution in the Krylov subspace. The n-th order Krylov subspace K_n, as given by

$$K_n = span\{b, Ab, A^2b, A^3b, \dots, A^{n-1}b\}$$

involves sequentially the multiplication of the matrix $\bar{\bar{A}}$ to a vector (the last column of K_{n-1}). If the matrix-vector product could be implemented fast enough, such as $\Theta(NlogN)$, the overall complexity to solve the linear system would be $n_{iter}\Theta(NlogN)$, with $n_{iter} \ll N$, and with a little overhead in GMRES.

At step n, we approximate the exact solution $x^* = A^{-1}b$ by a vector $x_n \in K_n$ such that the residual $\|r_n\| = \|Ax_n - b\|$ is minimized.

$$\min_{x_n}\|r_n\| = \min_{x_n}\|Ax_n - b\|$$

The minimization is assisted by finding the orthonormal basis for the Krylov subspace K_n, denoted by Q_n: $\{q_1, q_2, \dots, q_n\}$, which can be obtained following a general Gram-Schmidt orthonormal process. We then express the approximate solution x_n using this orthonormal basis, $x_n = Q_n y$, then

$$\|r_n\| = \|AQ_n y - b\|$$

The norm $\|r_n\|$ is further simplified by finding $\widetilde{H}_n$, an upper Hessenberg matrix of dimension $(n+1) \times n$ (zero entries below the first sub-diagonal), that satisfies the partial similarity transformation relation,

$$AQ_n = Q_{n+1}\widetilde{H}_n$$

where in practice Q_n and $\widetilde{H}_n$ are updated together in a process called Arnoldi iteration. Q_n and Q_{n+1} are unitary. Then

$$\|r_n\| = \left\|Q_{n+1}\widetilde{H}_n y - b\right\| = \left\|\widetilde{H}_n y - Q_{n+1}^{\dagger} b\right\| = \left\|\widetilde{H}_n y - \|b\|e_1\right\|$$

where $e_1 = [1,0,\dots,0]^T \in R^{(n+1)\times 1}$, $\widetilde{H}_n \in C^{(n+1)\times n}$, and $y \in C^{n\times 1}$.

We arrive at the Hessenberg least squares problem of a small dimension $\left\|\widetilde{H}_n y - \|b\|e_1\right\| \to \min$, which can be solved easily, for example, by QR factorization, or by Givens rotation.

The approach of the Givens rotation is illustrated as follows. With Givens rotation, we find another unitary matrix $Q \in C^{(n+1)\times(n+1)}$, that when multiplied towards $\widetilde{H}_n$, we get an upper triangular matrix $R \in C^{(n+1)\times n}$.

$$Q\widetilde{H}_n = R$$

Thus

$$\|r_n\| = \left\|Q\left(\widetilde{H}_n y - \|b\|e_1\right)\right\| = \|Ry - \|b\|Qe_1\| = \|Ry - g\|$$

where $g = \|b\|Qe_1$. Considering the fact that R is upper triangular,

$$\|r_n\|_{\min} = \|Ry - g\|_{\min} = g_{n+1}, \text{when } [R]_{n\times n}\, y = [g]_{n\times 1}$$

The resulting linear system, $[R]_{n\times n}\, y = [g]_{n\times 1}$, is of dimension $n \times n$, where n is the current iteration number. It can easily solved by backward substitution. When y is solved and $\|r_n\|_{\min}/\|b\|$ is small enough, one can terminate the iteration with approximate solution $x_n = Q_n y$.

The convergence rate of GMRES is optimal, however, the storage requirement increases with the iteration number. One need to store the orthonormal basis $Q_n: \{q_1, q_2, \dots, q_n\}$. Thus a restarted GMRES is devised to confine the iteration to a maximum number $k_{\max}$, and then restart the iteration using a better initial guess of x from the previous run. The maximum memory

requirement for the restarted GMRES is $\Theta(k_{\max}N)$, at the expense of a slightly slower convergence rate.

3.3.6 Acceleration of matrix-vector multiplication by fast Fourier transforms

As indicated before, the most time consuming part in an iterative linear system solver is the matrix-vector product calculation. A direct dense matrix-vector multiplication takes $\Theta(N^2)$ algebraic operations, and the storage of the dense matrix takes $\Theta(N^2)$ memory. Both become unbearable as N becomes large. Thus we take advantage of the symmetry in the dyadic Green's functions, which is the kernel of the matrix elements, that

$$\begin{aligned}\overline{\overline{G}}_0\left(\bar{r}_i,\bar{r}_j\right)&=\overline{\overline{G}}_0\left(x_n-x_{n'},y_m-y_{m'},z_l-z_{l'}\right)\\ \overline{\overline{G}}_R\left(\bar{r}_i,\bar{r}_j\right)&=\overline{\overline{G}}_R\left(x_n-x_{n'},y_m-y_{m'},z_l+z_{l'}\right)\end{aligned} \tag{3.172}$$

The symmetry suggests that if we choose the sampling points $\bar{r}_i,\bar{r}_j$ uniformly, i.e., let $x_n=-\frac{L_x}{2}+(n+\frac{1}{2})d$, $y_m=-\frac{L_y}{2}+\left(m+\frac{1}{2}\right)d$, and $z_l=\left(l+\frac{1}{2}\right)d$, where $0\le n\le N_x-1$, $0\le m\le N_y-1$, $0\le l\le N_z-1$, and $N=N_xN_yN_z$, then we only needs to evaluate $\bar{\bar{G}}_0\left(\bar{r}_i,\bar{r}_j\right)$ and $\bar{\bar{G}}_R\left(\bar{r}_i,\bar{r}_j\right)$ on a much smaller set of grid points,

$$\begin{aligned}\overline{\overline{G}}_0\left(\bar{r}_i,\bar{r}_j\right)&=\overline{\overline{G}}_0\left(\left(n-n'\right)d,\left(m-m'\right)d,\left(l-l'\right)d\right)\triangleq\overline{\overline{G}}_0\left(n-n',m-m',l-l'\right)\\ \overline{\overline{G}}_R\left(\bar{r}_i,\bar{r}_j\right)&=\overline{\overline{G}}_R\left(\left(n-n'\right)d,\left(m-m'\right)d,\left(1+l+l'\right)d\right)\triangleq\overline{\overline{G}}_R\left(n-n',m-m',l+l'\right)\end{aligned} \tag{3.173}$$

where $-(N_x-1)\le n-n'\le N_x-1$, $-\left(N_y-1\right)\le m-m'\le N_y-1$, $-(N_z-1)\le l-l'\le N_z-1$, and $0\le l+l'\le 2(N_z-1)$. Note that we only need to sample over $(2N_x-1)\times\left(2N_y-1\right)\times(2N_z-1)$ points instead of $\left(N_xN_yN_z\right)^2$ points without this translational symmetry. The savings are huge in that only a very small fraction of $(2N_x-1)\times\left(2N_y-1\right)\times(2N_z-1)/\left(N_xN_yN_z\right)^2\approx 8/N$ of the original memory is needed.

The resulting matrix on uniform grids (canonical grids) is Toeplitz in the sense that

$$\begin{aligned}\overline{\overline{G}}_0\left(\bar{r}_i+\left(\hat{x}s_x+\hat{y}s_y+\hat{z}s_z\right),\bar{r}_j+\left(\hat{x}s_x+\hat{y}s_y+\hat{z}s_z\right)\right)&=\overline{\overline{G}}_0\left(\bar{r}_i,\bar{r}_j\right)\\ \overline{\overline{G}}_R\left(\bar{r}_i+\left(\hat{x}s_x+\hat{y}s_y+\hat{z}s_z\right),\bar{r}_j+\left(\hat{x}s_x+\hat{y}s_y-\hat{z}s_z\right)\right)&=\overline{\overline{G}}_R\left(\bar{r}_i,\bar{r}_j\right)\end{aligned} \tag{3.174}$$

thus different rows are related to each other by a proper rotation.

The techniques we developed in section 3.1.5 of using fast Fourier transform (FFT) to accelerate the Toeplitz matrix-vector multiplication can be readily generalized to 3D case to handle $\sum_{j\neq i}\overline{\overline{G}}_0\left(\bar{r}_i,\bar{r}_j\right)\cdot\bar{p}_j$ and $\sum_j\overline{\overline{G}}_R\left(\bar{r}_i,\bar{r}_j\right)\cdot\bar{p}_j$ as appeared in (3.94), as the key step in solving the DDA matrix equations using an iterative solver, such as GMRES.

To illustrate, we first convert the vector version of the matrix-vector multiplication into 9 scalar counterparts, formally,

$$\begin{aligned}\left[\overline{\overline{G}}\cdot\bar{p}\right]_x&=G_{xx}p_x+G_{xy}p_y+G_{xz}p_z\\ \left[\overline{\overline{G}}\cdot\bar{p}\right]_y&=G_{yx}p_x+G_{yy}p_y+G_{yz}p_z\\ \left[\overline{\overline{G}}\cdot\bar{p}\right]_z&=G_{zx}p_x+G_{zy}p_y+G_{zz}p_z\end{aligned} \tag{3.175}$$

Then we are left to deal with each of the scalar versions of the matrix-vector multiplications of the following two different forms,

$$q(n,m,l)=\sum_{n'=0}^{N_x-1}\sum_{m'=0}^{N_y-1}\sum_{l'=0}^{N_z-1}g\left(n-n',m-m',l-l'\right)p\left(n',m',l'\right) \tag{3.176}$$

$$q_R(n,m,l)=\sum_{n'=0}^{N_x-1}\sum_{m'=0}^{N_y-1}\sum_{l'=0}^{N_z-1}g_R\left(n-n',m-m',l+l'\right)p\left(n',m',l'\right) \tag{3.177}$$

These can be readily accelerated using three dimensional FFTs and Inverse FFTs (IFFT) [34, 119, 135], such that

$$\tilde{q}(n,m,l)=\mathrm{FT}^{-1}_{2N_x\times 2N_y\times 2N_z}\left\{G(i,j,k)\cdot P(i,j,k)\right\} \tag{3.178}$$

$$\tilde{q}_R(n,m,l) = \mathrm{FT}^{-1}_{2N_x \times 2N_y \times 2N_z}\left\{G_R(i,j,k) \cdot P(i,j,-k)\right\} \tag{3.179}$$

where · denotes element-wise multiplication of the two matrices,

$$P(i,j,k) = \mathrm{FT}_{2N_x \times 2N_y \times 2N_z}\left\{\tilde{p}(n,m,l)\right\} \tag{3.180}$$

$$G(i,j,k) = \mathrm{FT}_{2N_x \times 2N_y \times 2N_z}\left\{\tilde{g}(n,m,l)\right\} \tag{3.181}$$

$$G_R(i,j,k) = \mathrm{FT}_{2N_x \times 2N_y \times 2N_z}\left\{\tilde{g}_R(n,m,l)\right\} \tag{3.182}$$

$$P(i,j,-k) = P(i,j,2N_z - k), 1 \le \mathrm{k} \le 2N_z - 1 \tag{3.183}$$

where $\tilde{p}$, $\tilde{g}$ and $\tilde{g}_R$ are all of dimensions $2N_x \times 2N_y \times 2N_z$. $\tilde{p}$ is a zero padded version of p (of dimension $N_x \times N_y \times N_z$). And q and q_R are truncated version of $\tilde{q}$ and $\tilde{q}_R$ taking the data in the first quadrant.

Using the short hand notation

$$\begin{aligned} p(n,m,l) &= p(x_0 + n\Delta x, y_0 + m\Delta y, z_0 + n\Delta z) \\ g(n,m,l) &= g(n\Delta x, m\Delta y, n\Delta z) \\ g_R(n,m,l) &= g_R(n\Delta x, m\Delta y, 2z_0 + n\Delta z) \end{aligned}$$

Then

$$\tilde{p}(n,m,l) = \begin{cases} p(n,m,l), & 0 \le n \le N_x - 1, 0 \le m \le N_y - 1, 0 \le n \le N_z - 1 \\ 0, & \text{otherwise} \end{cases} \tag{3.184}$$

$$\tilde{g}(n,m,l) = \begin{cases} 0, & n = N_x \text{ or } m = N_y \text{ or } l = N_z \\ g(n',m',l'), & \text{otherwise} \end{cases} \tag{3.185}$$

where

$$n' = \begin{cases} n, & 0 \le n \le N_x - 1 \\ n - 2N_x, & N_x + 1 \le n \le 2N_x - 1 \end{cases}$$

$$m' = \begin{cases} m, & 0 \le m \le N_y - 1 \\ m - 2N_y, & N_y + 1 \le m \le 2N_y - 1 \end{cases}$$

$$l' = \begin{cases} l, & 0 \le l \le N_z - 1 \\ l - 2N_z, & N_z + 1 \le l \le 2N_z - 1 \end{cases}$$

and

$$\tilde{g}_R(n,m,l) = \begin{cases} 0, \; n = N_x \text{ or } m = N_y \text{ or } l = 2N_z - 1 \\ g_R(n',m',l), \text{ otherwise} \end{cases} \tag{3.186}$$

where n' and m' are the same as in (3.185).

And the final results,

$$q(n,m,l) = \tilde{q}(n,m,l), \quad 0 \le n \le N_x - 1, 0 \le m \le N_y - 1, 0 \le l \le N_z - 1 \tag{3.187}$$

$$q_R(n,m,l) = \tilde{q}_R(n,m,l), \quad 0 \le n \le N_x - 1, 0 \le m \le N_y - 1, 0 \le l \le N_z - 1 \tag{3.188}$$

The FFT technique significantly improves the CPU requirements from $O(N^2)$ to $O(N \log N)$, and the memory requirements from $O(N^2)$ to $O(N)$, where $N = N_x N_y N_z$. One can further make use of the symmetry and parity of the components of the dyadic Green's functions to reduce the computational complexity and memory requirements.

3.3.7 Parallel computing for large scale simulation

The computational demand of the full wave approach is huge. The ice grains in the snowpack are on the order of 0.5mm, thus in order to describe a shallow snowpack of 10cm thickness over a small area of 50cm x 50cm, which is equivalent to the finest achievable resolution of an airborne synthetic aperture radar, one need ~200 million uniform cubic cells. A rough estimation of the memory consumption is about 640GB. The memory requirement grows in order $\Theta(N)$, while the CPU in order $n_{\text{iter}}\Theta(N \lg N)$, where N is the number of cubes and n_{iter} is the total number of iterations in the linear system solver. Such large memory and CPU requirements makes

parallel computing necessary, and distributed memory parallel computing with message passing interface (MPI) is the solution to get around the memory and computing bottleneck.

In this section, I describe those elements and designs that are crucial to the distributed memory parallel computing through MPI, including the memory/ CPU requirement estimation, the data layout and parallel strategy, and the parallelized fast Fourier transforms (FFT), etc.

(a) The problem size and CPU/ memory estimation

The parallelization is driven by the large memory consumption. Thus we need an accurate estimation of the memory requirement.

Suppose we have a $N = N_x \times N_y \times N_z$ discretized grid. We need memory to store the 18 three dimensional Fourier transforms ($G_{xx}, G_{xy}, G_{xz}, G_{yy}, G_{yz}, G_{zz}$ and $G^R_{xx}, G^R_{xy}, G^R_{xz}, G^R_{yy}, G^R_{yz}, G^R_{zz}$, and P_x, P_y, P_z, and three intermedia arrays of $\left[\bar{\bar{G}} \cdot \bar{P}\right]_x$, $\left[\bar{\bar{G}} \cdot \bar{P}\right]_y$, and $\left[\bar{\bar{G}} \cdot \bar{P}\right]_z$ to facilitate the vector version of the matrix-vector multiplication), each of size $2N_x \times 2N_y \times 2N_z$. We only consider the memory to hold the input/ output data for the Fourier transform, ignoring possible data manipulation overhead. This give rise to $18 \times 8N = 144N$ complex numbers. Of these 18 Fourier transforms, 12 of them related to $\bar{\bar{G}}$ are done once upon initialization, while the other 6 Fourier transforms are to be computed at each iteration to perform the matrix-vector multiplication.

We also need memory to store complex unknowns p_x, p_y, and p_z, each with dimension $N_x \times N_y \times N_z$. We also need a complex array of $k_{\max} \times 3\left(N_x \times N_y \times N_z\right)$ in the GMRES solver with restart number $k_{\max}$ to store the orthonormal basis $Q_n: \{q_1, q_2, \ldots, q_n\}$ in the Krylov subspaces. This give rise to another $3(k_{\max} + 1)N$ complex numbers.

Thus the total memory requirement is $[144 + 3(k_{\max} + 1)]N$ complex numbers, or $16 \times (147 + 3k_{\max})N$ bytes using double precision. To make the numbers simple, let $k_{\max} = 18$, then we need $\sim 200N$ complex numbers and ~3200N bytes memory.

In Table III-1, we estimate the memory requirements with several problem dimensions. We also estimate the minimum number of processors required to deal with such problems assuming each processor has 4GB usable memory.

Table III-1. Theoretical memory and CPU scaling with problem size

Physical dimension (cm^3)	N (#cells) grid size: 0.5mm	Memory requirements	# processor	t_{CPU}	t_{wall}: $\frac{t_{CPU}}{\#proc}$
$0.5 \times 0.5 \times 0.5$	10^3	3.2MB	1		
$5 \times 5 \times 5$	10^6	3.2GB	1	1min	1min
$15 \times 15 \times 5$	9×10^6	28.8GB	8	10.43min	1.30min
$25 \times 25 \times 10$	50×10^6	160GB	40	1.069hrs	1.604min
$50 \times 50 \times 20$	400×10^6	1.28TB	320	9.558hrs	1.792min

Note that in Table III-1, the total CPU time for each case is roughly estimated by scaling the CPU for the reference case ($5 \times 5 \times 5 cm^3$ with $N = 10^6$) estimated from its runtime on a single processor assuming ideal parallelization efficiency. The scale is done using $\Theta(N \log N)$ of FFT. The wall time is obtained by dividing the CPU time by the number of processors. The table shows the great benefits out of the parallelization.

(b) The data layout and parallel strategy

In order to fill in the matrix elements, to carry out the GMRES iteration, and to perform the 3D FFT in parallel, one need to distribute data among different processors. A better data layout and parallel strategy helps to balance the CPU load and to minimize the computation cost.

One should note the conflict in determining the global data layout. Since the FFT operation is on a matrix dimension of $2N_x \times 2N_y \times 2N_z$, while the matrix elements initialization and the Arnoldi iteration (to find the orthonormal basis Q_n: $\{q_1, q_2, \dots, q_n\}$) in the GMRES procedure are

operated on a matrix dimension of $N_x \times N_y \times N_z$, corresponding to the first octant of the larger dataset. Thus an evenly distribution of both the larger arrays (of size $2N_x \times 2N_y \times 2N_z$) and the smaller arrays (of size $N_x \times N_y \times N_z$) across procedures will cause unpleasant and cumbersome data moving, as illustrated in Figure III.7. The $N_x \times N_y \times N_z$ arrays spread on N_p processors need to be redistributed to the first half $N_p/2$ processors. The communication cost is heavy.

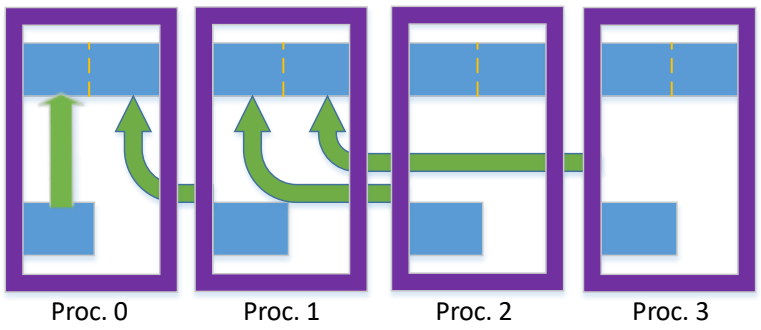

Figure III.7. Balanced data layout with communication cost (re-distribution)

We choose to sacrifice some CPU power to minimize communication. We distribute the $2N_x \times 2N_y \times 2N_z$ arrays evenly across all the N_p processors, but separate the $N_x \times N_y \times N_z$ arrays only on the first half $N_p/2$ processors, as illustrated in Figure III.8. In reality, it may not be exactly one half of the processors depending on the total number of processors, and how much data to put on each of them, but the idea is to keep the $N_x \times N_y \times N_z$ arrays attached to their owners according to how the $2N_x \times 2N_y \times 2N_z$ arrays are distributed. In this way, those operations on the $N_x \times N_y \times N_z$ arrays (initialization, and the Arnoldi iterations) are only performed by part of the processors, but one saves the effort to redistribute data across different processors after each iteration. Considering the most time consuming part is to perform the 3D Fourier transforms on

the $2N_x \times 2N_y \times 2N_z$ arrays and communication, while the CPU on initialization and Arnoldi iterations are marginal, this choice is good.

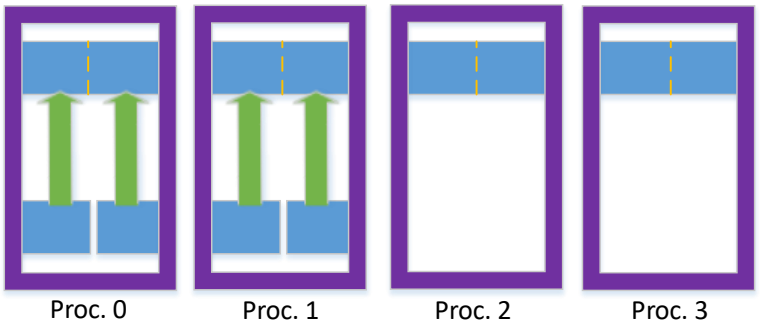

Figure III.8. Non-balanced data layout with no re-distribution.

Another significant communication saving strategy is to exploit the inherent structure of multi-dimensional FFT and IFFT. To illustrate the concepts, let us take 2D FFT for example. 2 dimensional FFT is computed by two groups of 1D FFTs. One first apply 1D FFT over each row (or column) of the 2D array and store the results in the same matrix format, and then apply another 1D FFT over each column (or row) of the intermediate array to get the final results. But with distributed memory parallel computing, each processor only owns a portion of the 2D arrays. It is natural to distribute the array along rows (or columns), such that each processor owns the whole data chunk of several rows (or columns) and could perform independent 1D FFTs on their own data share. But there must be a synchronization and transposition after the FFTs along the first dimension before the processors can work on the FFTs along the second dimensions. The transposition is a global data redistribution and is heavy in communication, but it is unavoidable in making the data local to the working processors. After the FFTs along the 2nd dimension are finished, the data is actually in a transposed order of the original layout. Another transposition is required to get data back to their original layout.

Noticing that our matrix-vector multiplication is being computed by a pair of forward FFT and inverse FFTs, we can actually take advantage of it to keep the transformed data transposed, which, after succeeding inverse transforms, naturally gets data back to the original layout. This strategy, as illustrated in Figure III.9, saves the communication cost significantly. In Figure III.9, the design is illustrated using 4 processors. The $2N_x \times 2N_y \times 2N_z$ arrays (originally in spatial domain) are evenly distributed among all the 4 processors along x direction; the $N_x \times N_y \times N_z$ arrays (also in spatial domain), are distributed among the first 2 processors along x direction. After the forward Fourier transforms, the $2N_x \times 2N_y \times 2N_z$ arrays (now in spectral domain) are evenly distributed among all the 4 processors along y directions. Notice that in our data structure for the 3D arrays, the x and y directions are the lowest two dimensions with fast changing index. The succeeding inverse Fourier transforms then put data back to the original layout. The algebraic operation in the spectral domain and the truncation and expanding in the spatial domain do not involve any data communication.

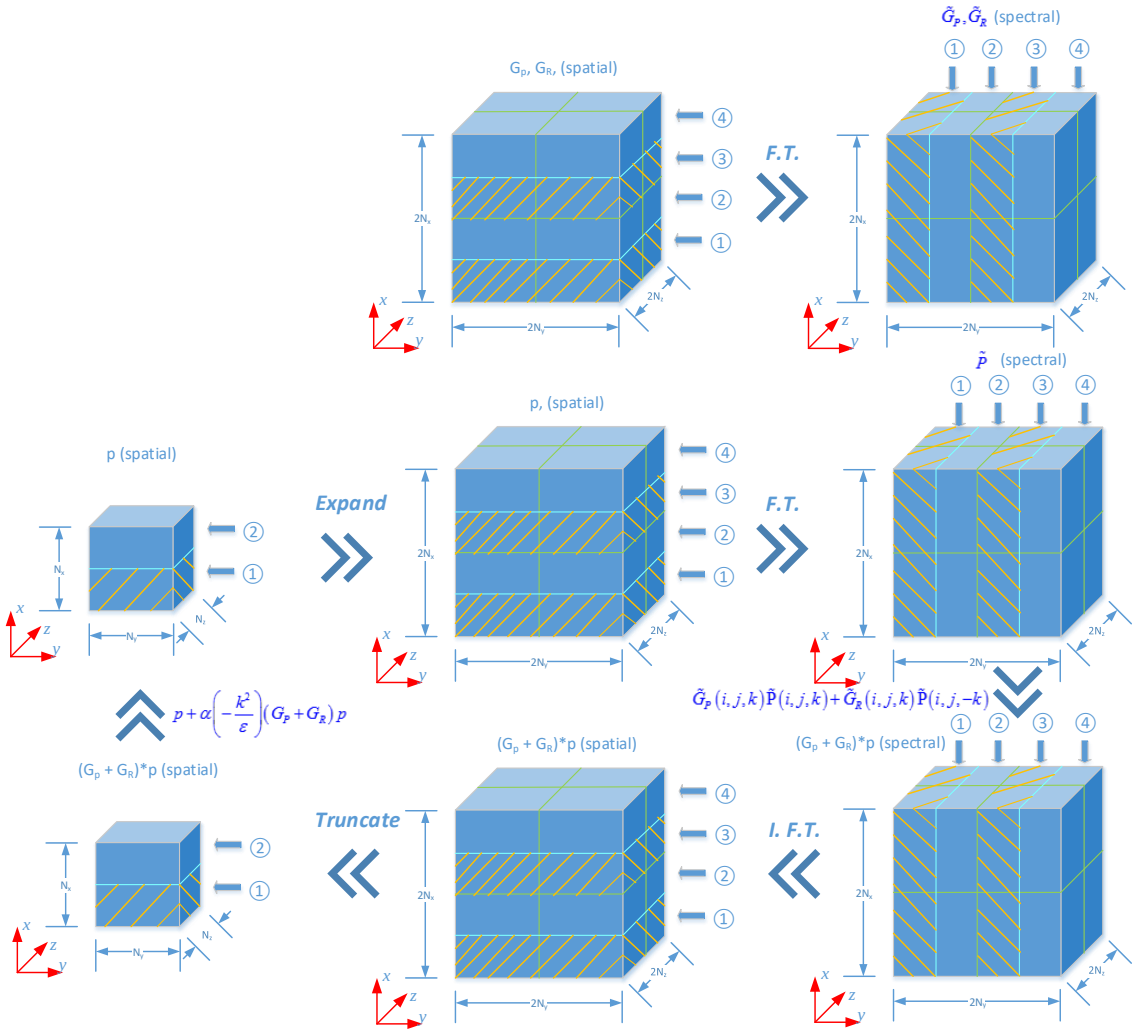

Figure III.9. The implemented data layout and parallel strategy. The small box on the left of the 2nd row denotes the $N_x \times N_y \times N_z$ arrays of p being distributed along $\hat{x}$ direction in the first two processors. The arrays are then being expanded into size of $2N_x \times 2N_y \times 2N_z$ by padding zeros and distributed along $\hat{x}$ direction in all of the four processors. Parallel fast Fourier transforms (FFT) are then applied to the $2N_x \times 2N_y \times 2N_z$ arrays of $\tilde{p}$, and the results $\tilde{P}$ are distributed along $\hat{y}$ direction in all of the four processors, being transposed to the original data layout. Meanwhile, as illustrated in the top row, the arrays of the Green's functions G, of size $2N_x \times 2N_y \times 2N_z$, as being distributed along $\hat{x}$ direction in the four processors, are also being transformed into spectral domain $\tilde{G}$ by parallel FFT, and distributed along $\hat{y}$, as transposed to the original layout. The element-wise multiplication of $\tilde{G}$ and $\tilde{P}$ in the spectral domain does not involve any communication as illustrated in the right column going downward. In the bottom row, parallel inverse FFTs are applied to the results of the product, restoring the data layout in the spectral domain. The results are then being truncated into size $N_x \times N_y \times N_z$ for the valid results, again distributed along $\hat{x}$ direction in the first half of the processors.

(c) The distributed memory parallel FFT

The open source library *FFTW* [136, 137] is used to perform the most time consuming discrete Fourier Transforms. FFTW adapts to the hardware structure to maximize its performance and supports "SIMD" instructions. The FFTW implementation also supports multi-threaded shared memory parallelization and distributed memory parallelization with message passing interface (MPI), of which the latter is adopted.

The general usage of the *FFTW* library with MPI is as follows:

1) Setup the data layout

This is done by calling the function `fftw_mpi_local_size_many_transposed`.

```
ptrdiff_t fftw_mpi_local_size_many_transposed(int rnk, const ptrdiff_t *n, ptrdiff_t howmany, ptrdiff_t block0, ptrdiff_t block1, MPI_Comm comm, ptrdiff_t *local_n0, ptrdiff_t *local_0_start, ptrdiff_t *local_n1, ptrdiff_t *local_1_start);
```

Given the processor id, the complete matrix dimensions (stored in array `n` with the highest dimension going first), the desired block size along the first two dimensions, and the `howmany`-tuples of continuous numbers involved in the Fourier transforms, this call tells the actual local block size (`local_n0` and `local_n1`) and the staring elements id (`local_0_start and local_1_start`) along the first two dimensions, and also returns the required number of elements to allocate on each processor. This call considers the fact that we want to set the input and output in transposed manner, and tries to balance as much the load distribution.

2) Allocate memory

This is done by calling the function `fftw_alloc_complex`, which allocates the memory to store `n` complex numbers. The argument `n` is the return value from the previous step,

and it includes the overhead storage to perform intermediate FFT operations. But the address for the local slice of the array starts at the beginning of the allocated memory.

```
fftw_complex *fftw_alloc_complex(size_t n);
```

3) Create *plan*s for FFT, execute *plans* to perform FFT, and destroy the *plans*.

A *plan* is an object that contains all the data the FFTW needs to compute the FFT. *Plan: To bother about the best method of accomplishing an accidental result* [Ambrose Bierce, The enlarged Devil's Dictionary] [136]. A *plan* tries to figure out the most efficient way to work out the Fourier transform with a specific data layout (dimension, length, etc.). Upon creation, it could be used (executed) multiple times to perform FFTs until the explicit destroy of the plan.

These are done by the following function calls, respectively.

```
fftw_plan fftw_mpi_plan_many_dft(int rank, const ptrdiff_t *n, ptrdiff_t howmany, ptrdiff_t block, ptrdiff_t tblock, fftw_complex *in, fftw_complex *out, MPI_Comm comm, int sign, usigned flags);

void fftw_execute(const fftw_plan plan);

void fftw_destroy_plan(fftw_plan plan);
```

Note that in the *plan* creation function `fftw_mpi_plan_many_dft`, one can use `sign` (`FFTW_FORWAR` or `FFTW_BACKWARD`) to specify the direction of FFT (forward or inverse), and use the `flags` (`FFTW_MPI_TRANSPOSED_IN` or `FFTW_MPI_TRANSPOSED_OUT`) to indicate the input and output data layout.

4) Initialization and cleanup

Call `fftw_mpi_init` before all the fftw calls (after `MPI_Init`) and `fftw_mpi_cleanup` at the end (before `MPI_Finalize`) to get rid of all memory and resources allocated internally by FFTW.

```
fftw_mpi_init(void);
fftw_mpi_cleanup(void);
```

(d) Other aspects for parallelization

Special care needs to be excised in the GMRES related linear algebra operations such as finding the norm of a vector and performing the dot product of two vectors as the data are distributed. Care should also be taken in the matrix initialization, and scattering field computation, as each processor only owns part of the data.

3.3.8 Simulation results

We consider plane wave incident upon a layer of snow of 5cm thickness. The results are computed at 17.2GHz with 40 degree incidence angle over a computational domain of 50cm x 50cm x 5cm. The bicontinuous media has $\langle\zeta\rangle = 5000m^{-1}$, $b = 1.0$, and $f_v = 0.3$. Such bicontinuous media has an exponential correlation length of 0.36mm. The ground underneath the snowpack has permittivity of $(1 + i0.5)\varepsilon_0$. The ice permittivity is taken as $(3.2 + 0.001i)\varepsilon_0$. The snow layer has an effective optical thickness $\tau = 0.16$.

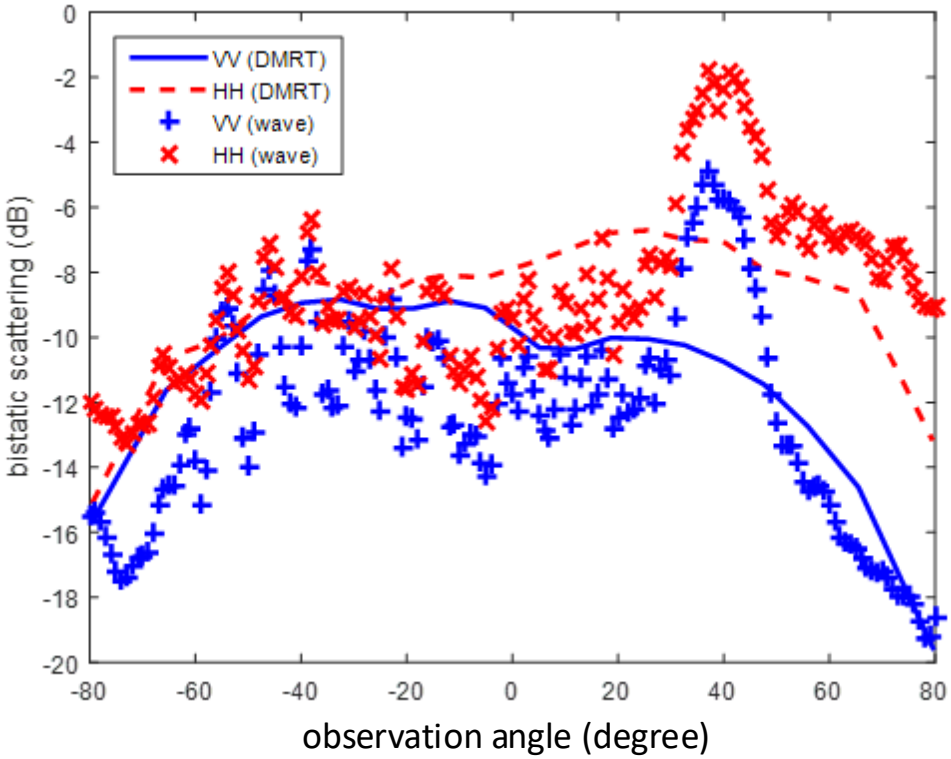

Figure III.10. Comparison of the incoherent bistatic scattering pattern from 3D full wave simulation with the results of DMRT.

The results of incoherent bistatic scattering coefficients are compared with the results of the partially coherent approach of DMRT in Figure III.10. The full wave simulation results are averaged over 100 Monte Carlo simulations. Note that the overall trend of the incoherent bistatic scattering coefficients agree with the results of DMRT. And there is a notable peak on the order of ~2dB near the backscattering direction, demonstrating the backscattering enhancement effects.

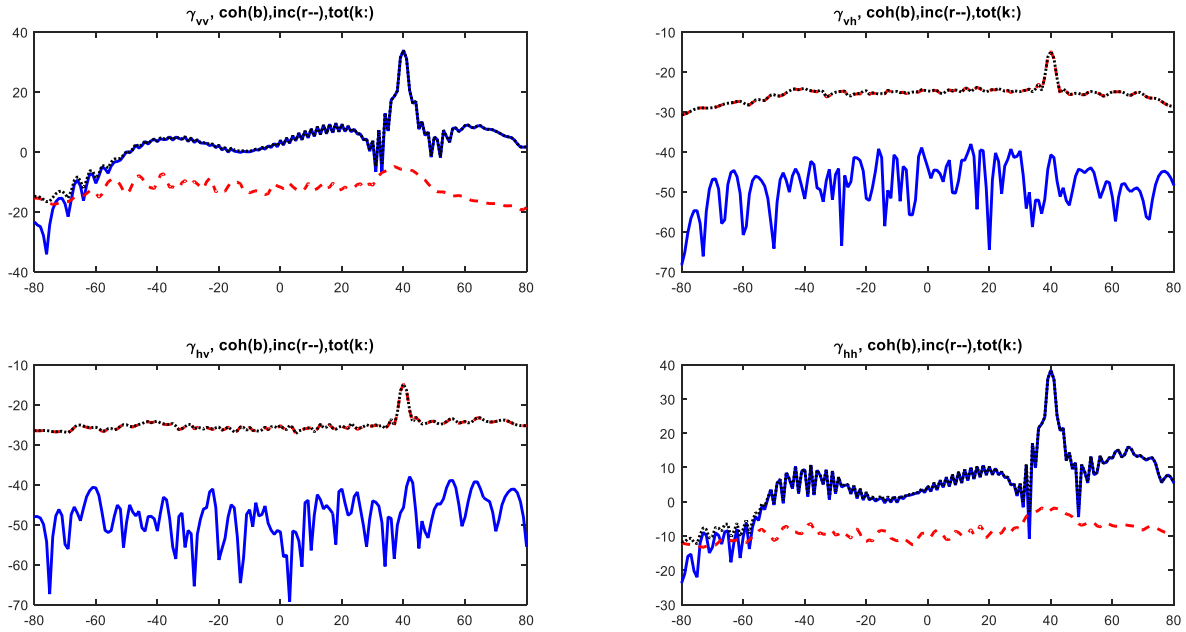

Figure III.11. Comparing of coherent and incoherent bistatic scattering coefficients of 3D full wave simulation of a finite snowpack. (a) top-left, γ_{vv} (b) top-right, γ_{vh} (c) bottom-left, γ_{hv} (d) bottom-right, γ_{hh}.

The bistatic scattering coefficients are separated into the coherent and incoherent components in Figure III.11. The coherent wave is again most strong in the specular direction for co-polarization. However, different from the 2D case, the coherent wave spreads out widely for the co-polarization, and is almost 20dB stronger than the incoherent wave in the backward scattering direction. The spreading of strong coherent waves into backward scattering direction is possible to pollute the weak incoherently scattered power. On the other hand, the incoherent wave dominates the cross-polarization in all scattering directions with nearly no coherent wave contribution as expected. The incoherent bistatic scattering coefficient distributes more uniformly as a function of the scattering angle.

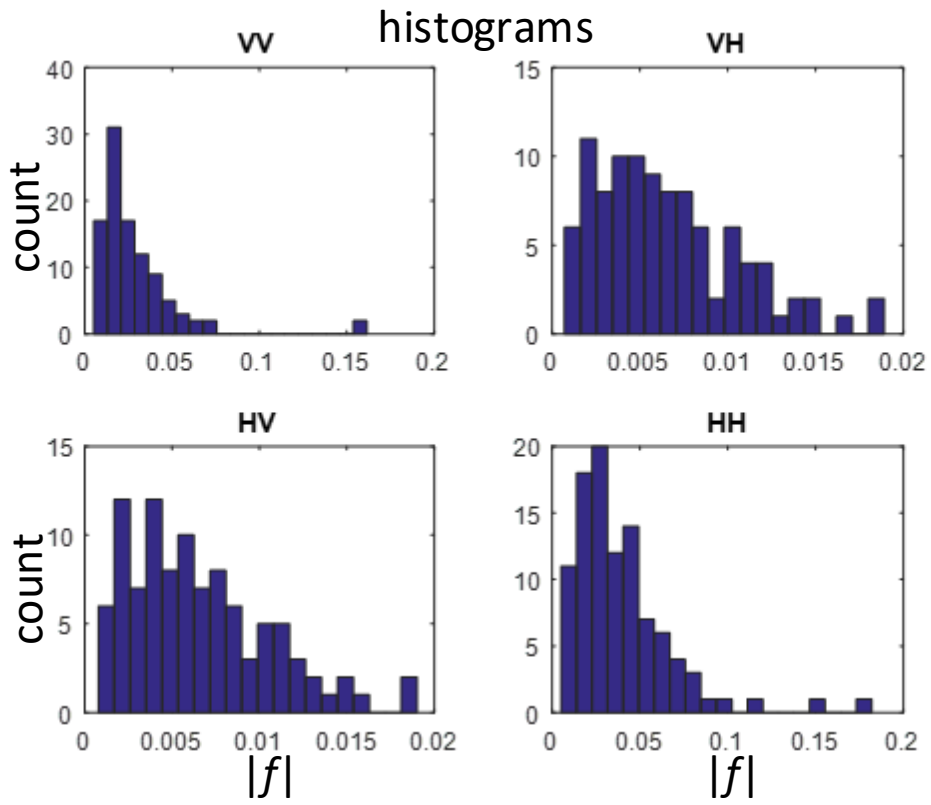

Figure III.12. Speckle statistics of the scattering amplitude

We can also derive the speckle statistics from the full wave simulation results. Speckles are arising from the random phase fluctuations of the microwave return from each of the scatterers. The histogram of the total backward scattering amplitude are plotted in Figure III.12 from the 100 Monte Carlo simulations. The results agree with the theoretical prediction of Rayleigh distribution using first order scattering approximation for a homogeneous scene. Also note that VH and HV are close following reciprocity, while the small differences are due to numerical noise.

To illustrate the achieved performance of the highly parallelized computing, we show in Table III-2 the recorded computing resources usage when deployed on the Flux high performance computing (HPC) cluster operated by University of Michigan. In the standard configuration, each node support up to 16 processors / CPU cores, and each processor (core) owns 4GB memory. And the memory of the same node is shared among all the processors. The recorded wall time in Table

III-2 is for one realization, viz. solving the DDA equations twice for two of the incidence polarizations. The scalability of the code and its deployment on HPC makes the toughest problem tractable. The code has also been deployed on the Stampede HPC clusters as part of the NSF funded Extreme Science and Engineering Discovery Environment (XSEDE).

Table III-2. Recorded computing resources usage on U Michigan Flux cluster.

dimension	# of cells	Memory (estimated)	# of cores	wall time (recorded)
$25cm \times 25cm \times 10cm$	5×10^7	160GB	50	43.5 min
$50cm \times 50cm \times 5cm$	1×10^8	320GB	100	29.1 min
$50cm \times 50cm \times 10cm$	2×10^8	640GB	200	68.5 min

3.4 Plane wave excitation of an infinite 2D snow layer emulated by periodic boundary conditions

The motivation to apply a periodic boundary condition in the horizontal directions is to derive passive remote sensing observables such as emissivity and brightness temperatures from the full wave simulation. Guided by the general principle of reciprocity, the passive emission problem can be solved from the active scattering problem [16], given that we know how much power is being scattered and reflected, how much power is being transmitted, and how much power is being absorbed. And the energy must conserve that the sum of the three parts should equal to the total incidence power. With the plane wave excitation of a truncated snow volume, it is difficult to rigorously derive how much power is transmitted and reflected (scattered) per unit area with the existence of a half dielectric space. On the other hand, the edge refraction effect from a finite snow volume manifests itself in the higher coherent scattering component spreading to a wide range of scattering angles as compared to the incoherent scattering component. These considerations drive us to examine the plane wave excitation of an infinite snow layer emulated by periodic boundary

conditions. Periodic boundary condition has been used to study random rough surface scattering [64, 138-140].

With periodic boundary condition, we will use periodic Green's function to formulate the integral equation. We need to compute the periodic Green's function including the reflection contribution from the bottom half space, and deal with its singularities. The scattered wave and transmitted wave will be concentrated in discrete directions other than continuous directions as required by the Bloch wave conditions. The general translational invariance of the Green's function is conserved, and thus FFT still applies to accelerate the matrix-vector multiplication.

In this section we use 2D simulation to demonstrate the possibility of full wave simulation in producing consistent scattering and emission results. We're going to derive rigorously the reciprocity relation between the active problem and passive problem. We will also compare the scattering results with periodic boundary conditions to the results from a truncated snow volume.

3.4.1 The admissible scattering angles

The requirements as imposed by the Bloch wave condition is implied in the spectral domain representation of the periodic Green's function.

In two dimension, the admissible scattering angles are given by

$$k_{xs} = k_{xi} + \frac{2\pi}{P} m \tag{3.189}$$

where $k_{xi} = k \sin\theta_i$, $k_{xs} = k \sin\theta_s$, P is the period, and $m = 0, \pm 1, \pm 2, \ldots$. For propagating waves, $|k_{xs}| < k$, this leads to

$$-\frac{P}{\lambda}\left(1+\sin\theta_i\right) < m < \frac{P}{\lambda}\left(1-\sin\theta_i\right) \tag{3.190}$$

giving around $2P/\lambda$ scattering angles determined by

$$\sin\theta_s = \sin\theta_i + m\frac{\lambda}{P} \tag{3.191}$$

We can in practice properly choose P such that the backscatter angle with $\theta_s = -\theta_{\text{inc}}$ is in the discrete admissible angles.

In three-dimension case, k_{ys} is determined by a similar relation $k_{ys} = k_{iy} + n2\pi/P_y$. Figure III.13 is a demonstration of such propagating modes limited by $k_{xs}^2 + k_{ys}^s < k^2$ with $P_x = P_y = 15\lambda$ and $\theta_{\text{inc}} = 40°$. There are a total of 704 propagating Bloch waves, and the two red crosses denote the backward and specular scattering direction.

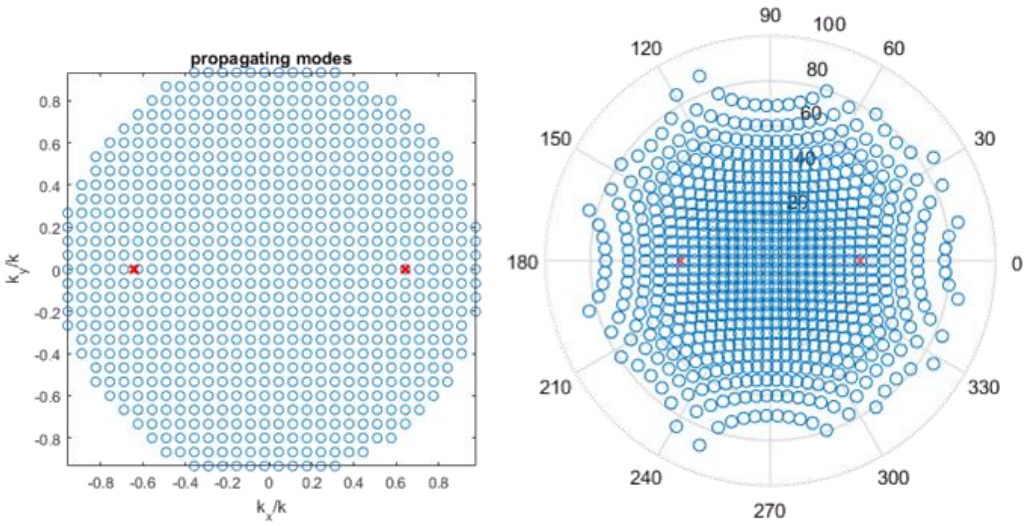

(a) propagating modes in k-space (b) propagating modes in angular-space

Figure III.13. Propagating Bloch waves (a) in k-space (b) in angular space. The angular space, (θ, ϕ) in polar plot, are related to the k-space, (k_x, k_y) in Cartesian plot, by $k_x = k\sin\theta\cos\phi$, $k_y = k\sin\theta\sin\phi$.

3.4.2 The 2D volume integral equation with periodic boundary condition and the discrete dipole approximation (DDA)

We consider the TE polarization case and start from the regular 2D volume integral equation as we derived in section 3.1.1, with the integral domain over the entire layer,

$$\psi(x,z)=\psi^{\text{inc}}(x,z)+k^2\int_{-\infty}^{\infty}dx'\int_0^H dz' g(x,z,x',z')\left(\varepsilon_r(x',z')-1\right)\psi(x',z') \tag{3.192}$$

With periodic boundary condition,

$$\psi(x+mP,z)=\psi(x,z)\exp(ik_{ix}mP) \tag{3.193}$$

Then

$$\psi(x,z)=\psi^{\text{inc}}(x,z)+k^2\int_{-P/2}^{P/2}dx'\int_0^H dz' g_P(x,z;x',z';k_{ix})\left(\varepsilon_r(x',z')-1\right)\psi(x',z') \tag{3.194}$$

where $g_P(x,z;x',z';k_{ix})$ is known as the periodic Green's function,

$$g_P(x,z;x',z';k_{ix})=\sum_{m=-\infty}^{\infty} g(x,z,x'+mP,z')\exp(ik_{ix}mP) \tag{3.195}$$

Since

$$g(x,z;x',z')=g^0(x,z;x',z')+g^R(x,z;x',z') \tag{3.196}$$

We also decompose $g_P(x,z;x',z';k_{ix})$ into two parts,

$$g_P(x,z;x',z';k_{ix})=g_P^0(x,z;x',z';k_{ix})+g_P^R(x,z;x',z';k_{ix}) \tag{3.197}$$

where

$$g_P^0(x,z;x',z';k_{ix})=\sum_{m=-\infty}^{\infty} g^0(x,z,x'+mP,z')\exp(ik_{ix}mP) \tag{3.198}$$

$$g_P^R(x,z;x',z';k_{ix})=\sum_{m=-\infty}^{\infty} g^R(x,z,x'+mP,z')\exp(ik_{ix}mP) \tag{3.199}$$

Then the discretized dipole approximation (DDA) of the volume integral equation is

$$p_m = \alpha_m \left[\psi^{\text{inc}}\left(x_m, z_m\right) + \frac{k^2}{\varepsilon} \sum_{n \neq m} p_n g_P^0\left(x_m, z_m; x_n, z_n; k_{ix}\right) + \frac{k^2}{\varepsilon} \sum_n p_n g_P^R\left(x_m, z_m; x_n, z_n; k_{ix}\right) \right] \tag{3.200}$$

where

$$p_n = \Delta^2 \varepsilon \left(\varepsilon_r\left(x_n, z_n\right) - 1\right) \psi\left(x_n, z_n\right) \tag{3.201}$$

$$\alpha_m = \frac{\Delta^2 \varepsilon \left(\varepsilon_r\left(x_m, z_m\right) - 1\right)}{1 - k^2 \left(\varepsilon_r\left(x_m, z_m\right) - 1\right) S} \tag{3.202}$$

$$S = \int_{\sigma_m} dx' dz' g_P^0\left(x_m, z_m; x', z'; k_{ix}\right) \tag{3.203}$$

where Δ is the edge length of the square unit cell, and Δ^2 is the area of the discretization unit.

It is to be shown that g_P^0 and g_P^R share the same translational invariance as g^0 and g^R, respectively, thus the FFT techniques also apply in accelerating the matrix-vector multiplications,

$$p_m = \alpha_m \left[\psi^{\text{inc}}\left(x_m, z_m\right) + \frac{k^2}{\varepsilon} \sum_{n \neq m} p_n g_P^0\left(x_m - x_n, z_m - z_n; k_{ix}\right) + \frac{k^2}{\varepsilon} \sum_n p_n g_P^R\left(x_m - x_n, z_m + z_n; k_{ix}\right) \right] \tag{3.204}$$

Comparing to the previous formulation in section 3.1.2, nothing is changed except that $g_P \to g_P^0$, $g_R \to g_P^R$, and $s \to S$ in defining the polarizability α. Thus the matrix-vector multiplication procedure do not change at all.

3.4.3 The periodic Green's function in 2D and the matrix elements

(a) The spectral domain representation

The representation in (3.198) and (3.199) is in spatial domain, by using the integral representation of $g^0(x, z)$

$$g^0(x,z) = \frac{i}{4\pi}\int_{-\infty}^{\infty} dk_x \exp(ik_x x)\frac{1}{k_z}\exp(ik_z|z|) \tag{3.205}$$

And making use of the Poisson summation,

$$\sum_{m=-\infty}^{\infty}\exp(i\alpha mP) = \frac{2\pi}{P}\sum_{m=-\infty}^{\infty}\delta\left(\alpha - m\frac{2\pi}{P}\right) \tag{3.206}$$

We can put the periodic Green's function in spectral domain representation,

$$g_P^0(x,z;x',z';k_{ix}) = \frac{i}{2P}\sum_{m=-\infty}^{\infty}\exp\left(ik_{xm}(x-x')\right)\frac{1}{k_{zm}}\exp\left(ik_{zm}|z-z'|\right) \tag{3.207}$$

where

$$k_{xm} = k_{ix} + m\frac{2\pi}{P} \tag{3.208}$$

$$k_{zm} = \sqrt{k^2 - k_{xm}^2} \tag{3.209}$$

Since each term in (3.207) represents a plane wave component, we immediately get the reflected wave, assuming the boundary between medium 0 and 1 is at $z = 0$,

$$g_P^R(x,z;x',z';k_{ix}) = \frac{i}{2P}\sum_{m=-\infty}^{\infty}\exp\left(ik_{xm}(x-x')\right)\frac{R(k_{xm})}{k_{zm}}\exp\left(ik_{zm}(z+z')\right) \tag{3.210}$$

where $R(k_{xm})$ is the Fresnel reflection coefficient.

(b) Transformation to improve the convergence of the series of $g_P^0(x,z;x',z';k_{ix})$ when $|z-z'|$ is small

Notice that the spectral domain summation of (3.207) converges slowly when $|z-z'|$ is small. So we move back to the spatial domain summation, given explicitly as follows,

$$g_P^0(x,z;x',z';k_{ix}) = \frac{i}{4}\sum_{m=-\infty}^{\infty}H_0^{(1)}\left(k\sqrt{\left(x-(x'+mP)\right)^2+(z-z')^2}\right)\exp(ik_{ix}mP) \tag{3.211}$$

and try to convert this series into a fast converging integral. The approach follows the appendix of [140], and follows [34] Chapter 3, Section 1.3, page 65-67.

The approach is based on the identity

$$\sum_{m=1}^{\infty} e^{imt} Q(m) = e^{it} \int_0^{\infty} dv \frac{q(v)}{e^v - e^{it}} \tag{3.212}$$

where $Q(m)$ is the Laplace transform of $q(v)$,

$$Q(m) = \int_0^{\infty} dv e^{-mv} q(v) \tag{3.213}$$

Making use of the Laplace transform

$$e^{-is} H_0^{(1)}\left(\sqrt{s^2 + a^2}\right) = -\frac{i2}{\pi} \int_0^{\infty} dy e^{-sy} \frac{\cos\left(a\sqrt{y^2 - 2iy}\right)}{\sqrt{y^2 - 2iy}} \tag{3.214}$$

we can cast (3.211) into

$$\begin{aligned} g_P^0(x, z; x', z'; k_{ix}) = \frac{i}{4} H_0^{(1)}\left(k\sqrt{(x - x')^2 + (z - z')^2}\right) \\ + g_P^{0+}(x, z; x', z'; k_{ix}) + g_P^{0-}(x, z; x', z'; k_{ix}) \end{aligned} \tag{3.215}$$

where

$$\begin{aligned} g_P^{0+}(x, z; x', z'; k_{ix}) &= \frac{\exp\left(i(k + k_{ix})P - ik(x - x')\right)}{\pi} \\ &\times \int_0^{\infty} du \frac{\exp\left(-u^2 kP + k(x - x')u^2\right)}{1 - \exp\left(-u^2 kP + i(k + k_{ix})P\right)} \frac{\cos\left(k(z - z')u\sqrt{u^2 - 2i}\right)}{\sqrt{u^2 - 2i}} \\ g_P^{0-}(x, z; x', z'; k_{ix}) &= \frac{\exp\left(i(k - k_{ix})P + ik(x - x')\right)}{\pi} \\ &\times \int_0^{\infty} du \frac{\exp\left(-u^2 kP - k(x - x')u^2\right)}{1 - \exp\left(-u^2 kP + i(k - k_{ix})P\right)} \frac{\cos\left(k(z - z')u\sqrt{u^2 - 2i}\right)}{\sqrt{u^2 - 2i}} \end{aligned} \tag{3.216}$$

The formulation of (3.215) is effective due to the exponential decay in $\exp(-u^2 kP \pm k(x - x')u^2)$. The formulation applies when

$$\begin{aligned} \left|x-x'\right| &< P \\ \left|z-z'\right| &\ll P \end{aligned} \tag{3.217}$$

The integrand diverges when $|z-z'|$ is large. When $|z-z'|$ is small, truncating the integral $\int_0^\infty du$ at $\int_0^{u_{\max}} du$ is in general good enough with

$$u_{\max} \geq \frac{5}{\sqrt{kP}} \tag{3.218}$$

In using (3.215) in the DDA formulation with d being the unit cell size, could choose

$$\left|z-z'\right| \leq 10d \tag{3.219}$$

as a rule of thumb to select between this integral formulation and the spectral domain series summation.

On the other hand, $|x-x'| < P$ can be always satisfied by using the Bloch wave condition of the periodic Green's function,

$$g_P^0\left(x+P,z;x',z';k_{ix}\right) = g_P^0\left(x,z;x',z';k_{ix}\right)e^{ik_{ix}P} \tag{3.220}$$

With method of moments (MoM) in DDA,

$$-\frac{P}{2} \leq x,x' \leq \frac{P}{2} \Rightarrow -P \leq x-x' \leq P \tag{3.221}$$

We can shrink the span of $|x-x'|$ to $|x-x'| \leq \frac{P}{2}$ by letting

$$\begin{aligned} &\tilde{x} = x+P, \text{ when } x-x' < -\frac{P}{2}, \text{ then } g_P^0\left(x,z;x',z';k_{ix}\right) = g_P^0\left(\tilde{x},z;x',z';k_{ix}\right)e^{-ik_{ix}P} \\ &\tilde{x} = x-P, \text{ when } x-x' > -\frac{P}{2}, \text{ then } g_P^0\left(x,z;x',z';k_{ix}\right) = g_P^0\left(\tilde{x},z;x',z';k_{ix}\right)e^{ik_{ix}P} \end{aligned} \tag{3.222}$$

The formulation is tested to be in agreement with the spectral domain summation when both approaches apply.

(c) Singular integral at self-patch

We need to evaluate (3.203) over the self-patch,

$$S = \int_{\sigma_m} dx'dz' g_P^0\left(x_m, z_m; x', z'; k_{ix}\right)$$

Following (3.215),

$$\begin{aligned} S = &\int_{\sigma_m} dx'dz' g^0\left(x_m, z_m; x', z'\right) \\ &+\Delta^2\left[g_P^{0+}\left(x_m, z_m; x_m, z_m; k_{ix}\right) + g_P^{0-}\left(x_m, z_m; x_m, z_m; k_{ix}\right)\right] \end{aligned} \tag{3.223}$$

where

$$\begin{aligned} g_P^{0+}\left(x_m, z_m; x_m, z_m; k_{ix}\right) &= \frac{\exp\left(i\left(k + k_{ix}\right)P\right)}{\pi}\int_0^\infty du \frac{\exp\left(-u^2 kP\right)}{1-\exp\left(-u^2 kP + i\left(k + k_{ix}\right)P\right)}\frac{1}{\sqrt{u^2 - 2i}} \\ g_P^{0-}\left(x_m, z_m; x_m, z_m; k_{ix}\right) &= \frac{\exp\left(i\left(k - k_{ix}\right)P\right)}{\pi}\int_0^\infty du \frac{\exp\left(-u^2 kP\right)}{1-\exp\left(-u^2 kP + i\left(k - k_{ix}\right)P\right)}\frac{1}{\sqrt{u^2 - 2i}} \end{aligned} \tag{3.224}$$

The first term is simply s_0 defined in (3.15) and is given explicitly in (3.22).

3.4.4 The scattering field and bistatic scattering coefficients

(a) The scattering field

The scattering field can be identified from the volume integral equation (3.194) by subtracting out the incident field,

$$\psi_s\left(x, z\right) = k^2\int_{-P/2}^{P/2} dx' \int_0^H dz' g_P\left(x, z; x', z'; k_{ix}\right)\left(\varepsilon_r\left(x', z'\right) - 1\right)\psi\left(x', z'\right) \tag{3.225}$$

Substituting into (3.225) the spectral domain representation of g_P^0 and g_P^R, and invoking the discrete dipole approximation, it is easy to show,

$$\psi_s(x,z) = \sum_{m=-\infty}^{\infty} \exp\left(ik_{xm}x + ik_{zm}z\right) B_m \tag{3.226}$$

where

$$B_m = \frac{k^2}{\varepsilon}\frac{i}{2P}\frac{1}{k_{zm}}\sum_j \exp\left(-ik_{xm}x_j\right)\left[\exp\left(-ik_{zm}z_j\right) + R\exp\left(ik_{zm}z_j\right)\right] p_j \tag{3.227}$$

It is also noticed that only propagating mode with $|k_{xm}| \le k$ contributes to scattering far field. The term $\exp(ik_{zm}z) \to 0$ as $z \to \infty$ for evanescent mode.

(b) Reflectivity and bistatic scattering coefficient

The scattered power P_s per w-width in the $\hat{y}$ direction,

$$P_s = \frac{1}{2} w \int_0^P dx \hat{z} \bullet \mathrm{Re}\left[\bar{E}_s \times \bar{H}_s^*\right] \tag{3.228}$$

Note that this is different from the way we calculated scattered power in section 3.1.8 by integrating the half circle at infinity because we have plane wave mode in scattering instead of cylindrical wave. It can be show that for TE polarization,

$$P_s = \frac{1}{2} w \int_0^P dx \,\mathrm{Re}\left[\frac{\psi_s}{-i\omega\mu}\frac{\partial \psi_s^*}{\partial z}\right] \tag{3.229}$$

Taking the fact that different Bloch modes are orthogonal, it is easy to show

$$P_s = \frac{1}{2}\frac{1}{\omega\mu} Pw \,\mathrm{Re}\left[\sum_{m=-\infty}^{\infty} k_{zm}\left|B_m\right|^2\right] = \frac{1}{2}\frac{1}{\omega\mu} Pw \sum_{|k_{xm}|<k} k_{zm}\left|B_m\right|^2 \tag{3.230}$$

On the other hand, the incident power per w width in $\hat{y}$ and per period P in $\hat{x}$ is

$$P_{inc} = \frac{1}{2\eta} Pw\cos\theta_{inc} \tag{3.231}$$

The reflectivity r and bistatic scattering coefficient $\sigma(\theta_s)$ is then defined such that

$$r = \frac{P_s}{P_{inc}} = \sum_{|k_{xm}|<k} \frac{\cos\theta_m}{\cos\theta_{inc}} \left|B_m\right|^2 \tag{3.232}$$

And

$$r = \int_{-\pi/2}^{\pi/2} d\theta_s \sigma\left(\theta_s\right) \tag{3.233}$$

We follow [34] chapter 3, section 1.4, pp. 67 to convert the summation into integral,

Let

$$\Delta m = 1 \tag{3.234}$$

Considering

$$k_{xm} = k_{ix} + m\frac{2\pi}{P} \tag{3.235}$$

Then

$$\Delta k_{xm} = \frac{2\pi}{P}\Delta m \Rightarrow \Delta m = \Delta k_{xm}\frac{P}{2\pi} \tag{3.236}$$

Thus

$$\begin{aligned} r = \frac{P_s}{P_{inc}} &= \sum_{|k_{xm}|<k} \frac{\cos\theta_m}{\cos\theta_{inc}} \left|B_m\right|^2 \Delta m = \sum_{|k_{xm}|<k} \frac{\cos\theta_m}{\cos\theta_{inc}} \left|B_m\right|^2 \Delta k_{xm}\frac{P}{2\pi} \\ &= \frac{P}{2\pi}\int_{-k}^{k} dk_x \frac{\cos\theta}{\cos\theta_{inc}} \left|B_m\right|^2 = \frac{Pk}{2\pi}\int_{-\pi/2}^{\pi/2} d\theta \frac{\cos^2\theta}{\cos\theta_{\text{inc}}} \left|B_m\right|^2 \end{aligned} \tag{3.237}$$

Comparing with the definition of $\sigma(\theta_s)$ in (3.233), we get

$$\sigma\left(\theta_s\right) = \frac{Pk}{2\pi}\frac{\cos^2\theta}{\cos\theta_{inc}} \left|B_m\right|^2 \tag{3.238}$$

Note that $\sigma(\theta_s)$ is only defined on discrete scattering angles when B_m is defined. The angles are given by

$$k_{xm} = k_{ix} + m\frac{2\pi}{P} = k\sin\theta_m \tag{3.239}$$

(c) Complexity due to the half space configuration

Note that in (3.226), the scattering field is due to the direct incidence field $\psi_{inc}^{\text{direct}}$ plus the reflected incidence field $\psi_{inc}^{\text{reflected}}$, where

$$\psi_{inc}^{\text{directed}} = \exp\left(ik_{ix}x - ik_{iz}z\right) \tag{3.240}$$

$$\psi_{inc}^{\text{reflected}} = \exp\left(ik_{ix}x + ik_{iz}z\right)R\left(k_{ix}\right) \tag{3.241}$$

Note $\psi_{inc}^{\text{reflected}}$ is a plane wave of the zero-th Bloch mode,

$$\psi_{inc}^{\text{reflected}} = \exp\left(ik_{x0}x + ik_{z0}z\right)R\left(k_{x0}\right) \tag{3.242}$$

In defining the reflectivity and the bistatic scattering coefficient as in (3.232) and (3.233), we should consider the scattered field resulting from the direct incidence wave $\psi_{inc}^{\text{direct}}$, which is,

$$\tilde{\psi}_s = \sum_{m=-\infty}^{\infty} \exp\left(ik_{xm}x + ik_{zm}z\right)\left(B_m + \delta_{m0}R\left(k_{x0}\right)\right) \tag{3.243}$$

Define

$$\tilde{B}_m = B_m + \delta_{m0}R\left(k_{x0}\right) \tag{3.244}$$

then the reflectivity and the bistatic scattering coefficient will be

$$r = \frac{P_s}{P_{inc}} = \sum_{m,|k_{zm}<k|} \frac{\cos\theta_m}{\cos\theta_{inc}}\left|\tilde{B}_m\right|^2 \tag{3.245}$$

$$\sigma\left(\theta_s\right) = \frac{Pk}{2\pi}\frac{\cos^2\theta}{\cos\theta_{inc}}\left|\tilde{B}_m\right|^2 \tag{3.246}$$

(d) Decomposition of coherent and incoherent scattering coefficients

When the periodic boundary condition is applied, the boundary effects are eliminated and the coherent scattering field is concentrated in the specular direction. Thus the decomposition of scattering field into coherent and incoherent components is no longer a must in deriving the

backscatter and bistatic scattering coefficients. But formally, one can still perform the decomposition by viewing $\tilde{B}_m$ as the scattering amplitude. Thus

$$\sigma^{\text{coh}}\left(\theta_s\right) = \frac{Pk}{2\pi}\frac{\cos^2\theta}{\cos\theta_{inc}}\left|\left\langle \tilde{B}_m \right\rangle\right|^2 \tag{3.247}$$

$$\sigma^{\text{incoh}}\left(\theta_s\right) = \frac{Pk}{2\pi}\frac{\cos^2\theta}{\cos\theta_{inc}}\left(\left\langle \left|\tilde{B}_m\right|^2 \right\rangle - \left|\left\langle \tilde{B}_m \right\rangle\right|^2\right) \tag{3.248}$$

The incoherent bistatic scattering coefficients can be compared to the results derived in section 3.1.8 when periodic boundary condition is not applied to examine the finite edge effects. It is numerically verified that the coherent field component only contributes in the specular direction.

3.4.5 The passive problem: transmissivity, absorptivity and brightness temperature

(a) Simple case with lossless snowpack

The brightness temperature is calculated straightforward from reciprocity,

$$T_b = eT_g = tT_g = \left(1-r\right)T_g \tag{3.249}$$

where e is the emissivity and is equal to the transmissivity t; r is the reflectivity; and T_g is the physical temperature of the bottom half space. The energy conservation relation is

$$r + t = 1 \tag{3.250}$$

In order to check the energy conservation relation, one needs to independently calculate t through the power ratio,

$$t = \frac{P_t}{P_{\text{inc}}} \tag{3.251}$$

where P_{inc} is the incidence power per period and is given in (3.231), P_t is the transmitted power on the interface ($z = 0$) between snow and ground. P_t is evaluated by the surface integral of Poynting's vector of the total field on the boundary,

$$P_t = \frac{1}{2} w \int_0^P dx (-\hat{z}) \cdot \text{Re}\left[\bar{E}_t \times \bar{H}_t^* \right] \tag{3.252}$$

where the subscript t is interpreted as the total field, which is the same as transmitted field.

It can be easily shown that for TE polarized wave,

$$P_t = \frac{1}{2} w \int_0^P dx \, \text{Re}\left[\frac{\psi_t}{i\omega\mu} \frac{\partial \psi_t^*}{\partial z} \right] \tag{3.253}$$

We then express ψ_t and $\partial \psi_t / \partial z$ explicitly at $z = 0$.

$$\psi_t = \psi_{inc} + \psi_s \tag{3.254}$$

where

$$\psi_{inc}(x, z) = \exp(ik_{ix} x)\left(\exp(-ik_{iz} z) + \exp(ik_{iz} z) R\right) \tag{3.255}$$

thus

$$\psi_{inc}(x, z = 0) = \exp(ik_{ix} x)(1 + R) \tag{3.256}$$

And

$$\begin{aligned} \psi_s &= k^2 \int_0^P dx' \int_0^H dz' g_P(x, z; x', z'; k_{ix}) \left(\varepsilon_r(x', z') - 1\right) \psi(x', z') \\ &= \frac{k^2}{\varepsilon} \sum_j \left[g_P^0(x, z; x_j, z_j; k_{ix}) + g_P^R(x, z; x_j, z_j; k_{ix}) \right] p_j \end{aligned} \tag{3.257}$$

Using (3.207) and (3.210), and realizing $z = 0$ is below the snow volume thus $z < z'$, one can readily show that

$$\psi_s(x, z) = \sum_{m=-\infty}^{\infty} C_m \left[\exp(-ik_{zm} z) + R(k_{xm}) \exp(ik_{zm} z) \right] \exp(ik_{xm} x) \tag{3.258}$$

where

$$C_m = \frac{k^2}{\varepsilon}\frac{i}{2P}\frac{1}{k_{zm}}\sum_j \exp\left(-ik_{xm}x_j + ik_{zm}z_j\right)p_j \tag{3.259}$$

Adding up ψ_{inc} and ψ_s,

$$\psi_t\left(x, z=0\right) = \sum_{m=-\infty}^{\infty} \tilde{C}_m \exp\left(ik_{xm}x\right) \tag{3.260}$$

where

$$\tilde{C}_m = \left(C_m + \delta_{m0}\right)\left(1 + R\left(k_{xm}\right)\right) \tag{3.261}$$

Similarly, from (3.255) and (3.258), one can readily show that

$$\left.\frac{\partial\psi_t\left(x,z\right)}{\partial z}\right|_{z=0} = \sum_{m=-\infty}^{\infty} \tilde{D}_m \exp\left(ik_{xm}x\right) \tag{3.262}$$

where

$$\tilde{D}_m = ik_{zm}\left(C_m + \delta_{m0}\right)\left[-1 + R\left(k_{xm}\right)\right] \tag{3.263}$$

Substituting (3.260) and (3.262) into (3.253), and invoking the orthogonality of the Bloch waves, one can readily show that,

$$P_t = \frac{1}{2}Pw\,\mathrm{Re}\left[\frac{1}{i\omega\mu}\sum_{m=-\infty}^{\infty}\tilde{C}_m\tilde{D}_m^*\right] \tag{3.264}$$

Substituting the definitions of $\tilde{C}_m$ and $\tilde{D}_m$, we can separate the contribution from propagating mode and evanescent mode to P_t,

$$\begin{aligned} P_t &= \frac{1}{2}Pw\frac{1}{\omega\mu}\sum_{m=-\infty}^{\infty}\left|C_m + \delta_{m0}\right|^2 \mathrm{Re}\left[k_{zm}^*\left(1 - \left|R\left(k_{xm}\right)\right|^2 + 2i\,\mathrm{Im}\left[R\left(k_{xm}\right)\right]\right)\right] \\ &= \frac{1}{2}Pw\frac{1}{\omega\mu}\sum_{m,\text{propagating}}\left|C_m + \delta_{m0}\right|^2 k_{zm}\left(1 - \left|R\left(k_{xm}\right)\right|^2\right) \\ &\quad + \frac{1}{2}Pw\frac{1}{\omega\mu}\sum_{m,\text{evanescent}}\left|C_m + \delta_{m0}\right|^2 2\,\mathrm{Im}\left[k_{zm}\right]\mathrm{Im}\left[R\left(k_{xm}\right)\right] \end{aligned} \tag{3.265}$$

If the bottom half space is lossless, i.e., k_1 and ε_1 are real,

$$\mathrm{Im}\left[R\right]=0 \text{ for } \left|k_{xm}\right|\le k \text{ or } \left|k_{xm}\right|\ge k_1$$

thus the contributing evanescent waves are only those satisfying

$$k<\left|k_{xm}\right|<k_1$$

These are modes evanescent in medium 0, but propagating in medium 1.

However, for lossy bottom medium, all the evanescent modes of medium 0 contribute. But the contribution rapidly decays to negligible.

Substituting P_t and P_{inc} into (3.251), we get the transmissivity t from medium 0 to medium 1,

$$\begin{aligned} t &= \frac{1}{k_{iz}}\mathrm{Re}\left[\frac{1}{i}\sum_{m=-\infty}^{\infty}\tilde{C}_m\tilde{D}_m^*\right]=\frac{1}{k_{iz}}\mathrm{Im}\left[\sum_{m=-\infty}^{\infty}\tilde{C}_m\tilde{D}_m^*\right] \\ &= \sum_{m,\text{propagating}}\left|C_m+\delta_{m0}\right|^2\frac{k_{zm}}{k_{iz}}\left(1-\left|R\left(k_{xm}\right)\right|^2\right) \\ &+ \sum_{m,\text{evanescent}}\left|C_m+\delta_{m0}\right|^2 2\,\mathrm{Im}\left[\frac{k_{zm}}{k_{iz}}\right]\mathrm{Im}\left[R\left(k_{xm}\right)\right] \end{aligned} \tag{3.266}$$

(b) General case with lossy snowpack and varying snow temperature profile

When snowpack is lossy, the energy conservation relation is

$$r+a+t=1 \tag{3.267}$$

where both the absorptivity a and transmissivity t contributes to emission.

The absorptivity a of the snowpack is defined by the ratio of the absorbed power P_a to the incident power P_{inc},

$$a=\frac{P_a}{P_{inc}} \tag{3.268}$$

The absorbed power P_a per period P and per width w in $\hat{y}$ direction,

$$P_a = w\int_0^P dx' \int_0^H dz' \frac{1}{2}\omega\varepsilon'' \left|\bar{E}\right|^2 \tag{3.269}$$

and for TE polarization,

$$P_a = \frac{1}{2}\omega w\Delta^2 \sum_n \varepsilon''\left(x_n, z_n\right)\left|\psi\left(x_n, z_n\right)\right|^2 \tag{3.270}$$

where Δ is the discretization size.

When the background media is lossless,

$$P_a = \frac{1}{2}\omega w\Delta^2 \sum_{n\in\text{scatterer}} \varepsilon''\left(x_n, z_n\right)\left|\psi\left(x_n, z_n\right)\right|^2 \tag{3.271}$$

Considering the definition of the dipole moment p_n,

$$p_n = \Delta^2 \varepsilon_b \left(\varepsilon_r\left(x_n, z_n\right) - 1\right)\psi\left(x_n, z_n\right) \tag{3.272}$$

Equation (3.271) can be represented using p_n instead of ψ

$$P_a = \frac{1}{2}\frac{\omega}{\varepsilon_b} w \frac{1}{\Delta^2} \sum_{n\in\text{scatterer}} \varepsilon_b''\left(x_n, z_n\right)\left|\frac{p_n}{\varepsilon_r\left(x_n, z_n\right) - 1}\right|^2 \tag{3.273}$$

For a two-phase random media with background permittivity ε_b and scatterer permittivity of ε_p, it is further reduced to, considering $p_n = 0$ in the background,

$$P_a = \frac{1}{2}\frac{\omega}{\varepsilon_b} w \frac{1}{\Delta^2} \frac{\varepsilon_{pr}''}{\left|\varepsilon_{pr} - 1\right|^2} \sum_n \left|p_n\right|^2 \tag{3.274}$$

Substitute P_a and P_{inc} into (3.268), the absorptivity a

$$a = \frac{1}{\cos\theta_{inc}} \frac{1}{P} \frac{k}{\varepsilon_b^2} \frac{1}{\Delta^2} \frac{\varepsilon_{pr}''}{\left|\varepsilon_{pr} - 1\right|^2} \sum_n \left|p_n\right|^2 \tag{3.275}$$

Once we know a and t, if the snow is of constant temperature T_s, and the ground is of constant temperature T_g, the brightness temperature is readily available from reciprocity,

$$T_b = aT_s + tT_g \tag{3.276}$$

In the special case of $T_s = T_g$, we have $T_b = (a + t)T_g = (1 - r)T_g$ which has the same form as the last identity in (3.249).

If we also consider the downward solar radiation with temperature T_0, (3.276) is generalized into

$$T_b = rT_0 + aT_s + tT_g \tag{3.277}$$

The reciprocity relation of (3.276) can be generalized for varying snow temperature profile,

$$T_b\left(\theta_{inc}\right) = \int_{V_{snow}} da\left(\bar{r}'\right) T_s\left(\bar{r}'\right) + tT_g \tag{3.278}$$

where $da(\bar{r}) = \frac{dP_a(\bar{r})}{P_{inc}}$ is the differential absorptivity. It naturally reduces to (3.276) when $T_s(\bar{r}) = T_s$ is constant. After discretization,

$$T_b\left(\theta_{inc}\right) = \sum_n \Delta a_n T_s\left(\bar{r}_n\right) + tT \tag{3.279}$$

where

$$\Delta a_n = \frac{1}{\cos\theta_{inc}} \frac{1}{P} \frac{k}{\varepsilon_b^2} \frac{1}{\Delta^2} \frac{\varepsilon''_{pr}\left(\bar{r}_n\right)}{\left|\varepsilon_{pr}\left(\bar{r}_n\right) - 1\right|^2} \left|p_n\right|^2 \tag{3.280}$$

3.4.6 The generalized reciprocity between active and passive problem

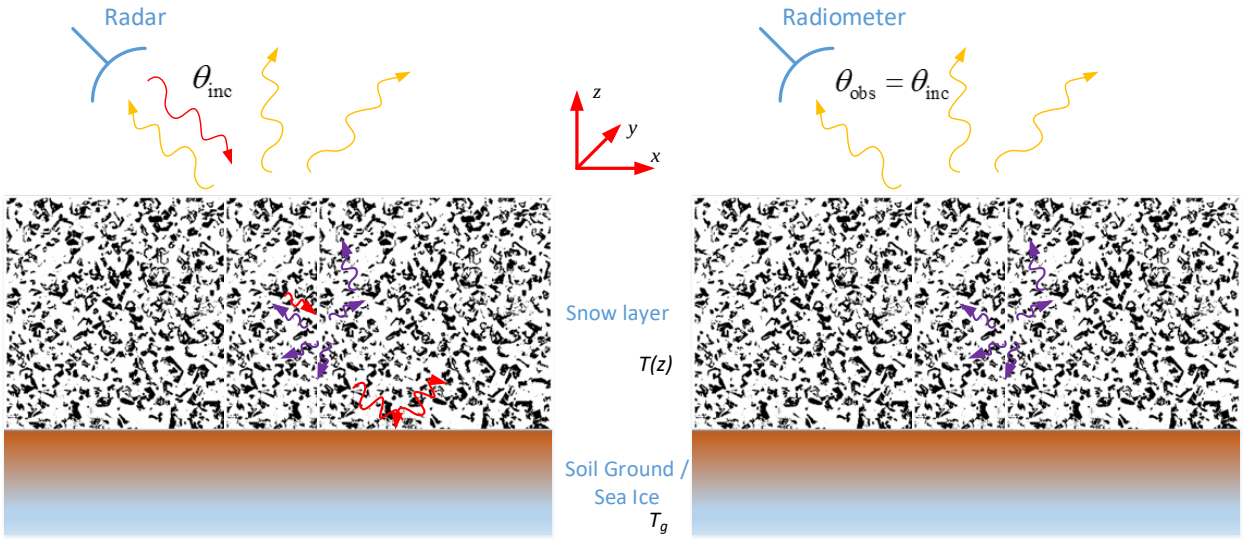

(a) active problem A (b) passive problem B

Figure III.14. Reciprocity between the active and passive problems.

In this subsection, we derive the generalized reciprocity relation (3.278) between the active scattering and passive emission problem, Figure III.14. We consider an active problem A, where the snowpack is illuminated by an incidence plane wave, and a passive problem B, where the thermal emission from the snowpack is observed in the direction that is opposite to the incidence direction of the active problem. It is difficult to solve the passive problem B directly, but we show that the solution of the brightness temperature can be represented using the field solution that we already obtained for the active problem A. The derivation here is an extension of [16] chapter 7, section 5, pp. 344-349.

(a) The active remote sensing problem A

The time-averaged Poynting's vector $\bar{S}^{(A)}$,

$$\bar{S}^{(A)} = \frac{1}{2}\mathrm{Re}\left(\bar{E}\times\bar{H}^{*}\right) = \frac{1}{4}\left[\bar{E}\times\bar{H}^{*} + \bar{H}\times\bar{E}^{*}\right] \tag{3.281}$$

Substituting into (3.281)

$$\bar{H} = \frac{1}{i\omega\mu}\nabla \times \bar{E}$$

and making use of the vector identity

$$\nabla \cdot \left(\bar{A} \times \bar{B}\right) = \bar{B} \cdot \nabla \times \bar{A} - \bar{A} \cdot \nabla \times \bar{B}$$

one can show that, assuming μ is real, representing no magnetic losses,

$$\nabla \cdot \bar{S}^{(A)} = \frac{1}{4}\frac{-1}{i\omega\mu} 2i \,\mathrm{Im}\left[\bar{E}^{*} \cdot \nabla \times \nabla \times \bar{E}\right] \tag{3.282}$$

$\bar{E}$, short for $\bar{E}^{(A)}$, the electric field of problem A, obeys the vector wave equation,

$$\nabla \times \nabla \times \bar{E}\left(\bar{r}\right) - \omega^2 \mu\varepsilon\left(\bar{r}\right)\bar{E}\left(\bar{r}\right) = 0 \tag{3.283}$$

Thus

$$\nabla \cdot \bar{S}^{(A)} = -\frac{\omega}{2}\varepsilon''\left(\bar{r}\right)\left|\bar{E}^{(A)}\left(\bar{r}\right)\right|^2 \tag{3.284}$$

where ε'' denotes the imaginary part of ε. Thus

$$\int_S d\bar{S}\hat{n} \cdot \bar{S}^{(A)} = \int_V d\bar{r}\nabla \cdot \bar{S}^{(A)} = -\frac{\omega}{2}\int_V d\bar{r}\,\varepsilon''\left(\bar{r}\right)\left|\bar{E}^{(A)}\left(\bar{r}\right)\right|^2 \tag{3.285}$$

Equation (3.285) is actually the Poynting's theorem in a source free region stating that the time averaged net power flow into a closed surface is being absorbed.

(b) The passive thermal emission problem B

The thermal currents, satisfying the fluctuation dissipation theorem, creates the radiation field $\bar{E}(\bar{r}, \omega)$.

$$\left\langle \bar{J}\left(\bar{r}, \omega\right)\bar{J}\left(\bar{r}', \omega'\right)\right\rangle = \frac{4}{\pi}\omega\varepsilon''\left(\bar{r}\right)K_b T\left(\bar{r}\right)\bar{\bar{I}}\,\delta\left(\omega - \omega'\right)\delta\left(\bar{r} - \bar{r}'\right) \tag{3.286}$$

where K_b is the Boltzmann constant.

We want to compute the thermal emission proportional to

$$\int_{\Delta\omega} d\omega \left\langle \bar{E}\left(\bar{r},\omega\right)\bar{E}^{*}\left(\bar{r},\omega\right)\right\rangle$$

The vector wave equation governing $\bar{E}(\bar{r},\omega)$

$$\nabla\times\nabla\times\bar{E}\left(\bar{r}\right)-\omega^{2}\mu\varepsilon\left(\bar{r}\right)\bar{E}\left(\bar{r}\right)=i\omega\mu J\left(\bar{r}\right) \tag{3.287}$$

The vector wave equation governing the dyadic Green's function $\bar{\bar{G}}(\bar{r},\bar{r}')$

$$\nabla\times\nabla\times\bar{\bar{G}}\left(\bar{r},\bar{r}'\right)-\omega^{2}\mu\varepsilon\left(\bar{r}\right)\bar{\bar{G}}\left(\bar{r},\bar{r}'\right)=\bar{\bar{I}}\,\delta\left(\bar{r}-\bar{r}'\right) \tag{3.288}$$

We can express $\bar{E}(\bar{r})$ using $\bar{\bar{G}}(\bar{r},\bar{r}')$ and $J(\bar{r})$,

$$\bar{E}\left(\bar{r}\right)=i\omega\mu\int d\bar{r}\bar{\bar{G}}\left(\bar{r},\bar{r}'\right)\cdot J\left(\bar{r}'\right) \tag{3.289}$$

Note that this Green's function $\bar{\bar{G}}(\bar{r},\bar{r}')$ considers all the complexities in geometry, and the radiation source using $\bar{\bar{G}}$ as the propagator is only the thermal currents. This is different from the half space Green's function we used to formulate the active scattering problem, where the polarization currents act as radiation source.

It is ready to show that from (3.289) and (3.286) that

$$\int_{\Delta\omega} d\omega\left\langle\left|\hat{\alpha}\cdot\bar{E}\left(\bar{r},\omega\right)\right|^{2}\right\rangle=\int d\bar{r}'\left|\bar{\bar{G}}\left(\bar{r},\bar{r}'\right)\cdot\hat{\alpha}\right|^{2}\omega^{2}\mu^{2}\frac{4}{\pi}\omega\varepsilon''\left(\bar{r}'\right)K_{b}T\left(\bar{r}'\right) \tag{3.290}$$

where $\hat{\alpha}$ denotes the polarization. And the brightness temperature at $\hat{\alpha}$ polarization and angle θ

$$T_{b}^{\alpha\alpha}\left(\omega\right)=\lim_{r\to\infty}\frac{16\pi^{2}\eta r^{2}}{A_{0}\cos\theta}\int_{V}d\bar{r}'\omega\varepsilon''\left(\bar{r}'\right)T\left(\bar{r}'\right)\left|\hat{\alpha}\cdot\bar{\bar{G}}\left(\bar{r},\bar{r}'\right)\right|^{2} \tag{3.291}$$

where $\eta=\sqrt{\mu_0/\varepsilon_0}$ is the free-space wave impedance, and A_0 is the horizontal surface area of the region V where we perform the integration.

The reciprocity that connect the passive problem to the active problem

$$\lim_{r\to\infty} \hat{\alpha}\cdot\bar{\bar{G}}\left(\bar{r},\bar{r}'\right) = \frac{e^{ikr}}{4\pi r}\bar{E}^{(A)}\left(\bar{r}'\right) \tag{3.292}$$

where $\bar{E}^{(A)}$ is the electric field due to an incidence plane wave of unit magnitude and polarized in $\hat{\alpha}$. The factor $\frac{\exp(ikr)}{4\pi r}$ is to account for the effect that $\bar{E}^{(A)}$ is the response to a plane wave with phase referenced at origin. This only applies to far field, where a spherical wave differs from a plane wave by a diverging factor of $\frac{\exp(ikr)}{4\pi r}$.

Substituting (3.292) into (3.291), it immediately follows that

$$T_b^{\alpha\alpha}\left(\omega\right) = \frac{\eta}{A_0\cos\theta}\int d\bar{r}'\omega\varepsilon''\left(\bar{r}'\right)\left|\bar{E}^{(A)}\left(\bar{r}'\right)\right|^2 T\left(\bar{r}'\right) \tag{3.293}$$

Making use of (3.284), we can also put

$$T_b^{\alpha\alpha}\left(\omega\right) = -\frac{2\eta}{A_0\cos\theta}\int d\bar{r}'\nabla\cdot\bar{S}^{(A)}\left(\bar{r}'\right)T\left(\bar{r}'\right) \tag{3.294}$$

Equation (3.293) and (3.294) represents the brightness temperature using the field solution of the active scattering problem, where the volume integration extends to $z\to-\infty$.

(c) Snowpack scattering / emission on half space

Confining to our snow scattering / emission on half space problem, we can split the volume integral in (3.293) into the integration in snowpack and in the bottom half-space. For the latter part, we use the form of (3.294).

$$\begin{aligned} T_b\left(\theta\right) = &\frac{\eta}{A_0\cos\theta}\int_{V_{snow}} d\bar{r}'\omega\varepsilon''\left(\bar{r}'\right)\left|\bar{E}^{(A)}\left(\bar{r}'\right)\right|^2 T\left(\bar{r}'\right) \\ &-\frac{2\eta}{A_0\cos\theta}\int_{V_{ground}} d\bar{r}'\nabla\cdot\bar{S}^{(A)}\left(\bar{r}'\right)T\left(\bar{r}'\right) \end{aligned} \tag{3.295}$$

Note that the first term represents the emission from snow volume and the second term represents the emission from the underlying half-space. The second term can be simplified when

we can assume a constant ground temperature T_g. Under this condition, we can apply the Gaussian divergence theorem to convert the volume integral into a surface integral. Note that the surface integral on the four side walls cancel out under the statistical translational invariance along the horizontal direction for both the geometry and the incidence plane wave. The surface integral over the bottom wall at $z \to -\infty$ also vanishes where we can assume the power flow decays to zero. Thus only the integral over the snow/ground interface contributes. Upon these assumptions, we have

$$\begin{aligned} T_b^{ground} &= -\frac{2\eta}{A_0 \cos\theta} T_g \int_A d\bar{r}' \hat{z} \cdot \bar{S}^{(A)}\left(\bar{r}'\right) \\ &= -\frac{\eta}{A_0 \cos\theta} T_g \int_A d\bar{r}' \hat{z} \cdot \mathrm{Re}\left[\bar{E}^{(A)}\left(\bar{r}'\right) \times \bar{H}^{(A)*}\left(\bar{r}'\right)\right] \end{aligned} \tag{3.296}$$

Putting everything together,

$$\begin{aligned} T_b\left(\theta_{inc}\right) = &\frac{\eta}{A_0 \cos\theta_{inc}} \int_{V_{snow}} d\bar{r}' \omega \varepsilon''\left(\bar{r}'\right) \left|\bar{E}^{(A)}\left(\bar{r}'\right)\right|^2 T\left(\bar{r}'\right) \\ &-\frac{\eta}{A_0 \cos\theta_{inc}} T_g \int_A d\bar{r}' \hat{z} \cdot \mathrm{Re}\left[\bar{E}^{(A)}\left(\bar{r}'\right) \times \bar{H}^{(A)*}\left(\bar{r}'\right)\right] \end{aligned} \tag{3.297}$$

Comparing with the definition of P_{inc} in (3.231), P_a in (3.269), and P_t in (3.252), we can readily rewrite (3.297),

$$T_b\left(\theta_{inc}\right) = \int_{V_{snow}} \frac{dP_a\left(\bar{r}'\right)}{P_{inc}} T_s\left(\bar{r}'\right) + t\frac{P_t}{P_{inc}} \tag{3.298}$$

This proves the general reciprocal relation between the active and passive problem as given in (3.278).

3.4.7 Simulation results

We first illustrate the decomposition of scattering waves into coherent and incoherent waves in Figure III.15. We consider a snowpack of 10cm thickness on ground. The finite horizontal computation domain is truncated at 50cm applying periodic boundary conditions. The impinging wave is at 17.2GHz, and has an incidence angle of 40°. Thus the computational domain is of $28.7\lambda \times 5.7\lambda$. The ground has permittivity $(5 + i0.5)\varepsilon_0$. The ice has permittivity $(3.2 + 0.001i)\varepsilon_0$. The bicontinuous media has parameters of $\langle\zeta\rangle = 5000/\text{m}$, $b = 1$, and $f_v = 0.3$. The 2D bicontinuous media is simply taken from independent cross sections of the 3D bicontinuous medium.

The bistatic scattering coefficient as shown in Figure III.15 are calculated from 500 Monte Carlo simulations. As we discussed before, the periodic boundary condition emulates a layer of snow of infinite horizontal extent, and thus the coherent scattering wave is only exhibited in the specular scattering direction. Thus the total scattering coefficients can be used to model radar observations directly without the complexity of decomposition.

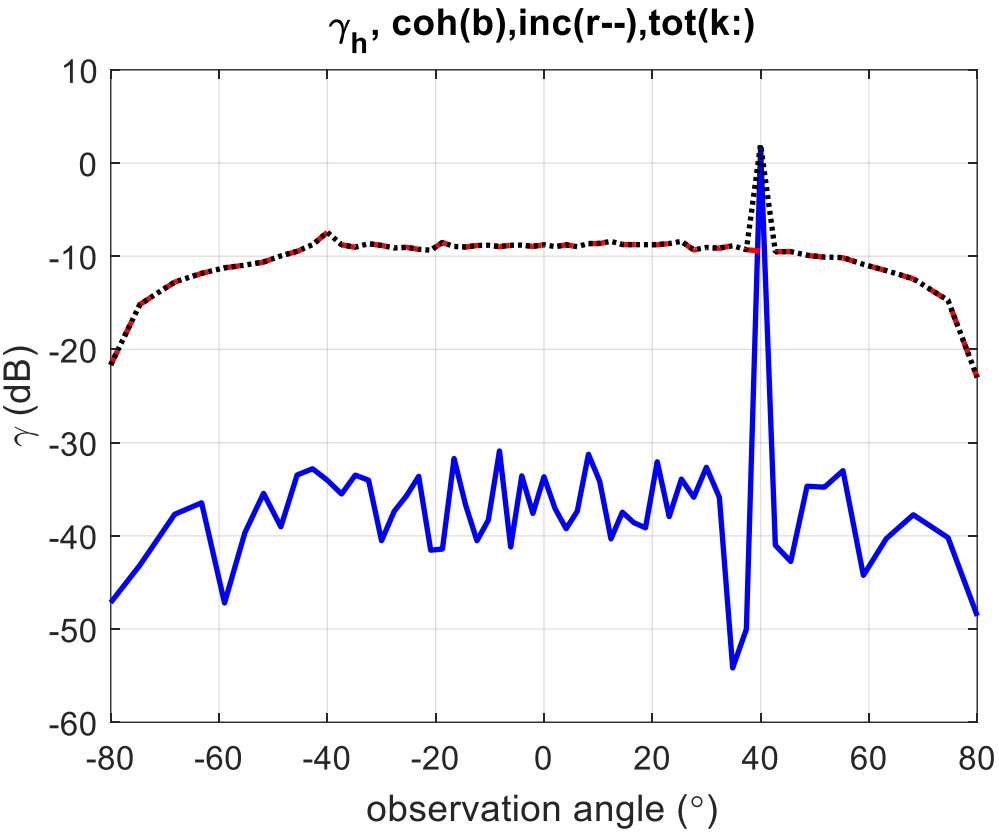

Figure III.15. Decomposition of bistatic scattering coefficients into coherent and incoherent parts for 2D simulation with periodic boundary condition.

The incoherent bistatic scattering coefficients are again plotted in Figure III.16, comparing to the 2D full wave simulation results without applying the periodic boundary conditions (i.e., the results of Figure III.4 with horizontal truncation domain of 1m and 1000 Monte Carlo simulations). The results agree quite well for scattering angles less than ~50 degrees, while the results with periodic boundary conditions significantly decreases as the scattering angle increases to near grazing. This effect is physical showing that the periodic boundary condition effectively removes the artificial edge diffraction effects due to truncating the computational domain. The vertical lines in Figure III.16 denote the discrete scattering angles as a results of the Floquet boundary conditions. But with $P \gg \lambda$, the available scattering angles are fine enough to resolve the angular patterns of bistatic scattering coefficient. Meanwhile, the peak in the backscattering direction is

again noticeable on the order of ~2dB demonstrating the backscattering enhancement, quantitatively in agreement with the results without boundary conditions.

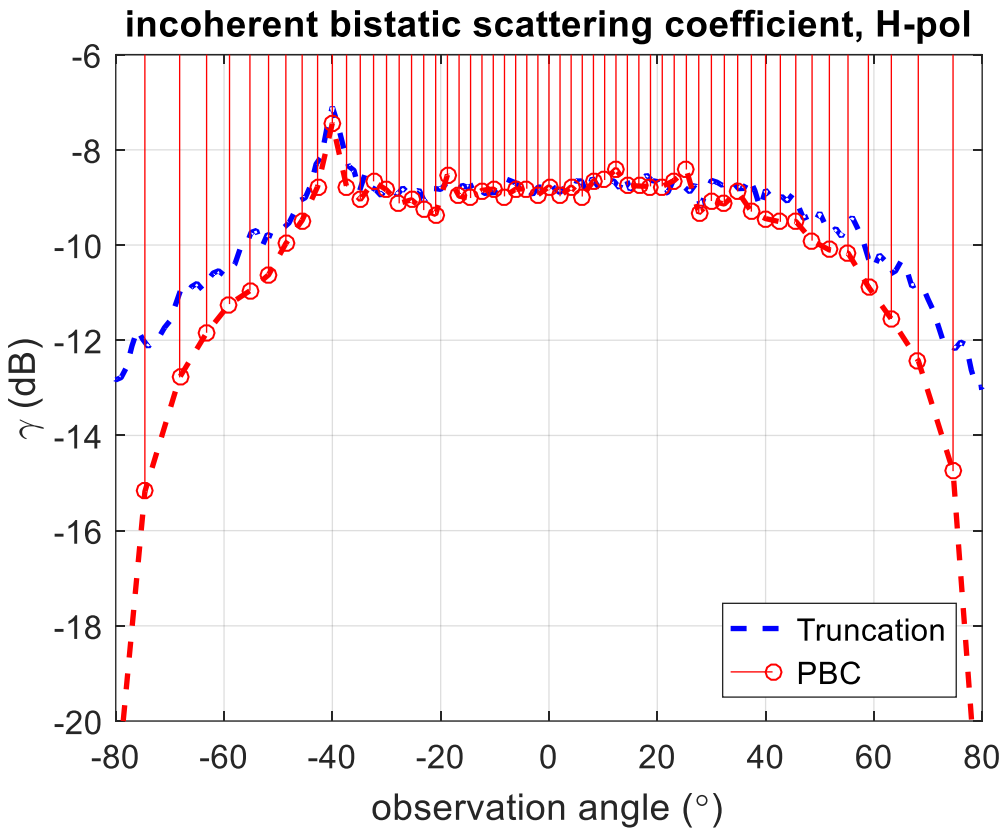

Figure III.16. Comparison of incoherent bistatic scattering coefficients with and without periodic boundary conditions.

The energy conservation as demonstrated by the previous example is perfect: it has a reflectivity $r = 0.3559$, absorptivity $a = 0.0161$, and transmissivity $t = 0.6295$, adding up to $r + a + t = 1.0015$, and thus the energy is conserved to the precision of less than 0.2%. Numerical tests with snow depth up to 30cm show that stable results for backscatter and brightness temperature are obtained for the period $P \geq 10\lambda$, quite robust to the thickness of the snow layer. Tests also show that convergence is achieved for Monte Carlo simulation of ~100 realizations.

To illustrate the results of brightness temperature, we simulate a case of thermal emission from a layer of ice on top of dielectric half-space. The ground has permittivity $(5 + i0.5)\varepsilon_0$ and temperature of 273.15K. The ice has permittivity $(3.2 + 0.001i)\varepsilon_0$ and temperature of 260K. The thickness of the ice layer is 5cm. We also truncate the horizontal domain at 5cm applying periodic boundary conditions. The brightness temperature at Ku band of 17.2GHz is calculated as a function of the observation angle and compared with the analytical results of layered medium emission, Figure III.17. The results are in good agreement, and the oscillation of the brightness temperature as a function of angle confirms the coherent layer effects. The discretization for the calculation is 1.0mm. Using a finer discretization would further improve the agreements.

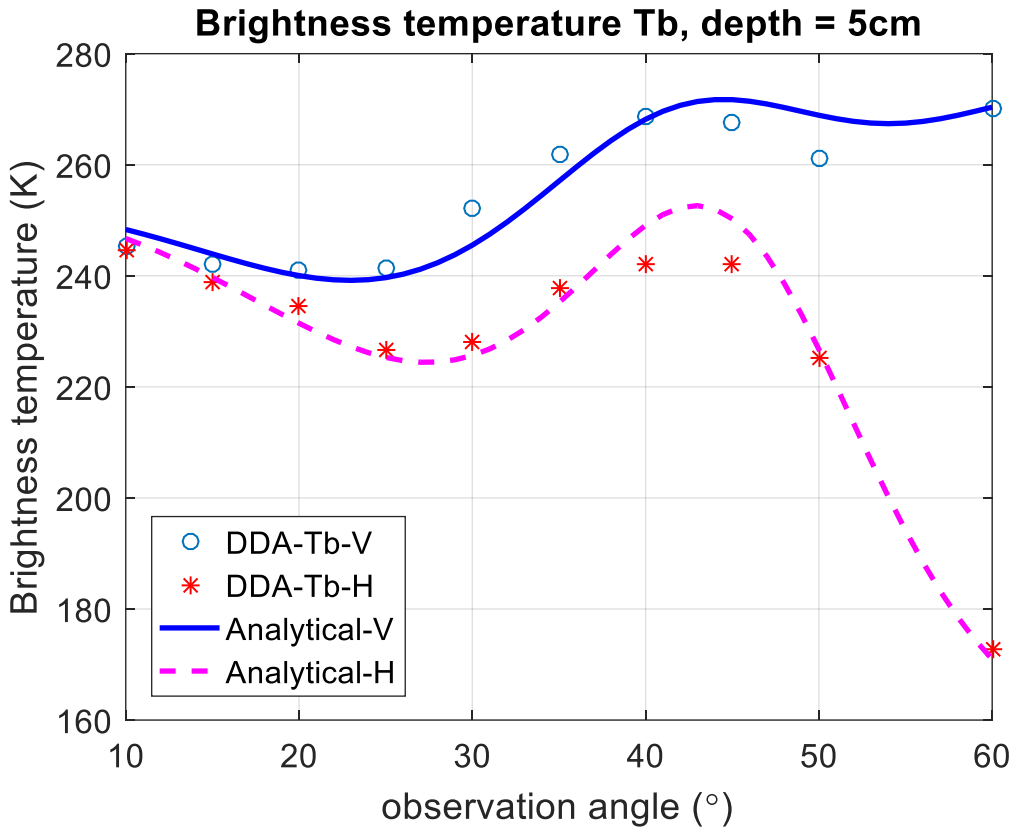

Figure III.17. Brightness temperature simulation of a layer of ice on dielectric ground

3.5 Plane wave excitation of an infinite 3D snow layer emulated by periodic boundary conditions

In this section, we move on to the 3D case considering a plane wave impinging upon an infinite snow layer emulated by periodic boundary conditions. Again, the 3D scenario is parallel to its 2D counterpart in concepts but much more involved in math. Not only we need to apply the periodic boundary conditions in both $\hat{x}$ and $\hat{y}$ direction, the Green's function takes a form of a dyad rather than a scalar. We're going to apply the Ewald summation method in dealing with the 3D dyadic Green's function with 2D periodicity. In 3D the full wave simulation results can be compared to the partially coherent approach of DMRT to examine the limitation of the DMRT theory.

3.5.1 The volume integral equation in 3D with periodic boundary condition

In analog to 2D case, we start from the 3D volume integral equation applied to an infinite snow layer,

$$\bar{E}\left(\bar{r}\right) = \bar{E}_{inc}\left(\bar{r}\right) + k^2 \int d\bar{r}' \bar{\bar{G}}\left(\bar{r},\bar{r}'\right)\left(\varepsilon_r\left(\bar{r}'\right) - 1\right)\bar{E}\left(\bar{r}'\right) \tag{3.299}$$

Applying the Bloch wave condition on a periodic structure,

$$\bar{E}\left(\bar{r} + \bar{\rho}_{pq}\right) = \bar{E}\left(\bar{r}\right)\exp\left(i\bar{k}_{i\rho} \cdot \bar{\rho}_{pq}\right) \tag{3.300}$$

where

$$\bar{\rho}_{pq} = p\bar{a}_1 + q\bar{a}_2 \tag{3.301}$$

where p, and q are integers, and $\bar{a}_1$ and $\bar{a}_2$ are lattice vectors (period) in the horizontal plane. We choose $\bar{a}_1 = \hat{x}L_x$ and $\bar{a}_2 = \hat{y}L_y$, but they can be more general vectors. With the periodicity

$$\varepsilon_r\left(\bar{r}' + \bar{\rho}_{pq}\right) = \varepsilon_r\left(\bar{r}'\right) \tag{3.302}$$

we can readily convert the integral domain to one period,

$$\bar{E}(\bar{r}) = \bar{E}_{inc}(\bar{r}) + k^2 \int_{\Omega_0} d\bar{r}' \bar{\bar{G}}_P(\bar{r}, \bar{r}'; \bar{k}_{i\rho}) (\varepsilon_r(\bar{r}') - 1) \bar{E}(\bar{r}') \tag{3.303}$$

where Ω_0 denotes one period. The period centered at origin can be defined as $-\frac{L_x}{2} < x < \frac{L_x}{2}$, $-\frac{L_y}{2} < x < \frac{L_y}{2}$, where L_x and L_y are the two horizontal dimensions of the finite snow volume along x and y, respectively.

$$\bar{\bar{G}}_P(\bar{r}, \bar{r}'; \bar{k}_{i\rho}) = \sum_{p,q} \bar{\bar{G}}(\bar{r}, \bar{r}' + \bar{\rho}_{pq}) \exp(i\bar{k}_{i\rho} \cdot \bar{\rho}_{pq}) \tag{3.304}$$

Equation (3.303) is the volume integral equation in 3D with periodic boundary conditions in the two horizontal directions.

3.5.2 The discrete dipole approximation with periodic Green's function

In a half space configuration, $\bar{\bar{G}} = \bar{\bar{G}}_0 + \bar{\bar{G}}_R$ as in section 3.3. With periodic boundary conditions, we decompose $\bar{\bar{G}}_P$ into the free space response $\bar{\bar{G}}_P^0$ and the reflection contribution $\bar{\bar{G}}_P^R$,

$$\bar{\bar{G}}_P(\bar{r}, \bar{r}'; \bar{k}_{i\rho}) = \bar{\bar{G}}_P^0(\bar{r}, \bar{r}'; \bar{k}_{i\rho}) + \bar{\bar{G}}_P^R(\bar{r}, \bar{r}'; \bar{k}_{i\rho}) \tag{3.305}$$

Singularity is only within $\bar{\bar{G}}_P^0$ when $\bar{r} - \bar{r}' = \bar{\rho}_{pq}$, and thus limited to $\bar{r} - \bar{r}' = 0$ within one unit cell. $\bar{\bar{G}}_P^0$ and $\bar{\bar{G}}_P^R$ have different translational symmetry,

$$\bar{\bar{G}}_P^0(\bar{r}, \bar{r}'; \bar{k}_{i\rho}) = \bar{\bar{G}}_P^0(\bar{r} - \bar{r}'; \bar{k}_{i\rho}) \tag{3.306}$$

$$\bar{\bar{G}}_P^R(\bar{r}, \bar{r}'; \bar{k}_{i\rho}) = \bar{\bar{G}}_P^R(\bar{\rho} - \bar{\rho}', z + z'; \bar{k}_{i\rho}) \tag{3.307}$$

We reorganize the volume integral equation,

$$\begin{aligned} \bar{E}(\bar{r}) = \bar{E}_{inc}(\bar{r}) &+ k^2 \int_{\Omega_0} d\bar{r}' \bar{\bar{G}}_P^0(\bar{r}, \bar{r}'; \bar{k}_{i\rho}) (\varepsilon_r(\bar{r}') - 1) \bar{E}(\bar{r}') \\ &+ k^2 \int_{\Omega_0} d\bar{r}' \bar{\bar{G}}_P^R(\bar{r}, \bar{r}'; \bar{k}_{i\rho}) (\varepsilon_r(\bar{r}') - 1) \bar{E}(\bar{r}') \end{aligned} \tag{3.308}$$

Discretizing the snow volume into small cubes with cube edge length d and volume $V_C^{(j)}$, where the superscript (j) denotes the j-th cube, and applying pulse basis function to represent $\bar{E}$, we can apply the discrete dipole approximation (DDA) to (3.308).

Let us define the singular integral over the self-cube $\bar{\bar{S}}$,

$$\bar{\bar{S}} = \int_{V_C^{(0)}} d\bar{r}' \bar{\bar{G}}_P^0 \left(0, \bar{r}'; \bar{k}_{i\rho}\right) \tag{3.309}$$

Also define the dipole moment $\bar{p}_i$,

$$\bar{p}_i = \Delta V \varepsilon \left(\varepsilon_r \left(\bar{r}_i\right) - 1\right) \bar{E}\left(\bar{r}_i\right) \tag{3.310}$$

And the polarizability $\bar{\bar{\alpha}}_i$ for each cube,

$$\bar{\bar{\alpha}}_i = \Delta V \varepsilon \left(\varepsilon_r \left(\bar{r}_i\right) - 1\right) \left(\bar{\bar{I}} - k^2 \left(\varepsilon_r \left(\bar{r}_i\right) - 1\right) \bar{\bar{S}}\right)^{-1} \tag{3.311}$$

Then we get the DDA equation

$$\bar{p}_i = \bar{\bar{\alpha}}_i \left[\bar{E}_{inc}\left(\bar{r}_i\right) + \frac{k^2}{\varepsilon} \sum_{j \neq i} \bar{\bar{G}}_P^0 \left(\bar{r}_i, \bar{r}_j; \bar{k}_{i\rho}\right) \bar{p}_j + \frac{k^2}{\varepsilon} \sum_j \bar{\bar{G}}_P^R \left(\bar{r}_i, \bar{r}_j; \bar{k}_{i\rho}\right) \bar{p}_j \right] \tag{3.312}$$

This is of exactly the same structure as what we obtained before with the half space Green's function without applying the periodic boundary condition. What left is to compute $\bar{\bar{G}}_P^0$, $\bar{\bar{G}}_P^R$, and $\bar{\bar{S}}$. The FFT acceleration technique still applies as the symmetry relation remain unchanged.

Let us first consider the evaluation of $\bar{\bar{S}}$ as defined in (3.309). We decompose $\bar{\bar{G}}_P^0$ into the free space response $\bar{\bar{G}}^0$ and the regularized response $\tilde{\bar{\bar{G}}}_P^0$,

$$\bar{\bar{G}}_P^0 \left(\bar{r}, \bar{r}'; \bar{k}_{i\rho}\right) = \bar{\bar{G}}^0 \left(\bar{r}, \bar{r}'\right) + \tilde{\bar{\bar{G}}}_P^0 \left(\bar{r}, \bar{r}'; \bar{k}_{i\rho}\right) \tag{3.313}$$

This also defines the regularized free space dyadic periodic Green's function $\tilde{\bar{\bar{G}}}_P^0$, which is of no singularity,

$$\bar{\bar{\tilde{G}}}_P^0\left(\bar{r},\bar{r}';\bar{k}_{i\rho}\right)=\bar{\bar{G}}_P^0\left(\bar{r},\bar{r}';\bar{k}_{i\rho}\right)-\bar{\bar{G}}^0\left(\bar{r},\bar{r}'\right) \tag{3.314}$$

Then

$$\bar{\bar{S}}=\int_{V_C^{(0)}}d\bar{r}'\bar{\bar{G}}^0\left(0,\bar{r}'\right)+\int_{V_C^{(0)}}d\bar{r}'\bar{\bar{\tilde{G}}}_P^0\left(0,\bar{r}';\bar{k}_{i\rho}\right) \tag{3.315}$$

The first term is already taken care of in Section 3.3.1 with the results restated as follows,

$$\int_{V_C^{(0)}}d\bar{r}'\bar{\bar{G}}^0\left(0,\bar{r}'\right)=\bar{\bar{I}}s_0 \tag{3.316}$$

$$s_0\approx-\frac{1}{3k^2}+\frac{1}{k^2}\frac{1}{4\pi}\left[\left(\frac{4\pi}{3}\right)^{1/3}k^2d^2+\frac{i2k^3d^3}{3}\right] \tag{3.317}$$

The second term, with a smooth integrand with no singularity,

$$\int_{V_C^{(0)}}d\bar{r}'\bar{\bar{\tilde{G}}}_P^0\left(0,\bar{r}';\bar{k}_{i\rho}\right)=\Delta V\bar{\bar{\tilde{G}}}_P^0\left(0,0;\bar{k}_{i\rho}\right) \tag{3.318}$$

The value of the regularized free space dyadic periodic Green's function at origin, is to be examined,

$$\bar{\bar{\tilde{G}}}_P^0\left(0,0;\bar{k}_{i\rho}\right)=\lim_{\bar{r}\to 0}\bar{\bar{\tilde{G}}}_P^0\left(\bar{r};\bar{k}_{i\rho}\right) \tag{3.319}$$

The results is a symmetric 3×3 matrix that is not scalar proportional to $\bar{\bar{I}}$. Thus

$$\bar{\bar{S}}=\bar{\bar{I}}s_0+\Delta V\bar{\bar{\tilde{G}}}_P^0\left(0,0;\bar{k}_{i\rho}\right) \tag{3.320}$$

3.5.3 Computing the 3D scalar periodic Green's function in free space

(a) Spatial and spectral domain representation

The 3D scalar free space Green's function

$$g\left(\bar{r},\bar{r}'\right)=\frac{\exp\left(ik\left|\bar{r}-\bar{r}'\right|\right)}{4\pi\left|\bar{r}-\bar{r}'\right|} \tag{3.321}$$

The periodic scalar Green's function in 3D space with 2D periodic lattice, in spatial domain

$$g_P\left(\bar{r},\bar{r}';\bar{k}_i\right)=\sum_{p,q}\frac{\exp\left(ik\left|\bar{r}-\bar{r}'-\bar{\rho}_{pq}\right|\right)}{4\pi\left|\bar{r}-\bar{r}'-\bar{\rho}_{pq}\right|}\exp\left(i\bar{k}_{i\rho}\cdot\bar{\rho}_{pq}\right) \tag{3.322}$$

where $\bar{\rho}_{pq}=p\bar{a}_1+q\bar{a}_2$, and $\bar{a}_1$ and $\bar{a}_2$ are the lattice vectors.

The spectral domain representation can be derived from the Poisson summation, which states

$$\sum_{p,q}f\left(\bar{r}-\bar{\rho}_{pq}\right)\exp\left(i\bar{k}_{i\rho}\cdot\bar{\rho}_{pq}\right)=\frac{1}{\Omega}\sum_{m,n}F\left(\bar{k}_{i\rho}+\bar{K}_{mn}\right)\exp\left(i\left(\bar{k}_{i\rho}+\bar{K}_{mn}\right)\cdot\bar{\rho}\right) \tag{3.323}$$

where

$$F\left(\bar{k}_\rho\right)=\int d\bar{\rho}\exp\left(-i\bar{k}_\rho\cdot\bar{\rho}\right)f\left(\bar{r}\right) \tag{3.324}$$

$$\bar{K}_{mn}=m\bar{b}_1+n\bar{b}_2 \tag{3.325}$$

$$\Omega=\left|\bar{a}_1\times\bar{a}_2\right| \tag{3.326}$$

and $\bar{b}_1$ and $\bar{b}_2$ are the reciprocal lattice vectors.

$$\bar{b}_1=\frac{2\pi}{\Omega}\left(\bar{a}_2\times\hat{z}\right) \tag{3.327}$$

$$\bar{b}_2=-\frac{2\pi}{\Omega}\left(\bar{a}_1\times\hat{z}\right) \tag{3.328}$$

Let

$$f\left(\bar{r}\right)=g\left(\bar{r}\right) \tag{3.329}$$

which satisfies the wave equation,

$$\left(\nabla^2+k^2\right)g\left(\bar{r}\right)=-\delta\left(\bar{r}\right)=-\delta\left(\bar{\rho}\right)\delta\left(z\right)$$

It is easy to show that

$$F\left(\bar{k}_\rho\right) = G\left(\bar{k}_\rho, z\right) = \frac{i}{2k_z}\exp\left(ik_z\left|z\right|\right) \tag{3.330}$$

Now with Poisson summation,

$$g_P\left(\bar{r},\bar{r}';\bar{k}_i\right) = \frac{1}{\Omega}\sum_{m,n}\frac{i}{2k_{z,mn}}\exp\left(ik_{z,mn}\left|z-z'\right|\right)\exp\left(i\bar{k}_{i,mn}\cdot\left(\bar{\rho}-\bar{\rho}'\right)\right) \tag{3.331}$$

where

$$\bar{k}_{i,mn} = \bar{k}_{i\rho} + \bar{K}_{mn} \tag{3.332}$$

$$k_{z,mn} = \sqrt{k^2 - k_{i,mn}^2} = \sqrt{k^2 - \left|\bar{k}_{i,mn}\right|^2} \tag{3.333}$$

Using a combined notation α for (m,n), then

$$g_P^0\left(\bar{r},\bar{r}';\bar{k}_i\right) = \frac{i}{2\Omega}\sum_{\alpha}\frac{1}{k_{z\alpha}}\exp\left(ik_{z\alpha}\left|z-z'\right|\right)\exp\left(i\bar{k}_{i\alpha}\cdot\left(\bar{\rho}-\bar{\rho}'\right)\right) \tag{3.334}$$

This is the spectral summation representation of g_P. Note that we have introduced the superscript 0 to denote the free space response. It follows straightforward that the surface reflection term, assuming the boundary is at $z = 0$, is

$$g_P^R\left(\bar{r},\bar{r}';\bar{k}_i\right) = \frac{i}{2\Omega}\sum_{\alpha}\frac{R\left(k_{i\alpha}\right)}{k_{z\alpha}}\exp\left(ik_{z\alpha}\left|z-z'\right|\right)\exp\left(i\bar{k}_{i\alpha}\cdot\left(\bar{\rho}-\bar{\rho}'\right)\right) \tag{3.335}$$

Equation (3.322) and (3.334) are the spatial and spectral domain representation of g_P^0, and (3.335) is the spectral domain representation of g_P^R.

(b) Ewald's Method to compute g_P^0

Note that the spatial domain summation in general converges slowly unless k is complex (lossy background media). The spectral domain summation converges slowly when $z \to z'$. We use Ewald summation technique [34] to improve the convergence of the series when $z \to z'$.

We start from the spatial domain summation (3.322), restated as follows,

$$g_P\left(\bar{r},\bar{k}_i\right)=\sum_{p,q} g\left(\bar{r}-\bar{\rho}_{pq}\right)\exp\left(i\bar{k}_{i\rho}\cdot\bar{\rho}_{pq}\right) \tag{3.336}$$

Realizing

$$g\left(\bar{r}\right)=\frac{\exp\left(ikr\right)}{4\pi r}=\frac{ik}{4\pi}h_0^{(1)}\left(kr\right) \tag{3.337}$$

where $h_0^{(1)}(\quad)$ is the first kind of spherical Hankel function of order 0. On the other hand, using integral representation, Eq. (3.4.5, 3.4.49) of [34], pp. 94,

$$h_0^{(1)}\left(kr\right)=\frac{1}{ik}\frac{2}{\sqrt{\pi}}\int_{0,C}^{\infty}ds\exp\left(\frac{k^2}{4s^2}-r^2s^2\right) \tag{3.338}$$

where C is the proper chosen contour path to ensure convergence both at $s\to 0$ and $s\to\infty$. Then

$$g_P\left(\bar{r},\bar{k}_i\right)=\frac{1}{4\pi}\sum_{p,q}\exp\left(i\bar{k}_{i\rho}\cdot\bar{\rho}_{pq}\right)\frac{2}{\sqrt{\pi}}\int_{0,C}^{\infty}ds\exp\left(\frac{k^2}{4s^2}-\left|\bar{r}-\bar{\rho}_{pq}\right|^2s^2\right) \tag{3.339}$$

The technique of Ewald summation is to split the integral into two part $(0,E)$ and (E,∞), where E is the splitting parameter,

$$g_P\left(\bar{r};\bar{k}_i\right)=g_1\left(\bar{r};\bar{k}_i\right)+g_2\left(\bar{r};\bar{k}_i\right) \tag{3.340}$$

$$g_1\left(\bar{r},\bar{k}_i\right)=\frac{1}{4\pi}\sum_{p,q}\exp\left(i\bar{k}_{i\rho}\cdot\bar{\rho}_{pq}\right)\frac{2}{\sqrt{\pi}}\int_{0,C}^{E}ds\exp\left(\frac{k^2}{4s^2}-\left|\bar{r}-\bar{\rho}_{pq}\right|^2s^2\right) \tag{3.341}$$

$$g_2\left(\bar{r},\bar{k}_i\right)=\frac{1}{4\pi}\sum_{p,q}\exp\left(i\bar{k}_{i\rho}\cdot\bar{\rho}_{pq}\right)\frac{2}{\sqrt{\pi}}\int_{E,C}^{\infty}ds\exp\left(\frac{k^2}{4s^2}-\left|\bar{r}-\bar{\rho}_{pq}\right|^2s^2\right) \tag{3.342}$$

(i) Calculation of $g_1\left(\bar{r};\bar{k}_i\right)$

We exchange the summation and integral,

$$g_1\left(\bar{r},\bar{k}_i\right)=\frac{1}{4\pi}\frac{2}{\sqrt{\pi}}\int_{0,C}^{E}ds\exp\left(\frac{k^2}{4s^2}-z^2s^2\right)\sum_{p,q}\exp\left(i\bar{k}_{i\rho}\cdot\bar{\rho}_{pq}\right)\exp\left(-\left|\bar{\rho}-\bar{\rho}_{pq}\right|^2s^2\right) \tag{3.343}$$

And again invoke the Poisson summation by finding

$$F\left(\bar{k}_\rho\right)=\int d\bar{\rho}\exp\left(-i\bar{k}_\rho\cdot\bar{\rho}\right)\exp\left(-\rho^2 s^2\right)=\frac{\pi}{s^2}\exp\left(-\frac{k_\rho^2}{4s^2}\right) \tag{3.344}$$

Thus

$$\sum_{p,q}\exp\left(i\bar{k}_{i\rho}\cdot\bar{\rho}_{pq}\right)\exp\left(-\left|\bar{\rho}-\bar{\rho}_{pq}\right|^2 s^2\right)=\frac{1}{\Omega}\sum_\alpha\frac{\pi}{s^2}\exp\left(-\frac{\left|\bar{k}_{i\alpha}\right|^2}{4s^2}\right)\exp\left(i\left(\bar{k}_{i\alpha}\right)\cdot\bar{\rho}\right) \tag{3.345}$$

where α denotes the combined index (m,n), and $\bar{k}_{i,mn}=\bar{k}_{i\rho}+\bar{K}_{mn}$ as given in (3.332).

Using (3.345) in (3.343), exchanging the summation and integration again, and realizing $k_{z,mn}=\sqrt{k^2-\left|\bar{k}_{i,mn}\right|^2}$ as given in (3.333), we have

$$g_1\left(\bar{r},\bar{k}_i\right)=\frac{1}{4\Omega}\sum_\alpha\exp\left(i\bar{k}_{i\alpha}\cdot\bar{\rho}\right)\frac{2}{\sqrt{\pi}}\int_{0,C}^{E}ds\,\frac{1}{s^2}\exp\left(\frac{k_{z\alpha}^2}{4s^2}-z^2s^2\right) \tag{3.346}$$

Let $\frac{1}{s}\rightarrow s$, then

$$g_1\left(\bar{r},\bar{k}_i\right)=\frac{1}{4\Omega}\sum_\alpha\exp\left(i\bar{k}_{i\alpha}\cdot\bar{\rho}\right)\frac{2}{\sqrt{\pi}}\int_{1/E,C}^{\infty}ds\exp\left(\frac{k_{z\alpha}^2s^2}{4}-\frac{z^2}{s^2}\right) \tag{3.347}$$

(ii) Represent $g_1\left(\bar{r};\bar{k}_i\right)$ in terms of complementary error function

The complementary error function

$$\operatorname{erfc}(z)=\frac{2}{\sqrt{\pi}}\int_z^\infty dw\exp\left(-w^2\right) \tag{3.348}$$

Now considering

$$\exp\left(\frac{k_{z\alpha}^2s^2}{4}-\frac{z^2}{s^2}\right)=\exp\left(-\left(\frac{-ik_{z\alpha}s}{2}+\frac{z}{s}\right)^2\right)\exp\left(-ik_{z\alpha}z\right) \tag{3.349}$$

And similarly

$$\exp\left(\frac{k_{z\alpha}^2 s^2}{4}-\frac{z^2}{s^2}\right)=\exp\left(-\left(\frac{-ik_{z\alpha}s}{2}-\frac{z}{s}\right)^2\right)\exp\left(ik_{z\alpha}z\right) \tag{3.350}$$

Note that

$$\frac{d}{ds}\left(\frac{-ik_{z\alpha}s}{2}+\frac{z}{s}\right)=\frac{-ik_{z\alpha}}{2}-\frac{z}{s^2} \tag{3.351}$$

$$\frac{d}{ds}\left(\frac{-ik_{z\alpha}s}{2}-\frac{z}{s}\right)=\frac{-ik_{z\alpha}}{2}+\frac{z}{s^2} \tag{3.352}$$

Thus

$$\exp\left(\frac{k_{z\alpha}^2 s^2}{4}-\frac{z^2}{s^2}\right)=\frac{1}{-ik_{z\alpha}}\left[\left(\frac{-ik_{z\alpha}}{2}-\frac{z}{s^2}\right)+\left(\frac{-ik_{z\alpha}}{2}+\frac{z}{s^2}\right)\right]\exp\left(\frac{k_{z\alpha}^2 s^2}{4}-\frac{z^2}{s^2}\right) \tag{3.353}$$

$$\begin{aligned}\exp\left(\frac{k_{z\alpha}^2 s^2}{4}-\frac{z^2}{s^2}\right)=&\frac{1}{-ik_{z\alpha}}\frac{d}{ds}\left(\frac{-ik_{z\alpha}s}{2}+\frac{z}{s}\right)\exp\left(-\left(\frac{-ik_{z\alpha}s}{2}+\frac{z}{s}\right)^2\right)\exp\left(-ik_{z\alpha}z\right)\\&+\frac{1}{-ik_{z\alpha}}\frac{d}{ds}\left(\frac{-ik_{z\alpha}s}{2}-\frac{z}{s}\right)\exp\left(-\left(\frac{-ik_{z\alpha}s}{2}-\frac{z}{s}\right)^2\right)\exp\left(ik_{z\alpha}z\right)\end{aligned} \tag{3.354}$$

And

$$\begin{aligned}g_1\left(\bar{r},\bar{r}',\bar{k}_i\right)=&\frac{i}{2\Omega}\sum_{\alpha}\exp\left(i\bar{k}_{i\alpha}\cdot\left(\bar{\rho}-\bar{\rho}'\right)\right)\frac{1}{k_{z\alpha}}\\&\times\frac{1}{2}\left[\exp\left(-ik_{z\alpha}\left|z-z'\right|\right)\operatorname{erfc}\left(\frac{-ik_{z\alpha}}{2E}+E\left|z-z'\right|\right)\right.\\&\left.+\exp\left(ik_{z\alpha}\left|z-z'\right|\right)\operatorname{erfc}\left(\frac{-ik_{z\alpha}}{2E}-E\left|z-z'\right|\right)\right]\end{aligned} \tag{3.355}$$

Notice that (3.355) is in direct analog to the spectral domain summation of (3.334).

(iii) Calculation of $g_2\left(\bar{r};\bar{k}_i\right)$, convert into complimentary error functions

Noticing the similarity between the term $\exp\left(\frac{k^2}{4s^2}-\left|\bar{r}-\bar{\rho}_{pq}\right|^2 s^2\right)$ and $\exp\left(\frac{k_{z\alpha}^2}{4}-\frac{z^2}{s^2}\right)$,

$$\exp\left(\frac{k^2}{4s^2}-\left|\bar{r}-\bar{\rho}_{pq}\right|^2 s^2\right)$$
$$=\frac{1}{2\left|\bar{r}-\bar{\rho}_{pq}\right|}\left[\frac{d}{ds}\left(\left|\bar{r}-\bar{\rho}_{pq}\right|s+\frac{ik}{2s}\right)\exp\left(-\left(\left|\bar{r}-\bar{\rho}_{pq}\right|s+\frac{ik}{2s}\right)^2\right)\exp\left(ik\left|\bar{r}-\bar{\rho}_{pq}\right|\right)\right] \quad (3.356)$$
$$+\frac{1}{2\left|\bar{r}-\bar{\rho}_{pq}\right|}\left[\frac{d}{ds}\left(\left|\bar{r}-\bar{\rho}_{pq}\right|s-\frac{ik}{2s}\right)\exp\left(-\left(\left|\bar{r}-\bar{\rho}_{pq}\right|s-\frac{ik}{2s}\right)^2\right)\exp\left(-ik\left|\bar{r}-\bar{\rho}_{pq}\right|\right)\right]$$

Then

$$g_2\left(\bar{r},\bar{r}';\bar{k}_i\right)=\sum_{pq}\frac{\exp\left(i\bar{k}_{i\rho}\cdot\bar{\rho}_{pq}\right)}{4\pi\left|\bar{r}-\bar{r}'-\bar{\rho}_{pq}\right|} \times\mathrm{Re}\left[\exp\left(ik\left|\bar{r}-\bar{r}'-\bar{\rho}_{pq}\right|\right)\mathrm{erfc}\left(\left|\bar{r}-\bar{r}'-\bar{\rho}_{pq}\right|E+\frac{ik}{2E}\right)\right] \quad (3.357)$$

Notice that (3.357) is in direct analog to the spatial domain summation of (3.322).

(iv) The complementary error function with complex arguments

We will need to evaluate (3.355) and (3.357) which involves the complementary error functions with complex arguments. We summarize the relations between commonly used error functions.

The error function erf( )

$$\mathrm{erf}\left(z\right)=\frac{2}{\sqrt{\pi}}\int_0^z dw\exp\left(-w^2\right) \quad (3.358)$$

The complementary error function erfc( )

$$\mathrm{erfc}\left(z\right)=\frac{2}{\sqrt{\pi}}\int_z^\infty dw\exp\left(-w^2\right) \quad (3.359)$$

$$\mathrm{erfc}\left(z\right)=1-\mathrm{erf}\left(z\right) \quad (3.360)$$

The scaled complementary error function erfcx( )

$$\mathrm{erfcx}\left(z\right)=\exp\left(z^2\right)\mathrm{erfc}\left(z\right) \quad (3.361)$$

The imaginary error function erfi( )

$$\mathrm{erfi}(x) = -i\mathrm{erf}\,(ix) = \frac{2}{\sqrt{\pi}}\int_0^x dt\exp\left(t^2\right) = \frac{2}{\sqrt{\pi}}\exp\left(x^2\right)D(x) \tag{3.362}$$

$$\mathrm{erf}\,(ix) = i\mathrm{erfi}(x) \tag{3.363}$$

$$\mathrm{erf}\,(-ix) = -\mathrm{erf}\,(ix) \tag{3.364}$$

$$\mathrm{erfi}(-x) = -\mathrm{erfi}(x) \tag{3.365}$$

The Dawson function $D(\ \ )$

$$D(x) = \frac{\sqrt{\pi}}{2}\exp\left(-x^2\right)\mathrm{erfi}(x) \tag{3.366}$$

The Faddeeva function $w(\ \ )$

$$\begin{aligned} w(z) &= \mathrm{erfcx}(-iz) = \exp\left(-z^2\right)\mathrm{erfc}(-iz) \\ &= \exp\left(-z^2\right)\left[1-\mathrm{erf}\,(-iz)\right] \\ &= \exp\left(-z^2\right)\left[1+i\mathrm{erfi}(z)\right] \end{aligned} \tag{3.367}$$

$$\mathrm{erfc}(z) = \exp\left(-z^2\right)w(iz) \tag{3.368}$$

$$w(iz) = \exp\left(z^2\right)\mathrm{erfc}(z) = \mathrm{erfcx}(z) \tag{3.369}$$

Steven G. Johnson [141] provides an implementation of these functions in C/C++ that are portable to Matlab, http://ab-initio.mit.edu/wiki/index.php/Faddeeva_Package.

Matlab Symbolic Math Toolbox also provides implementations to these functions, for example: `double(erf(sym(1+1i)))` calculates $\mathrm{erf}(1+1i)$.

(v) Selection of the splitting parameter E

E_{opt} is chosen to balance the convergence rate of the spectral and spatial domain series. If E is increased beyond E_{opt} then successive terms in the spatial series of g_2 decay faster while successive terms in the spectral series of g_1 decay slower.

Asymptotically, the complementary error function, [121] pp. 298, (7.1.23)

$$\operatorname{erfc}(w) \to \frac{\exp\left(-w^2\right)}{\sqrt{\pi}w} \tag{3.370}$$

Thus we want to balance

$$\operatorname{erfc}\left(\frac{-ik_{z\alpha}}{2E} \pm E\left|z-z'\right|\right) \sim \operatorname{erfc}\left(\frac{\sqrt{\left|\bar{k}_{i\rho}+\bar{K}_{\alpha}\right|^2-k^2}}{2E}\right) \sim \operatorname{erfc}\left(\frac{\sqrt{\bar{K}_{\alpha}}}{2E}\right) \tag{3.371}$$

and

$$\operatorname{erfc}\left(\left|\bar{r}-\bar{r}'-\bar{\rho}_{pq}\right|E \pm \frac{ik}{2E}\right) \sim \operatorname{erfc}\left(\left|\bar{r}-\bar{r}'-\bar{\rho}_{pq}\right|E\right) \sim \operatorname{erfc}\left(\left|\bar{\rho}_{pq}\right|E\right) \tag{3.372}$$

Balancing the two parts,

$$\frac{\left|\bar{K}_{\alpha}\right|}{2E} \sim \left|\bar{\rho}_{pq}\right|E \Rightarrow E_{\text{opt}} \sim \sqrt{\frac{\left|\bar{K}_{\alpha}\right|}{2\left|\bar{\rho}_{pq}\right|}} = \sqrt{\frac{\left|m\bar{b}_1+n\bar{b}_2\right|}{2\left|p\bar{a}_1+q\bar{a}_2\right|}} \tag{3.373}$$

Take $|m| = |n| = |p| = |q|$,

$$E_{\text{opt}} \sim \sqrt{\frac{\left|\bar{b}_1 \pm \bar{b}_2\right|}{2\left|\bar{a}_1+\bar{a}_2\right|}} \tag{3.374}$$

Considering the definition of the reciprocal lattice vectors $\bar{b}_1$ and $\bar{b}_2$ as in (3.327) and (3.328), it follows that,

$$E_{\text{opt}} \sim \sqrt{\frac{\pi}{\Omega}\frac{\left|\bar{a}_2\times\hat{z}+\bar{a}_1\times\hat{z}\right|}{\left|\bar{a}_1+\bar{a}_2\right|}} = \sqrt{\frac{\pi}{\Omega}} \tag{3.375}$$

In the special case of rectangular lattice with $\bar{a}_1 = a_x\hat{x}$ and $\bar{a}_2 = a_y\hat{y}$,

$$E_{\text{opt}} = \sqrt{\frac{\pi}{a_x a_y}} \tag{3.376}$$

Note that E_{opt} has the unit of wavenumber k. In [142], it is pointed out that this choice of E_{opt} is only appropriate for small period with respect to wavelength. This is because for large period, $E_{\text{opt}} \ll k$, thus $\frac{k}{E} \gg 1$, so the imaginary part of the arguments in $\text{erfc}\left(\frac{-ik_{z\alpha}}{2E} \pm E\left|z-z'\right|\right)$ and $\text{erfc}\left(\left|\bar{r}-\bar{r}'-\bar{\rho}_{pq}\right|E \pm \frac{ik}{2E}\right)$ can be large for the first few terms. They are of different signs. Adding large numbers with opposite sign is subject to numerical errors. Thus E should be adjusted (larger than E_{opt}) in our application with large P/λ. We choose $E = \max\left(E_{\text{opt}}, \frac{k}{3}\right)$, and truncate the spatial series at $\max\left(\frac{3}{PE}, \frac{3k}{PE^2}\right)$, and truncate the spectral series at $(1+\sin\theta_{\text{inc}})\frac{P}{\lambda} + \frac{3PE}{\pi}$.

(c) Self-term singularity subtraction

Define the regularized periodic Green's function as

$$\tilde{g}_P\left(\bar{r};\bar{k}_i\right) = g_P\left(\bar{r};\bar{k}_i\right) - g\left(\bar{r}\right) \tag{3.377}$$

Then $\tilde{g}_P\left(\bar{r};\bar{k}_i\right)$ is smooth, well-behaved and non-singular. We are interested in evaluating

$$\begin{aligned}
\lim_{\bar{r}\to 0}\tilde{g}_P\left(\bar{r};\bar{k}_i\right) &= \lim_{\bar{r}\to 0}\left[g_P\left(\bar{r};\bar{k}_i\right) - g\left(\bar{r}\right)\right] \\
&= \lim_{\bar{r}\to 0}\left[g_1\left(\bar{r};\bar{k}_i\right) + g_2\left(\bar{r};\bar{k}_i\right) - g\left(\bar{r}\right)\right] \\
&= \lim_{\bar{r}\to 0} g_1\left(\bar{r};\bar{k}_i\right) + \lim_{\bar{r}\to 0}\left[g_2\left(\bar{r};\bar{k}_i\right) - g_2^{00}\left(\bar{r}_i\right)\right] \\
&\quad + \lim_{\bar{r}\to 0}\left[g_2^{00}\left(\bar{r}\right) - g\left(\bar{r}\right)\right]
\end{aligned} \tag{3.378}$$

where we have used g_2^{00} to denote the $(p,q) = (0,0)$ term in g_2. g_2^{00} is independent of $\bar{k}_i$.

We can show that

$$\lim_{\bar{r}\to 0} g_1\left(\bar{r};\bar{k}_i\right) = \frac{i}{2\Omega}\sum_{\alpha}\frac{1}{k_{z\alpha}}\text{erfc}\left(\frac{-ik_{z\alpha}}{2E}\right) \tag{3.379}$$

$$\begin{aligned}&\lim_{\bar{r}\to 0}\left[g_2\left(\bar{r};\bar{k}_i\right)-g_2^{00}\left(\bar{r};\bar{k}_i\right)\right]\\&=\sum_{(p,q)\neq(0,0)}\frac{\exp\left(i\bar{k}_{i\rho}\cdot\bar{\rho}_{pq}\right)}{4\pi\left|\bar{\rho}_{pq}\right|}\mathrm{Re}\left[\exp\left(ik\left|\bar{\rho}_{pq}\right|\right)\mathrm{erfc}\left(\left|\bar{\rho}_{pq}\right|E+\frac{ik}{2E}\right)\right]\end{aligned}\tag{3.380}$$

And

$$\lim_{\bar{r}\to 0}\left[g_2^{00}\left(\bar{r}\right)-g\left(\bar{r}\right)\right]=-\frac{1}{4\pi}\left[\frac{2}{\sqrt{\pi}}E\exp\left(\left(\frac{k}{2E}\right)^2\right)-k\mathrm{erfi}\left(\frac{k}{2E}\right)+ik\right]\tag{3.381}$$

3.5.4 The 3D periodic dyadic Green's function in free space

The periodic dyadic Green's function in free space is defined as follows,

$$\bar{\bar{G}}_P\left(\bar{r},\bar{r}';\bar{k}_i\right)=\sum_{p,q}\bar{\bar{G}}\left(\bar{r},\bar{r}'+\bar{\rho}_{pq}\right)\exp\left(i\bar{k}_{i\rho}\cdot\bar{\rho}_{pq}\right)\tag{3.382}$$

Considering

$$\bar{\bar{G}}\left(\bar{r},\bar{r}'\right)=\left(\bar{\bar{I}}+\frac{\nabla\nabla}{k^2}\right)g\left(\bar{r},\bar{r}'\right)\tag{3.383}$$

$$g\left(\bar{r},\bar{r}'\right)=\frac{\exp\left(ik\left|\bar{r}-\bar{r}'\right|\right)}{4\pi\left|\bar{r}-\bar{r}'\right|}\tag{3.384}$$

$$g_P\left(\bar{r},\bar{r}';\bar{k}_i\right)=\sum_{p,q}g\left(\bar{r},\bar{r}'+\bar{\rho}_{pq}\right)\exp\left(i\bar{k}_{i\rho}\cdot\bar{\rho}_{pq}\right)\tag{3.385}$$

It follows that

$$\begin{aligned}\bar{\bar{G}}_P\left(\bar{r},\bar{r}'\right)&=\left(\bar{\bar{I}}+\frac{\nabla\nabla}{k^2}\right)g_P\left(\bar{r},\bar{r}';\bar{k}_i\right)\\&=\bar{\bar{I}}g_P\left(\bar{r},\bar{r}';\bar{k}_i\right)+\frac{1}{k^2}\nabla\nabla g_P\left(\bar{r},\bar{r}';\bar{k}_i\right)\end{aligned}\tag{3.386}$$

We have already worked out the calculation of $g_P\left(\bar{r},\bar{r}';\bar{k}_i\right)$, and now we consider the calculation of $\frac{1}{k^2}\nabla\nabla g_P\left(\bar{r},\bar{r}';\bar{k}_i\right)$. Considering the translational invariance with respect to $\bar{r}-\bar{r}'$, let $\bar{r}'=0$, and consider $\frac{1}{k^2}\nabla\nabla g_P\left(\bar{r};\bar{k}_i\right)$.

(a) Ewald method of periodic dyadic Green's function in free space

Using Ewald method,

$$g_P\left(\bar{r};\bar{k}_i\right)=g_1\left(\bar{r};\bar{k}_i\right)+g_2\left(\bar{r};\bar{k}_i\right) \tag{3.387}$$

$$g_1\left(\bar{r};\bar{k}_i\right)=\frac{i}{4\Omega}\sum_{\alpha}\exp\left(i\bar{k}_{i\alpha}\cdot\bar{\rho}\right)\frac{1}{k_{z\alpha}}f_\alpha\left(z\right) \tag{3.388}$$

$$g_2\left(\bar{r};\bar{k}_i\right)=\frac{1}{8\pi}\sum_{p,q}\exp\left(i\bar{k}_{i\rho}\cdot\bar{\rho}_{pq}\right)\frac{h\left(\left|\bar{r}-\bar{\rho}_{pq}\right|\right)}{\left|\bar{r}-\bar{\rho}_{pq}\right|} \tag{3.389}$$

where

$$f_\alpha\left(z\right)=\exp\left(-ik_{z\alpha}z\right)\operatorname{erfc}\left(\frac{-ik_{z\alpha}}{2E}+Ez\right)+\exp\left(ik_{z\alpha}z\right)\operatorname{erfc}\left(\frac{-ik_{z\alpha}}{2E}-Ez\right) \tag{3.390}$$

$$h\left(r\right)=\exp\left(ikr\right)\operatorname{erfc}\left(rE+\frac{ik}{2E}\right)+\exp\left(-ikr\right)\operatorname{erfc}\left(rE-\frac{ik}{2E}\right) \tag{3.391}$$

Thus

$$\nabla\nabla g_P\left(\bar{r};\bar{k}_i\right)=\nabla\nabla g_1\left(\bar{r};\bar{k}_i\right)+\nabla\nabla g_2\left(\bar{r};\bar{k}_i\right) \tag{3.392}$$

(i) Calculation of $\nabla\nabla g_1\left(\bar{r};\bar{k}_i\right)$

We work out $\nabla\nabla g_1\left(\bar{r};\bar{k}_i\right)$ in Cartesian coordinate,

$$\nabla=\nabla_\perp+\hat{z}\frac{\partial}{\partial z} \tag{3.393}$$

$$\nabla\nabla = \left(\nabla_\perp + \hat{z}\frac{\partial}{\partial z}\right)\left(\nabla_\perp + \hat{z}\frac{\partial}{\partial z}\right) = \nabla_\perp\nabla_\perp + \nabla_\perp\hat{z}\frac{\partial}{\partial z} + \hat{z}\frac{\partial}{\partial z}\nabla_\perp + \hat{z}\hat{z}\frac{\partial^2}{\partial z^2} \tag{3.394}$$

Then

$$\nabla\nabla g_1\left(\bar{r};\bar{k}_i\right) = \frac{i}{4\Omega}\sum_\alpha \frac{\exp\left(i\bar{k}_{i\alpha}\cdot\bar{\rho}\right)}{k_{z\alpha}}\begin{bmatrix} -k_{x\alpha}^2 f_\alpha(z) & -k_{x\alpha}k_{y\alpha} f_\alpha(z) & ik_{x\alpha} f_\alpha'(z) \\ -k_{y\alpha}k_{x\alpha} f_\alpha(z) & -k_{y\alpha}^2 f_\alpha(z) & ik_{y\alpha} f_\alpha'(z) \\ ik_{x\alpha} f_\alpha'(z) & ik_{y\alpha} f_\alpha'(z) & f_\alpha''(z) \end{bmatrix} \tag{3.395}$$

Notice that $\nabla\nabla g_1\left(\bar{r};\bar{k}_i\right)$ is symmetric, and the parity of its elements with respect to z depends on $f_\alpha(z)$.

$$f_\alpha(-z) = f_\alpha(z) \tag{3.396}$$

$$f_\alpha'(-z) = -f_\alpha'(z) \tag{3.397}$$

$$f_\alpha''(-z) = f_\alpha''(z) \tag{3.398}$$

The explicit form of $f_\alpha'(z)$ and $f_\alpha''(z)$ are as follows,

$$\begin{aligned} f_\alpha'(z) = {} & \exp\left(-ik_{z\alpha}z\right)\left[-ik_{z\alpha}\operatorname{erfc}\left(\frac{-ik_{z\alpha}}{2E}+Ez\right) - \frac{2}{\sqrt{\pi}}E\exp\left(-\left(\frac{-ik_{z\alpha}}{2E}+Ez\right)^2\right)\right] \\ & + \exp\left(ik_{z\alpha}z\right)\left[ik_{z\alpha}\operatorname{erfc}\left(\frac{-ik_{z\alpha}}{2E}-Ez\right) + \frac{2}{\sqrt{\pi}}E\exp\left(-\left(\frac{-ik_{z\alpha}}{2E}-Ez\right)^2\right)\right] \end{aligned} \tag{3.399}$$

$$\begin{aligned} f_\alpha''(z) = {} & \exp\left(-ik_{z\alpha}z\right)\left[-k_{z\alpha}^2\operatorname{erfc}\left(\frac{-ik_{z\alpha}}{2E}+Ez\right) + \frac{4E^2}{\sqrt{\pi}}\left(\frac{-ik_{z\alpha}}{2E}-Ez\right)\exp\left(-\left(\frac{-ik_{z\alpha}}{2E}+Ez\right)^2\right)\right] \\ & + \exp\left(ik_{z\alpha}z\right)\left[-k_{z\alpha}^2\operatorname{erfc}\left(\frac{-ik_{z\alpha}}{2E}-Ez\right) - \frac{4E^2}{\sqrt{\pi}}\left(\frac{-ik_{z\alpha}}{2E}+Ez\right)\exp\left(-\left(\frac{-ik_{z\alpha}}{2E}-Ez\right)^2\right)\right] \end{aligned} \tag{3.400}$$

(ii) Calculation of $\nabla\nabla g_2\left(\bar{r};\bar{k}_i\right)$

In spherical coordinate,

$$\nabla \psi(r) = \hat{r} \frac{\partial \psi}{\partial r} \tag{3.401}$$

$$\nabla\nabla \psi(r) = \nabla \hat{r} \frac{\partial \psi}{\partial r} + \hat{r}\hat{r} \frac{\partial^2 \psi}{\partial r^2} = \frac{1}{r} \frac{\partial \psi}{\partial r} \bar{\bar{I}} + \hat{r}\hat{r} \left(\frac{\partial^2 \psi}{\partial r^2} - \frac{1}{r} \frac{\partial \psi}{\partial r} \right) \tag{3.402}$$

$$\nabla\nabla \frac{h(r)}{r} = \left(\frac{h'(r)}{r^2} - \frac{h(r)}{r^3} \right) \bar{\bar{I}} + \left(\frac{h''(r)}{r} - \frac{3h'(r)}{r^2} + \frac{3h(r)}{r^3} \right) \hat{r}\hat{r} \tag{3.403}$$

Thus

$$\nabla\nabla g_2(\bar{r}; \bar{k}_i) = \frac{1}{8\pi} \sum_{p,q} \exp\left(i\bar{k}_{i\rho} \cdot \bar{\rho}_{pq} \right) \nabla_{\bar{R}_{pq}} \nabla_{\bar{R}_{pq}} \frac{h(R_{pq})}{R_{pq}} \tag{3.404}$$

where

$$\bar{R}_{pq} = \bar{r} - \bar{\rho}_{pq} \tag{3.405}$$

$$R_{pq} = \left| \bar{r} - \bar{\rho}_{pq} \right| \tag{3.406}$$

$$\begin{aligned} \nabla_{\bar{R}_{pq}} \nabla_{\bar{R}_{pq}} \frac{h(R_{pq})}{R_{pq}} = & \left(\frac{h'(R_{pq})}{R_{pq}^2} - \frac{h(R_{pq})}{R_{pq}^3} \right) \bar{\bar{I}} \\ & + \left(\frac{h''(R_{pq})}{R_{pq}} - \frac{3h'(R_{pq})}{R_{pq}^2} + \frac{3h(R_{pq})}{R_{pq}^3} \right) \hat{R}_{pq} \hat{R}_{pq} \end{aligned} \tag{3.407}$$

$h'(r)$ and $h''(r)$ are given as follows,

$$h'(r) = 2\,\mathrm{Re}\left[\exp(ikr) \left[ik\,\mathrm{erfc}\left(rE + \frac{ik}{2E} \right) - \frac{2}{\sqrt{\pi}} E \exp\left(-\left(rE + \frac{ik}{2E} \right)^2 \right) \right] \right] \tag{3.408}$$

$$h''(r) = 2\,\mathrm{Re}\left[\exp(ikr) \left(-k^2\,\mathrm{erfc}\left(rE + \frac{ik}{2E} \right) + \exp\left(-\left(rE + \frac{ik}{2E} \right)^2 \right) \left(rE - \frac{ik}{2E} \right) \frac{4E^2}{\sqrt{\pi}} \right) \right] \tag{3.409}$$

(b) Regularization

The regularized dyadic Green's function is defined as

$$\begin{aligned}\tilde{\bar{\bar{G}}}_P\left(\bar{r};\bar{k}_i\right) &= \bar{\bar{G}}_P\left(\bar{r};\bar{k}_i\right) - \bar{\bar{G}}\left(\bar{r}\right) \\ &= \bar{\bar{I}}\left(g_P\left(\bar{r};\bar{k}_i\right) - g\left(\bar{r}\right)\right) + \frac{1}{k^2}\left(\nabla\nabla g_P\left(\bar{r};\bar{k}_i\right) - \nabla\nabla g\left(\bar{r}\right)\right) \\ &= \bar{\bar{I}}\tilde{g}_P\left(\bar{r};\bar{k}_i\right) + \frac{1}{k^2}\nabla\nabla\tilde{g}_P\left(\bar{r};\bar{k}_i\right)\end{aligned} \tag{3.410}$$

We have considered the evaluation of $\lim_{\bar{r}\to 0}\tilde{g}_P\left(\bar{r};\bar{k}_i\right)$, and now consider $\lim_{\bar{r}\to 0}\nabla\nabla\tilde{g}_P\left(\bar{r};\bar{k}_i\right)$

$$\begin{aligned}\lim_{\bar{r}\to 0}\nabla\nabla\tilde{g}_P\left(\bar{r};\bar{k}_i\right) &= \lim_{\bar{r}\to 0}\left[\nabla\nabla g_P\left(\bar{r};\bar{k}_i\right) - \nabla\nabla g\left(\bar{r}\right)\right] \\ &= \lim_{\bar{r}\to 0}\nabla\nabla g_1\left(\bar{r};\bar{k}_i\right) + \lim_{\bar{r}\to 0}\left[\nabla\nabla g_2\left(\bar{r};\bar{k}_i\right) - \nabla\nabla g\left(\bar{r}\right)\right] \\ &= \nabla\nabla g_1\left(0;\bar{k}_i\right) + \sum_{(p,q)\neq(0,0)}\nabla\nabla g_2^{(p,q)}\left(0;\bar{k}_i\right) \\ &\quad + \lim_{\bar{r}\to 0}\left[\nabla\nabla g_2^{(0,0)}\left(\bar{r}\right) - \nabla\nabla g\left(\bar{r}\right)\right]\end{aligned} \tag{3.411}$$

where $\nabla\nabla g_2^{(p,q)}\left(\bar{r};\bar{k}_i\right)$ denotes the (p,q)-th term in the spatial series of g_2.

One can show that

$$\begin{aligned}\lim_{\bar{r}\to 0}\left[\nabla\nabla g_2^{(0,0)}\left(\bar{r}\right) - \nabla\nabla g\left(\bar{r}\right)\right] &= \frac{1}{8\pi}\lim_{\bar{r}\to 0}\left[\nabla\nabla\frac{h(r) - 2\exp(ikr)}{r}\right] \\ &= \frac{1}{24\pi}\left[h'''(0) + 2ik^3\right]\bar{\bar{I}}\end{aligned} \tag{3.412}$$

where

$$\begin{aligned}h'''(r) &= 2\,\mathrm{Re}\left[\exp(ikr)\left[ik\left(-k^2\,\mathrm{erfc}\left(rE + \frac{ik}{2E}\right)\right)\right]\right] \\ &\quad + 2\,\mathrm{Re}\left[\exp(ikr)\left[\exp\left(-\left(rE + \frac{ik}{2E}\right)^2\right)\left(2ikrE^2 + k^2 - 4r^2E^4 + 2E^2\right)\frac{2}{\sqrt{\pi}}E\right]\right]\end{aligned} \tag{3.413}$$

Thus

$$h'''(0) = -k^2 h'(0) + \frac{8E^3}{\sqrt{\pi}} \exp\left(\left(\frac{k}{2E}\right)^2\right) \tag{3.414}$$

where

$$h'(0) = 2\left[k\text{erfi}\left(\frac{k}{2E}\right) - \frac{2}{\sqrt{\pi}} E \exp\left(\left(\frac{k}{2E}\right)^2\right)\right] \tag{3.415}$$

One can also show that

$$h(0) = 2 \tag{3.416}$$

$$h''(0) = -2k^2 \tag{3.417}$$

On the other hand,

$$\nabla\nabla g_1\left(0;\bar{k}_i\right) = \frac{i}{4\Omega}\sum_\alpha \frac{1}{k_{z\alpha}} \begin{bmatrix} -k_{x\alpha}^2 f_\alpha(0) & -k_{x\alpha}k_{y\alpha} f_\alpha(0) & ik_{x\alpha} f_\alpha'(0) \\ -k_{y\alpha}k_{x\alpha} f_\alpha(0) & -k_{y\alpha}^2 f_\alpha(0) & ik_{y\alpha} f_\alpha'(0) \\ ik_{x\alpha} f_\alpha'(0) & ik_{y\alpha} f_\alpha'(0) & f_\alpha''(0) \end{bmatrix} \tag{3.418}$$

where

$$f_\alpha(0) = 2\text{erfc}\left(-\frac{ik_{z\alpha}}{2E}\right) \tag{3.419}$$

$$f_\alpha'(0) = 0 \tag{3.420}$$

$$f_\alpha''(0) = 2\left[-k_{z\alpha}^2 \text{erfc}\left(\frac{-ik_{z\alpha}}{2E}\right) + \frac{2E}{\sqrt{\pi}}\left(ik_{z\alpha}\right)\exp\left(-\left(\frac{-ik_{z\alpha}}{2E}\right)^2\right)\right] \tag{3.421}$$

Using $f_\alpha(0)$ and $h'(0)$, we can rewrite (3.379) and (3.381) as follows,

$$\lim_{\bar{r}\to 0} g_1\left(\bar{r};\bar{k}_i\right) = \frac{i}{4\Omega}\sum_\alpha \frac{1}{k_{z\alpha}} f_\alpha(0) \tag{3.422}$$

$$\lim_{\bar{r}\to 0}\left[g_2^{00}\left(\bar{r}\right) - g\left(\bar{r}\right)\right] = \frac{1}{8\pi}\left[h'(0) - 2ik\right] \tag{3.423}$$

These results compare well with [143].

3.5.5 The 3D periodic dyadic Green's function in half space

Using the spectral domain representation of g_P, we can put down the free space periodic dyadic Green's function as follows,

$$\bar{\bar{G}}_P^0\left(\bar{r},\bar{r}';\bar{k}_i\right)=\begin{cases}\dfrac{i}{2\Omega}\displaystyle\sum_\alpha\frac{1}{k_{z\alpha}}\left[\bar{\bar{I}}-\frac{\bar{k}_\alpha\bar{k}_\alpha}{k^2}\right]\exp\left(i\bar{k}_\alpha\cdot\left(\bar{r}-\bar{r}'\right)\right) & z-z'>0\\ \dfrac{i}{2\Omega}\displaystyle\sum_\alpha\frac{1}{k_{z\alpha}}\left[\bar{\bar{I}}-\frac{\bar{K}_\alpha\bar{K}_\alpha}{k^2}\right]\exp\left(i\bar{K}_\alpha\cdot\left(\bar{r}-\bar{r}'\right)\right) & z-z'<0\end{cases} \tag{3.424}$$

where

$$\bar{k}_\alpha=\bar{k}_{i\alpha}+\hat{z}k_{z\alpha} \tag{3.425}$$

$$\bar{K}_\alpha=\bar{k}_{i\alpha}-\hat{z}k_{z\alpha} \tag{3.426}$$

Using the polarization vectors $\hat{e}_\alpha$ and $\hat{h}_\alpha$ that forms a triplet with $\hat{k}_\alpha=\hat{h}_\alpha\times\hat{e}_\alpha$,

$$\hat{e}_\alpha\left(k_{z\alpha}\right)=\hat{e}_\alpha\left(-k_{z\alpha}\right)=\frac{1}{k_{\rho\alpha}}\left(k_{y\alpha}\hat{x}-k_{x\alpha}\hat{y}\right) \tag{3.427}$$

$$\hat{h}_\alpha\left(k_{z\alpha}\right)=-\frac{k_{z\alpha}}{kk_{\rho\alpha}}\left(k_{z\alpha}\hat{x}+k_{y\alpha}\hat{y}\right)+\frac{k_{\rho\alpha}}{k}\hat{z} \tag{3.428}$$

$$\hat{h}_\alpha\left(-k_{z\alpha}\right)=\frac{k_{z\alpha}}{kk_{\rho\alpha}}\left(k_{z\alpha}\hat{x}+k_{y\alpha}\hat{y}\right)+\frac{k_{\rho\alpha}}{k}\hat{z} \tag{3.429}$$

We have

$$\bar{\bar{G}}_P^0\left(\bar{r},\bar{r}';\bar{k}_i\right)$$
$$=\begin{cases}\dfrac{i}{2\Omega}\sum\limits_\alpha\dfrac{1}{k_{z\alpha}}\left[\hat{e}_\alpha\left(k_{z\alpha}\right)\hat{e}_\alpha\left(k_{z\alpha}\right)+\hat{h}_\alpha\left(k_{z\alpha}\right)\hat{h}_\alpha\left(k_{z\alpha}\right)\right]\exp\left(i\bar{k}_\alpha\cdot\left(\bar{r}-\bar{r}'\right)\right) & z-z'>0\\ \dfrac{i}{2\Omega}\sum\limits_\alpha\dfrac{1}{k_{z\alpha}}\left[\hat{e}_\alpha\left(-k_{z\alpha}\right)\hat{e}_\alpha\left(-k_{z\alpha}\right)+\hat{h}_\alpha\left(-k_{z\alpha}\right)\hat{h}_\alpha\left(-k_{z\alpha}\right)\right]\exp\left(i\bar{K}_\alpha\cdot\left(\bar{r}-\bar{r}'\right)\right) & z-z'<0\end{cases}$$

(3.430)

We immediately get the reflection contribution $\bar{\bar{G}}_P^R\left(\bar{r},\bar{r}';\bar{k}_i\right)$, assuming boundary at $z=0$, and the field point $z\geq 0$, and the source point $z'\geq 0$,

$$\bar{\bar{G}}_P^R\left(\bar{r},\bar{r}';\bar{k}_i\right)=\frac{i}{2\Omega}\sum_\alpha\frac{\exp\left(i\bar{k}_\alpha\cdot\bar{r}\right)\exp\left(-i\bar{K}_\alpha\cdot\bar{r}'\right)}{k_{z\alpha}}\times\left[R^{\mathrm{TE}}\hat{e}_\alpha\left(k_{z\alpha}\right)\hat{e}_\alpha\left(-k_{z\alpha}\right)+R^{\mathrm{TM}}\hat{h}_\alpha\left(k_{z\alpha}\right)\hat{h}_\alpha\left(-k_{z\alpha}\right)\right] \tag{3.431}$$

Realizing

$$\exp\left(i\bar{k}_\alpha\cdot\bar{r}\right)\exp\left(-i\bar{K}_\alpha\cdot\bar{r}'\right)=\exp\left(i\bar{k}_{i\alpha}\cdot\left(\bar{\rho}-\bar{\rho}\right)\right)\exp\left(ik_{z\alpha}\left(z+z'\right)\right) \tag{3.432}$$

It follows the translational invariance relation of $\bar{\bar{G}}_P^R\left(\bar{r},\bar{r}';\bar{k}_i\right)$

$$\bar{\bar{G}}_P^R\left(\bar{r},\bar{r}';\bar{k}_i\right)=\bar{\bar{G}}_P^R\left(\bar{\rho}-\bar{\rho},z+z';\bar{k}_i\right) \tag{3.433}$$

It is inspiring when comparing (3.430) and (3.431) with the point source response without periodic repeating,

$$\bar{\bar{G}}^0\left(\bar{r},\bar{r}'\right)=\begin{cases}\dfrac{i}{8\pi^2}\iint dk_x dk_y\,\dfrac{1}{k_z}\left[\hat{e}\left(k_z\right)\hat{e}\left(k_z\right)+\hat{h}\left(k_z\right)\hat{h}\left(k_z\right)\right]\exp\left(i\bar{k}\cdot\left(\bar{r}-\bar{r}'\right)\right) & z-z'>0\\ \dfrac{i}{8\pi^2}\iint dk_x dk_y\,\dfrac{1}{k_z}\left[\hat{e}\left(-k_z\right)\hat{e}\left(-k_z\right)+\hat{h}\left(-k_z\right)\hat{h}\left(-k_z\right)\right]\exp\left(i\bar{K}\cdot\left(\bar{r}-\bar{r}'\right)\right) & z-z'<0\end{cases}$$

(3.434)

$$\bar{\bar{G}}^R\left(\bar{r},\bar{r}'\right)=\frac{i}{8\pi^2}\iint dk_x dk_y\,\frac{\exp\left(i\bar{k}\cdot\bar{r}\right)\exp\left(-i\bar{K}\cdot\bar{r}'\right)}{k_z}\times\left[R^{\mathrm{TE}}\hat{e}\left(k_z\right)\hat{e}\left(-k_z\right)+R^{\mathrm{TM}}\hat{h}\left(k_z\right)\hat{h}\left(-k_z\right)\right] \tag{3.435}$$

It is encouraging to notice the balance of coefficients considering (take rectangular lattice for example),

$$\frac{i}{2\Omega}\Delta\alpha=\frac{i}{2a_x a_y}\Delta m\Delta n=\frac{i}{2a_x a_y}\left(\frac{a_x}{2\pi}\Delta k_x\right)\left(\frac{a_y}{2\pi}\Delta k_y\right)=\frac{i}{8\pi^2}\Delta k_x\Delta k_y \tag{3.436}$$

An alternative way to derive (3.430) and (3.431) is by substituting (3.434) and (3.435) into (3.304) directly.

The summation for $\bar{\bar{G}}_P^R\left(\bar{r},\bar{r}';\bar{k}_i\right)$ in spectral domain is easier to handle than the continuous integration in $\bar{\bar{G}}^R\left(\bar{r},\bar{r}'\right)$ with a single point source. The complexity increases when $z+z'\to 0$ due to the increasing terms to be included in the series. We're less troubled by this difficulty in DDA since $z+z'\geq d$, where d is the finite discretization size.

3.5.6 The scattering field and the bistatic scattering coefficients

(a) The scattering field

Substituting the spectral domain representation of $\bar{\bar{G}}_P^0$ in (3.430) with $z\gg z'$ in the far field and $\bar{\bar{G}}_P^R$ in (3.431) into (3.308) to identify the scattering field $\bar{E}_s(\bar{r})$,

$$\bar{E}_s\left(\bar{r}\right)=\sum_s\exp\left(i\bar{k}_\alpha\cdot\bar{r}\right)\bar{B}_\alpha \tag{3.437}$$

where

$$\bar{B}_\alpha = \frac{k^2}{\varepsilon}\frac{i}{2\Omega}\frac{1}{k_{z\alpha}}$$
$$\times\left[\left[\hat{e}_\alpha\left(k_{z\alpha}\right)\hat{e}_\alpha\left(k_{z\alpha}\right)+\hat{h}_\alpha\left(k_{z\alpha}\right)\hat{h}_\alpha\left(k_{z\alpha}\right)\right]\cdot\sum_j \exp\left(-i\bar{k}_\alpha\cdot\bar{r}_j\right)\bar{p}_j\right.$$
$$\left.+\left[R^{\mathrm{TE}}\left(k_{z\alpha}\right)\hat{e}_\alpha\left(k_{z\alpha}\right)\hat{e}_\alpha\left(-k_{z\alpha}\right)+R^{\mathrm{TM}}\left(k_{z\alpha}\right)\hat{h}_\alpha\left(k_{z\alpha}\right)\hat{h}_\alpha\left(-k_{z\alpha}\right)\right]\cdot\sum_j \exp\left(-i\bar{K}_\alpha\cdot\bar{r}_j\right)\bar{p}_j\right] \tag{3.438}$$

$\bar{B}_\alpha$ plays the same role as the scattering amplitude $\bar{f}$ in the case of a single scatterer. We call $\bar{B}_\alpha$ the discretized scattering amplitudes arising from periodic scatterers.

Similar to our discussion in section 3.4.4, we should consider the reflected field of the directed incidence wave from the half-space as scattered wave. Thus the corrected discrete scattering amplitudes $\bar{\bar{B}}_\alpha$.

$$\bar{\bar{B}}_\alpha = \bar{B}_\alpha + \delta_{\alpha 0}\left[R^{\mathrm{TE}}\left(k_{z0}\right)\hat{e}_\alpha\left(k_{z0}\right)\hat{e}_\alpha\left(-k_{z0}\right)+R^{\mathrm{TM}}\left(k_{z0}\right)\hat{h}_\alpha\left(k_{z0}\right)\hat{h}_\alpha\left(-k_{z0}\right)\right]\cdot\hat{q}_i \tag{3.439}$$

where $\hat{q}_i$ denotes the polarization of the incidence wave, which in general is a linear combination of $\hat{e}(-k_{iz})$ and $\hat{h}(-k_{iz})$,

$$\hat{q}_i = \alpha\hat{e}\left(-k_{iz}\right)+\beta\hat{h}\left(-k_{iz}\right) \tag{3.440}$$

Then

$$\bar{E}_s\left(\bar{r}\right) = \sum_s \exp\left(i\bar{k}_\alpha\cdot\bar{r}\right)\bar{\bar{B}}_\alpha \tag{3.441}$$

(b) The scattering power, the reflectivity and the bistatic scattering coefficients

The scattered power per unit cell can be calculated by

$$P_s = \int_\Omega d\bar{\rho}\hat{z}\cdot\bar{S}_s = \frac{1}{2}\int_\Omega d\bar{\rho}\hat{z}\cdot\mathrm{Re}\left[\bar{E}_s\times\bar{H}_s^*\right] \tag{3.442}$$

where Ω is the unit cell area.

Substituting (3.441) into (3.442) and using Faraday's law to represent $\bar{H}_s$, after some mathematical manipulation,

$$P_s = \frac{1}{2}\frac{1}{\omega\mu}\Omega\sum_{\alpha}\exp\left(-2k''_{z\alpha}z\right)k'_{z\alpha}\left|\tilde{\bar{B}}_{\alpha}\right|^2 \tag{3.443}$$

For scattering far field, only the propagating wave contributes. For real background media,

$$P_s = \frac{1}{2}\frac{1}{\omega\mu}\Omega\sum_{\text{propagating}}k_{z\alpha}\left|\tilde{\bar{B}}_{\alpha}\right|^2 \tag{3.444}$$

Considering the incidence power per lattice cell,

$$P_{\text{inc}} = \frac{1}{2\eta}\Omega\cos\theta_{\text{inc}} \tag{3.445}$$

we get the reflectivity r,

$$r = \frac{P_s}{P_{\text{inc}}} = \frac{1}{k_{iz}}\sum_{\alpha}\text{Re}\left[k_{z\alpha}\right]\left|\tilde{\bar{B}}_{\alpha}\right|^2 \tag{3.446}$$

The bistatic scattering coefficients $\gamma(\theta,\phi)$ are defined such that

$$r = \frac{P_s}{P_{\text{inc}}} = \frac{1}{4\pi}\int_0^{2\pi}d\phi\int_0^{\pi/2}d\theta\sin\theta\gamma\left(\theta,\phi\right) \tag{3.447}$$

For rectangular lattice, one can easily connect $\Delta\alpha = \Delta m\Delta n$ with $\Delta k_x\Delta k_y$,

$$1 = \Delta\alpha = \Delta m\Delta n = \frac{\Omega}{4\pi^2}\Delta k_x\Delta k_y \tag{3.448}$$

And

$$dk_x dk_y = d\phi dk_\rho k_\rho = d\phi d\theta k^2\cos\theta\sin\theta \tag{3.449}$$

Thus

$$\frac{P_s}{P_{\text{inc}}} = \frac{1}{k_{iz}}\sum_{\alpha}\text{Re}\left[k_{z\alpha}\right]\left|\tilde{\bar{B}}_{\alpha}\right|^2\Delta\alpha = \frac{1}{k_{iz}}\sum_{\alpha}\text{Re}\left[k_{z\alpha}\right]\left|\tilde{\bar{B}}_{\alpha}\right|^2\frac{\Omega}{4\pi^2}\Delta k_x\Delta k_y \tag{3.450}$$

Converting the summation into integrals,

$$\begin{aligned}\frac{P_s}{P_{\text{inc}}} &= \frac{1}{k_{iz}} \iint dk_x dk_y \,\text{Re}\left[k_{z\alpha}\right] \left|\tilde{\tilde{B}}_\alpha\right|^2 \frac{\Omega}{4\pi^2} \\ &= k^2 \frac{\Omega}{4\pi^2} \int_0^{2\pi} d\phi \int_0^{\pi/2} d\theta \cos\theta \sin\theta \frac{\text{Re}\left[k_{z\alpha}\right]}{k_{iz}} \left|\tilde{\tilde{B}}_\alpha\right|^2\end{aligned} \tag{3.451}$$

Only the propagating modes contribute,

$$\frac{P_s}{P_{\text{inc}}} = k^2 \frac{\Omega}{4\pi^2} \int_0^{2\pi} d\phi \int_0^{\pi/2} d\theta \sin\theta \frac{\cos^2\theta}{\sin\theta_{\text{inc}}} \left|\tilde{\tilde{B}}_\alpha\right|^2 \tag{3.452}$$

Comparing (3.452) with (3.447), it follows that

$$\gamma\left(\theta,\phi\right) = k^2 \frac{\Omega}{\pi} \frac{\cos^2\theta}{\cos\theta_{\text{inc}}} \left|\tilde{\tilde{B}}_\alpha\right|^2 \tag{3.453}$$

The bistatic scattering coefficients $\gamma(\theta,\phi)$ are only defined at the discrete scattering angles by the Floquet modes at $\left(k_{x\alpha}, k_{y\alpha}\right)$.

The polarization decomposition yields

$$\begin{aligned}\gamma_V\left(\theta,\phi\right) &= k^2 \frac{\Omega}{\pi} \frac{\cos^2\theta}{\cos\theta_{\text{inc}}} \left|\hat{h}_\alpha \cdot \tilde{\tilde{B}}_\alpha\right|^2 \\ \gamma_H\left(\theta,\phi\right) &= k^2 \frac{\Omega}{\pi} \frac{\cos^2\theta}{\cos\theta_{\text{inc}}} \left|\hat{e}_\alpha \cdot \tilde{\tilde{B}}_\alpha\right|^2\end{aligned} \tag{3.454}$$

The above expression (3.453) for $\gamma(\theta,\phi)$ is the total scattering coefficients in a single realization. As usual, the coherent and incoherent part are given by, statistically, in the Monte Carlo simulation,

$$\gamma^{\text{coh}}\left(\theta,\phi\right) = k^2 \frac{\Omega}{\pi} \frac{\cos^2\theta}{\cos\theta_{\text{inc}}} \left|\left\langle \tilde{\tilde{B}}_\alpha \right\rangle\right|^2 \tag{3.455}$$

$$\gamma^{\text{tot}}\left(\theta,\phi\right) = k^2 \frac{\Omega}{\pi} \frac{\cos^2\theta}{\cos\theta_{\text{inc}}} \left\langle \left|\tilde{\tilde{B}}_\alpha\right|^2 \right\rangle \tag{3.456}$$

And

$$\gamma^{\text{incoh}}\left(\theta,\phi\right) = \gamma^{\text{tot}}\left(\theta,\phi\right) - \gamma^{\text{coh}}\left(\theta,\phi\right) \tag{3.457}$$

With periodic boundary conditions, the coherent scattering field is concentrated in the specular scattering direction.

3.5.7 The transmissivity, absorptivity and the brightness temperature

(a) The transmitted power and the boundary field

Similar to the way we calculate the scattered power, the transmitted power per unit lattice is

$$P_t = \int_{\Omega_0} d\bar{\rho}\left(-\hat{z}\right)\cdot \bar{S}_t = \frac{1}{2}\int_{\Omega_0} d\bar{\rho}\left(-\hat{z}\right)\cdot \mathrm{Re}\left[\bar{E}_t \times \bar{H}_t^*\right] \tag{3.458}$$

where $\bar{E}_t$ and $\bar{H}_t$ are the total field on the boundary of the half space at $z = 0$.

We express the boundary field as the sum of incidence field and scattered field. This is done by substituting the spectral domain representation of $\bar{\bar{G}}_P^0$ in (3.430) and $\bar{\bar{G}}_P^R$ in (3.431) into (3.308), noticing $z = 0 < z'$. Then the scattering field is

$$\bar{E}_s\left(\bar{r}\right) = \sum_\alpha \left[\bar{C}_\alpha^0 \exp\left(i\bar{K}_\alpha \cdot \bar{r}\right) + \bar{C}_\alpha^R \exp\left(i\bar{k}_\alpha \cdot \bar{r}\right)\right] \tag{3.459}$$

where

$$\bar{C}_\alpha^0 = \frac{k^2}{\varepsilon}\sum_j \frac{i}{2\Omega}\frac{\exp\left(-i\bar{K}_\alpha \cdot \bar{r}_j\right)}{k_{z\alpha}}\left[\hat{e}_\alpha\left(-k_{z\alpha}\right)\hat{e}_\alpha\left(-k_{z\alpha}\right) + \hat{h}_\alpha\left(-k_{z\alpha}\right)\hat{h}_\alpha\left(-k_{z\alpha}\right)\right]\cdot \bar{p}_j \tag{3.460}$$

$$\begin{aligned}\bar{C}_\alpha^R = {} & \frac{k^2}{\varepsilon}\sum_j \frac{i}{2\Omega}\frac{\exp\left(-i\bar{K}_\alpha \cdot \bar{r}_j\right)}{k_{z\alpha}} \\ & \times\left[R^{\mathrm{TE}}\left(k_{z\alpha}\right)\hat{e}_\alpha\left(k_{z\alpha}\right)\hat{e}_\alpha\left(-k_{z\alpha}\right) + R^{\mathrm{TM}}\left(k_{z\alpha}\right)\hat{h}_\alpha\left(k_{z\alpha}\right)\hat{h}_\alpha\left(-k_{z\alpha}\right)\right]\cdot \bar{p}_j\end{aligned} \tag{3.461}$$

Putting together with $\bar{E}_{inc}$, we have

$$\bar{E}_t\left(\bar{r}\right) = \sum_\alpha \left[\tilde{\bar{C}}_\alpha^0 \exp\left(i\bar{K}_\alpha \cdot \bar{r}\right) + \tilde{\bar{C}}_\alpha^R \exp\left(i\bar{k}_\alpha \cdot \bar{r}\right)\right] \tag{3.462}$$

where

$$\tilde{\bar{C}}_\alpha^0 = \bar{C}_\alpha^0 + \delta_{\alpha 0}\left[\hat{e}_0\left(-k_{z0}\right)\hat{e}_0\left(-k_{z0}\right) + \hat{h}_0\left(-k_{z0}\right)\hat{h}_0\left(-k_{z0}\right)\right]\cdot\hat{q}_i \tag{3.463}$$

$$\tilde{\bar{C}}_\alpha^R = \bar{C}_\alpha^R + \delta_{\alpha 0}\left[R^{\mathrm{TE}}\left(k_{z0}\right)\hat{e}_0\left(k_{z0}\right)\hat{e}_0\left(-k_{z0}\right) + R^{\mathrm{TM}}\left(k_{z0}\right)\hat{h}_\alpha\left(k_{z0}\right)\hat{h}_0\left(-k_{z0}\right)\right]\cdot\hat{q}_i \tag{3.464}$$

where $\hat{q}_i$ denotes the polarization of the incidence wave.

The total magnetic field is readily at hand from Faraday's law. Specifically, at $z = 0$,

$$\bar{\bar{E}}_t\left(\bar{\rho}, z=0\right) = \sum_\alpha \left[\tilde{\bar{C}}_\alpha^0 + \tilde{\bar{C}}_\alpha^R\right]\exp\left(i\bar{k}_{\rho\alpha}\cdot\bar{\rho}\right) \tag{3.465}$$

$$\bar{\bar{H}}_t\left(\bar{\rho}, z=0\right) = \frac{1}{i\omega\mu}\sum_\alpha \left[i\bar{K}_\alpha \times \tilde{\bar{C}}_\alpha^0 + i\bar{k}_a \times \tilde{\bar{C}}_\alpha^R\right]\exp\left(i\bar{k}_{\rho\alpha}\cdot\bar{\rho}\right) \tag{3.466}$$

(b) The transmitted power and the transmissivity

Substituting (3.465) and (3.466) into (3.458), and making use of the orthogonality of the Floquet modes,

$$P_t = \frac{1}{2}\frac{1}{\omega\mu}\Omega_0\sum_\alpha\left(-\hat{z}\right)\cdot\mathrm{Re}\left[\left(\tilde{\bar{C}}_\alpha^0 + \tilde{\bar{C}}_\alpha^R\right)\times\left(\bar{K}_\alpha^* \times \tilde{\bar{C}}_\alpha^{0*} + \bar{k}_\alpha^* \times \tilde{\bar{C}}_\alpha^{R*}\right)\right] \tag{3.467}$$

Assuming a lossless background media of the top half space, further manipulation yields:

(i) For propagating waves in the top half-space

$$P_t^{\text{propagating}} = \frac{1}{2}\frac{1}{\omega\mu}\Omega_0\sum_{\alpha,\text{propagating}} k_{z\alpha}\left(\left|\tilde{\bar{C}}_\alpha^0\right|^2 - \left|\tilde{\bar{C}}_\alpha^R\right|^2\right) \tag{3.468}$$

(ii) For evanescent waves in the top half-space

$$P_t^{\text{evanescent}} = \frac{1}{2}\frac{1}{\omega\mu}\Omega_0\sum_{\alpha,\text{evanescent}}\left[-2\,\mathrm{Im}\left(k_{z\alpha}\right)\mathrm{Im}\left(\tilde{\bar{C}}_\alpha^0\tilde{\bar{C}}_\alpha^{R*}\right)\right] \tag{3.469}$$

Putting together,

$$P_t = \frac{1}{2}\frac{1}{\omega\mu}\Omega_0\sum_\alpha\left[\mathrm{Re}\left(k_{z\alpha}\right)\left(\left|\tilde{\bar{C}}_\alpha^0\right|^2 - \left|\tilde{\bar{C}}_\alpha^R\right|^2\right) - 2\,\mathrm{Im}\left(k_{z\alpha}\right)\mathrm{Im}\left(\tilde{\bar{C}}_\alpha^0\tilde{\bar{C}}_\alpha^{R*}\right)\right] \tag{3.470}$$

The transmissivity t is then

$$t = \frac{P_t}{P_{\text{inc}}} = \frac{1}{k_{iz}} \sum_{\alpha} \left[\text{Re}\left(k_{z\alpha}\right) \left(\left| \tilde{\bar{C}}_{\alpha}^{0} \right|^2 - \left| \tilde{\bar{C}}_{\alpha}^{R} \right|^2 \right) - 2\,\text{Im}\left(k_{z\alpha}\right) \text{Im}\left(\tilde{\bar{C}}_{\alpha}^{0} \tilde{\bar{C}}_{\alpha}^{R*} \right) \right] \tag{3.471}$$

One can represent $\tilde{\bar{C}}_{\alpha}^{0}$ and $\tilde{\bar{C}}_{\alpha}^{R}$ into their two orthogonal polarizations to further simplify the calculations.

(c) The absorbed power and absorptivity

This is in direct parallel to the 2D case as we discussed in section 3.4.5. The absorbed power per unit lattice

$$P_a = \iint_{\Omega_0} dxdy \int_0^H dz \frac{1}{2} \omega \varepsilon''\left(\bar{r}\right) \left| \bar{E}\left(\bar{r}\right) \right|^2 = \sum_j \Delta V \frac{1}{2} \omega \varepsilon''\left(\bar{r}_j\right) \left| \bar{E}\left(\bar{r}_j\right) \right|^2 \tag{3.472}$$

Assuming lossless background media,

$$P_a = \sum_{j \in \text{scatterer}} \Delta V \frac{1}{2} \omega \varepsilon''\left(\bar{r}_j\right) \left| \frac{\bar{p}_j}{\Delta V \varepsilon \left(\varepsilon_r\left(\bar{r}_j\right) - 1 \right)} \right|^2 \tag{3.473}$$

In two-phase random media,

$$P_a = \frac{1}{\Delta V} \frac{1}{2} \frac{\omega}{\varepsilon} \frac{\varepsilon_{pr}''}{\left| \varepsilon_{pr} - 1 \right|^2} \sum_j \left| \bar{p}_j \right|^2 \tag{3.474}$$

The absorptivity is then defined by

$$a = \frac{P_a}{P_{\text{inc}}} = \frac{1}{\cos\theta_{\text{inc}}} \frac{1}{\Omega_0} \frac{k}{\varepsilon^2} \frac{1}{\Delta V} \frac{\varepsilon_{pr}''}{\left| \varepsilon_{pr} - 1 \right|^2} \sum_j \left| \bar{p}_j \right|^2 = \sum_j \Delta a_j \tag{3.475}$$

where Δa_j is the differential absorptivity per small cube,

$$\Delta a_j = \frac{1}{\cos\theta_{\text{inc}}} \frac{1}{\Omega_0} \frac{k}{\varepsilon^2} \frac{1}{\Delta V} \frac{\varepsilon_{pr}''}{\left| \varepsilon_{pr} - 1 \right|^2} \left| \bar{p}_j \right|^2 \tag{3.476}$$

(d) The brightness temperature

Following the reciprocity relation between the scattering and emission problem as we derived in section 3.4.6, the brightness temperature T_B for the snowpack,

$$T_B\left(\theta_{inc}\right) = \int_{V_{\text{snow}}} da\left(\bar{r}'\right) T_s\left(\bar{r}'\right) + tT_g = \sum_j \Delta a_j T_s\left(\bar{r}_j\right) + tT_g \tag{3.477}$$

where the integration domain is over one unit lattice, and T_s and T_g are the physical temperatures of the snowpack and the ground (the bottom half-space) in Kelvin.

For constant snow temperature,

$$T_B\left(\theta_{inc}\right) = aT_s + tT_g \tag{3.478}$$

(e) The energy conservation

The energy conservation relation exhibits itself as

$$r + a + t = 1 \tag{3.479}$$

3.5.8 Simulation results

We consider the scattering from a layer of snow as represented by bicontinuous media with parameters of $\langle\zeta\rangle = 5000/\text{m}$, $b = 1.0$, and $f_v = 0.3$. The random media has an effective exponential correlation length of 0.36mm. The snow layer has thickness $d = 10cm$. The two horizontal directions are truncated at $L_x = L_y = 15cm$, applying periodic boundary conditions. The microwave frequency is set at Ku band of 17.2 GHz, at which the computational domain is of 8.6λx8.6λx5.8λ. A plane wave is impinging upon the snow layer at 40 degree. The bottom half space has dielectric constant of 5+0.5i. The ice has dielectric constant of 3.2+i0.001. The snow layer has an effective optical thickness of 0.32.

In Figure III.18, the incoherent bistatic scattering coefficients is plotted as a function of scattering angle in the incidence plane and compared with the results of the partially coherent approach of DMRT. Note that the results of full wave simulation are discrete as a result of Floquet boundary conditions. The bistatic scattering coefficients are averaged over 100 Monte Carlo simulations. There is overall good agreement between the full wave simulation and DMRT. The notable peak in the backscattering direction on the order of ~2dB is a demonstration of the backscattering enhancement effects [33, 15, 31, 32, 144].

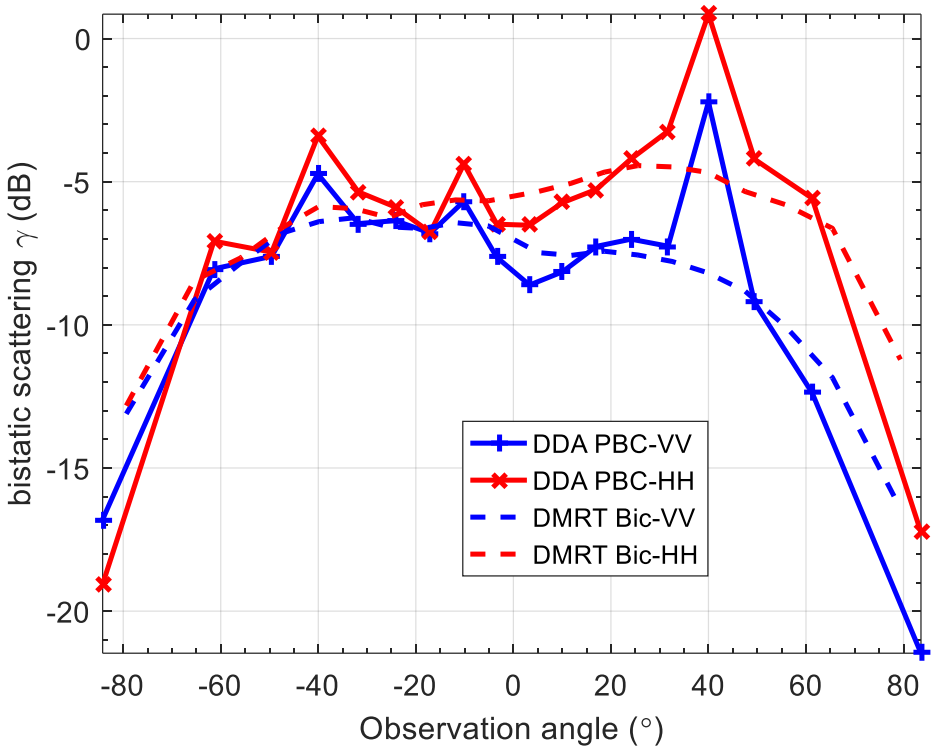

Figure III.18. Incoherent bistatic scattering coefficients as a function of observation angle.

In Figure III.19, the bistatic scattering coefficients are plotted in the entire top hemisphere as a function of k_{sx} and k_{sy} for all the four combination of polarizations. The scattering patterns

are as expected that the co-polarized scattering power are concentrated close to the incidence plane while the cross-polarized scattering power are directed perpendicular to the incidence plane.

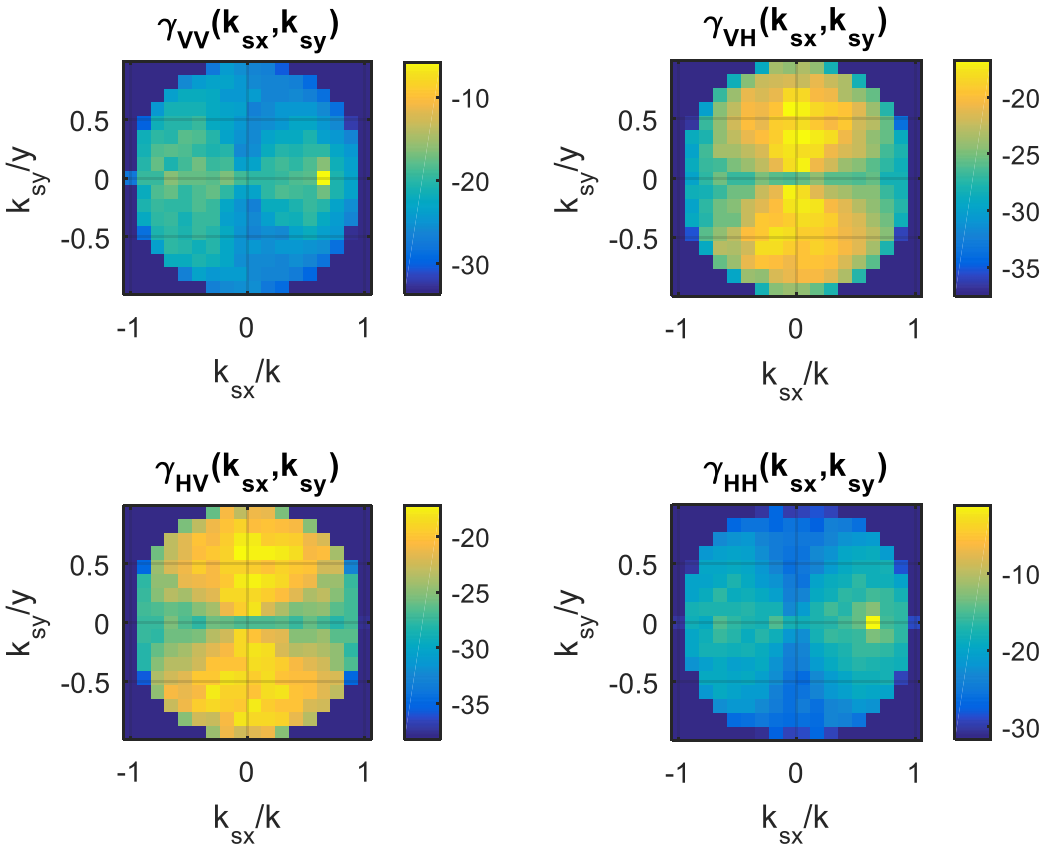

Figure III.19. Incoherent bistatic scattering coefficients from 3D full wave simulation.

In Figure III.20, the speckle statistics obtained from the 100 Monte Carlo simulations are plotted for the four polarizations in the backward scattering direction. The scattering matrix S is scaled such that $\sigma = |S|^2$ [37]. The amplitude distribution of S agrees with Rayleigh distribution for statistical homogeneous snowpack, while the phase distribution are shown to be uniform in $0 \sim 2\pi$. The close agreement in VH and HV is the result of reciprocity.

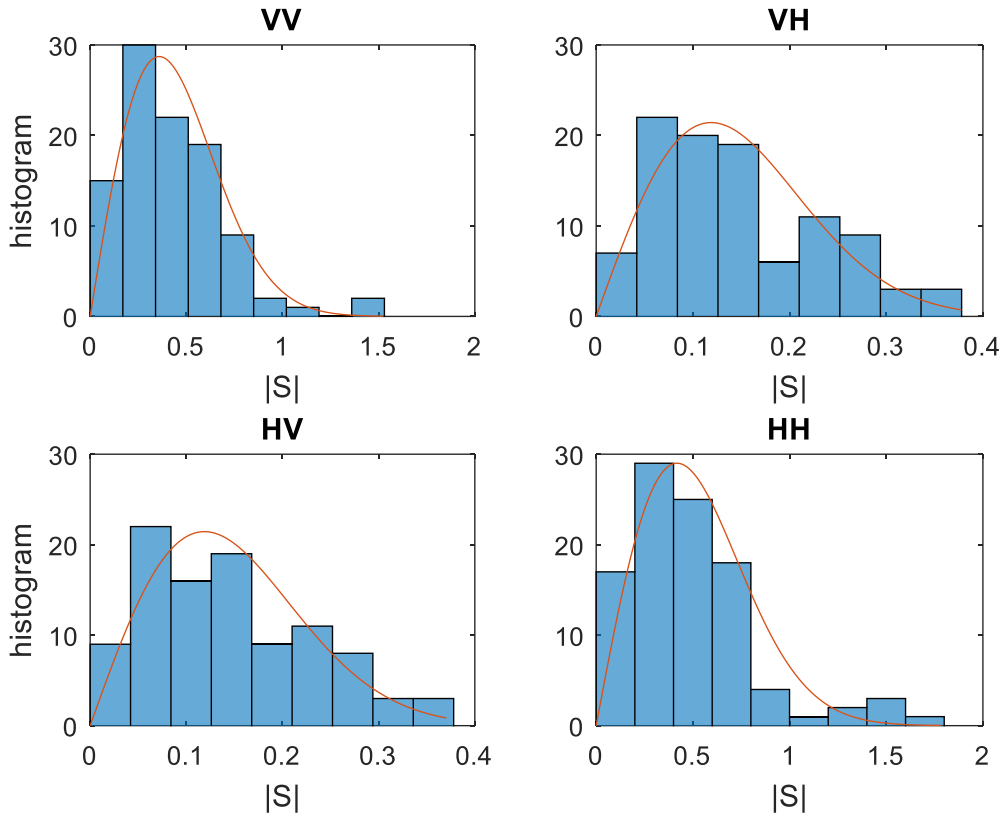

Figure III.20. The speckle statistics of the backward scattering amplitude from 3D full wave simulation with periodic boundary conditions.

In this example, the energy conservation is again shown to be perfect: for vertical polarization, reflectivity $r = 0.1321$, absorptivity $a = 0.0147$, and transmissivity $t = 0.8517$, adding up to $r + a + t = 0.9985$; for horizontal polarization, reflectivity $r = 0.1965$, absorptivity $a = 0.0142$, and transmissivity $t = 0.7878$, adding up to $r + a + t = 0.9985$. Thus the energies are both conserved to the precision of less than 0.2%.

The backscatters and brightness temperatures from the same snowpack with 10cm thickness are calculated as a function of incidence / observation angle, and plotted in Figure III.21 and Figure III.22, respectively. In the brightness temperature simulation, the snowpack temperature and ground temperature are set to be 260K and 273.15K, respectively. The DMRT

results are calculated using the same bicontinuous media parameters and are including the cyclical corrections for backscatter.

In Figure III.21, the solid curves are the results of the fully coherent approach of NMM3D with periodic boundary conditions; the dashed curves are the results of the partially coherent approach of DMRT. The NMM3D results oscillates around the DMRT results demonstrating that the coherent layering effects causes multiple reflections and coherent wave interferences.

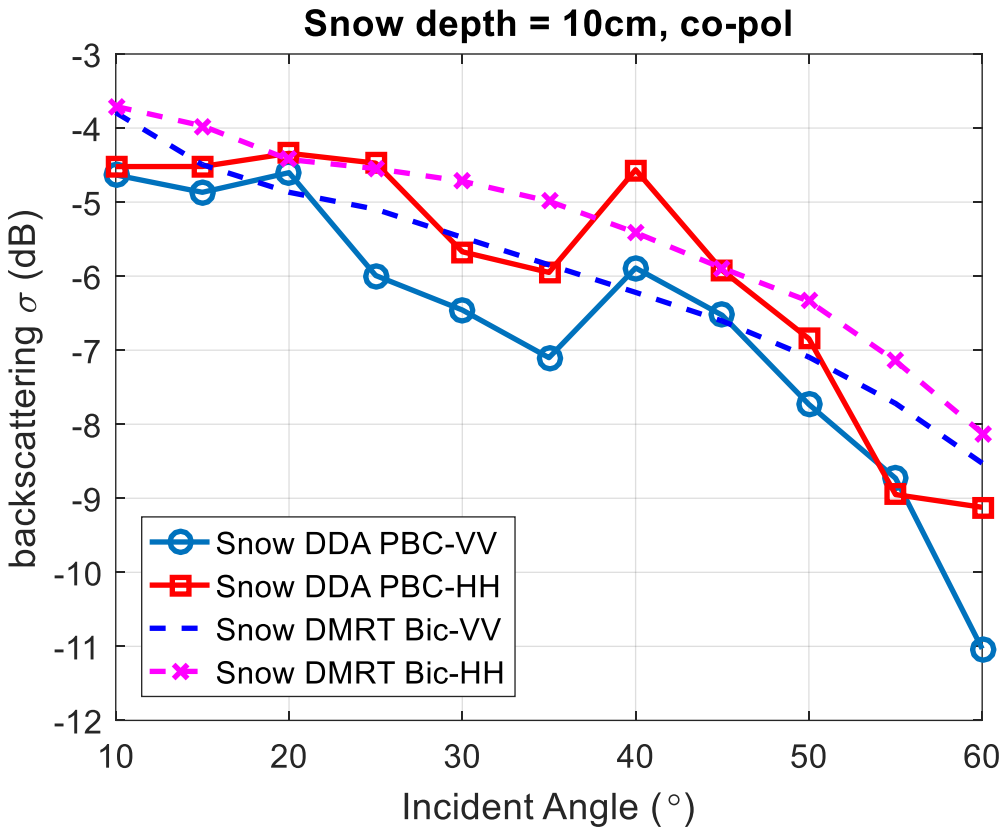

Figure III.21. Backscatter as a function of incidence angle compared with DMRT results.

In Figure III.22, the markers are the results of the fully coherent approach of NMM3D; the solid curves are the results of layered media emission theory with the snow layer being approximated by an effective permittivity $\varepsilon_{eff} = 1.48\varepsilon_0$, only considering coherent wave

reflections at interfaces but completely ignoring volumetric scattering effects. The dashed curves are the results of the partially coherent approach of DMRT. The NMM3D results oscillates around the DMRT results with much weaker variation than the layered media emission results. The comparison shows damped oscillations and decreased brightness temperatures in the NMM3D results due to scattering. The coherent layer effects are still exhibited in the weak oscillations, and the coherent layer effects are shown to be stronger for horizontal polarizations than vertical polarizations especially at larger observation angles.

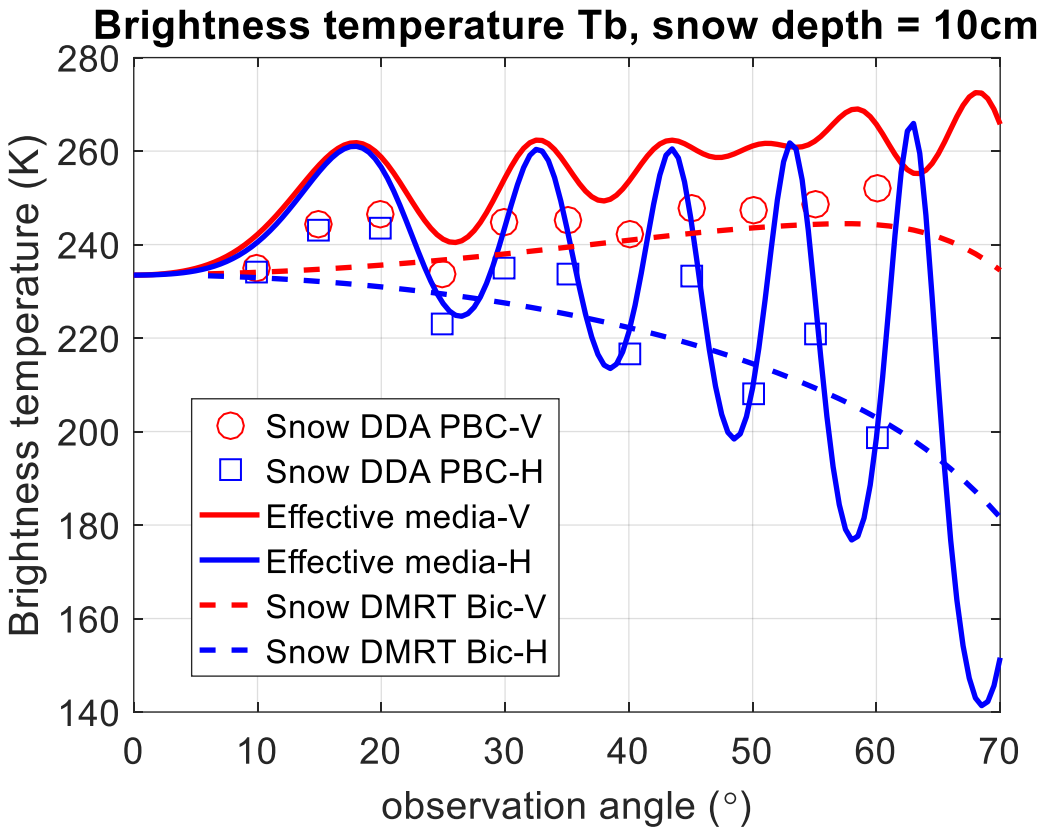

Figure III.22. Brightness temperature as a function of observation angle compared to the results of DMRT and layered media emission.

The backscatters and brightness temperatures are also computed as a function of snow depth in Figure III.23 and Figure III.24, respectively. The incidence / observation angle is fixed at

40 degree. The snowpack microstructure and ground parameters are the same as before. In both cases the full wave simulation results are compared with DMRT results. The DMRT results are calculated using the same bicontinuous media parameters and are including the cyclical corrections for backscatter [33].

In Figure III.23, the solid curves are the results of full wave simulation with periodic boundary conditions, while the dashed curves are the results of DMRT. The results of the backscattering coefficients are generally within 1dB. The oscillation pattern of the full wave simulation results preserves for snow depth up to 25cm, demonstrating the coherent wave effects.

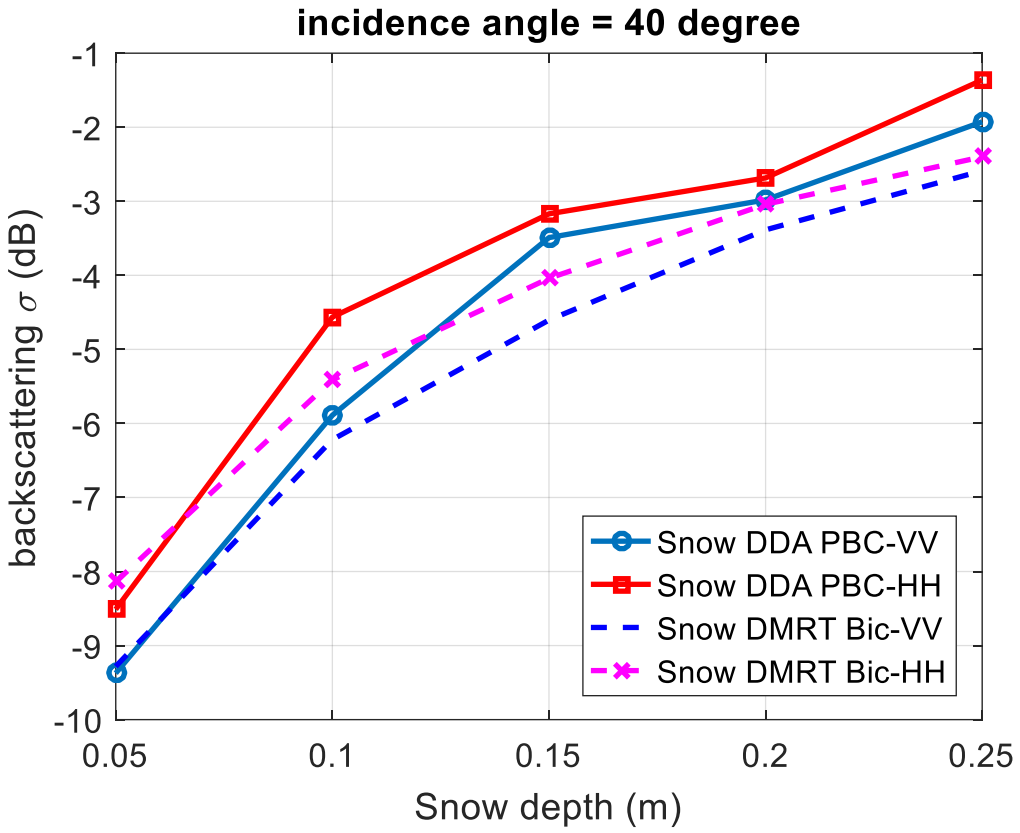

Figure III.23. Backscatter as a function of snow depth compared with DMRT results.

In Figure III.24, the markers are the results of the fully coherent approach of NMM3D; the dashed curves are the results of layered media with effective permittivity $\varepsilon_{eff} = 1.48\varepsilon_0$ considering coherent wave reflections at interfaces but ignoring volumetric scattering effects. The solid curves are the results of the partially coherent approach of DMRT. There are larger discrepancies in the horizontal polarization than in the vertical polarization between the NMM3D brightness temperatures and DMRT results. The difference in the horizontal polarizations are most significant at small thicknesses. The comparison shows that the horizontal polarization is more sensitive to coherent layer effects due to its relatively larger reflection coefficients; and the coherent layer effects are most significant at small thickness. The comparison between the full wave results and the effective media results indicates that scattering smooths coherent oscillations and decreases brightness temperatures. The decreasing magnitude of the oscillation of the brightness temperatures in horizontal polarization from the full wave simulation around the DMRT results at larger snow depths implies the weakening of coherent layer effects as suppressed by the increasing volumetric scattering.

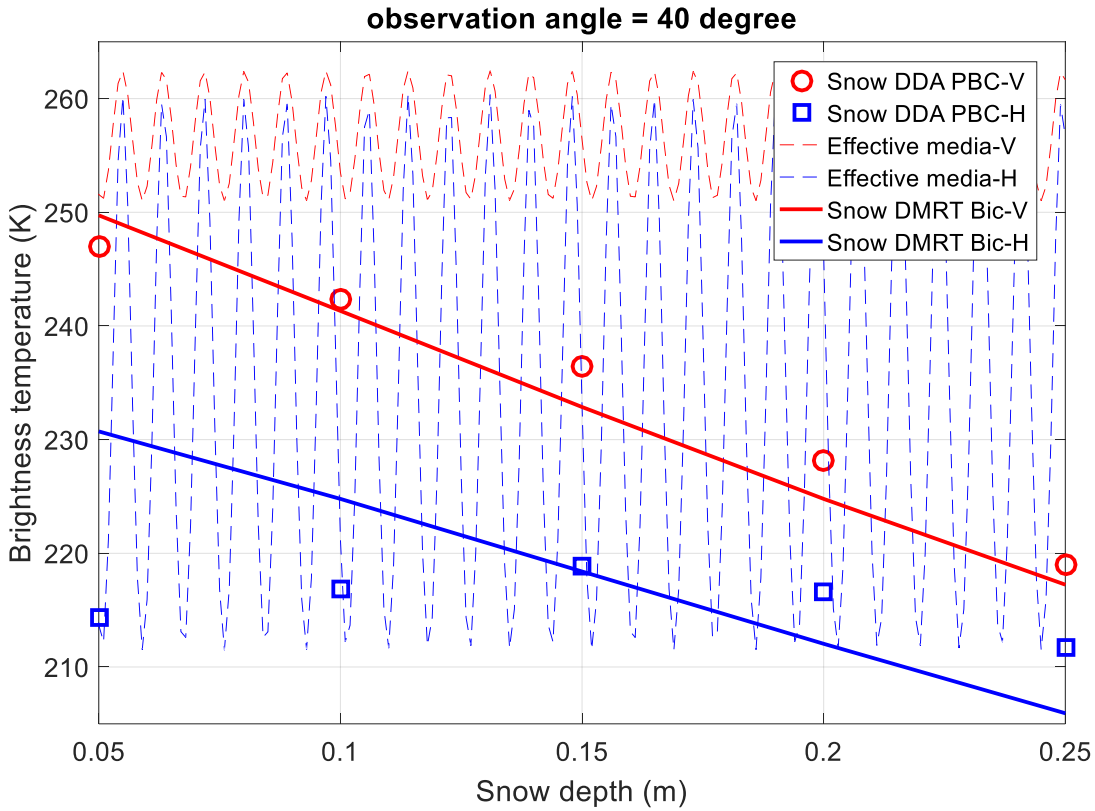

Figure III.24. Brightness temperature as a function of snow depth compared with DMRT and layered media emission results.

3.6 Conclusions

In this chapter, we formulated and implemented a fundamentally new approach in dealing with the scattering and emission problem from layered snowpack on top of a dielectric half-space. The approach is based on solving Maxwell's equations directly without introducing the approximations assumed by the radiative transfer equations. On the other hand, the dense media radiative transfer approach is a partially coherent approach and is an approach of homogenization where the snowpack is represented by its effective permittivity, extinction coefficient and the effective scattering phase matrices. This homogenization process is only valid for homogenous snowpack extending in many wavelengths. The thin layers in the snowpack causing coherent multiple reflections and the coherent volume-surface interactions and coherent far-field volume-

volume scattering interaction are not included in the radiative transfer equations. The fully coherent approach, standing on full wave simulations, confirms the backscattering enhancement effects and the coherent layer effects under certain configurations.

Besides calculating the incoherent scattering coefficients, the fully coherent approach is capable of computing the complex scattering matrix of the snowpack, including both magnitude and phase. The availability of the phase information enables new capabilities to model SAR polarimetry, such as coherency matrix and speckle statistics, and to generate coherent microwave images, such as SAR-tomograms to reveal the vertical structure of the snowpack through multiple microwave acquisitions of the snowpack over a limited range of angles and frequency.

In terms of modeling approaches, we systematically compared the 2D and 3D simulation process, and we compared the effects of simply truncating the horizontal domain of the snowpack or introducing periodic boundary conditions. By apply the periodic boundary conditions on the truncated domain, the artificial edge diffraction effects are eliminated. The periodic boundary condition also makes it possible to derive passive microwave observables, such as brightness temperatures, by making use of the general reciprocity between the active scattering and passive emission problems. Good energy conservation is obtained in the full wave simulation.

The full wave simulation of natural snowpack is historically an “impossible-to-compute” problem. However, by sampling the space in uniform grids, and making use of the translational symmetry of the Green’s function, the technique of fast Fourier transform can be combined with the discrete dipole approximations, using the Green’s function of the half-space. A scalable and efficient DDA code package supporting half-space Green’s function and half-space periodic Green’s function is developed and deployed on high performance parallel computing clusters to attack this previously impossible problem.

CHAPTER IV

Uniaxial Effective Permittivity of Anisotropic Bicontinuous Random Media Extracted from NMM3D

In this chapter we generate anisotropic bicontinuous media with different vertical and horizontal correlation functions. With the computer generated bicontinuous medium, we then use NMM3D (Numerical solutions of Maxwell equations in 3-Dimensions) to calculate the anisotropic effective permittivities and the effective propagation constants of V and H polarizations. The co-polarization phase difference of VV and HH are then derived. The co-polarization phase differences have recently been applied to the retrieval of snow water equivalent (SWE), snow depth and anisotropy. The NMM3D simulation results are also compared with the results of the strong permittivity fluctuations (SPF) in the low frequency limit and compared against the Maxwell-Garnett mixing formula. The work described here has been partially published in [44].

4.1 Introduction

Recent measurements of radar remote sensing of terrestrial snow [39-42] showed that the phase of the complex backscattered scattering parameter can be used to retrieve snow depth. In the analysis of experimental measurements of the phase of backscattered signal [39-42], the snow layer is treated to be an effective medium with effective propagation constant without random volumetric scattering. This means only the coherent waves are dominant while the incoherent

waves due to volume scattering are neglected. Using such model, the radar backscattering arises from rough surface scattering. The phase of the backscattered signal is cumulating phase delays from the air-snow interface to the snow-ground interface, backscattered by the rough surface of snow-ground, and then added with phase delays on the return through the snow layer to the air-snow interface. Thus the snow depth / snow water equivalent (SWE) could be determined from the integrated phase shift in time series measurements by differential interferometry at X and Ku band [40, 41]. In addition, the snow layer can be anisotropic as a result of the snow settlement under gravity and snow metamorphism. Temperature gradient driven metamorphism forms orientated ice crystals inducing anisotropy in dielectric properties of the snowpack [39, 42]. The anisotropy creates birefringence due to the differences in propagation constants between V and H polarization. The snow anisotropy can be observed by the co-polarization phase difference (CPD) between VV and HH. The co-polarization phase difference is proportional to the thickness of the snow layer. The depth of fresh snow (new fallen snow), has less volumetric scattering and was shown to be retrievable from the CPD. The polarimetric radar time series observations were recently verified using both the ground based SnowScat radar observations and the satellite TerraSAR-X observations in X band [39, 41, 42]. Theoretical studies in [39, 42] used a discrete scatter model of ellipsoids with preferred orientations. The approach assumed a quasi-static Maxwell-Garnet type mixing formula of ellipsoidal scatterers [39, 42, 43]. The depolarization factors of the ellipsoid are in one-to-one correspondence with the anisotropic parameter Q derivable from the correlation function of oriented spheroids [42], suggesting to use Q as a general descriptor of anisotropy for random media.

In this chapter, we use a random medium model to calculate the polarization phase difference [19-21, 26, 28]. We apply two approaches for performing the calculations. In the first

approach, we use computer generated bicontinuous media [19-21, 28]. In the second approach, we use strong permittivity fluctuation (SPF) model [26]. The advantages of random media are that correlation functions are used to describe random media. Such correlation functions can be and have been determined from microstructures of snow [145, 146, 150].

In the first approach, we use computer generated bicontinuous media [19-21, 28] to represent the microstructure of snow. The bicontinuous media is generated by level cutting a random field that is the sum of a large number of randomly oriented standing waves [147]. By limiting the orientation distributions of the elementary standing waves, we generate random structures with a preferred orientation. Such structures visually resembles snow microstructures and can be quantitatively compared to snow using autocorrelation functions. Previous studies [21, 28] suggest that the autocorrelation functions of bicontinuous media with Gamma distribution of wavenumbers decay less rapidly with distance than exponential decay and this accounts for the weaker frequency dependence in scattering. In this chapter we derive the correlation functions for anisotropic bicontinuous media.

We next compute the effective permittivity by full wave simulations of the solutions Maxwell's equations (NMM3D) for the computer generated bicontinuous media. Such approach includes multiple scattering effects and is applicable to a wide range of microwave frequencies and snow conditions.

In NMM3D, we use the discrete dipole approximation (DDA) [19, 34] to solve the volume integral equations of the anisotropic bicontinuous medium. The sample volume of bicontinuous media is a sphere with diameter of a few wavelengths. We perform such simulation over a large number of samples (realizations). We compute the coherent scattering field of the bicontinuous media by taking realization averages of the scattered field. The coherent scattered field is then

compared with the Mie scattering from a homogeneous sphere of the same size. The effective permittivity of the bicontinuous medium is then equated with the permittivity of the Mie sphere in the sense of least mean square error (LMSE). Such concept of comparing mean scattering field was previously used by Chew et.al. [45] to compute the effective permittivity of a random sphere mixture at a very low frequency. Siqueira and Sarabandi have also used such concept to validate the effectivity predicted by quasi-crystalline approximation (QCA) of cylindrical particles in 2D [46] and spherical particles in 3D [47]. In this study we consider the effective permittivity of irregular and anisotropic bicontinuous media, and perform the simulations at low to moderate frequencies with correlation lengths of the random media smaller than or comparable to wavelengths. After the uniaxial effective permittivities of the random medium are obtained, we calculate the effective propagation constants for V and H polarization and compute the co-polar phase differences (CPD) for a variety of snow conditions.

In the second approach, we use the strong permittivity fluctuations (SPF) theory [26] to calculate the uniaxial effective permittivity which applied the bilocal approximation to the Dyson's equation of mean field with the singularity extraction of the dyadic Green's function. We extend the SPF theory [26] to take arbitrary correlation functions with azimuth symmetry by taking the Fourier transform of the correlation function numerically. The key integrals of Eq. (84) of [26] are also performed numerically. We then apply the SPF theory to the correlation functions of the anisotropic bicontinuous media. It should be noted that in [148], the uniaxial effective permittivity tensor is also derived for arbitrary random media of azimuthal symmetry within a strong contrast expansion in terms of n-point correlation functions. The formalism, however, is difficult to apply to an arbitrary correlation function that cannot be cast into a functional form of $C(r/l(\cos\theta))$ [149]. The 2nd order strong contrast expansion reduces to the Maxwell-Garnett mixing formula in

the low frequency limit [42] while the SPF theory [26] reduces to the Polder and van Santen mixing. The difference between the two originates from their different choice of Green's function in formulating the integral equation. In this study, we also extract the exponential correlation lengths of the anisotropic bicontinuous media from its correlation function, and use them to calculate the Q factor [42, 149] of the media by assuming the functional form of the correlation function. This enables us to compare the results against the Maxwell-Garnett dielectric mixing [42].

4.2 Anisotropic Bicontinuous Media and Its Autocovariance Function

We describe the generation of anisotropic bicontinuous media and its characterization by autocorrelation function.

4.2.1 Generation of Anisotropic Bicontinuous Media

The procedure follows [19] with the following modifications. We define a zero mean random field S of position $\bar{r}$ by superimposing a large number of stochastic standing waves.

$$S(\bar{r}) = \frac{1}{\sqrt{N}} \sum_{n=1}^{N} \cos(\bar{\zeta}_n \cdot \bar{r} + \phi_n) \tag{4.1}$$

where N is a sufficiently large number, ϕ_n is the random phase distributed uniformly between 0 and 2π, $\bar{\zeta}_n$ is the random wave vector $\bar{\zeta}_n = \zeta_n \hat{\zeta}_n$. The magnitude ζ_n follows gamma distribution $p_{\mathrm{Z}}(\zeta)$ with mean value $\langle\zeta\rangle$ and standard deviation $\langle\zeta\rangle/\sqrt{b+1}$, where $\langle\zeta\rangle$ has a unit of $1/\mathrm{m}$, and b unit 1.

$$p_{\mathrm{Z}}(\zeta) = \frac{1}{\Gamma(b+1)} \frac{(b+1)^{b+1}}{\langle\zeta\rangle} \left(\frac{\zeta}{\langle\zeta\rangle}\right)^{b} e^{-(b+1)\frac{\zeta}{\langle\zeta\rangle}} \tag{4.2}$$

Previously, in [19] the unit vectors $\hat{\zeta}_n$ are uniformly distributed on a unit spherical surface, forming statistically isotropic random field. To create anisotropy, we limit $\hat{\zeta}_n$ to be around the equator or around the poles, to form vertical structures and horizontal structures, respectively. We choose the probability distribution function of the inclination angle θ of $\hat{\zeta}_n$, as follows,

$$p_\Theta(\theta) = C\frac{\sin\theta}{2}, \theta \in \Theta_D \tag{4.3}$$

where Θ_D is the definition domain of θ, and C is a normalization constant. We introduce an anisotropy parameter μ, $0 < \mu < 1$. For vertical structure, Θ_D is defined by $|\cos\theta| \leq \mu$, and $C = 1/\mu$; for horizontal structure, Θ_D is defined by $|\cos\theta| \geq \mu$, and $C = 1/(1-\mu)$. The azimuth angle φ of $\hat{\zeta}_n$ is, as before, uniformly distributed between 0 and 2π, such that the random field is statistically isotropic in the xOy plane.

The two-phase bicontinuous medium is defined by an indicator function $\Theta_\alpha(\bar{r})$.

$$\Theta_\alpha(\bar{r}) = \begin{cases} 1 & S(\bar{r}) > \alpha \\ 0 & otherwise \end{cases} \tag{4.4}$$

where α is the cutting level related to the volume fraction f_v of the random media, and $f_v = \langle\Theta_\alpha(\bar{r})\rangle = \mathrm{erfc}(\alpha)/2$, where $\mathrm{erfc}(\cdot)$ is the complementary error function.

In Figure IV.1, we illustrate the cross section images of the bicontinuous media along the xOz plane for various anisotropy parameter μ. It can be seen that the vertical structures become more visible as μ approaches 0, while the horizontal structures become clearer as μ approaches 1.

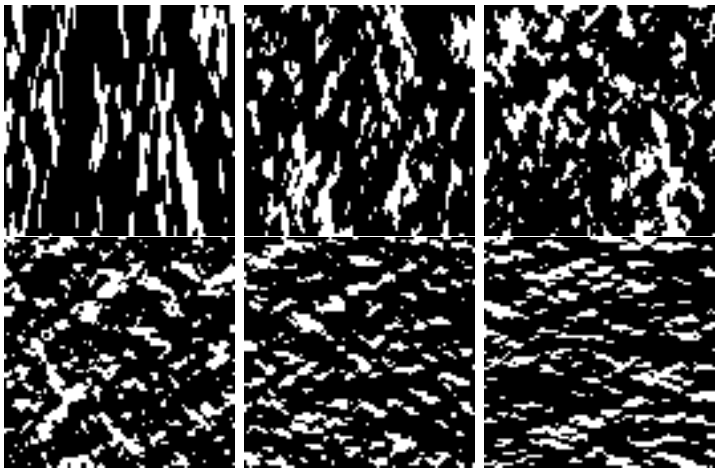

Figure IV.1. Cross section images of anisotropic bicontinuous media (xOz): first row for vertical structures and second row for horizontal structures; μ is ¼, ½, ¾, respectively, from left to right. $\langle\zeta\rangle$ is 9988.789, b is 1.2, and f_v is 0.2179. $\langle\zeta\rangle, b$ and f_v are unchanged along the chapter unless specified. Image size is of 8.715mm with each pixel 0.1mm.

4.2.2 Characterization of Anisotropic Bicontinuous Media by Autocorrelation Functions

Since $S(\bar{r})$ is a Gaussian random process, the autocorrelation function of the bicontinuous media $\Gamma_\alpha(\bar{r}) = \langle\Theta_\alpha(\bar{r})\Theta_\alpha(0)\rangle$ can be expressed in terms of $\mathrm{C}_s(\bar{r})$, the normalized autocovariance function of $S(\bar{r})$, [19, 147]

$$\Gamma_\alpha(\bar{r}) = f_v^2 + \sum_{m=1}^{\infty} C_m(\alpha)[C_s(\bar{r})]^m \tag{4.5}$$

where $C_m(\alpha) = e^{-2\alpha^2}[H_{m-1}(\alpha)]^2/(\pi m!\, 2^m)$, and $H_m(\cdot)$ is the m-th order Hermite polynomial.

The function $\mathrm{C}_s(\bar{r}) = \langle S(\bar{r})S(0)\rangle/\langle S^2(0)\rangle$ is

$$\mathrm{C}_s(\bar{r}) = \int_0^{+\infty} d\zeta p_{\mathrm{Z}}(\zeta)\langle\cos\left(\zeta\hat{\zeta}_n\cdot\bar{r}\right)\rangle \tag{4.6}$$

For anisotropic bicontinuous media,

$$\langle\cos\left(\zeta\hat{\zeta}_n\cdot\bar{r}\right)\rangle = \int_{\Theta_D} d\theta p_\Theta(\theta)\cos(\zeta z\cos\theta)J_0(\zeta\rho\sin\theta) \tag{4.7}$$

where $\rho = \sqrt{x^2 + y^2}$ and (x, y, z) are the coordinates of $\bar{r}$. When Θ_D expands over the whole domain of $[0, \pi]$, i.e., the isotropic case, $\langle \cos(\zeta \hat{\zeta}_n \cdot \bar{r}) \rangle = j_0(\zeta r) = \sin(\zeta r)/(\zeta r)$.

The normalized autocovariance function of bicontinuous media is $\tilde{C}_\alpha(\bar{r}) = (\Gamma_\alpha(\bar{r}) - f_v^2)/(f_v - f_v^2)$. In Figure IV.2, we compare $\tilde{C}_\alpha(\bar{r})$ along x and z axis for the vertical structures and the horizontal structures using anisotropy $\mu = 1/2$. It is noted that $\tilde{C}_\alpha(\bar{r})$ has a larger correlation length in z direction for vertical structures and a larger correlation length in x direction for horizontal structures. The autocovariance functions are also extracted numerically in a similar procedure to Eq. (4) of [145] by computing the cross correlation of a reference subsample volume with the entire sample volume.

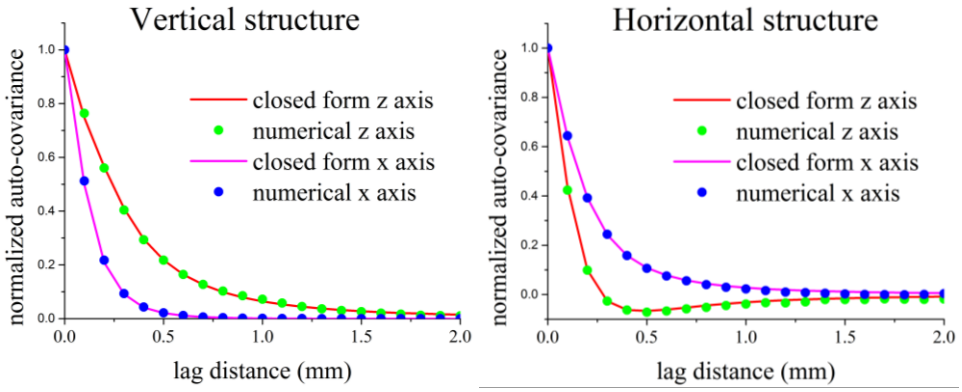

Figure IV.2. Normalized auto-covariance functions of anisotropic bicontinuous media along x and z axes: comparison of closed form and numerical results. Left for vertical and right for horizontal structure. Anisotropy μ is ½.

As shown in Figure IV.2, the numerically extracted correlation functions of bicontinuous media samples are in excellent agreement with the numerical evaluations of Eqs. (5-7) where 5000 terms are included in the summation of Eq. (5) to ensure convergence. Note that $\tilde{C}_\alpha(\bar{r})$ can be negative for highly anisotropic media as illustrated by $\tilde{C}_\alpha(z)$ of the horizontal structure. This agrees with experiments [145, 150]. The negative values are not modeled by exponential functions.

The shape of the correlation function bicontinuous media depends on the choice of $p_{\mathrm{Z}}(\zeta)$ and $p_{\Theta}(\theta)$, and in general does not have a functional form of $C(r/l(\cos\theta))$ and a close form of parameter Q [149]. Recent measurements also show the oscillatory behavior of snow correlation function that cannot be described by a single length scale [150].

4.3 Uniaxial Effective Permittivity and Propagation Constants of Anisotropic Bicontinuous Media

In this section, we derive the effective permittivities of the anisotropic bicontinuous media from full wave solutions.

4.3.1 Effective Propagation Constants of TE and TM Waves and the Co-polar Phase Difference

A uniaxial media, characterized by a diagonal tensor permittivity $\bar{\bar{\varepsilon}}_1$ with diagonal elements of ε_1, ε_1 and ε_{1z}, respectively, supports two kinds of characteristic waves: the ordinary wave and the extraordinary wave. The horizontally polarized wave, or TE wave, is ordinary; and the vertically polarized wave, or TM wave, is extraordinary. The two waves satisfy different dispersion relationships as follows

$$\text{TE: } k_\rho^2 + k_{1z}^2 = \omega^2\mu\varepsilon_1 \tag{4.8a}$$

$$\text{TM: } k_\rho^2 + \frac{\varepsilon_{1z}}{\varepsilon_1}k_{1z}^2 = \omega^2\mu\varepsilon_{1z} \tag{4.8b}$$

where $k_\rho^2 = k_x^2 + k_y^2$, k_x, k_y and k_{1z} are the x, y, z components of the wavenumber in the uniaxial media, respectively. Consider an incidence wave upon a flat layer of media with $\bar{\bar{\varepsilon}}_1$ from an isotropic media with permittivity ε and $k = \omega\sqrt{\mu\varepsilon}$ with incidence angle θ_{inc}, where $k_\rho =$

$k \sin\theta_{\text{inc}}$ following phase continuity. The effective propagation constants $k_{\text{eff}} = \sqrt{k_\rho^2 + k_{1z}^2}$ are as follows for the two polarizations,

$$k_{\text{eff}}^{\text{TE}} = \omega\sqrt{\mu\varepsilon_1} \tag{4.9a}$$

$$k_{\text{eff}}^{\text{TM}} = \omega\sqrt{\mu\left(\varepsilon_1 + \left(1 - \frac{\varepsilon_1}{\varepsilon_{1z}}\right)\varepsilon \sin^2\theta_{\text{inc}}\right)} \tag{4.9b}$$

The effective propagation constant of TE wave is invariant with respect to the incidence angle, while that of TM wave increases with incidence angles.

The co-polar phase difference (ϕ_{CPD}) is the two-way phase difference between the VV polarized signal and HH polarized signal on the snow/ ground interface, as observed by the receiver [42]. Considering an anisotropic snow layer of thickness d and uniaxial permittivity $\bar{\bar{\varepsilon}}_1$ above ground,

$$\phi_{\text{CPD}} = 2(k_{1z}^{\text{TM}} - k_{1z}^{\text{TE}})d \tag{4.10}$$

4.3.2 Extraction of Effective Permittivity Using NMM3D

From the dispersion relationship of the TE and TM waves, we notice that by setting k_{1z} to be zero, $k_{\text{eff}}^{\text{TE}} = \omega\sqrt{\mu\varepsilon_1}$ and $k_{\text{eff}}^{\text{TM}} = \omega\sqrt{\mu\varepsilon_{1z}}$. Thus by impinging a plane wave propagating in the xOy plane in the anisotropic bicontinuous media and extracting the effective propagation constants of the TE and TM waves, we can obtain the two constitutive parameters ε_1 and ε_{1z}, of the uniaxial permittivity. The effective propagation constants are extracted by fitting the coherent scattering field from the random media sample with the Mie scattering solution of a homogeneous and isotropic sphere.

In NMM3D, the sample volume of the bicontinuous medium is a sphere of radius a, where a is of several wavelengths. The discrete dipole approximation is applied to solve volume integral equations over each sample. The coherent scattering field is computed as the mean scattering field,

$$\bar{E}^s_{\text{coh}}(\Theta) = \frac{1}{N_r}\sum_{n=1}^{N_r} \bar{E}^s_n(\Theta) \tag{4.11}$$

where Θ is the angle between the scattering direction $\hat{k}_s$ and the incidence direction $\hat{k}_i$, N_r is the number of realizations, and $\bar{E}^s_n(\Theta)$ is the scattering field from the n-th realization. We choose $\hat{k}_i = \hat{x}$, and vary $\hat{k}_s$ on the xOy plane by changing Θ from 0 to π (see inset in Figure IV.3 (a) for illustration). The coherent field is considered to be the scattering field from a homogeneous sphere of permittivity ε_p with the same radius a. The Mie scattering field from the sphere is computed as $\bar{E}^s_{\text{Mie}}(\Theta, \varepsilon_p)$. Then the effective permittivity is chosen to be ε_p that minimizes the differences in the least mean square error sense

$$\varepsilon_{\text{eff}} = \min_{\varepsilon_p} \int_0^{\pi} d\Theta \left|\bar{E}^s_{\text{coh}}(\Theta) - \bar{E}^s_{\text{Mie}}(\Theta, \varepsilon_p)\right|^2 \tag{4.12}$$

ε_1 and ε_{1z} are taken to be the extracted ε_{eff} with the incidence wave propagation along $\hat{x}$, and polarized along $\hat{y}$ (TE wave) and $\hat{z}$ (TM wave), respectively.

In Figure IV.3, we compare the coherent scattering field with Mie scattering (from a homemade Mie scattering code) associated with the optimal ε_p. The bicontinuous media has vertical orientation preference with anisotropy $\mu = 1/2$. The results are given in terms of scattering matrix elements S_{11} and S_{22} on the xOy scattering plane for the extraction of ε_{1z} (using TM wave) and ε_1 (using TE wave), respectively. The agreements are excellent in both cases. In Figure IV.3, S_{22} (TM) and S_{11}(TE) on the xOz scattering plane are also computed and compared to Mie scattering. The agreements indicate the flexibility in the choice of $\hat{k}_s$ directions. The better

agreement in S_{11} than S_{22} is possibly due to that Mie scattering has not included the uniaxial behavior of the effective permittivity.

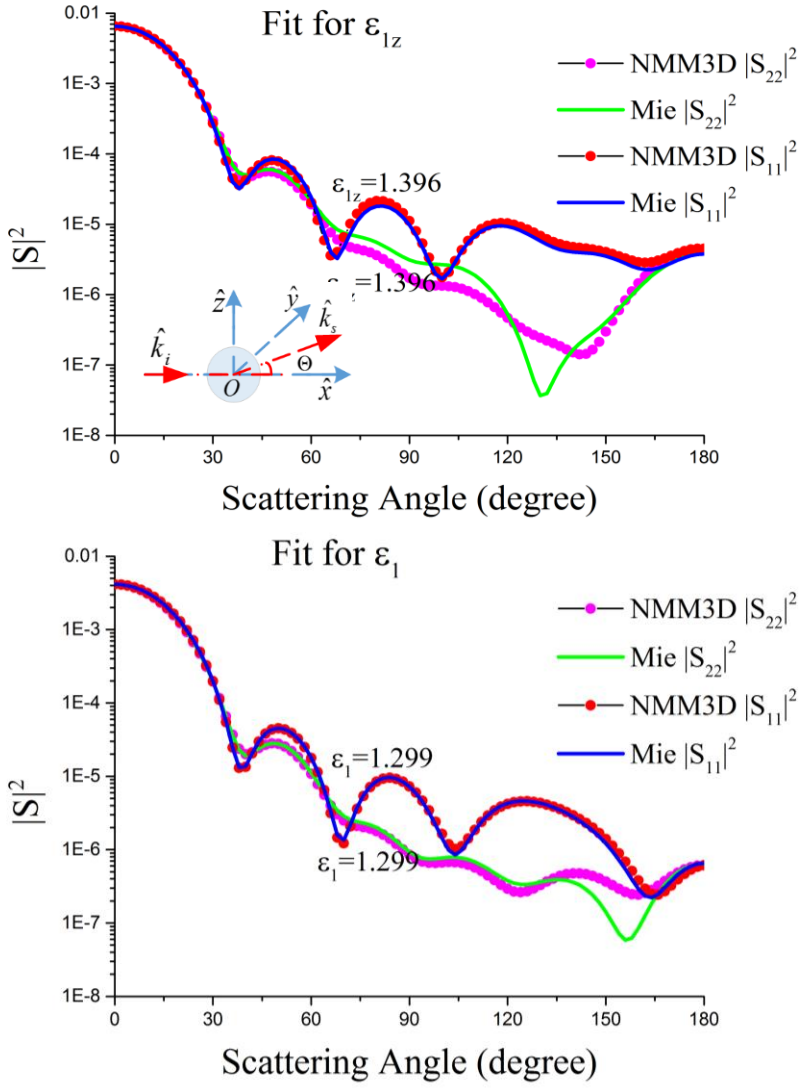

Figure IV.3. Comparison of coherent field with Mie scattering in the 1-2 frame using TM (a, top) and TE (b, bottom) incidence wave for the extraction of ε_{1z} and ε_1, respectively. The inset in (a) illustrates the wave vectors and the spherical sample volume in the xOy plane. Wave is propagating along x direction at 17.2GHz. Vertical structure has μ of ½. The spherical sample of the media has a diameter of 20.93mm (1.2×free space wavelength) divided along each direction with uniform grid size of 0.133mm.

4.4 Strong Permittivity Fluctuation Theory Applied to an Arbitrary Correlation Function with Azimuthal Symmetry

The strong permittivity fluctuation (SPF) theory predicts the effective permittivity of a random media from its correlation functions. The SPF results with general anisotropic correlation functions of azimuthal symmetry are reported here as an extension of [26] where the anisotropic correlation functions are assumed to be of certain forms.

The effective permittivity of the random media $\bar{\bar{\varepsilon}}_{eff}$ is uniaxial when the anisotropic correlation function has azimuthal symmetry. For a two phase random media with background permittivity ε_b and scatterer ε_p with volume fraction f_v, SPF predicts at low frequency with wavenumber k_0 that

$$\bar{\bar{\varepsilon}}_{eff} = \bar{\bar{\varepsilon}}_g + \varepsilon_0 \bar{\bar{\xi}}^{(0)}_{eff}(k_0) \tag{4.13}$$

Both $\bar{\bar{\varepsilon}}_g$ and $\bar{\bar{\xi}}^{(0)}_{eff}$ are uniaxial, $\bar{\bar{\varepsilon}}_g = \text{diag}\{\varepsilon_g, \varepsilon_g, \varepsilon_{gz}\}$ and $\bar{\bar{\xi}}^{(0)}_{eff} = \text{diag}\{\xi_1, \xi_1, \xi_3\}$. $\bar{\bar{\varepsilon}}_g$ is identical to the Polder and van Santern mixing formula in the very low frequency limit for isotropic correlation functions.

$$\xi_1 = (\xi_p - \xi_b)^2 f_v(1 - f_v)(I_1 + S) \tag{4.14a}$$

$$\xi_3 = (\xi_{pz} - \xi_{bz})^2 f_v(1 - f_v)(I_3 + S_z) \tag{4.14b}$$

where $\xi_p = (\varepsilon_p - \varepsilon_g)/(\varepsilon_0 + S(\varepsilon_p - \varepsilon_g))$, $\xi_b = (\varepsilon_b - \varepsilon_g)/(\varepsilon_0 + S(\varepsilon_b - \varepsilon_g))$, $\xi_{pz} = (\varepsilon_p - \varepsilon_{gz})/(\varepsilon_0 + S_z(\varepsilon_p - \varepsilon_{gz}))$ and $\xi_{bz} = (\varepsilon_b - \varepsilon_{gz})/(\varepsilon_0 + S_z(\varepsilon_b - \varepsilon_{gz}))$. ε_g and ε_{gz} are to be determined. $S = -I_1(k_0 = 0)$, and $S_z = -I_3(k_0 = 0)$, where $I_1(k_0)$ and $I_3(k_0)$ are defined as follows,

$$I_1(k_0) = -\pi \frac{\varepsilon_0}{\varepsilon_{gz}} \int_0^\infty dk_\rho k_\rho \int_{-\infty}^\infty dk_z \left[\frac{-k_0^2 \varepsilon_{gz}}{\varepsilon_0 \left(k_\rho^2 + k_z^2 - k_0^2 \varepsilon_g / \varepsilon_0\right)} + \frac{k_\rho^2 - k_0^2 \varepsilon_{gz}/\varepsilon_0}{k_z^2 + \left(k_\rho^2 - k_0^2 \varepsilon_{gz}/\varepsilon_0\right)\varepsilon_g/\varepsilon_{gz}} \right] \Phi_\xi\left(k_\rho, k_z\right) \tag{4.15a}$$

$$I_3(k_0) = -2\pi \frac{\varepsilon_0}{\varepsilon_{gz}} \int_0^\infty dk_\rho k_\rho \int_{-\infty}^\infty dk_z \left[\frac{k_z^2 - k_0^2 \frac{\varepsilon_g}{\varepsilon_0}}{k_z^2 + \left(k_\rho^2 - \frac{k_0^2 \varepsilon_{gz}}{\varepsilon_0}\right)\frac{\varepsilon_g}{\varepsilon_{gz}}} \right] \Phi_\xi\left(k_\rho, k_z\right) \tag{4.15b}$$

where $\Phi_\xi\left(k_\rho, k_z\right)$ is the 3D Fourier transform of the normalized autocovariance function of the random media $\tilde{C}_\alpha(\bar{r})$ as defined in Section 4.2.2 (same as $R_\xi(\rho, z)$ of [26]),

$$\Phi_\xi\left(k_\rho, k_z\right) = \frac{1}{4\pi^2} \int_0^\infty d\rho \rho J_0\left(k_\rho \rho\right) \int_{-\infty}^\infty dz \tilde{C}_\alpha(\rho, z) \exp(i k_z z) \tag{4.16}$$

Finally, ε_g and ε_{gz} are the roots of the following coupled non-linear equation set, and can be solved iteratively.

$$\xi_p f_v + \xi_b (1 - f_v) = 0 \tag{4.17a}$$

$$\xi_{pz} f_v + \xi_{bz} (1 - f_v) = 0 \tag{4.17b}$$

4.5 Results and Comparison

In this section, we illustrate results of the uniaxial effective permittivities using typical snow parameters. In Figure IV.4, we examine the effective permittivities at Ku band as functions of fractional volume (a) and anisotropy (b), respectively. The NMM3D results are compared with the results of SPF and the Maxwell-Garnett mixing. The SPF results are computed using the anisotropic correlation functions of the bicontinuous media. The Maxwell-Garnett mixing formula is driven by the exponential correlation lengths of the bicontinuous media extracted from its correlation functions, and is in correspondence to the anisotropic parameter Q [42, 149]. The

extracted Q parameter from the correlation lengths is also plotted against the parameter μ. For fixed anisotropy, the uniaxial effective permittivities of ε_{1z} and ε_1 increase with volume fraction. The difference between ε_{1z} and ε_1 increases with volume fraction until saturation and then decreases. SPF results show weak frequency dependence and predict slight larger effective permittivities and earlier saturation in $\varepsilon_{1z} - \varepsilon_1$ with density and less peak difference. For the same volume fraction, the vertical structure has a larger ε_{1z} than ε_1, while the horizontal structure has a smaller ε_{1z} than ε_1. The difference $|\varepsilon_{1z} - \varepsilon_1|$ increases as the structure becomes more anisotropic (decreasing μ for vertical and increasing μ for horizontal structures). All the models provide similar dependences. The agreements between the models are better with smaller volume fractions when multiple scattering effects are weaker.

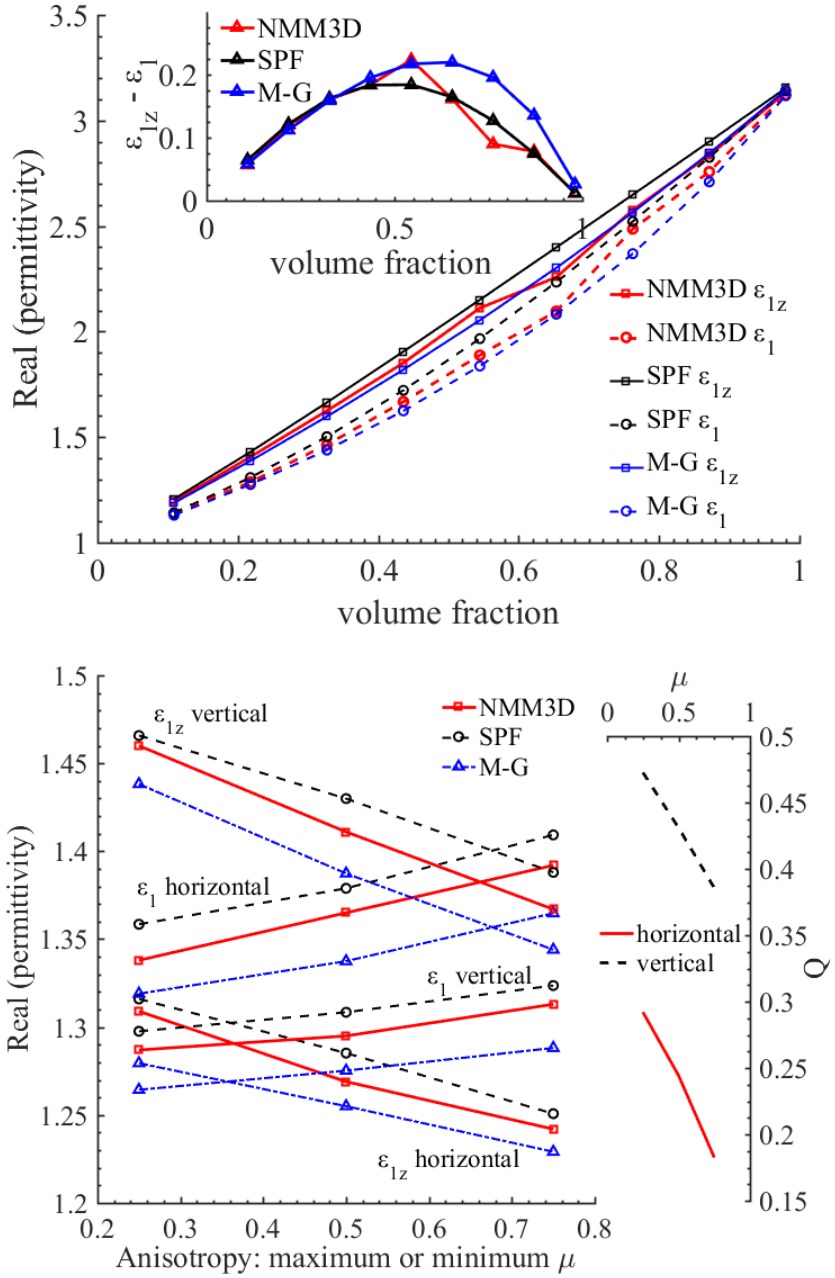

Figure IV.4. Extracted uniaxial permittivity from NMM3D at 17.2GHz as a function of volume fraction (a, top) and anisotropy (b, bottom). (a) Vertical structure with μ of ½. NMM3D results are compared against SPF results. The inset shows the difference between ε_{1z} and ε_z. (b) Ice volume fraction f_v is 0.218. The inset on the right plots Q against μ.

In Figure IV.5, we illustrate the co-polar phase differences (CPD) against snow anisotropy and densities for various incidence angles at Ku band, similar to Figs. 3 and 4 of [42]. The CPD,

defined as $\phi_{\mathrm{VV}} - \phi_{\mathrm{HH}}$, is positive for vertical structure and negative for horizontal structure. Its magnitude increases as the structure becomes more anisotropic. The magnitude of CPD also increases with incidence angles. It can be as large as 100 degree per 10 cm snow at 40 degree incidence angle for structures with strong anisotropy and it quickly increases to ~200 degree per 10 cm snow at 55 degree incidence angle. The dependence of CPD against volume fraction is non-monotonic. For a vertical structure with modest anisotropy μ of ½, the CPD increases with volume fraction before it reaches a maximum at a moderate volume fraction of ~0.33 and then decreases. This is a result of the change in the difference between ε_{1z} and ε_1 and also the increase of ε_{1z} and ε_1 with volume fraction.

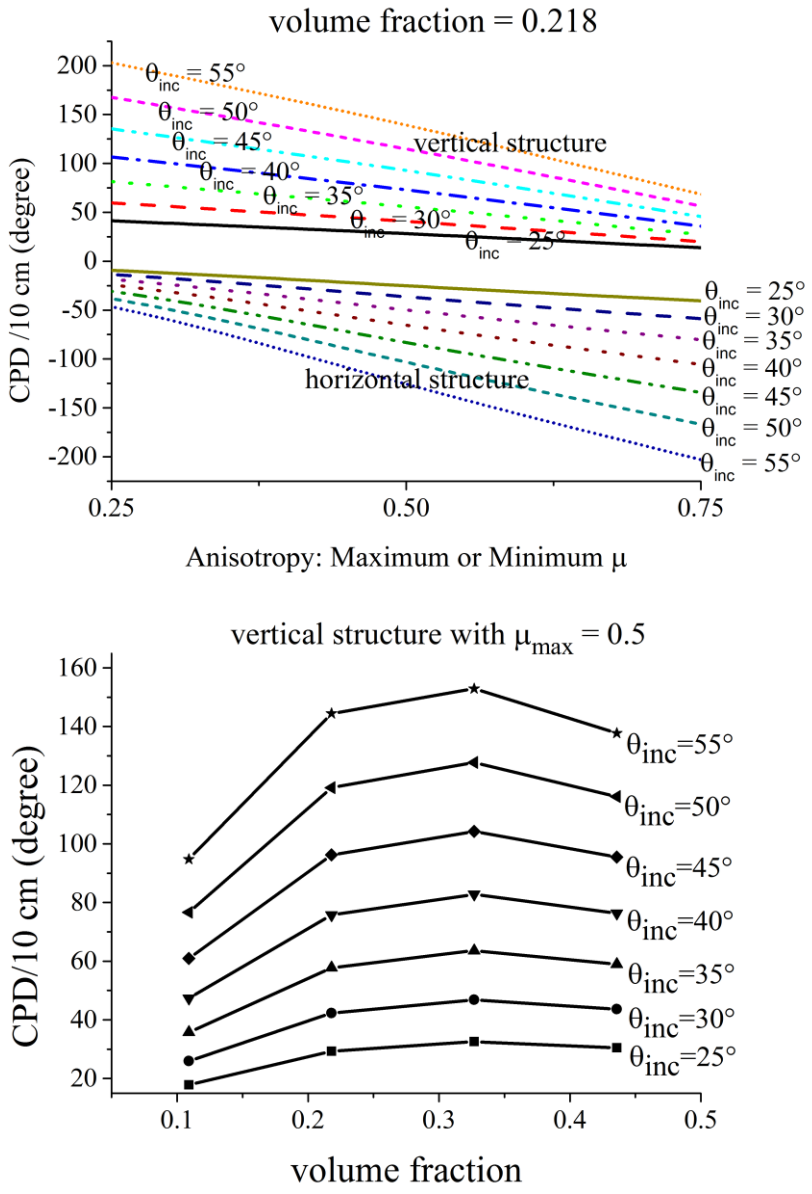

Figure IV.5. CPD vs. anisotropy for different incidence angles (a, top); CPD vs. volume fraction for different incidence angles (b, bottom)

4.6 Conclusion

Anisotropic bicontinuous media are generated to model anisotropies in snow. The uniaxial effective permittivities of the anisotropic structure are extracted from full wave simulations using NMM3D. The approach considers the actual geometry of the random media, includes the fully

coherent wave interaction within the inhomogeneities and the multiple scattering effects. It is applicable to a wide range of frequency, permittivity contrast, and volume fraction. It provides more accurate predictions than the dielectric mixing formulas and is widely applicable. The results are compared with the strong permittivity fluctuation (SPF) theory and the Maxwell-Garnett mixing, all with similar density and anisotropy dependences. The SPF theory is extended to take directly the correlation functions of bicontinuous media. The behavior of the correlation function at larger lag distance affects the scattering loss, but is found to have less effect on the real part of the effective permittivity. The results of co-polar phase differences are calculated and can be used to retrieve the thickness of fresh snow and to monitor changes in snow morphologies.

CHAPTER V

The Fully and Partially Coherent Approach in Random Layered Media Scattering Applied to Polar Ice Sheet Emission from 0.5 to 2GHz

In this chapter we investigate physical effects influencing 0.5-2 GHz brightness temperatures of layered polar firn to support the Ultra Wide Band Software Defined Radiometer (UWBRAD) experiment to be conducted in Greenland and in Antarctica. We find that because ice particle grain sizes are very small compared to the 0.5-2 GHz wavelengths, volume scattering effects are small. Variations in firn density over cm to m- length scales however cause significant effects. Both incoherent and coherent models are used to examine these effects. Incoherent models include a "cloud model" that neglects any reflections internal to the ice sheet, and the DMRT-ML and MEMLS radiative transfer codes that are publicly available. The coherent model is based on the layered medium implementation of the fluctuation dissipation theorem for thermal microwave radiation from a medium having a non-uniform temperature. Density profiles are modeled using a stochastic approach, and model predictions are averaged over a large number of realizations to take into account an averaging over the radiometer footprint. Density profiles are described by combining a smooth average density profile with a spatially correlated random process to model density fluctuations. It is shown that coherent model results after ensemble averaging depend on the correlation lengths of the vertical density fluctuations. If the correlation length is moderate or long compared with the wavelength (~0.6x longer or greater for Gaussian correlation function

without regard for layer thinning due to compaction), coherent and incoherent model results are similar (within ~1K). However, when the correlation length is short compared to the wavelength, coherent model results are significantly different from the incoherent model by several tens of kelvins. For a 10cm correlation length, the differences are significant between 0.5 and 1.1GHz, and less for 1.1GHz to 2GHz. Model results are shown to be able to match the v-pol SMOS data closely and predict the h-pol data for small observation angles.

A partially coherent model is then designed to improve the efficiency of the fully coherent model by dividing the ice sheet into blocks. Within each block we apply the coherent model, but within adjacent blocks we use radiative transfer theory to incoherent cascading the block parameters. By using a block size of several wavelengths, the partially coherent approach reproduces the results of fully coherent results but requires much smaller number of realizations to reach convergence. The partially coherent model, when combined with the two scale density variation model, predicts the angular brightness temperatures that agrees with L-band SMOS observations over Greenland Summit. The partially coherent model also enables modeling the multiple rough interface effects in coupling the emissions among angles and polarizations.

The material covered in this Chapter has been partially published in [58], and been reported in several conference papers [59, 170-172].

5.1 Physical Models of Layered Polar Firn Brightness Temperatures: Comparison of the Fully Coherent and Incoherent Approaches

5.1.1 Introduction

Ice sheet internal temperature is a key variable in ice dynamics, and up to the present, direct information on ice sheet internal temperature comes primarily from borehole measurements [51,

151]. Recently, ultra-wideband radiometry (~0.5 – ~2 GHz) has been proposed as a remote sensing method to retrieve ice sheet internal temperature. The motivation to explore wide band radiometry is based on three observations. First, electromagnetic waves in the 0.5 to 2 GHz band can have penetration depths (as defined in equation. (5.6)) of hundreds of meters or more in ice. Second, analysis of ESA's Soil Moisture Ocean Salinity (SMOS) brightness temperature data shows sensitivity at L-band to subsurface temperature effects in Antarctica [152]. Finally, preliminary retrieval studies suggest the possibility of using this concept in estimation of the internal temperature [51, 52].

A physical model of brightness temperature over the UWBRAD frequency range is necessary to understand ice sheet emission physics and to support future UWBRAD experiments to be conducted in Greenland and Antarctica. In this paper we investigate physical effects influencing the 0.5-2 GHz brightness temperatures of layered polar firn using both incoherent and coherent models. The incoherent models include the cloud model [15, 51, 153, 169], the Dense Media Radiative Transfer – Multi Layers model (DMRT-ML) [14, 16] and the Microwave Emission Model of Layerd Snowpacks (MEMLS) [12, 154]. The coherent model [15] is based on the layered medium model implementation of the fluctuation dissipation theorem. Coherent and incoherent model results are compared for various firn and ice layer profile configurations. The "cloud" radiative transfer model ignores all intermediate reflections inside the ice sheet, which is partially justified by the nearly homogenous nature of the ice sheet below about 100-200 m depth [15, 51, 153]. The model gives insight into how the overall brightness temperature is determined by the ice sheet internal temperature profile. The other two incoherent models considered (DMRT-ML and MEMLS) are more sophisticated. They model the incoherent energy flow inside a stratified structure considering attenuation, scattering, and reflections based on radiative transfer

theory [12, 14, 16, 154]. DMRT-ML [14] applies physical scattering models of the Quasi-crystalline Approximaation with Coherent Potential (QCA-CP) [16], whereas MEMLS considers either empirical scattering coefficients for small snow grains [12] or physical scattering models of improved Born approximation for large snow grains [154]. Previous studies have shown that brightness temperatures and emissivities can be accurately simulated with DMRT-ML at Ku band and Ka band [155, 156], and results are also promising with proper parameterizations at L-band and C–band [157]. However, the use of these models at lower frequencies 0.5-2 GHz has yet to be examined in detail, especially when near surface density fluctuations [54, 157] produce a large number of closely spaced reflective boundaries, as observed with Aquarius [56]. Recent works have shown the importance of including density fluctuations in the forward model in order to reproduce measured data at L-band [157]. An alternative method is to analyze the ice sheet emission problem using the fully coherent approach while ignoring the volume scattering effects [15, 24, 57, 158]. Volume scattering is quite small at the low frequency of 0.5-2.0 GHz [157] in contrast to its importance at Ku and Ka band [156]. Recently Leduc-Leballeur et al. applied the coherent model to L band SMOS brightness temperature at Dome C, Antarctica, and show that the brightness temperature from the coherent model is about 10K lower than that from the incoherent model [57].

This paper provides additional insight into the physical mechanisms of 0.5-2 GHz thermal emission from ice sheets by comparing coherent and incoherent model simulations in the presence of stochastic variations in density. The impact of the spatial scales of the density fluctuations (described by a correlation length parameter) are investigated in terms of brightness temperature ensemble averaged over the fluctuating density random process. The next section describes the ice sheet model utilized, and Section III reviews basic properties of the forward models included in

the study. A special layering scheme to discretize the density profile into distinct layers is described in Section IV, and results of brightness temperature are then examined and discussed in Section V.

5.1.2 Vertical Structure of Polar Ice

The polar ice sheet structure is approximated as a planar layered medium having vertical temperature and density profiles, as illustrated in Figure V.1.

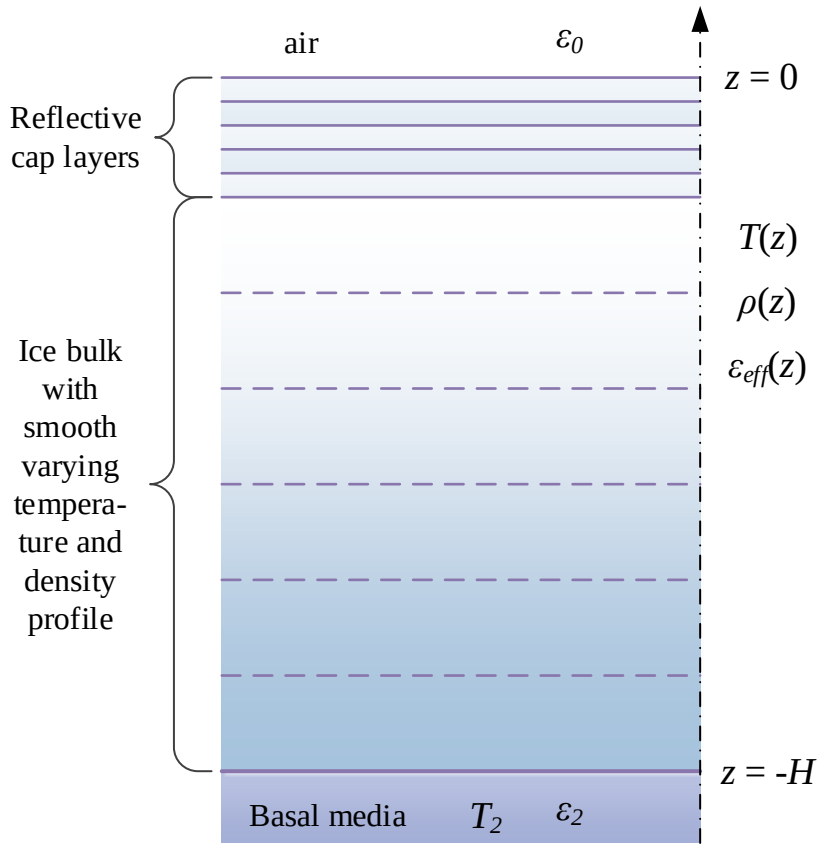

Figure V.1. Illustration of the vertical structure of the polar ice sheet in the microwave emission models

Except for the very top layers (about 10 meters) where the seasonal swing of the air temperature changes the ice temperature [54, 159, 160], the temperature of the rest of the ice sheet

generally increases with depth. Since the top layers contribute little to the ice-sheet thermal emission at low frequencies, in this study we ignore the near surface seasonal temperature variation and model the temperature profile $T(z)$ using the Robin temperature model described in [151],

$$T(z) = T_s + C \cdot \mathrm{erf}\left(\frac{H}{L}\right) - C \cdot \mathrm{erf}\left(\frac{z+H}{L}\right), -H \le z \le 0 \tag{5.1}$$

where $C = \frac{LG\sqrt{\pi}}{2k_c}$ and $L = \sqrt{\frac{2k_d H}{M}}$, erf(·) is the error function, $T_s = T(0)$ is the surface temperature, M is the accumulation rate, measured in meters per year ice equivalent, and H is the overall ice thickness. $G = 0.047W \cdot m^{-2}$ is the geothermal heat flux, $k_c = 2.7W \cdot m^{-1} \cdot K^{-1}$ is the ice thermal conductivity, and $k_d = 45m^2 \cdot \mathrm{yr}^{-1}$ is the ice thermal diffusivity. The Robin model assumes a planar stratified medium with homogenous thermal parameters driven by geothermal heat flux alone. These assumptions are significant but sufficient for the purpose of producing realistic temperature profile as a basis for assessing the impact on the frequency dependence of brightness temperature [51]. Two temperature profiles are illustrated in Figure V.2 (a) for $T_s = 216K$, $H = 3700m$ with M set to 0.01 and $0.05m \cdot \mathrm{yr}^{-1}$, respectively. These values are generally representative of the deep interior East Antarctic ice-sheet. The lower accumulation rate corresponds to the higher temperature. Also shown in Figure V.2 (a) is the Dome C bore hole temperature measured in December 2004 estimated from [168], fig. 1D. The modeled profiles are in reasonable agreement with measurements.

The average firn density $\rho(z)$ increases exponentially with depth [159-161]. Following the measurement of Alley et al. [161], we set $\rho(z)$ to be

$$\rho(z) = 0.922 - 0.564 \cdot \exp(0.0165z)\ g/cm^3 \tag{5.2}$$

The near surface density fluctuation $\tilde{\rho}(z)$ is modeled as the sum of the average density $\rho(z)$ and a damped noise $\rho_n(z)$,

$$\tilde{\rho}(z) = \rho(z) + \rho_n(z) \cdot \exp(z/\alpha) \tag{5.3}$$

with α as a damping factor, as previously proposed in [157]. Unlike [157], since the fluctuation is spatially correlated, the noisy part $\rho_n(z)$ is modeled as a Gaussian random process with Gaussian correlation function given by $\langle \rho_n(z)\rho_n(z') \rangle = \Delta^2 \exp\left(-\frac{(z-z')^2}{l^2}\right)$, where Δ^2 is the auto-covariance and l is the correlation length (reference [157] assumed $l = 0$). A random realization of density fluctuations with $\alpha = 30m$, $\Delta = 0.040\text{g/cm}^3$ and $l = 10\text{cm}$ is illustrated in Figure V.2 (b).

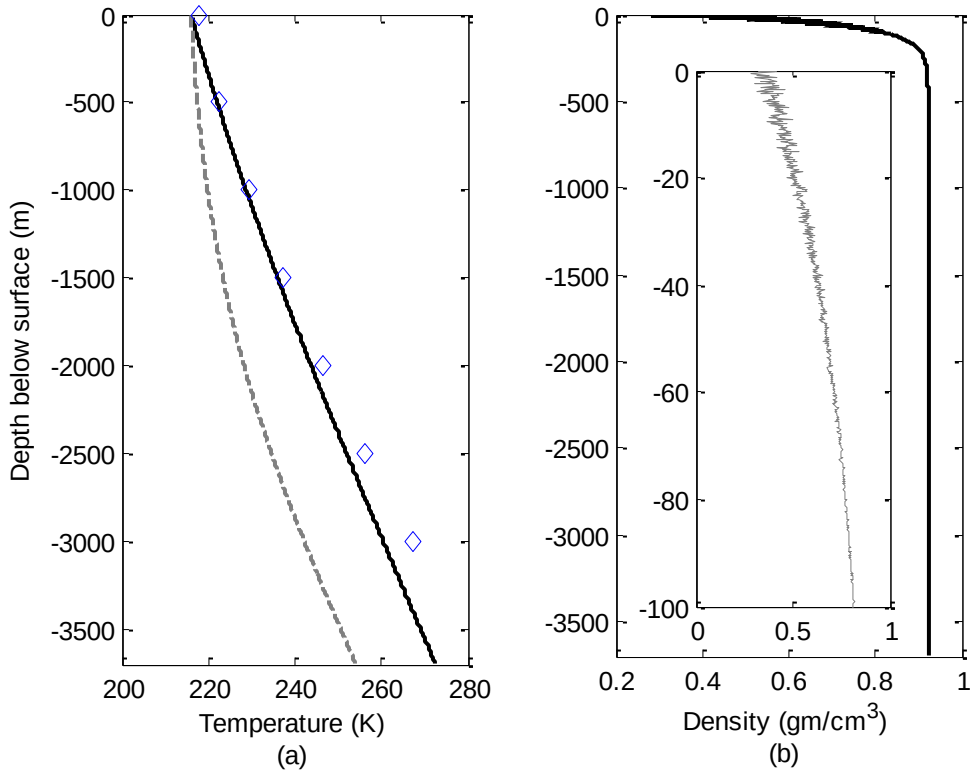

Figure V.2. Illustration of the ice sheet temperature profile (a) and density profile (b). In (a), the black solid line corresponds to $M = 0.01m \cdot \text{yr}^{-1}$, and the grey dashed line corresponds to $M = 0.05m \cdot \text{yr}^{-1}$. The blue diamonds are the Dome C bore hole temperature measured in Decemeber 2004 estimated from Fig. 1 (D) of ref [168]. The small inset in (b) shows the density fluctuation in the top 100 meters modeled by a damped Gaussian random process. The density profile is specified by $\alpha = 30m$, $\Delta = 0.040\text{g/cm}^3$ and $l = 10\text{cm}$.

A grain radius profile $a(z)$ following Zwally's [153] fit to Gow's [162] parameterization of Plateau station grain size between 0.5m and 71m is introduced to account for volume scattering effects.

$$a(z) = \sqrt[3]{0.0377 + 0.00472|z|}mm \tag{5.4}$$

with z in meters. We confine the volume scattering to the top 90m of the ice sheet considering the near-homogeneous ice composition below this depth [51].

The material beneath the ice sheet can be either frozen rock (relative permittivity 5 + 0.1i [163]) or liquid water (the relative permittivity of pure water varying form 87.6+4.6i at 0.5 GHz to 84.2+17.6i at 2.0 GHz with a temperature of 0°C [164]) depending on the basal temperature. When the basal temperature approaches the melting point of ice, sub-glacial water at 273K is assumed at the basal boundary; otherwise, an isothermal semi-infinite sub-glacial layer of frozen rock at the same temperature of the bottom of the ice sheet is assumed [51]. The impact of frequency variations in the basal medium permittivity are not examined in this Chapter for simplicity.

5.1.3 Physical Models of Brightness Temperature

In this section, we discuss the physical and mathematical basis for the four microwave models of brightness temperature considered.

(a) Cloud model

The "cloud" model is derived from the radiative transfer equation ignoring the source term from scattering [15, 51, 153, 169]. It also ignores all intermediate reflections inside the ice sheet, including reflections from the top air/snow interface and bottom ice/base interface only. With negligible scattering albedo, the predicted brightness temperature in nadir can be approximated by (5)

$$T_b = \left(1 - r_{\text{air/snow}}\right)\left[\int_{-H}^{0} dz T(z)\kappa_a(z) \exp\left(-\int_{z}^{0} dz'\kappa_a(z')\right)\right.$$
$$\left. + \left(1 - r_{\text{ice/base}}\right)T_{\text{base}} \exp\left(-\int_{-H}^{0} dz'\kappa_e(z')\right)\right] + rT^{Sky} \tag{5.5}$$

where $T(z)$ is the temperature profile, and $\kappa_e(z) = \kappa_a(z) + \kappa_s(z)$, with $\kappa_a(z)$ and $\kappa_s(z)$ as the absorption coefficient and scattering coefficient at depth z, respectively. The first term in brackets represents the emission from the icy medium. The second term represents the emission from the basal media attenuated by all the ice layers, where T_{base} is the physical temperature of the base. $r_{\text{air/snow}}$ and $r_{\text{ice/base}}$ are the reflectivities between the air/snow interface and ice/base interface, respectively. At nadir, $r_{\text{air/snow}}$ is typically 0.016 and $r_{\text{ice/base}}$ is 0.012 for frozen rock base and 0.46 for water base. Note in equation (5.5) the last term accounts for the sky radiation reflected by the surface and subsurface, where the solar and galactic radiation T^{Sky} depends on the polar sun elevations varying from place to place and day-of-year etc., and the surface reflectivity r depends on the assumptions about the density profile. In practice, the captured sky radiation contribution also depends on the given UWBRAD antenna pattern. Since the sky term varies substantially it is not explicitly included in the calculated graphs. We will apply the sky corrections for the particular case when we fly the instrument. We also ignore the atmosphere emission, which is typically small. The same assumption is used in the DMRT-ML, MEMLS and coherent models.

The penetration depth d_p is obtained by solving the integral identity

$$\int_{-d_p}^{0} dz\kappa_e(z) = 1 \tag{5.6}$$

Note that the extinction coefficient $\kappa_e(z)$ as a function of z depends on frequency, temperature and density. The real part of the relative effective permittivity $\varepsilon'_{\text{r,eff}}$ of the ice layer is

calculated with Mätzler's empirical formula [12, 165], and the imaginary part $\varepsilon''_{\mathrm{r,eff}}$ is calculated following the empirical model of Tiuri et al. for dry snow [166].

$$\varepsilon'_{r,eff} = 1 + 1.4667 f_v + 1.435 f_v^3, 0 < \rho \leq 0.4 g/cm^3 \tag{5.7a}$$

$$\varepsilon'_{r,eff} = \left[(1 - f_v)\varepsilon_h^b + f_v \varepsilon_s^b\right]^{1/b}, \rho > 0.4 g/cm^3 \tag{5.7b}$$

$$\varepsilon''_{r,eff} = \varepsilon''_{r,ice}(0.52\rho + 0.62\rho^2) \tag{5.7c}$$

where ρ is the snow/ice bulk density, $f_v = \rho/(0.917 g/\mathrm{cm}^3)$, $\varepsilon_h = 0.9974$, $\varepsilon_s = 3.215$, $b = 1/3$, and $\varepsilon''_{r,ice}$ is the imaginary part of ice permittivity. The complex dielectric constant of ice $\varepsilon_{r,ice} = \varepsilon'_{r,ice} + i\varepsilon''_{r,ice}$ is calculated following the semi-empirical model of [167], which predicts an increasing imaginary part of the relative permittivity as the temperature increases. The effective permittivity of the ice layer is then used to calculate the absorption coefficient through (8a) and the scattering coefficient through (8b) using QCA-CP of non-sticky spheres [16],

$$\kappa_a = k_0 \varepsilon''_{r,\mathrm{eff}} / \sqrt{\varepsilon'_{r,\mathrm{eff}}} \tag{5.8a}$$

$$\kappa_s = \frac{2}{9} k_0^4 a^3 f_v \left| \frac{\varepsilon_{r,\mathrm{ice}} - \varepsilon_0}{1 + \frac{\varepsilon_{r,\mathrm{ice}} - \varepsilon_0}{3\varepsilon_{r,\mathrm{eff}}}(1 - f_v)} \right|^2 \frac{(1 - f_v)^4}{(1 + 2f_v)^2} \tag{5.8b}$$

where a is the grain radius, and k_0 is the free space wave number.

(b) DMRT-ML and MEMLS

We apply two multi-layered incoherent models (DMRT-ML and MEMLS) that account for intermediate reflections between adjacent layers and volume scattering effects. Both models are based on radiative transfer theory and designed to model the microwave emission of layered snowpacks.

DMRT-ML [14, 16] solves the dense medium radiative transfer equation in the form of (9)

$$\cos\theta \frac{d}{dz}\bar{T}_B(z,\theta,\phi) = -\kappa_e \bar{T}_B(z,\theta,\phi) + \kappa_a T + \int_0^{\pi/2} \sin\theta' \, d\theta' \int_0^{2\pi} d\phi' \bar{\bar{P}}(\theta,\phi;\theta',\phi') \cdot \bar{T}_B(z,\theta',\phi') \tag{5.9}$$

subject to the incoherent boundary conditions, and applies the QCA-CP densely packed spheres scattering model [16] to calculate the effective permittivity and scattering coefficient κ_s; the extinction coefficient κ_e is then derived from the imaginary part of the effective permittivity. DMRT-ML assumes a Rayleigh scattering phase function. The DMRT equation is solved using the discrete ordinate method (DISORT), where a sufficient number of quadrature angles are chosen to discretize the integral over the inclination angle θ', followed by eigenvalue analysis to solve for the brightness temperature with multiple volume scattering effects included. DMRT-ML applies the same semi-empirical model of dielectric constant of ice as in [167], and the effective permittivity out of QCA-CP for non-sticky spheres is found to be quite close to the empirical model of equation (7), as shown in Figure V.3.

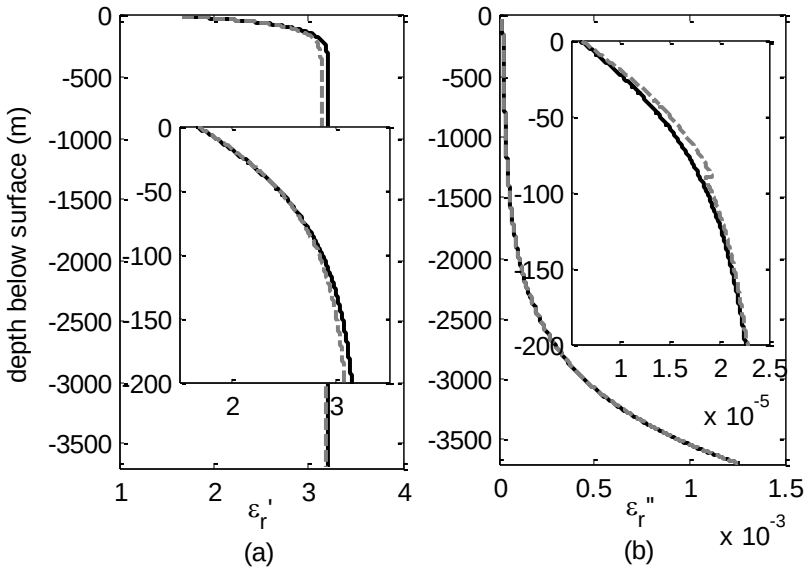

Figure V.3. Comparison of complex effective permittivity as a function of depth (real part: left; imaginary part: right) for the warmer ice sheet temperature profile with $M = 0.05m \cdot \mathrm{yr}^{-1}$ at 0.5GHz from Matzler and Tiuri's empirical formula of equation (7) and QCA-CP. Results of equation (7) are drawn as black solid lines, and results from QCA-CP are drawn as grey dash lines. The small insets are zoom-in views of the effective permittivity of the top 200 meters. The near constant offset beteen the real part at depth is a result of the value selection of ε_s in equation (7b); the jump of the imaginary part from QCA-CP at 90m is an artifact of grain radius vanishing in equation (4). These minor divergences will cause minimal influence to model predicted brightness temperature.

MEMLS [12, 154] on the other hand uses the six-flux theory to propagate the radiation through different layers. The radiative transfer equations of the brightness temperatures are of the type

$$-\frac{dT_{01}}{dz}|\cos\theta| = -\gamma_a(T_{01} - T) - \gamma_b(T_{01} - T_{02}) - \gamma_c(4T_{01} - T_{03} - T_{04} - T_{05} - T_{06}) \tag{5.10}$$

where the horizontal fluxes T_{03}, T_{04}, T_{05}, and T_{06} are equal and represent trapped radiation due to total reflection, and the vertical fluxes T_{01} and T_{02} represent downwelling and upwelling radiations within the critical angle, respectively. The absorption coefficient γ_a is derived from the effective permittivity which is calculated in a similar way to equation (7). The scattering

coefficient in the backward direction γ_b and the coefficient for coupling between the vertical and horizontal fluxes γ_c are related to the total scattering coefficient γ_s through the refractive index n of the layer. Unlike the "grain size" parameter used in the DMRT-ML (optical radius), MEMLS describes scatterers using a scatterer correlation length parameter so that the snow structure is described by a spatial two-point correlation function. However, the exponential correlation length p_{ex} can be related to an effective grain radius a through $p_{\mathrm{ex}} = a(1 - f_v)$ under certain assumptions, where f_v is the volume fraction [146]. The six-flux equations are solved by calculating eigenvalues (damping coefficient) in each layer and unknown coefficients are determined by matching incoherent boundary conditions, with the effective propagation direction θ of the vertical fluxes being corrected by the volume scattering effects, and the intermediate reflectivity being modified due to polarization mixing of volume scattering.

MEMLS treats a thin layer with one-way phase delay less than $3\pi/4$ separating two thick layers as coherent. The thin layer is completely replaced by a coherent reflectivity between the two thick layers while the volume scattering and absorption of the thin layer is ignored. In our calculation, however, this coherence feature is turned off because of the large number of adjacent thin layers.

(c) Coherent model

When volume scattering effects in the ice sheet are ignored, the thermal emission problem of a stratified medium has an exact solution with explicit formulas [15, 24]. The fluctuation-dissipation theorem connects the thermal motion inside a dissipative medium to fluctuating dipole moment with an equivalent current source $\bar{J}(\bar{r}, \omega)$ with expectation $\langle \bar{J}(\bar{r}, \omega)\bar{J}^*(\bar{r}', \omega') \rangle$ which is proportional to $\Theta(\omega, T) \approx KT$ at microwave frequencies following the Rayleigh-Jeans

approximation of Plank's radiation law, where K is the Boltzmann constant, and T is the absolute temperature. The equivalent current source $\bar{J}(\bar{r},\omega)$ generates radiation $\bar{E}(\bar{r},\omega)$ through the dyadic Green's function $\bar{\bar{G}}(\bar{r},\bar{r}'')$ with multilayer configuration. The brightness temperature as a spectral description of the differential radiation power is related to the auto-correlation of the radiation field. By applying a far-field approximation of the dyadic Green's function, one gets a closed form for the brightness temperature T_{B}:

$$
\begin{aligned}
T_{Bv}(\theta_o) = {} & \frac{k}{\cos\theta_o}\sum_{l=1}^{n}\frac{\varepsilon_l'' T_l}{2\varepsilon_0}\frac{(|k_{lz}|^2+k_x^2)}{|k_l|^2} \\
& \times\left\{\frac{|C_l|^2}{k_{lz}''}\left(e^{2k_{lz}''d_l}-e^{2k_{lz}''d_{l-1}}\right)-\frac{|D_l|^2}{k_{lz}''}\left(e^{-2k_{lz}''d_l}-e^{-2k_{lz}''d_{l-1}}\right)\right. \\
& \left.+\frac{|k_{lz}|^2-k_x^2}{|k_{lz}|^2+k_x^2}\cdot 2\mathrm{Re}\left[\frac{C_l D_l^*}{ik_{lz}'}\left(e^{-i2k_{lz}'d_l}-e^{-i2k_{lz}'d_{l-1}}\right)\right]\right\} \\
& +\frac{k}{\cos\theta_o}\frac{\varepsilon_t'' T_t}{2\varepsilon_0}\frac{(|k_{tz}|^2+k_x^2)}{k_{tz}''|k_t|^2}|T^{TM}|^2 e^{-2k_{tz}''d_n}
\end{aligned}
\tag{5.11a}
$$

$$
\begin{aligned}
T_{Bh}(\theta_o) = {} & \frac{k}{\cos\theta_o}\sum_{l=1}^{n}\frac{\varepsilon_l'' T_l}{2\varepsilon_0} \\
& \times\left\{\frac{|A_l|^2}{k_{lz}''}\left(e^{2k_{lz}''d_l}-e^{2k_{lz}''d_{l-1}}\right)-\frac{|B_l|^2}{k_{lz}''}\left(e^{-2k_{lz}''d_l}-e^{-2k_{lz}''d_{l-1}}\right)\right. \\
& \left.+2\mathrm{Re}\left[\frac{iA_l B_l^*}{k_{lz}'}\left(e^{-2k_{lz}'d_l}-e^{-2k_{lz}'d_{l-1}}\right)\right]\right\} \\
& +\frac{k}{\cos\theta_o}\frac{\varepsilon_t'' T_t}{2\varepsilon_0}\frac{1}{k_{tz}''}|T^{TE}|^2 e^{-2k_{tz}''d_n}
\end{aligned}
\tag{5.11b}
$$

The subscript l denotes the l-th snow/ice layer beneath the air/snow interface, while the subscript t denotes the bottom half space of the sub-glacial media. ε_l'' (ε_t'') and T_l (T_t) are the imaginary part of permittivity and the physical temperature of the l-th (t-th) layer, respectively.

$k_{lz} = \sqrt{k_l^2 - k_x^2}$, $k_l = k\sqrt{\varepsilon_l/\varepsilon_0}$ $k_x = k \sin\theta_o$, where θ_o is the observation angle measured in air. $z = -d_{l-1}$ and $z = -d_l$ are the top and bottom interface of the l-th snow/ice layer. T^{TM} and T^{TE} are the overall transmission coefficients of the layered media for vertical and horizontal polarization, respectively. A_l and B_l are the upward and downward electric field amplitude coefficients in the l-th layer for horizontal polarization, while C_l and D_l are the upward and downward electric field amplitude coefficients in the l-th layer for vertical polarization. A_l, B_l, C_l and D_l can be determined using the propagation matrix recursively, as documented in [15, 24].

The coherent model treats all the wave propagation and reflections in a fully coherent manner and thus is subject to strong wave interference in a single realization of the fluctuating density profile. The interference is sensitive to the thickness and density of each layer where intermediate reflection is significant. The ice layer effective permittivity model of equation (7) is applied in the coherent model.

Because a stochastic model of density fluctuations is utilized, results of the models are examined following an ensemble average of the predicted brightness temperature over multiple realizations. The ensemble average is performed using a Monte Carlo process. The results to be reported in the next section show that the Monte Carlo average reduces the brightness temperature fluctuations obtained from an individual density profile, particularly from the coherent model, into a more stable average pattern. The focus on comparison of ensemble average results is motivated by the typically large footprints of microwave radiometers (km or greater length scales) so that a single footprint is likely to contain many independent vertical density profiles.

5.1.4 Layering Scheme

All the models are designed to run with identical layer statistics. The continuous density profile represented by a Gaussian random process needs to be discretized into separate layers as

input to the models. Different layering schemes lead to different number of layers and different layer thickness, resulting in different microwave responses. Since we want to eliminate these layering artifacts and focus on the influence of the correlation length l of the density fluctuation to the brightness temperature predicted by different models, a special layering scheme is devised considering the sensitivity of all the models. We first generate the noisy part in the density profile of $\rho_n(z)$ in 1cm step, then locate its local maxima and minima as the points z_p of the layer, and divide the space around z_p to form layers. The density of each layer is calculated from equation (3) at the center of each layer z_c, i.e., $\tilde{\rho}(z_c) = \rho(z_c) + \rho_n(z_p) \cdot \exp(z_c/\alpha)$. This process is illustrated in Figure V.4 (a). It helps to discretize the density profile at an acceptable spatial scale as well as keeping maximum density contrast between adjacent layers. It also leads to a varying layer thickness. For a correlation length of 3cm, 5cm, 10cm and 40cm, the obtained mean layer thickness is 4.0cm, 6.5cm, 13cm and 53cm with standard deviation of 1.5cm, 2.5cm, 5.0cm and 20cm, respectively. The layering profile and the distribution of the derived layer thickness and density are depicted in Figure V.4 (a-c) with $\Delta = 0.040\text{g/cm}^3$ and $l = 3\text{cm}$.

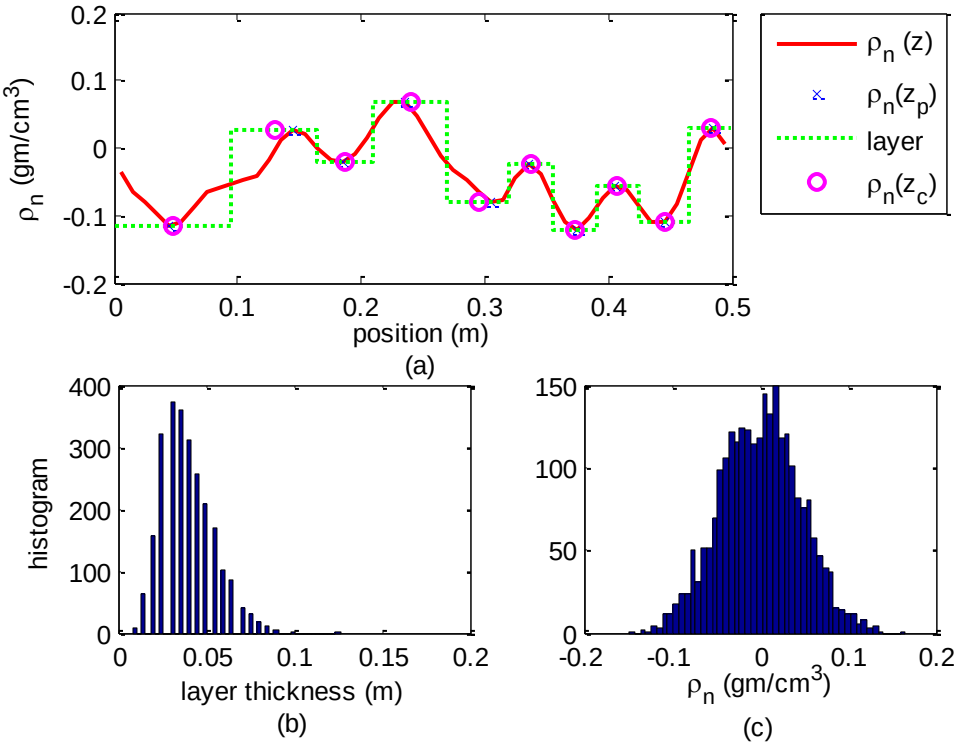

Figure V.4. Illustration of layering scheme using correlated density profile (a) discretization of the continuous density profile into layers, the continuous profile is obtained with $\Delta = 0.040\text{g/cm}^3$ and $l = 3$cm (b) distribution of derived layer thickness with a mean value of 4.0cm and standard deviation of 1.5cm (c) distribution of derived fluctuation of layer density with zero mean and standard deviation of 0.045 g/cm^3.

Since the density fluctuation quickly damps with depth, and since the models are insensitive to layer thickness for smoothly varying density profiles, a non-uniform layer thickness configuration below 100 meters are used to speed up computations. Specifically, we assume 50cm layer thickness between 100m and 300m, 1m layer thickness between 300m and 1000m, and 5m layer thickness between 1000m to bottom.

The discretization process applied may influence the final brightness temperatures computed. However analyses have shown that the general trends of the results (including the relationship between coherent and incoherent model predictions) remain the same even if other methods for discretizing the density profile are applied.

5.1.5 Model inter-comparison results and discussion

(a) Sensitivity to internal temperature profile and basal media

We first use the cloud model to illustrate general relationships between ice sheet brightness temperature and physical properties. This is similar to [51] except that we explicitly explore the frequency dependence. We calculate brightness temperature at nadir for the two temperature profiles shown in Figure V.2 (a) with M set to 0.01 and $0.05m \cdot \mathrm{yr}^{-1}$, respectively. The cloud model is computed with the average density profile of equation (2); note that the cloud model is insensitive to density fluctuations about the mean since it neglects any reflections caused by these variations: effects of fluctuations are averaged out via integration in computation of the brightness temperature. The penetration depth as a function of frequency for the two cases is plotted in Figure V.5 (a). The warmer temperature profile with $M = 0.01m \cdot \mathrm{yr}^{-1}$ in general has a smaller penetration depth due to the temperature enhanced attenuation rate. At higher frequency, the difference in penetration depth is smaller because the ice layers near the top have a larger influence and have similar and lower physical temperatures in the two cases. Even at the highest frequency of 2.0 GHz, the penetration depths are larger than 500m, thus the reflective cap layers of the top hundred meters are well within the penetration depth. Note the empirical permittivity model of equation (7c) does not take into account of impurities and inclusions in ice, which may possibly impact ice permittivity and reduce penetration.

The brightness temperature is computed for the cool profile with accumulation rate of $0.05m \cdot \mathrm{yr}^{-1}$ assuming a frozen rock base, and the warm profile with accumulation rate of $0.01m \cdot \mathrm{yr}^{-1}$ assuming a water base. For the warm profile, the brightness temperature is also calculated assuming a rock base. The results for the cloud model are shown in Figure V.5 (b). The warmer profile in general yields a higher brightness temperature. For the warmer profile, the brightness

temperature has very weak sensitivity to the basal media type. Only near the lowest frequency of 0.5GHz, a brightness temperature difference around 0.8K is observed benefitting from a large penetration depth; the brightness temperature with the water base is slightly lower. This result is consistent with [51]. The small temperature difference between the frozen and wet base indicates that the method is approaching the limit for sensing physical properties at depth in a cold-ice-sheet. In all the cases shown, the brightness temperature decreases monotonically with increasing frequency. In general, the larger brightness temperatures at lower frequencies relate closely to the warmer temperatures at greater depths.

In general, because the cloud model neglects internal reflections and therefore observes less reflection from the ice sheet in general, it should be expected that it will tend to obtain larger brightness temperatures than models that include internal reflections, if such reflections are significant.

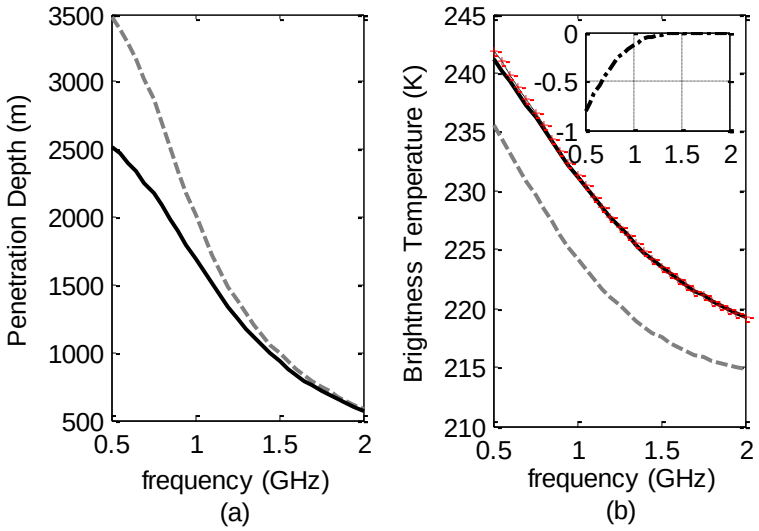

Figure V.5. Penetration depth (left) and brightness temperature (right) predicted by cloud model as a function of frequency. (a) Penetration depth for the warmer ice sheet temperature profile with $M = 0.01m \cdot \mathrm{yr}^{-1}$ (black solid curve) and the cooler profile with $M = 0.05m \cdot \mathrm{yr}^{-1}$ (grey dashed curve). (b) Brightness temperature for the cooler profile with frozen rock base (thick grey dashed curve), and the warmer profile with water base and rock base (shown as thick black solid curve and fine grey dashed curve with red marks, respectively). The inset shows the decrease in brightness temperature for the warmer profile when the base changes from frozen rock to water.

(b) Comparison of incoherent and coherent model results

The Cloud model, DMRT-ML, MEMLS and coherent models are deployed to run the same sets of ice sheet profiles. Density fluctuation constrained by correlation length is applied following equation (3) with $\Delta = 0.040\mathrm{g/cm^3}$ and then descritized using the scheme discribled in Section IV. Four cases of correlation length l of 3cm, 5cm, 10cm and 40cm are chosen to illustrate the results of nadir brightness temperature from 0.5GHz to 2.0GHz. In all cases, a water base is assumed with the warmer ice sheet temperature profile specified by $T_s = 216K$, $M = 0.01m \cdot \mathrm{yr}^{-1}$, and $H = 3700m$ in equation (1). The cloud model is again shown for the average density profile, while DMRT-ML, MEMLS, and coherent model predictions represent ensemble averages. DMRT-ML and MEMLS results are averages over ~150 realizations, while the coherent model is an average over 1000 realizations (to ensure sufficient averaging of the interference effects captured only by the coherent model). The computed brightness temperatures at nadir with the 40cm correlation length have a maximum standard deviation over the 0.5~2.0GHz spectra of 1.1K for DMRT-ML and MEMLS and 7.3K for the coherent model. This implies a much smaller number of realizations needed to achieve stable results with confidence. For the 3cm correlation length, however, the standard deviation could be as large as 2.0K for DMRT-ML and MEMLS and 52.5K for the coherent model, requiring sufficient large number of realizations for the coherent model to reach stable.

The brightness temperature of the cloud, DMRT-ML, MEMLS, and coherent models are compared in Figure V.6 (a, b, c, d) for correlation length of 3cm, 5cm, 10cm and 40cm, respectively.

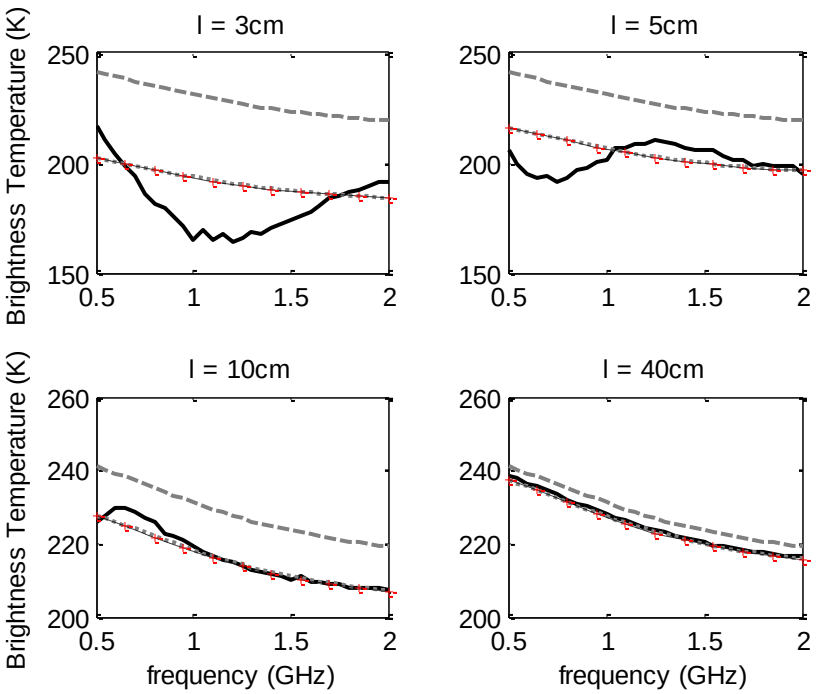

Figure V.6. Brightness temperature of incoherent and coherent models with correlation length of density fluctuation of (a) 3cm, (b) 5cm, (c) 10cm and (d) 40cm. The same Δ of $0.040\mathrm{g/cm}^3$ and α of $30m$ is applied to each case assuming a water base. The cloud model is run on the average density profile (grey dashed curve); DMRT-ML (grey dotted curve) and MEMLS (fine black dashed curve with red markers) are run on some 150 (100~200) realizations of density profile and averaged; coherent model is averaged over on 1000 Monte Carlo simulations (black solid curve). Note that the MEMLS and DMRT-ML results are nearly identical, and are difficult to distinguish in the figure. Their RMS difference aggregated across all frequencies is 0.23K, 0.32K, 0.30K and 0.34K for the correlation length of 3cm, 5cm, 10cm and 40cm, respectively.

As expected, the cloud model brightness temperatures are insensitive to correlation length. The other three models show that as the correlation length decreases, the brightness temperatures drop significantly. For a correlation length of 3cm, 5cm, 10cm and 40cm, DMRT-ML and MEMLS are approximately 83.8%, 89.4%, 94.5% and 98.5% of the cloud model. This follows the reduced amount of internal reflection expected as the correlation length becomes larger. The frequency dependence of DMRT-ML and MEMLS brightness temperatures is similar to that of the cloud model. The cloud model result at 2GHz is 21.8K less than at 0.5GHz. The DMRT-ML and MEMLS results drop about 18.3K, 19.5K, 20.6K and 21.5K across the spectrum for the

correlation length of 3cm, 5cm, 10cm and 40cm, respectively. The nearly uniform ratio between the cloud model and DMRT-ML and MEMLS as a function of frequency reveals that internal reflection effects have only a weak frequency dependence. This also implies a similar sensitivity to basal media type and internal temperature profile of DMRT-ML and MEMLS compared to the clould model except that a near constant transmissivity is to be applied to the cloud model results for each density fluctuation statistics.

The DMRT-ML and MEMLS results are nearly identical. Indeed, if differences are aggregated across all frequencies, the RMS differences between the models is 0.23K, 0.32K, 0.30K and 0.34K for the correlation length of 3cm, 5cm, 10cm and 40cm, respectively. The maximum difference is less than 0.5K. Especially for the nadir results presented here, this agreement is perhaps unsurprising, as similar permittivity models are used, scattering is unimportant, and the Fresnel reflection coefficients are treated identically in the two models. The models then differ only in their solution to the raditiave transfer equation. The results indicate that the six-flux approach of MEMLS is a good analog for the Gaussian quadrature approach, for this case.

The coherent results agree with DMRT-ML and MEMLS for profiles with large correlation length of 40cm. The difference between the simulated spectra is less than 1K point-wisely and about 0.65K in RMS difference. The minimal difference between the coherent model results and DMRT-ML/MEMLS is possibly due to different implementations of the effective permittivity models, since volume scattering effects are negligible with the assumed grain sizes.

For the smaller correlation lengths of 3cm, 5cm and 10cm, coherent model results show quite distinct frequency dependences from the DMRT-ML (and MEMLS) results. The resonance of the coherent results due to wave enhancement / cancellation depends on the correlation length of the density fluctuation. The period of resonance decreases as the correlation length increases.

The resonance pattern is quantitively explained by the reflection coefficient of a thin ice slab with refractive index n_1 embedded in two half spaces with refractive index n_0. The coherent reflectivity of the thin slab is enhanced if the round-trip phase delay is between $\pi/2$ and $3\pi/2$, giving rise to the maximum reflectivity at normal incidence when the thickness of the slab is of quarter-wavelength, corresponding to a minimum transmissivity. Assuming an ice fractional volume of 0.7, equation (7b) results to a refractive index of about 1.54. With 3cm correlation length, the mean layer thickness of 4.0cm is of quarter-wavelength inside the snow media at about 1.22GHz, corresponding closely to the minimum brightness temperature around 1.2GHz. The 5cm correlation length has a mean layer thickness of 6.5cm, shifting the minimum brightness temperature lower to around 0.75GHz. The coherent reflectivity of a single slab with fixed thickness is periodic. However, the random variation in layer thickness of the ice sheet cancels out the resonance at higher frequencies. With 10cm correlation length, the coherence effect extinguishes for frequency greater than 1.1GHz, where the average layer thickness of 13cm corresponds to 0.73 wavelength.

(c) Comparison of angular response of brightness temperature from DMRT-ML, MEMLS and the coherent model

The angular response of brightness temperature of the ice sheet is calculated by DMRT-ML, MEMLS and the coherent model at 1.4GHz and compared in Figure V.7 for both polarizations assuming two set of correlation lengths. The results with $l = 3cm$ are shown in Figure V.7 (a, b), and the results with $l = 10cm$ are shown in Figure V.7 (c, d). The ice sheet profiles and basal media types are the same as those used in Figure V.6 (a) and (c), respectively.

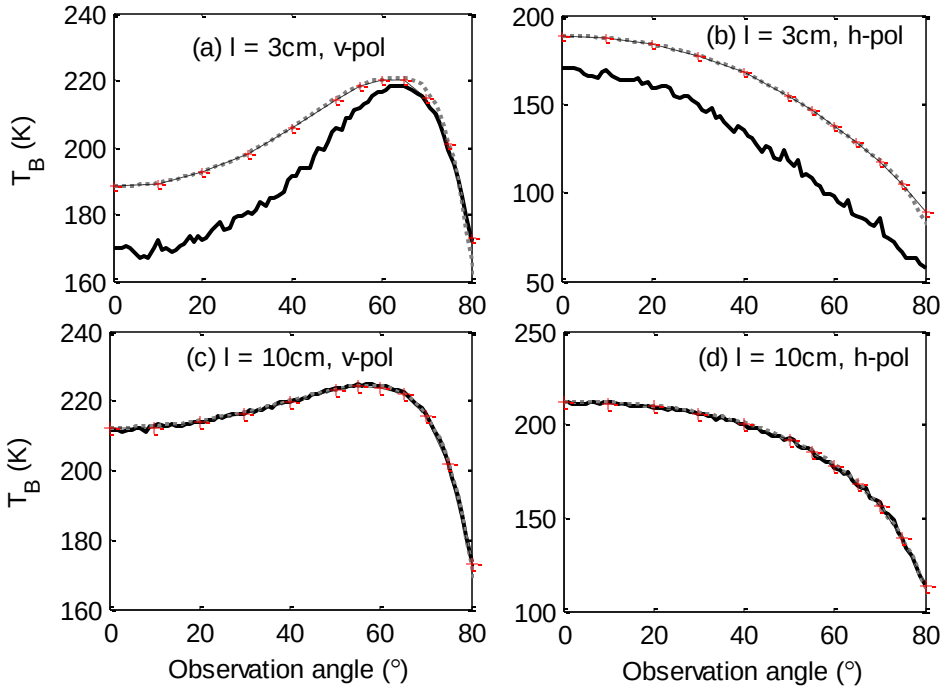

Figure V.7. Comparison of angular response of brightness temperature (left for v-pol and right for h-pol) at 1.4GHz predicted by DMRT-ML, MEMLS and the coherent model. The brightness temperatures are shown in (a, b) for $l = 3cm$, and (c, d) for $l = 10cm$. The coherent model results are shown as the thick black solid curve; DMRT-ML results are shown as the thick grey dotted curve; the MEMLS results are shown as the fine black dashed curve with red marks. Note that the MEMLS and DMRT-ML results are nearly identical, and are difficult to distinguish in the figure.

The results of DMRT-ML and MEMLS in general agree since the volume scattering effects are small. They follow exactly the same angular pattern. The pointwise differences are within 0.5K for small observation angle for both correlation lengths and smaller than 4K for large observation angles for $l = 3cm$ and smaller than 1K for large observation angles for $l = 10$cm. The RMS differences aggregated over observation angle are 2.0K, 1.6K, 0.56K, and 0.61K for $l = 3cm$ v-pol, $l = 3cm$ h-pol, $l = 10cm$ v-pol and $l = 10cm$ h-pol, respectively. The coherent model results agree closely with DMRT-ML and MEMLS for $l = 10cm$ when the coherence effects are distinguished as shown in Figure V.6 (c). The minimal RMS differences for v-pol and h-pol are 0.46K and 1.1K, respectively. For $l = 3cm$, when coherence effects are significant, the coherent

model results in v-pol seem to change more rapidly with respect to observation angle due to the phase enhanced interference. The coherence effects on angular dependence is further seen on Figure V.8, where the brightness temperature is computed at 0.5GHz and compared between the coherent model and DMRT-ML for $l = 10cm$ assuming the same ice sheet profile as in Figure V.6 (c). Although the nadir response is similar, the angular patterns diverge especially for h-pol.

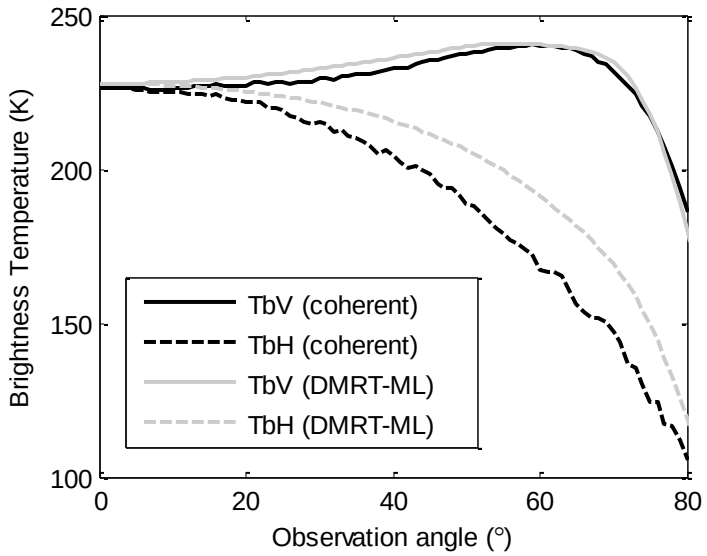

Figure V.8. Comparison of angular response of brightness temperature at 0.5GHz predicted by DMRT-ML and the coherent model. The ice sheet density fluctuation is quantified by $l = 10cm$, $\alpha = 30m$, and $\Delta = 0.040\text{g/cm}^3$.

In Figure V.9, the coherent model results and DMRT-ML results are compared against the L band SMOS angular data of Dome C Antarctica centered on Concordia Base [54]. The SMOS data are averaged over 4 months between November 2012 and March 2013, over a total of 274 images. There is good consistency between the SMOS data and the DOMEX-2 ground based radiometer observation. Airborne data were also acquired during DomeCAir campaign confirming the same trends with differences of around 1-2K. The coherent model and DMRT-ML are calculated on ice sheet profiles with 9cm correlation length leading to 11.54cm mean layer

thickness, a damping factor α of 70m, and Δ of $0.040\mathrm{g/cm^3}$ leading to a near surface layer density variation with standard deviation of $0.045\mathrm{g/cm^3}$. These parameters are within the range of field measurement at Dome C. Again, the coherent and incoherent model results are close as coherence effects are extinguished at L band with 9cm correlation length. Their RMS difference over $20^\circ\sim65^\circ$ observation angles is 1.1K for v-pol and 2.4K for h-pol. The DMRT-ML model predictions agree with the vertical-pol SMOS observations quite well with an RMS about 2.7K and mean difference of 2.5K. The RMS difference is on the level of the standard deviation of SMOS data. The model predictions also follow the horizontal-pol observations up to 35° with difference less than 1.7K. However, as the observation angle continue to increase, the predictions fall below the observations to ~20K by 60°. The higher h-pol brightness temperature observed implies an over-estimation of reflections at large observation angles, which is possibly due to the roughness of interfaces. The rough interface effects, should it be important, may also disturb the wave phase as it propagates over a long distance. This may weaken the coherence effects in brightness temperature with a relative small correlation length as depicted in Figure V.6.

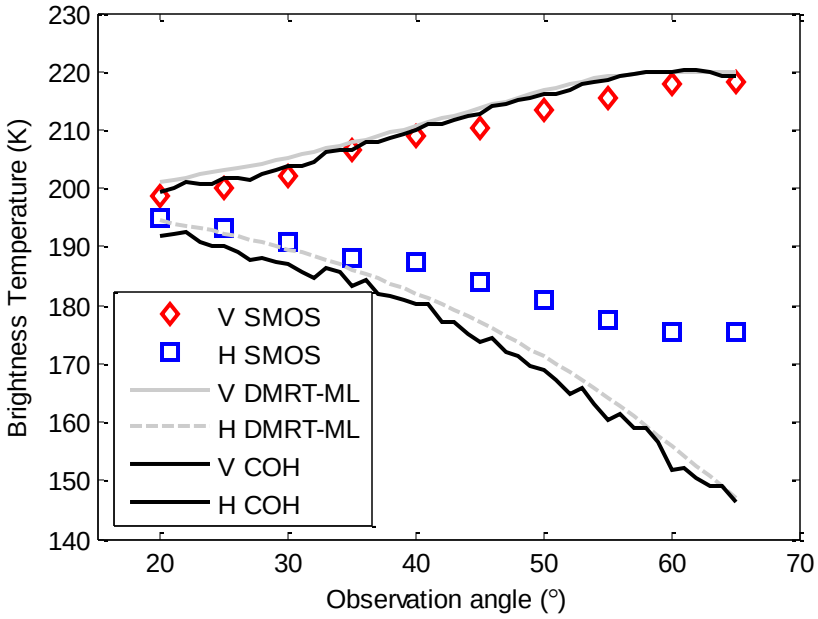

Figure V.9. Comparison of model prediction of brightness temperature from DMRT-ML and the coherent model with L band SMOS angular data at 1.4GHz. The ice sheet density fluctuation is quantified by $l = 9cm$, $\alpha = 70m$, and $\Delta = 0.040\mathrm{g/cm^3}$.

5.1.6 Conclusions

Three kinds of incoherent models, including the cloud model, DMRT-ML and MEMLS, and a coherent model based on the layered medium implementation of the fluctuation dissipation theorem are applied to model the brightness temperatures of the layered snow firn / ice sheet for the UWBRAD frequency band from 0.5GHz to 2GHz. The density fluctuation near the top hundred meters of the ice sheet is modeled as a correlated random process. The cloud model ignores all the intermediate reflections inside the ice sheet, and is suitable to study the sensitivity of brightness temperature to internal temperature profile and basal media type. All the other three models are affected by the density fluctuation effects near the top hundred meters of the ice sheet. Their results are averaged over a sufficiently large number of realizations to take into account of the lateral variations over the footprint. The results of DMRT-ML and MEMLS agree with each other with negligible volume scattering effects. The frequency dependence of DMRT-ML and

MEMLS are quite similar to the cloud model, but are lower than the cloud model as a result of intermediate reflections. The reduction in brightness temperature depends on the correlation length of the correlated fluctuating density profile. A 3cm correlation length of density fluctuation with standard deviation of $0.040\mathrm{g/cm^3}$ will cause a 16.2% decrease in brightness temperature. The coherent model has an extra frequency dependence on the correlation lengths of the rapid density fluctuations. If the correlation length is moderate or long compared with the wavelength, the coherent model results agree with the incoherent model results. The limiting case is a smooth density profile, for which case the coherent and incoherent approaches are identical. However, when the correlation length is less than half a wavelength, the coherent model gives significant differences from the incoherent model. Such differences are also frequency dependent over the frequency range of 0.5 to 2 GHz. The coherent model predicts a minimum brightness temperature when the mean layer thickness is of quarter wavelength inside the ice media. The coherence effects extinguishes when the mean layer thickness excesses some 0.73 wavelength at 1.1GHz. This is equivalent to a correlation length larger than 0.56 wavelength using the proposed layering scheme assuming a Gaussian correlation function. The coherent model results could be lower than DMRT-ML and MEMLS by ~27K at 1.2GHz with 3cm correlation length and $0.040\mathrm{g/cm^3}$ standard deviation of density fluctuation, larger than the dynamic range of 21.8K of the decrease in the clould model results across the 0.5~2.0GHz spectra. DMRT-ML, MEMLS and the coherent model have close angular patterns of brightness temperature for both polarizations when the coherence effects extinguishes. The model results with practical ice sheet density fluctuation quantified by $l = 9cm$, $\alpha = 70m$, and $\Delta = 0.040\mathrm{g/cm^3}$ are shown to be able to predict the v-pol SMOS data closely and match the h-pol data for small observation angles. A partially coherent approach is under investigation to account for the effects of rough interfaces to wave coherence. The gradual

layer thinning due to densification is to be examined and preliminary results imply that it could be partially represented by a smaller effective uniform mean layer thickness or correlation length of density fluctuation. This study is published in [58].

5.2 The Partially Coherent Approach Applied to Ice Sheet Emission

As discussed before, the surface of the polar ice sheet is characterized by rapid density variations on centimeter scales due to the accumulation process. The density variation induces permittivity fluctuations and cause reflections. These reflections, although small at each interface, accumulate from the large number of layers and decrease the overall emissivity. When the scale of density fluctuations is within one wavelength in the ice sheet, the coherent interference from reflections at multiple interfaces cannot be ignored. These coherent wave effects remains even after statistical averages over density profiles. We have studied the density fluctuation effects using both incoherent and coherent models. The coherent model agrees with the incoherent model for large correlation lengths of density fluctuation but differs from the incoherent model when the correlation length is less than half a wavelength.

Since coherent wave effects are “localized” in random layered media to spatial scales within a few wavelengths, we can divide the entire ice sheet into blocks, with each block on the order of a few wavelengths, and then apply fully coherent scattering models within a single block. The blocks are also sized to correspond to the bandwidth of the microwave channel so that interference effects within a channel can be captured. We then incoherently cascade the intensities among different blocks. A smaller number of realizations is then required in the Monte Carlo averaging process for each block due to the smaller number of interfaces. This partially coherent

approach has proved to be much more efficient than applying the fully coherent model to the entire ice sheet, and to produce results in agreement with the fully coherent approach [59, 170-172].

In summary, density variations near the top of the ice sheet form layers as well as introducing interface roughness [173]. The layering causes reflections and modulates the ice sheet emission. The interface roughness, on the other hand, causes angular and polarization coupling. The partially coherent approach enables us to examine interface roughness effects by applying a full wave small perturbation method up to second order (SPM2) to the multi-layered roughness scattering problem within the same block. The SPM2 has the advantage of conserving energy. Numerical results has been reported in checking energy conservation and in illustrating the angular and polarization coupling effects arising due to interface roughness [59-62, 170-172, 174].

5.2.1 The Formulation of the Partially Coherent Approach

(a) Coherent characterization of each block

We divide the many layers in the near surface reflective cap regions of the ice sheet, as depicted in Figure V.1, with density fluctuations into multiple blocks. Each block should be of several wavelengths and cover several correlation lengths of density variation. Then for each block, we apply the coherent model twice, one with the excitation / observation at the top of the block, and the second with the excitation / observation at the bottom of the block, to characterize the block, Figure V.10. Each block is characterized by five block parameters: $r^{(u)}$, $r^{(d)}$, $t = t^{(u)} = t^{(d)}$, $T_b^{(u)}$ and $T_b^{(d)}$. $r^{(u)}$, $t^{(u)}$ and $T_b^{(u)}$ are the reflectivity, transmissivity of the block and the brightness temperature emitted by the block, respectively, when the impinging wave is from the top and the observation is at the top of the block; vice versa for $r^{(d)}$, $t^{(d)}$ and $T_b^{(d)}$. Note that $t = t^{(u)} = t^{(d)}$ is guaranteed by reciprocity. All these parameters are functions of angles, and

polarizations. In this step, the coherent model as discussed before is applied to capture the coherent wave interactions within the block. A Monte Carlo simulation procedure is used to calculate the averaged block parameters. Since the number of layers within the same block is much smaller than the whole reflective cap region, the number of realizations needed for the results to converge is largely reduced. Each block can have a varying temperature profile $T(z)$ and a changing density profile $\rho(z)$. When $T(z) = T$ is constant within the same block, then $T_b^{(u)} = \left(1 - r^{(u)} - t\right)T$, and $T_b^{(d)} = \left(1 - r^{(d)} - t\right)T$. Also notice that since the blocks are arbitrarily divided, we apply the real part of the averaged effective permittivities at the boundaries $\mathrm{Re}[\varepsilon_{\mathrm{eff}}(z_u)]$ and $\mathrm{Re}[\varepsilon_{\mathrm{eff}}(z_d)]$ for the connecting regions above and below the block, respectively. These permittivities are taken to be real at the connections to facilitate the derivation of brightness temperatures which is a far field quantity.

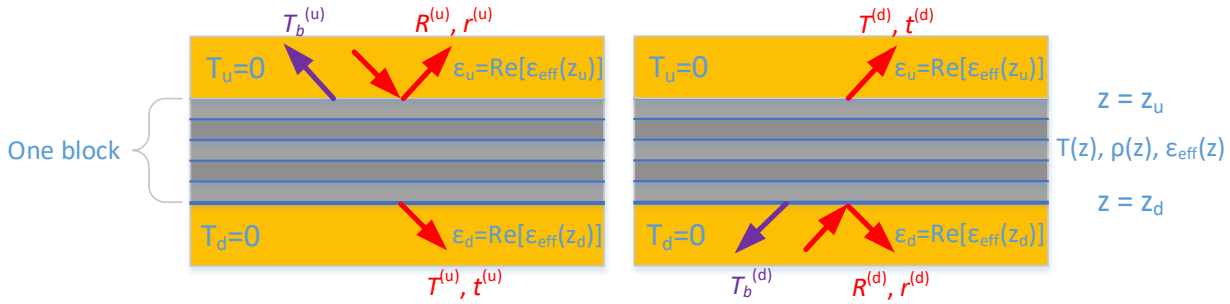

(a) excitation / observation from top (b) excitation / observation from bottom

Figure V.10. Characterization of one block of layers using coherent approach.

(b) Incoherent cascade between adjacent blocks

After each block is characterized with its block parameters, we then incoherently cascade these blocks by considering the boundary conditions between adjacent blocks using a radiative transfer approach. This process is done in a recursive manner, and in each step two adjacent blocks,

characterized by $T_{b1}^{(u)}, T_{b1}^{(d)}, r_1^{(u)}, r_1^{(d)}, t_1$ and $T_{b2}^{(u)}, T_{b2}^{(d)}, r_2^{(u)}, r_2^{(d)}, t_2$ are combined into one equivalent block with parameters $T_b^{(u)}, T_b^{(d)}, r^{(u)}, r^{(d)}, t$. This process is demonstrated in Figure V.11, where A and B denotes the upward and downward intensities in the connecting region, respectively.

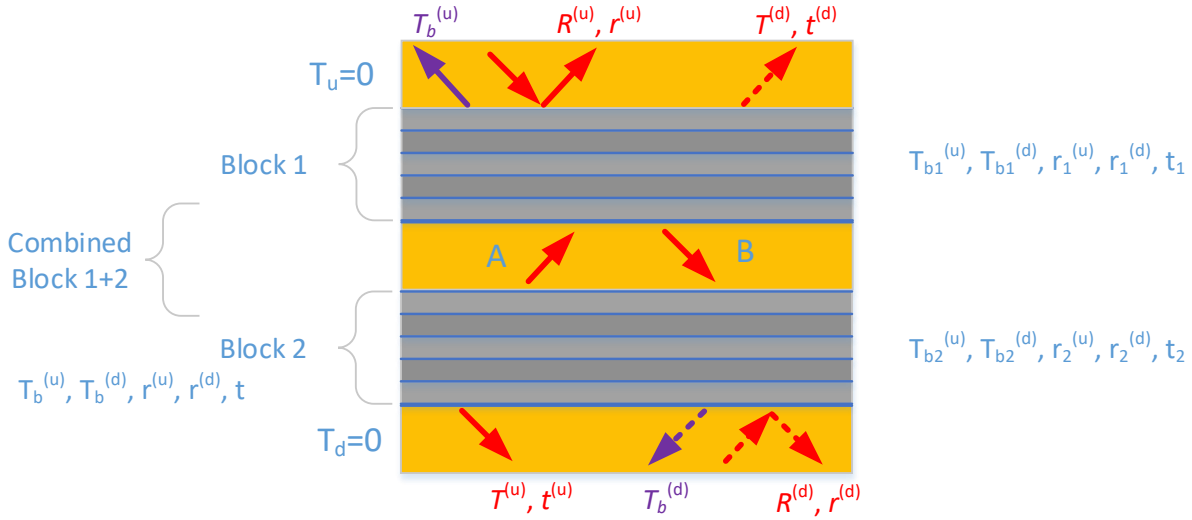

Figure V.11. Incoherent cascading of two adjacent blocks into one equivalent block.

1) For brightness temperatures, the boundary conditions imply

$$T_b^{(u)} = T_{b1}^{(u)} + At_1 \tag{5.12a}$$

$$T_b^{(d)} = T_{b2}^{(d)} + Bt_2 \tag{5.12b}$$

$$A = T_{b2}^{(u)} + Br_2^{(u)} \tag{5.12c}$$

$$B = T_{b1}^{(d)} + Ar_1^{(d)} \tag{5.12d}$$

From (12a-d), we could readily solve for A and B,

$$A = \frac{T_{b2}^{(u)} + T_{b1}^{(d)} r_2^{(u)}}{1 - r_1^{(d)} r_2^{(u)}} \tag{5.12e}$$

$$B = \frac{T_{b1}^{(d)} + T_{b2}^{(u)} r_1^{(d)}}{1 - r_1^{(d)} r_2^{(u)}} \tag{5.12f}$$

2) For the block reflectivity and transmissivity:

The boundary conditions are, for the excitation from the top,

$$r^{(u)} = r_1^{(u)} + A^{(u)} t_1 \tag{5.13a}$$

$$t^{(u)} = B^{(u)} t_2 \tag{5.13b}$$

$$A^{(u)} = B^{(u)} r_2^{(u)} \tag{5.13c}$$

$$B^{(u)} = t_1 + A^{(u)} r_1^{(d)} \tag{5.13d}$$

From (13a-d), we could readily solve for $r^{(u)}$ and $t^{(u)}$,

$$r^{(u)} = r_1^{(u)} + \frac{t_1^2 r_2^{(u)}}{1 - r_1^{(d)} r_2^{(u)}} \tag{5.13e}$$

$$t^{(u)} = \frac{t_1 t_2}{1 - r_1^{(d)} r_2^{(u)}} \tag{5.13f}$$

Similarly, with excitation from the bottom, we can readily solve for $r^{(d)}$ and $t^{(d)}$,

$$r^{(d)} = r_2^{(d)} + \frac{t_2^2 r_1^{(d)}}{1 - r_1^{(d)} r_2^{(u)}} \tag{5.13g}$$

$$t^{(d)} = \frac{t_1 t_2}{1 - r_1^{(d)} r_2^{(u)}} \tag{5.13h}$$

Note that (13f) and (13h) again confirms the fact that $t = t^{(u)} = t^{(d)}$.

(c) The ice bulk region with smooth temperature and density profile

Since there is no significant density fluctuations involved in this ice bulk region below the reflective cap region, as depicted in Figure V.1, all we want to capture is its smoothly varying temperature profile $T(z)$ and density profile $\rho(z)$, giving rise to a smoothly varying permittivity

profile $\varepsilon_{\text{eff}}(z)$. Thus either the coherent model or the incoherent model can be used to characterize this final block, with excitation / observation at the top, both yielding the same results. An incoherent model is implemented for this final block. The pre-described cascading procedure works for the connection between the reflective cap region and this ice bulk region as well.

5.2.2 Results of partially coherent model compared with the coherent model

The partially coherent approach are applied to the ice sheet emission problem and compared with results of the fully coherent approach. We define the ice sheet profile with parameters $M = 0.01m/\text{yr}$, $T_s = 216K$, $H = 3700m$; we assume a rock base with dielectric constant $5 + 0.1i$; the density fluctuations has surface standard deviation of $\Delta = 0.040g/\text{cm}^3$ and the damping coefficient $\alpha = 70m$. These are the same configuration as used in Figure V.6. We compare the brightness temperatures predicted by the two models in Figure V.12-Figure V.14, for three different correlation lengths of density fluctuation, $l = 3\text{cm}, 9\text{cm}$, and 40cm, respectively. The brightness temperatures are computed at nadir as a function of frequency. In all cases, the block size is chosen to be $\max(10\lambda, 10l)$, where λ is the free space wavelength and l is the correlation length of density fluctuation.

In Figure V.12, the correlation length $l = 3cm$, both the partially coherent results and the fully coherent results predicts a minimum brightness temperature at ~1.1GHz, where maximum reflection occurs when the correlation length is at roughly quarter wavelength in ice. This coherent feature is not captured by the incoherent approach. Included in the comparison are also results from an extreme configuration, labeled as "Cap + Bulk", where the coherent model is used to characterize the whole cap region before the results are combined with the underneath bulk region. The results from this computation is nearly identical to the fully coherent results where the

coherent model is used to simulate all the layers in the entire ice sheet including both the cap and bulk regions. However, the number of realizations for the "Cap + Bulk" calculation to reach reasonable convergence is 600, less than the 1000 times as needed in the fully coherent calculations. The partially coherent results on the other hand, only requires ~100 realizations to converge since its block is much smaller. Thus the partially coherent model produces results in agreement with the fully coherent approach but achieves significant speed up of about one order of magnitude.

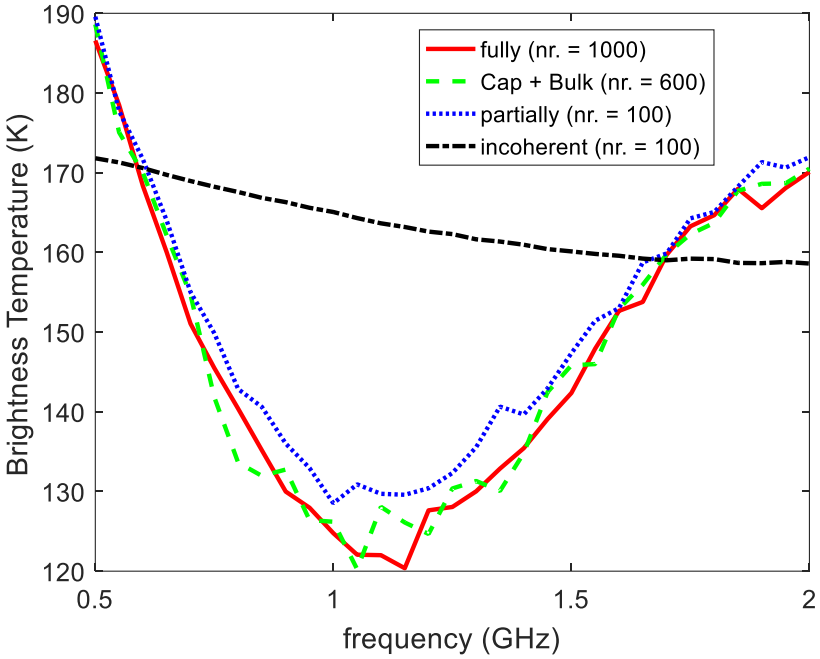

Figure V.12. Brightness temperature computed from partially coherent approach and fully coherent approach with $l = 3\text{cm}$

The same calculations are repeated in Figure V.13 for $l = 9\text{cm}$. Again the results agree showing a maximum brightness temperature at ~0.7GHz where minimum reflection occurs with correlation lengths at roughly half a wavelength in ice. Comparing to Figure V.12, the agreement between the partially coherent model and the fully coherent model becomes better as the

correlation length of density fluctuation increases. The speed up of the partially coherent model is similar as the previous case.

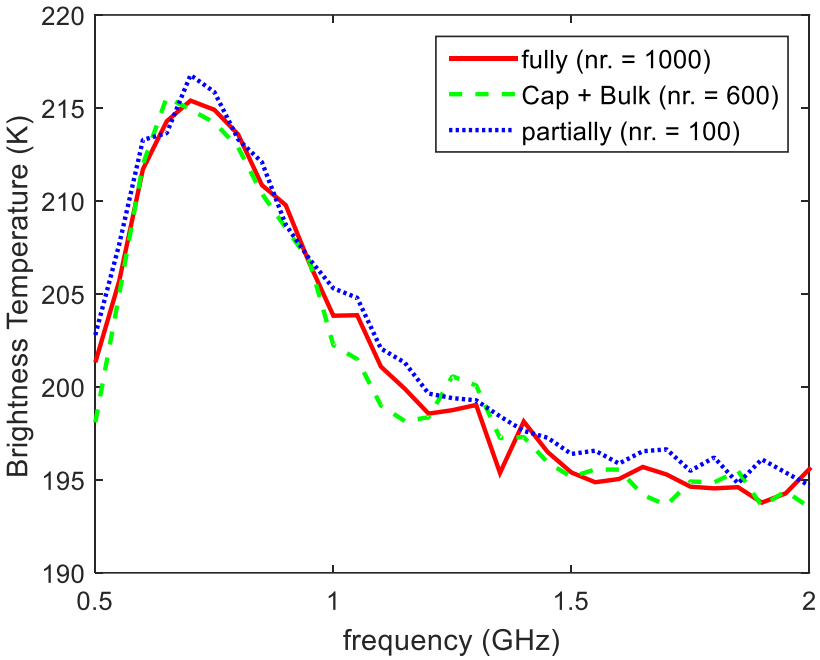

Figure V.13. Brightness temperature computed from partially coherent approach and fully coherent approach with $l = 9\text{cm}$.

We repeat the computation again with $l = 40\text{cm}$, Figure V.14. In this case, the results of partially coherent approach, the fully coherent approach and the incoherent approach all agree with each other, monotonically decreasing with frequency.

These examples confirms that the partially coherent model agrees with the coherent model in results, while at the same time it improves the computational efficiency by reducing the number of realizations in the Monte Carlo simulation.

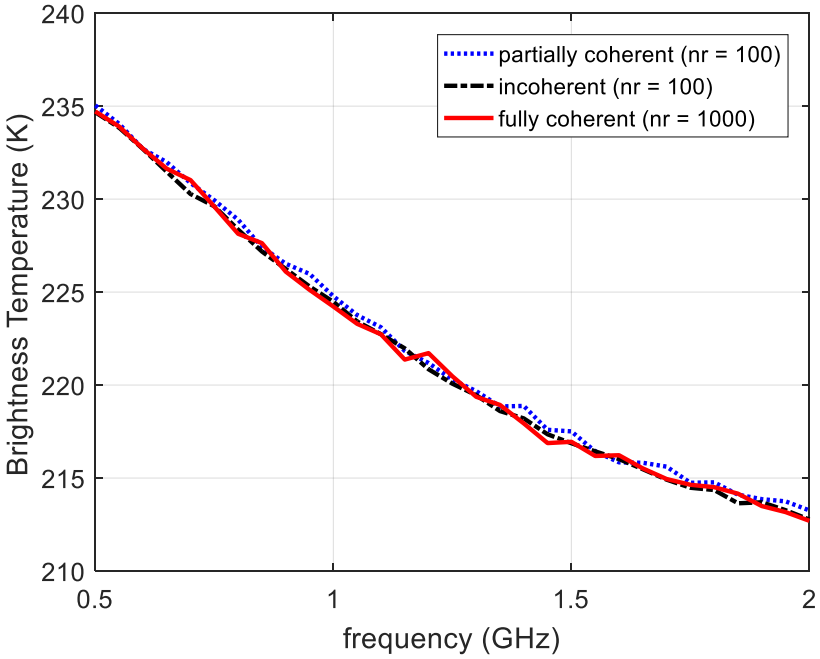

Figure V.14. Brightness temperature computed from partially coherent approach and fully coherent approach with $l = 40$cm.

5.2.3 Applied to Greenland Summit Ice Sheet Emission

The partially coherent model is applied to model the brightness temperature of the Greenland ice sheet and compared with the angular data from SMOS observations at L band. The model is validated at Greenland Summit where detailed ground truth are available from GISP borehole measurements. The temperature profile and density profile of the Greenland Summit are compared with the Antarctica Dome C in Figure V.15 (a) and (b), respectively. Note that temperature of Summit is much more uniform and higher in the top 2000 meters than the Dome C ice sheet. A rough estimation of the L-band penetration depth is 265m and 1000m at Summit and Dome C, respectively. Thus a much smaller brightness temperature gradient across the UWBRAD frequency spectrum is expected from the incoherent model predictions. The mean density profile of Summit saturates faster than Dome C with depth.

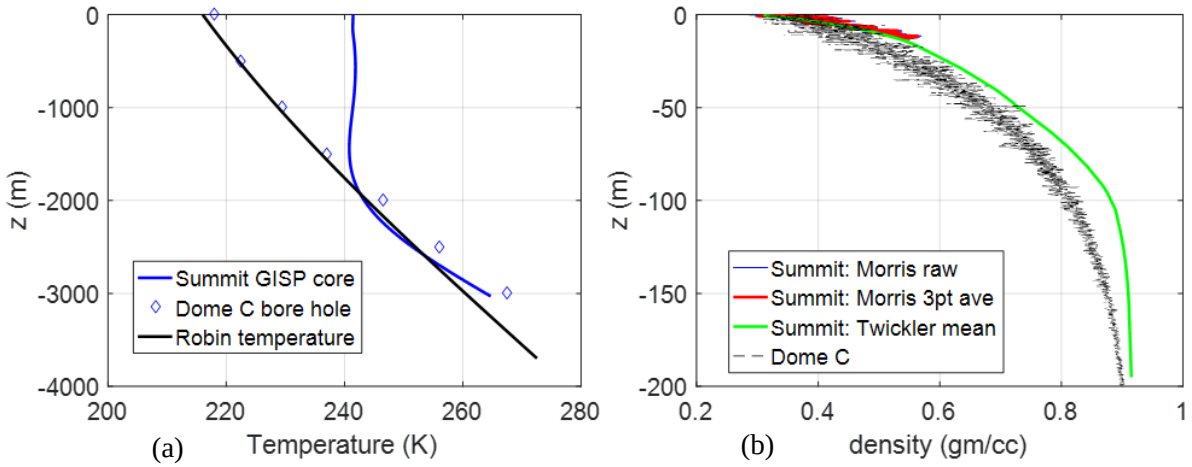

Figure V.15. Comparison of Greenland Summit and Antarctica Dome C (a) temperature profile (b) density profile

The Summit density profiles are again plotted in Figure V.16 (a) zooming in to the top ~12 meters. Included are the Twickler mean density profile at 1m resolution and the Morris neutron probe high resolution density profiles both at its original 1cm resolution and a 3-point moving average. In Figure V.16 (b), the normalized autocorrelation functions (ACFs) of the density variation are calculated from the 1cm high resolution Morris neutron probe measurements. The ACFs are extracted from a moving 1m window with top boundary starting at different depths. Both the density profile and its correlation functions suggests a two-scale density variation: a coarse scale at decimeter scale, and a fine scale at centimeter scale. The coarse scale variation quickly dies away while the fine scale fluctuation extends to depth and contributes to the overall reflections and exhibit the coherent layering effects.

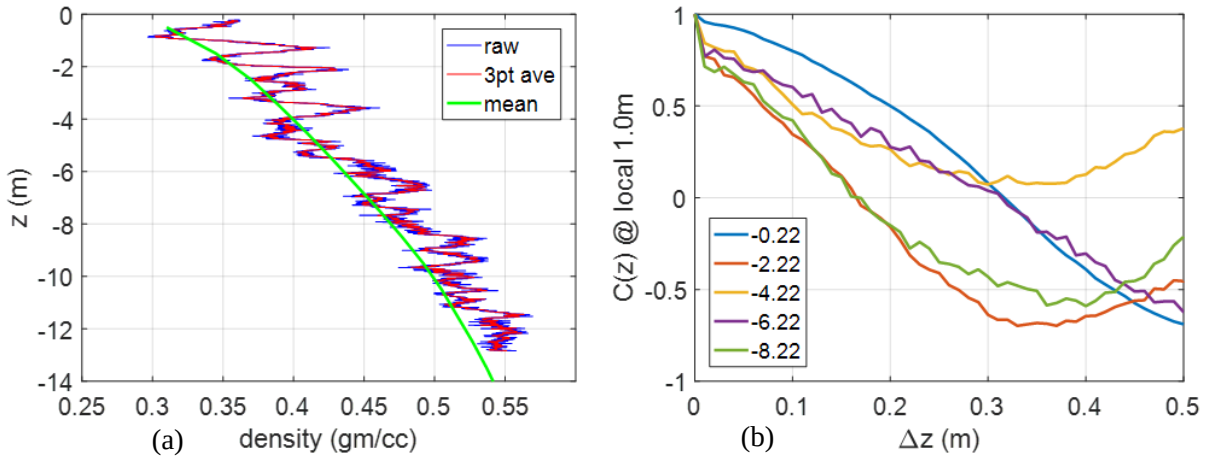

Figure V.16. The density profile and its correlation functions at Summit (a) The Morris neutron probe high resolution density profile and the Twickler mean density profile (b) Normalized auto correlation functions extracted from 1m window with top starting at different depths.

A two-scale density variation model is thus developed to model the density fluctuations. The model is an extension of Eq. (3) by adding up two independent fluctuations at different scales, while each of them is a correlated Gaussian random process with Gaussian correlation functions.

$$\rho(z) = \bar{\rho}(z) + \rho_n(z) \tag{5.14a}$$

$$\rho_n(z) = \rho_n^{(1)}(z)e^{z/\alpha_1} + \rho_n^{(2)}(z)e^{z/\alpha_2} \tag{5.14b}$$

$$\left\langle \rho_n^{(1)}(z)\rho_n^{(1)}(z') \right\rangle = \Delta_1^2 \exp\left(-\frac{(z-z')^2}{l_1^2}\right) \tag{5.14c}$$

$$\left\langle \rho_n^{(2)}(z)\rho_n^{(2)}(z') \right\rangle = \Delta_2^2 \exp\left(-\frac{(z-z')^2}{l_2^2}\right) \tag{5.14d}$$

where $\bar{\rho}(z)$ is the mean density profile taken from or interpolated from Twickler measurements.

The two scale density variation model is used to generate profiles and the synthesized density profile are compared with the Morris neutron probe measurements in Figure V.17 (a) and (b) with different zoom-in levels. The parameters used are $\Delta_1 = 0.040\text{g/cm}^3$, $l_1 = 20\text{cm}$, and $\alpha_1 = 8\text{m}$ for coarse scale, and are $\Delta_2 = 0.010\text{g/cm}^3$, $l_2 = 2\text{cm}$, and $\alpha_2 = 150\text{m}$ for fine scale. The results show promising agreement.

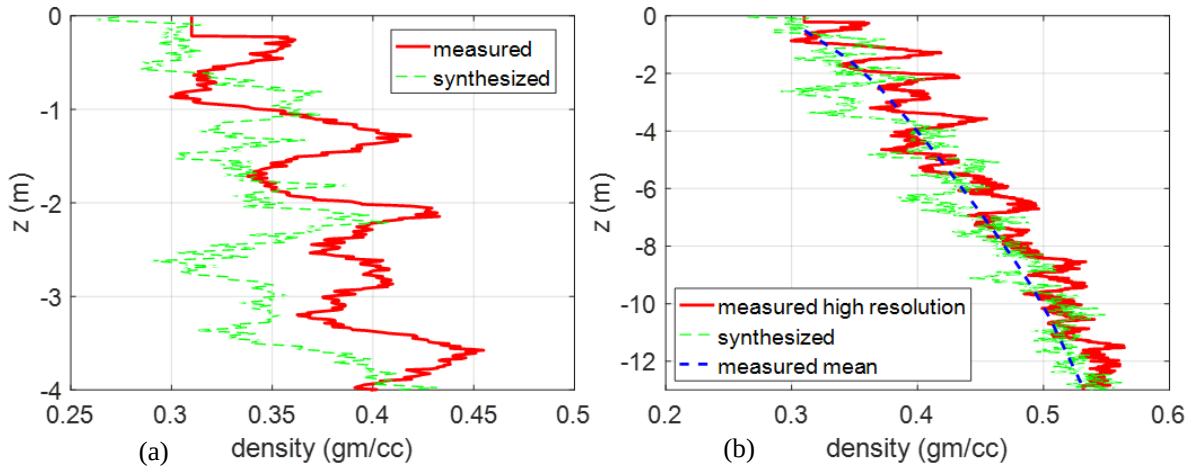

Figure V.17. Two scale density variation model compared with high resolution measurements.

The synthesized density profiles are used to feed the partially coherent model with the automated layering scheme as developed in Section 5.1.4. The predicted brightness temperatures are compared with SMOS observations as a function of angle at L band in Figure V.18 (a). The results from the incoherent model are also given. It is noted that the partially coherent model combined with the two scale density variations predicts an angular pattern in agreement with SMOS observations for both polarizations. The incoherent model, on the other hand, overestimate the brightness temperatures by ~10K. The models are also used to compute nadir brightness temperatures over the UWBRAD spectrum of 0.5~2.0GHz, Figure V.18 (b). It is shown that the partially coherent model produces a much larger dynamic range of ~25K as compared to ~4K predicted by the incoherent model in the UWBRAD spectrum. Considering the nearly constant physical temperature profile at Summit in the top ~2000m as compared to the penetration depths in Figure V.15 (a), the gradient in brightness temperatures across frequency is showing sensitivities to the near surface fine scale density variations.

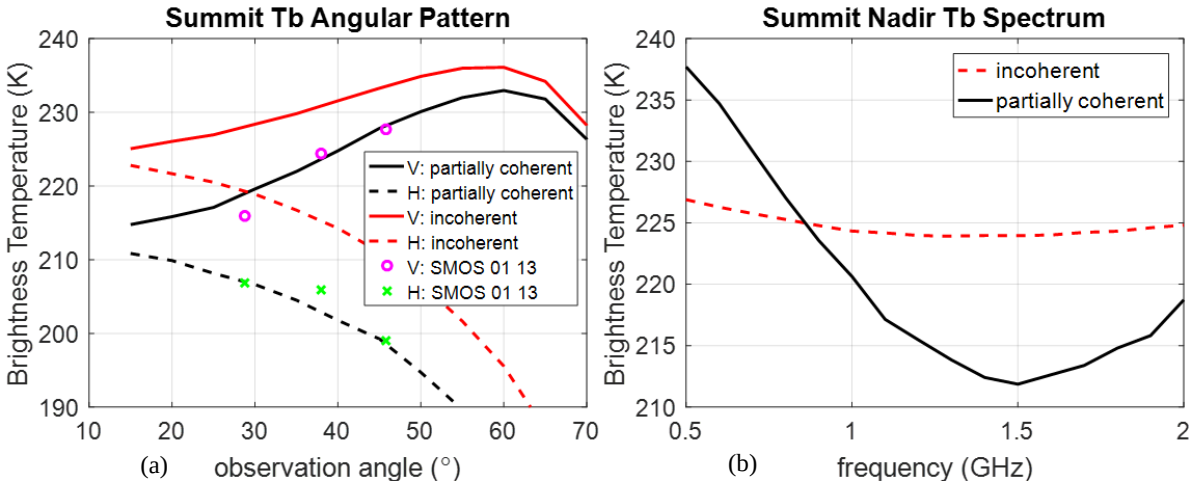

Figure V.18. Partially coherent model applied to Greenland brightness temperature simulation (a) angular pattern at L-band compared to SMOS observations (b) nadir brightness temperatures over the UWBRAD spectrum.

5.2.4 Partially coherent model to include multiple interface roughness

The partially coherent model not only improves the efficiency for the fully coherent model for the layered medium emission without sacrificing its coherent nature, it also provides a methodology to systematically include the roughness effects as caused by density fluctuations. All the interfaces between layers are rough. Roughness introduces angular coupling and polarization coupling that help to increase the brightness temperatures of H-pol at large angles without decreasing the V-pol brightness temperatures much. This will help to explain the mismatch between the model predictions and SMOS observations over Antarctica Dome C, as shown in Figure V.9, for large angles of H-pol.

Without the partially coherent model, it is computational unbearable to study the multi-layered roughness effects in 3D using a coherent approach, such as 2nd order small perturbation method (SPM2), considering the two-fold randomness introduced by random densities and random roughness. Using the partially coherent model, one only need to consider the multiple rough interfaces packed together in the same block. This concept is demonstrated in Figure V.19 as an

extension of Figure V.10 by introducing roughness. With roughness, one need to scan the incidence angle and polarization, and for each incidence wave exciting from the top and bottom, one need to characterize the block by the fully polarized bistatic scattering and transmission coefficients $\gamma_{\alpha\beta}(\theta,\phi;\theta',\phi')$. The emission from the block is also required at both polarizations and all the elevation angles. The scattering characterization of one block using SPM2 and the energy conservation of SPM2 has been studied in [61] for 2D, and in [62] for 3D. The efficient incoherent cascading of blocks including roughness is under progress [60, 174].

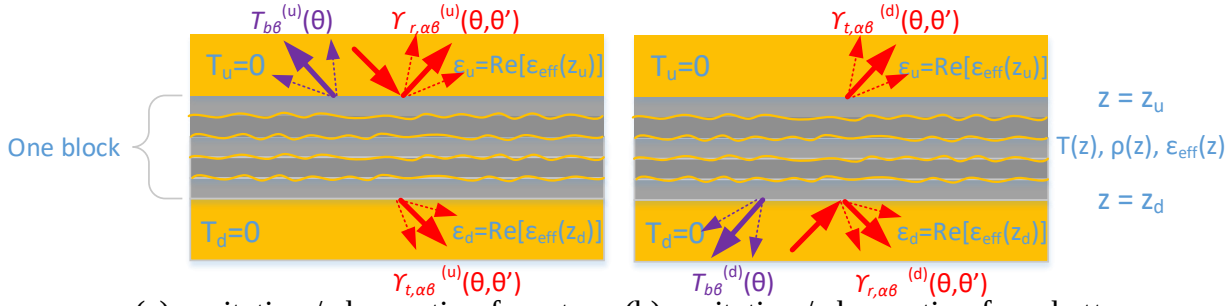

(a) excitation / observation from top (b) excitation / observation from bottom

Figure V.19. Extending the partially coherent model to include interface roughness.

CHAPTER VI

Calculations of Band Diagrams and Low Frequency Dispersion Relations of 2D Periodic Scatterers Using Broadband Green's Function with Low Wavenumber Extraction (BBGFL)

The broadband Green's function with low wavenumber extraction (BBGFL) is applied to the calculations of band diagrams of two-dimensional (2D) periodic structures with dielectric scatterers. Periodic Green's functions of both the background and the scatterers are used to formulate the dual surface integral equations by approaching the surface of the scatterer from outside and inside the scatterer. The BBGFL are applied to both periodic Green's functions. By subtracting a low wavenumber component of the periodic Green's functions, the broadband part of the Green's functions converge with a small number of Bloch waves. The method of moment (MoM) is applied to convert the surface integral equations to a matrix eigenvalue problem. Using the BBGFL, a linear eigenvalue problem is obtained with all the eigenmodes computed simultaneously giving the multiband results at a point in the Brillouin zone. Numerical results are illustrated for the honeycomb structure. The results of the band diagrams are in good agreement with the planewave method and the Korringa Kohn Rostoker (KKR) method. By using the lowest band around the Γ point, the low frequency dispersion relations are calculated which also give the effective propagation constants and the effective permittivity in the low frequency limit. The work discussed in this Chapter has been published in [81].

6.1 Introduction

The band solutions of waves in periodic structures are important in physics and engineering and in the design of photonic, electronic, acoustic, microwave and millimeter wave devices such as that in photonic crystals and metamaterials. The common approaches to calculate the bands include the planewave method [63, 84-87, 89, 175], and the Korringa Kohn Rostoker (KKR) method [96, 97]. The planewave method casts the problem into a linear eigenvalue problem and provides multiple band solutions simultaneously for a point in the Brillouin zone. However, in the planewave method, the permittivity (or potential) profile is expanded in Fourier series. For the case of abrupt profiles of large contrasts between background and scatterer, many terms are required in the Fourier series expansion. An artificially smeared dielectric function was also employed [175]. The convergence issue of the planewave method has been reported [87, 175]. The KKR method is a multiple scattering approach [98, 176] by forming the surface integral equations with periodic Green's function and the equation is solved by cylindrical or spherical waves expansions. The method is only convenient for scatterers with shapes of separable geometries such as circular cylinders or spheres. In the KKR/multiple scattering method, the eigenvalue problem is nonlinear requiring the root seeking procedure. One needs to repeat the non-linear root seeking one by one to find multiple band solutions. Numerical approaches such as the finite difference time domain method (FDTD) [92, 177] and finite element method (FEM) [94, 95, 178] have also been used.

In this chapter, the periodic Green's function is used to formulate the dual surface integral equations. The periodic Green's function has slow convergence. If the periodic Green's function is used for the surface integral equation to calculate the eigenvalues, the equation is nonlinear and an iterative search needs to be performed with one band at a time. Recently, the Broadband Green's

Function with Low wavenumber extraction (BBGFL) [82, 179-181] has been applied to wave propagation in waveguide/cavity of arbitrary shape. By using a single low wavenumber extraction, the convergence of the modal expansion of the Green's function is accelerated. Also the singularity of the Green's function has been extracted. The method has been shown to be efficient for broadband simulations of wave propagation in waveguides/ cavity. It was noted that the expression of modal expansion of Green's function in a waveguide is similar to the Floquet expansion of Green's function in a periodic structure [80]. In a recent paper [80] we adapted the BBGFL to calculate band diagrams in periodic structures where the scatterers obey Dirichlet boundary conditions. We use a low wavenumber extraction to accelerate the convergence of the periodic Green's function. The BBGFL is used to formulate the surface integral equations. Next applying the Method of Moments (MoM) gives a linear eigenvalue equation that gives all the multi-band solutions simultaneously for a point in the first Brillouin zone. We label this as "broadband simulations" as the multi-band solutions are calculated simultaneously rather than searching the band solution one at a time. The BBGFL method was shown to be accurate and computationally efficient. The choice of the low wavenumber was shown to be robust as the choice of the low wavenumber can be quite arbitrary. The application of MoM makes the method applicable to arbitrary shapes. It is noted that the Boundary Integral Resonant Mode Expansion (BIRME) method [182] was used to find the modes of an arbitrary shaped waveguide with PEC or perfect magnetic conductor (PMC) boundary conditions, using the Green’s functions of a rectangular waveguide or circular waveguide. In BIRME, a DC extraction is used for the Green’s function. In this chapter, we calculate band diagrams of periodic structures with general shapes of the unit cells and with dielectric scatterers embedded. Also, a low wavenumber extraction is used and the choice of the low wavenumbers is shown to be robust.

This chapter is an extension of BBGFL on perfect electric conductor [80] to periodic dielectric scatterers. The case of dielectric scatterers have much wider applications in devices of photonic crystals and metamaterials. For the case of dielectric scatterers, the dual surface integral equations are derived. A distinct feature in the formulation is that we use the periodic Green's function of the scatterers, in addition to using the periodic Green's function of the background. The application of the broadband periodic Green's function separates out the wavenumber dependence of Green's function, and allows the conversion of the non-linear root searching problem into a linear eigenvalue analysis problem. The low wavenumber extractions are applied to both periodic Green's functions for fast Floquet mode convergence and extraction of Green's function singularities. The use of MoM makes the method applicable to scatterers of arbitrary shape. In section 2, we formulate the dual surface integral equation using the extinction theorems and the periodic Green's functions. In Section 3, we apply BBGFL to the surface integral equations and derive the linear eigenvalue problem. In section 4, numerical results are illustrated for the band solution of circular air voids forming a honeycomb structure. The results are in good agreement with the plane wave method and the KKR method. We also describe the quick rejection of spurious modes by using extinction theorems. In Section 5, we use the lowest band around the Γ point to calculate the low frequency dispersion curves, the effective permittivity, and the effective propagation constants, all of which have wide applications in devices of metamaterials.

6.2 Extinction theorem and surface integral equations

Consider a periodic array in the xy plane of 2D dielectric scatterers embedded in a 2D lattice as illustrated in Figure VI.1. Let the primitive lattice vectors be $\bar{a}_1$ and $\bar{a}_2$ with lattice constant a and the primitive cell area $\Omega_0 = |\bar{a}_1 \times \bar{a}_2|$. The scatterer has dielectric constant ε_{rp} and

the background host ε_{rb}. Let S_{pq} denote the boundary of the scatterer in the (p,q)-th cell and A_{pq} is the domain of the scatterer in the (p,q) cell bounded by S_{pq}.

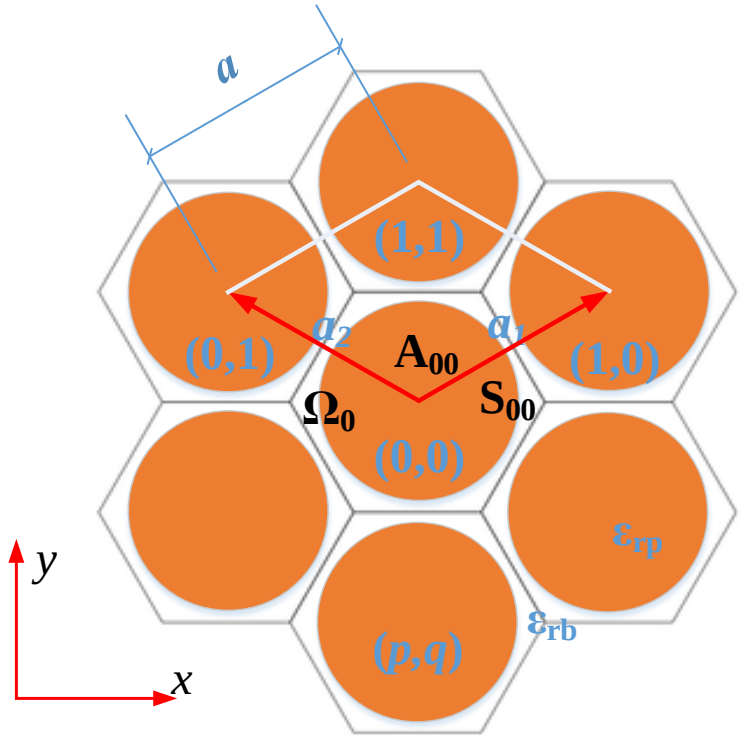

Figure VI.1. Geometry of the 2D scattering problem in 2D lattice. 2D dielectric scatterers form a periodic array with primitive lattice vectors $\bar{a}_1$ and $\bar{a}_2$, and lattice constant a. The primitive cell area $\Omega_0 = |\bar{a}_1 \times \bar{a}_2|$. The $(0,0)$-th scatterer has boundary S_{00} and cross section A_{00}. The scatterer and background has dielectric constant ε_{rp} and ε_{rb}, respectively.

We denote the field outside the scatterer as ψ and inside as ψ_1, where ψ represents E_z for TMz polarization and H_z for TEz polarization. TMz means that the magnetic field is perpendicular to the z direction while TEz means that the electric field is perpendicular to the z direction. The extinction theorems state that

$$\sum_{pq} \int_{S_{pq}} dl' [\psi(\bar{\rho}')\hat{n}' \cdot \nabla' g(\bar{\rho}, \bar{\rho}') - g(\bar{\rho}, \bar{\rho}')\hat{n}' \cdot \nabla' \psi(\bar{\rho}')] = 0 \tag{6.1a}$$

if $\bar{\rho}$ is inside any scatterer, and

$$-\int_{S_{pq}} dl'[\psi_1(\bar{\rho}')\hat{n}'\cdot\nabla' g_1(\bar{\rho},\bar{\rho}') - g_1(\bar{\rho},\bar{\rho}')\hat{n}'\cdot\nabla'\psi_1(\bar{\rho}')] = 0 \qquad (6.1b)$$

if $\bar{\rho}$ is not in A_{pq}.

In (1a) and (1b) $g(\bar{\rho},\bar{\rho}') = \frac{i}{4}H_0{}^{(1)}(k|\bar{\rho}-\bar{\rho}'|)$ and $g_1(\bar{\rho},\bar{\rho}') = \frac{i}{4}H_0{}^{(1)}(k_1|\bar{\rho}-\bar{\rho}'|)$ are the 2D free space Green's functions in the the background and in the scatterer, respectively. The wavenumbers are $k = \frac{\omega}{c}\sqrt{\varepsilon_{rb}}$, and $k_1 = \frac{\omega}{c}\sqrt{\varepsilon_{rp}}$ in the background and in the scatterer, respectively, where ω is the angular frequency and c is the speed of light.

Applying the Bloch wave condition to Eq. (1a), we have the surface integral to be only over S_{00} of the $(0,0)$ cell if $\bar{\rho}$ is inside any scatterer, then

$$\int_{S_{00}} dl'\left[\psi(\bar{\rho}')\hat{n}'\cdot\nabla' g_P\left(k,\bar{k}_i;\bar{\rho},\bar{\rho}'\right) - g_P\left(k,\bar{k}_i;\bar{\rho},\bar{\rho}'\right)\hat{n}'\cdot\nabla'\psi(\bar{\rho}')\right] = 0 \qquad (6.2a)$$

where $g_P\left(k,\bar{k}_i;\bar{\rho},\bar{\rho}'\right)$ is the periodic Green's function of the background and $\bar{k}_i$ is a point in the first Brillouin zone. In the KKR method [98], the integral equations in Eqs. (2a) and (1b) are used to calculate the band solutions meaning that the background Green's function is periodic while the scatterer Green's function is the free space Green's function. Instead of using (1b), we use periodic Green's function also for the scatterer and using extinction theorem, it can be shown that

$$-\int_{S_{00}} dl'\left[\psi_1(\bar{\rho}')\hat{n}'\cdot\nabla' g_{1P}\left(k_1,\bar{k}_i;\bar{\rho},\bar{\rho}'\right) - g_{1P}\left(k_1,\bar{k}_i;\bar{\rho},\bar{\rho}'\right)\hat{n}'\cdot\nabla'\psi_1(\bar{\rho}')\right] = 0 \qquad (6.2b)$$

if $\bar{\rho} \notin \cup A_{pq}$, i.e. $\bar{\rho}$ is in the background region. In (2b) $g_{1P}\left(k_1,\bar{k}_i;\bar{\rho},\bar{\rho}'\right)$ is the periodic Green's function of the scatterer. Thus, in the BBGFL formulations, we have periodic Green's functions for both integral equations. An interpretation is that the periodic Green's function is for an empty lattice, so that one can uses both g_P and g_{1P}.

Let $\bar{k}_i$ be a wavevector in the first irreducible Brillouin zone $\bar{k}_i = \beta_1 \bar{b}_1 + \beta^2 \bar{b}_2$, $0 \leq \beta_1, \beta_2 \leq 1/2$. $\bar{b}_1$ and $\bar{b}_2$ are the reciprocal lattice vectors.

$$\bar{b}_1 = 2\pi \frac{\bar{a}_2 \times \hat{z}}{\Omega_0}$$

$$\bar{b}_2 = 2\pi \frac{\hat{z} \times \bar{a}_1}{\Omega_0}$$

Then in the spectral domain the periodic Green's functions for, respectively, background and scatterer are

$$g_P\left(k, \bar{k}_i; \bar{\rho}, \bar{\rho}'\right) = \frac{1}{\Omega_0} \sum_{mn} \frac{\exp\left(i\bar{k}_{imn} \cdot (\bar{\rho} - \bar{\rho}')\right)}{\left|\bar{k}_{imn}\right|^2 - k^2} \tag{6.3a}$$

$$g_{1P}\left(k_1, \bar{k}_i; \bar{\rho}, \bar{\rho}'\right) = \frac{1}{\Omega_0} \sum_{mn} \frac{\exp\left(i\bar{k}_{imn} \cdot (\bar{\rho} - \bar{\rho}')\right)}{\left|\bar{k}_{imn}\right|^2 - k_1^2} \tag{6.3b}$$

where $\bar{k}_{imn} = \bar{k}_i + m\bar{b}_1 + n\bar{b}_2$. We will denote $\bar{k}_{imn}$by $\bar{k}_{i\alpha}$, where α is the short hand for the double index (m, n) of the Floquet mode.

The surface unknowns are $\psi(\bar{\rho}')$ and $\psi_1(\bar{\rho}')$, $\hat{n}' \cdot \nabla' \psi(\bar{\rho}')$ and $\hat{n}' \cdot \nabla' \psi_1(\bar{\rho}')$. There are boundary conditions for the TM case and the TE case giving a net of two surface unknowns $\psi(\bar{\rho}')$ and $\hat{n}' \cdot \nabla' \psi(\bar{\rho}')$ [34, 98]. Let $\bar{\rho}$ approach the boundary of S_{00}, the coupled surface integral equations in $\psi(\bar{\rho}')$ and $\hat{n}' \cdot \nabla' \psi(\bar{\rho}')$ are given as follows,

$$\int_{S_{00}} dl' \left[\psi(\bar{\rho}') \hat{n}' \cdot \nabla' g_P\left(k, \bar{k}_i; \bar{\rho}, \bar{\rho}'\right) - g_P\left(k, \bar{k}_i; \bar{\rho}, \bar{\rho}'\right) \hat{n}' \cdot \nabla' \psi(\bar{\rho}')\right] = 0\,, \bar{\rho} \to S_{00}^- \tag{6.4a}$$

$$\begin{aligned} -\int_{S_{00}} dl' \left[\psi(\bar{\rho}') \hat{n}' \cdot \nabla' g_{1P}\left(k_1, \bar{k}_i; \bar{\rho}, \bar{\rho}'\right) - g_{1P}\left(k_1, \bar{k}_i; \bar{\rho}, \bar{\rho}'\right) \frac{1}{s} \hat{n}' \cdot \nabla' \psi(\bar{\rho}')\right] \\ = 0, \bar{\rho} \to S_{00}^+ \end{aligned} \tag{6.4b}$$

where S_{00}^{+} and S_{00}^{-} denote approaching from the outside and inside of S_{00}, respectively. In Eqs. (4a) and (4b) $s = 1$ for TMz polarization and $s = \frac{\varepsilon_{rb}}{\varepsilon_{rp}}$ for TEz polarization.

Applying MoM with pulse basis functions and point matching, we discretize S_{00} into N patches. In matrix form, we obtain

$$\bar{\bar{S}}\bar{p} - \bar{\bar{L}}\bar{q} = 0 \tag{6.5a}$$

$$\bar{\bar{S}}^{(1)}\bar{p} - \frac{1}{s}\bar{\bar{L}}^{(1)}\bar{q} = 0 \tag{6.5b}$$

where $\bar{\bar{S}}$, $\bar{\bar{S}}$, $\bar{\bar{S}}^{(1)}$ and $\bar{L}^{(1)}$ are $N \times N$ matrices; and $\bar{p}$ and $\bar{q}$ are $N \times 1$ column vectors. Let $m, n = 1,2,\ldots,N$. The matrix elements are

$$S_{mn} = \frac{1}{\Delta t_n}\int_{S_{00}^{(n)}} dl'\left[\hat{n}' \cdot \nabla' g_P\left(k, \bar{k}_i; \bar{\rho}, \bar{\rho}'\right)\right], \bar{\rho} \to \bar{\rho}_m^{-} \tag{6.6a}$$

$$L_{mn} = \frac{1}{\Delta t_n}\int_{S_{00}^{(n)}} dl'\left[g_P\left(k, \bar{k}_i; \bar{\rho}_m, \bar{\rho}'\right)\right] \tag{6.6b}$$

$$S_{mn}^{(1)} = \frac{1}{\Delta t_n}\int_{S_{00}^{(n)}} dl'\left[\hat{n}' \cdot \nabla' g_{1P}\left(k_1, \bar{k}_i; \bar{\rho}, \bar{\rho}'\right)\right], \bar{\rho} \to \bar{\rho}_m^{+} \tag{6.6c}$$

$$L_{mn}^{(1)} = \frac{1}{\Delta t_n}\int_{S_{00}^{(n)}} dl'\left[g_{1P}\left(k_1, \bar{k}_i; \bar{\rho}_m, \bar{\rho}'\right)\right] \tag{6.6d}$$

$$p_n = \Delta t_n \psi(\bar{\rho}_n) \tag{6.7a}$$

$$q_n = \Delta t_n [\hat{n} \cdot \nabla\psi(\bar{\rho})]_{\bar{\rho}=\bar{\rho}_n} \tag{6.7b}$$

where $\bar{\rho}_n$ is the center and Δt_n the arc length of the n-th patch $S_{00}^{(n)}$. $\bar{\rho} \to \bar{\rho}_m^{-}$ and $\bar{\rho} \to \bar{\rho}_m^{+}$ means $\bar{\rho}$ approaches $\bar{\rho}_m$ from inside and outside of S_{00}, respectively.

6.3 BBGFL in surface integral equations

We want to find the wavenumbers that satisfy both the surface integral equations in Eq. (4). These wavenumbers are the band solutions, and the corresponding surface field ψ and $\hat{n} \cdot \nabla\psi$ are the modal currents. This is an eigenvalue problem. The technique of BBGFL is described below.

6.3.1 Low wavenumber extraction in the Broadband Periodic Green's function

In the BBGFL method, we choose a single low wavenumber k_L, which is quite arbitrary, to decompose $g_P\left(k, \bar{k}_i; \bar{\rho}, \bar{\rho}'\right)$ into $g_P\left(k_L, \bar{k}_i; \bar{\rho}, \bar{\rho}'\right)$ and the difference $g_B\left(k, k_L, \bar{k}_i; \bar{\rho}, \bar{\rho}'\right)$. They shall be labelled as the low wavenumber part and the broadband part, respectively.

$$g_P\left(k, \bar{k}_i; \bar{\rho}, \bar{\rho}'\right) = g_P\left(k_L, \bar{k}_i; \bar{\rho}, \bar{\rho}'\right) + g_B\left(k, k_L, \bar{k}_i; \bar{\rho}, \bar{\rho}'\right) \tag{6.8a}$$

Using the spectral domain of $g_P\left(k, \bar{k}_i; \bar{\rho}, \bar{\rho}'\right)$ from (3a), we then have

$$g_B\left(k, k_L, \bar{k}_i; \bar{\rho}, \bar{\rho}'\right) = \frac{k^2 - k_L^2}{\Omega_0} \sum_{\alpha} \frac{\exp\left(i\bar{k}_{i\alpha} \cdot (\bar{\rho} - \bar{\rho}')\right)}{\left(\left|\bar{k}_{i\alpha}\right|^2 - k^2\right)\left(\left|\bar{k}_{i\alpha}\right|^2 - k_L^2\right)} \tag{6.8b}$$

Note that $g_P\left(k_L, \bar{k}_i; \bar{\rho}, \bar{\rho}'\right)$ is independent of wavenumber k, and the series in $g_B\left(k, k_L, \bar{k}_i; \bar{\rho}, \bar{\rho}'\right)$ converges as $\left|\bar{k}_{i\alpha}\right|^{-4}$ instead of $\left|\bar{k}_{i\alpha}\right|^{-2}$.

For the case of dielectric scatterer, we also decompose the periodic Green's function of the scatterer $g_{1P}\left(k_1, \bar{k}_i; \bar{\rho}, \bar{\rho}'\right)$ into a low wavenumber part $g_{1P}\left(k_{1L}, \bar{k}_i; \bar{\rho}, \bar{\rho}'\right)$ with k_{1L} and a broadband part $g_{1B}\left(k_1, k_{1L}, \bar{k}_i; \bar{\rho}, \bar{\rho}'\right)$

$$g_{1P}\left(k_1, \bar{k}_i; \bar{\rho}, \bar{\rho}'\right) = g_{1P}\left(k_{1L}, \bar{k}_i; \bar{\rho}, \bar{\rho}'\right) + g_{1B}\left(k_1, k_{1L}, \bar{k}_i; \bar{\rho}, \bar{\rho}'\right) \tag{6.8c}$$

$$g_{1B}\left(k_1, k_{1L}, \bar{k}_i; \bar{\rho}, \bar{\rho}'\right) = \frac{k_1^2 - k_{1L}^2}{\Omega_0} \sum_{\alpha} \frac{\exp\left(i\bar{k}_{i\alpha} \cdot (\bar{\rho} - \bar{\rho}')\right)}{\left(\left|\bar{k}_{i\alpha}\right|^2 - k_1^2\right)\left(\left|\bar{k}_{i\alpha}\right|^2 - k_{1L}^2\right)} \tag{6.8d}$$

We next express g_B in the following form

$$g_B\left(k,k_L,\bar{k}_i;\bar{\rho},\bar{\rho}'\right)=\frac{1}{\Omega_0}\sum_{\alpha}\frac{1}{\frac{1}{k^2-k_L^2}-\frac{1}{\left|\bar{k}_{i\alpha}\right|^2-k_L^2}}\frac{\exp\left(i\bar{k}_{i\alpha}\cdot(\bar{\rho}-\bar{\rho}')\right)}{\left(\left|\bar{k}_{i\alpha}\right|^2-k_L^2\right)^2} \tag{6.8e}$$

$$=\sum_{\alpha}R_{\alpha}(k_L,\bar{\rho})W_{\alpha}(k,k_L)R_{\alpha}^{*}(k_L,\bar{\rho}') \tag{6.8f}$$

where

$$R_{\alpha}(k_L,\bar{\rho})=\frac{1}{\sqrt{\Omega_0}}\sum_{\alpha}\frac{\exp\left(i\bar{k}_{i\alpha}\cdot\bar{\rho}\right)}{\left|\bar{k}_{i\alpha}\right|^2-k_L^2} \tag{6.9a}$$

$$W_{\alpha}(k,k_L)=\frac{1}{\lambda(k,k_L)-D_{\alpha}(k_L)} \tag{6.9b}$$

$$\lambda(k,k_L)=\frac{1}{k^2-k_L^2} \tag{6.9c}$$

$$D_{\alpha}(k_L)=\frac{1}{\left|\bar{k}_{i\alpha}\right|^2-k_L^2} \tag{6.9d}$$

It follows that

$$\hat{n}'\cdot\nabla' g_B\left(k,k_L,\bar{k}_i,\bar{\rho},\bar{\rho}'\right)=\sum_{\alpha}R_{\alpha}(k_L,\bar{\rho})W_{\alpha}(k,k_L)Q_{\alpha}^{*}(k_L,\bar{\rho}') \tag{6.10}$$

where

$$Q_{\alpha}(k_L,\bar{\rho})=\hat{n}\cdot\nabla R_{\alpha}(k_L,\bar{\rho})=\left[\hat{n}\cdot\left(i\bar{k}_{i\alpha}\right)\right]R_{\alpha}(k_L,\bar{\rho}) \tag{6.11}$$

Both g_B and $\hat{n}'\cdot\nabla' g_B$ are smooth for arbitrary $\bar{\rho}-\bar{\rho}'$ and they converge everywhere including the self-point of $\bar{\rho}=\bar{\rho}'$. Because of fast convergence, we will truncate the series with M Floquet modes. Note the two dimensional index in α. (In our numerical implementation, each index is from -10 to 10, so that $M=(21)^2=441.$)

With the decomposition$g_P\left(k_L,\bar{k}_i;\bar{\rho},\bar{\rho}'\right)+g_B\left(k,k_L,\bar{k}_i;\bar{\rho},\bar{\rho}'\right)$, the matrices $\bar{\bar{S}}$ and $\bar{\bar{L}}$ (Eq. 6) are also in two parts which are the low wavenumber part and the broadband part

$$\bar{\bar{S}}(k)=\bar{\bar{S}}(k_L)+\bar{\bar{S}}(k_L)\bar{\bar{W}}(k_L,k)\bar{\bar{Q}}^{\dagger}(k_L) \tag{6.12a}$$

$$\bar{\bar{L}}(k)=\bar{\bar{L}}(k_L)+\bar{\bar{R}}(k_L)\bar{\bar{W}}(k_L,k)\bar{\bar{R}}^{\dagger}(k_L) \tag{6.12b}$$

$\bar{\bar{R}}$ and $\bar{\bar{Q}}$ are $N\times M$ matrices. The superscript † means Hermitian adjoint. The matrices $\bar{\bar{S}}(k_L)$, $\bar{\bar{L}}(k_L)$, $\bar{\bar{R}}(k_L)$ and $\bar{Q}(k_L)$ do not have wavenumber dependence. The only wavenumber dependence lies in the factor $\lambda(k,k_L)$ of the $M\times M$ diagonal matrix $\bar{\bar{W}}(k_L,k)$

$$\bar{\bar{W}}(k_L,k)=\left(\lambda(k,k_L)\bar{\bar{I}}-\bar{\bar{D}}(k_L)\right)^{-1} \tag{6.13a}$$

where $\bar{\bar{I}}$ is the $M\times M$ identity matrix and $\bar{\bar{D}}$ is the $M\times M$ diagonal matrix,

$$D_{\alpha\alpha}=D_{\alpha}(k_L) \tag{6.13b}$$

With the low wavenumber separation in $\bar{\bar{S}}$ and $\bar{\bar{L}}$, the matrix form of the surface integral equation Eq. (5a) becomes

$$\bar{\bar{S}}(k_L)\bar{p}-\bar{\bar{L}}(k_L)\bar{q}+\bar{\bar{R}}(k_L)\bar{\bar{W}}(k_L,k)\bar{\bar{Q}}^{\dagger}(k_L)\bar{p}-\bar{\bar{R}}(k_L)\bar{\bar{W}}(k_L,k)\bar{\bar{R}}^{\dagger}(k_L)\bar{q}=0 \tag{6.14a}$$

Using the surface integral equations with periodic Green's functions of the scatterer $g_{1P}\left(k_1,\bar{k}_i;\bar{\rho},\bar{\rho}'\right)$ which is also decomposed into a low wavenumber part and a broadband part, we have from Eq. (5b)

$$\begin{aligned}\bar{\bar{S}}^{(1)}(k_{1L})\bar{p}-\frac{1}{s}\bar{\bar{L}}^{(1)}(k_{1L})\bar{q}+\bar{\bar{R}}^{(1)}(k_{1L})\bar{\bar{W}}^{(1)}(k_{1L},k_1)\bar{\bar{Q}}^{(1)\dagger}(k_{1L})\bar{p}\\ -\frac{1}{s}\bar{\bar{R}}^{(1)}(k_{1L})\bar{\bar{W}}^{(1)}(k_{1L},k_1)\bar{\bar{R}}^{(1)\dagger}(k_{1L})\bar{q}=0\end{aligned} \tag{6.14b}$$

where $\bar{\bar{S}}^{(1)}$, $\bar{\bar{L}}^{(1)}$, $\bar{\bar{R}}^{(1)}$, $\bar{\bar{Q}}^{(1)}$, $\bar{\bar{D}}^{(1)}$ and $\bar{\bar{W}}^{(1)}$ have the same form of $\bar{\bar{S}}$, $\bar{\bar{L}}$, $\bar{\bar{R}}$, $\bar{\bar{Q}}$, $\bar{\bar{D}}$ and $\bar{\bar{W}}$, respectively, by changing k to k_1, and k_L to k_{1L}.

We also choose

$$k_{1L} = k_L\sqrt{\varepsilon_r} \tag{6.15a}$$

where $\varepsilon_r = \varepsilon_{rp}/\varepsilon_{rb}$. Then

$$\lambda(k_1, k_{1L}) = \frac{1}{\varepsilon_r}\lambda(k, k_L) \tag{6.15b}$$

$$\bar{\bar{W}}^{(1)}(k_{1L}, k_1) = \left(\frac{1}{\varepsilon_r}\lambda(k, k_L)\bar{\bar{I}} - \bar{\bar{D}}^{(1)}(k_L)\right)^{-1} \tag{6.15c}$$

In Appendix A, we describe efficient methods for calculating the matrix elements of $\bar{\bar{S}}$, $\bar{\bar{L}}$, $\bar{\bar{S}}^{(1)}$ and $\bar{\bar{L}}^{(1)}$, at low wavenumbers of k_L and k_{1L}.

6.3.2 Eigenvalue problem

We next convert the matrix equation Eq.(14) into an eigenvalue problem. Let

$$\bar{b} = \bar{\bar{W}}\bar{\bar{R}}^{\dagger}\bar{q} \tag{6.16a}$$

$$\bar{c} = \bar{\bar{W}}\bar{\bar{Q}}^{\dagger}\bar{p} \tag{6.16b}$$

$$\bar{b}^{(1)} = \bar{\bar{W}}^{(1)}\bar{\bar{R}}^{(1)\dagger}\bar{q} \tag{6.16c}$$

$$\bar{c}^{(1)} = \bar{\bar{W}}^{(1)}\bar{\bar{Q}}^{(1)\dagger}\bar{p} \tag{6.16d}$$

Then from Eq. (13a)

$$\bar{\bar{W}}^{-1}\bar{b} = \left(\lambda\bar{\bar{I}} - \bar{\bar{D}}\right)\bar{b} = \bar{\bar{R}}^{\dagger}\bar{q} \tag{6.17a}$$

$$\bar{\bar{W}}^{-1}\bar{c} = \left(\lambda\bar{\bar{I}} - \bar{\bar{D}}\right)\bar{c} = \bar{\bar{Q}}^{\dagger}\bar{p} \tag{6.17b}$$

Thus

$$\lambda\bar{b} = \bar{\bar{D}}\bar{b} + \bar{\bar{R}}^{\dagger}\bar{q} \tag{6.18a}$$

$$\lambda\bar{c} = \bar{\bar{D}}\bar{c} + \bar{\bar{Q}}^{\dagger}\bar{p} \tag{6.18b}$$

Similarly, with Eqs. (16c-d, 15c)

$$\lambda \bar{b}^{(1)} = \varepsilon_r \bar{\bar{D}}^{(1)} \bar{b}^{(1)} + \varepsilon_r \bar{\bar{R}}^{(1)\dagger} \bar{q} \tag{6.18c}$$

$$\lambda \bar{c}^{(1)} = \varepsilon_r \bar{\bar{D}}^{(1)} \bar{c}^{(1)} + \varepsilon_r \bar{\bar{Q}}^{(1)\dagger} \bar{p} \tag{6.18d}$$

Next, using the definitions of $\bar{b}$, $\bar{c}$, $\bar{b}^{(1)}$, $\bar{c}^{(1)}$, the matrix equation Eq. (14) becomes,

$$\bar{\bar{S}} \bar{p} - \bar{\bar{L}} \bar{q} + \bar{\bar{R}} \bar{c} - \bar{\bar{R}} \bar{b} = 0 \tag{6.19a}$$

$$\bar{\bar{S}}^{(1)} \bar{p} - \frac{1}{s} \bar{\bar{L}}^{(1)} \bar{q} + \bar{\bar{R}}^{(1)} \bar{c}^{(1)} - \frac{1}{s} \bar{\bar{R}}^{(1)} \bar{b}^{(1)} = 0 \tag{6.19b}$$

Next we express $\bar{p}$, $\bar{q}$ in $\bar{b}$, $\bar{c}$, $\bar{b}^{(1)}$, $\bar{c}^{(1)}$,

$$\begin{bmatrix} \bar{p} \\ \bar{q} \end{bmatrix} = \bar{\bar{A}} \begin{bmatrix} \bar{b} \\ \bar{c} \\ \bar{b}^{(1)} \\ \bar{c}^{(1)} \end{bmatrix} \tag{6.20}$$

where

$$\bar{\bar{A}} = \begin{bmatrix} \bar{\bar{S}} & -\bar{\bar{L}} \\ \bar{\bar{S}}^{(1)} & -\frac{1}{s} \bar{\bar{L}}^{(1)} \end{bmatrix}^{-1} \begin{bmatrix} \bar{\bar{R}} & -\bar{\bar{R}} & \bar{\bar{O}} & \bar{\bar{O}} \\ \bar{\bar{O}} & \bar{\bar{O}} & \frac{1}{s} \bar{\bar{R}}^{(1)} & -\bar{\bar{R}}^{(1)} \end{bmatrix} \tag{6.21}$$

where the $\bar{\bar{O}}$'s are matrices zero elements with appropriate dimensions. Eliminating $\bar{p}$ and $\bar{q}$ using Eqs. (18) and (20), we obtain the eigenvalue problem,

$$\bar{\bar{P}} \bar{x} = \lambda \bar{x} \tag{6.22}$$

where

$$\bar{\bar{P}} = \begin{bmatrix} \bar{\bar{D}} & \bar{\bar{O}} & \bar{\bar{O}} & \bar{\bar{O}} \\ \bar{\bar{O}} & \bar{\bar{D}} & \bar{\bar{O}} & \bar{\bar{O}} \\ \bar{\bar{O}} & \bar{\bar{O}} & \varepsilon_r \bar{\bar{D}}^{(1)} & \bar{\bar{O}} \\ \bar{\bar{O}} & \bar{\bar{O}} & \bar{\bar{O}} & \varepsilon_r \bar{\bar{D}}^{(1)} \end{bmatrix} + \begin{bmatrix} \bar{\bar{O}} & \bar{\bar{R}}^{\dagger} \\ \bar{\bar{Q}}^{\dagger} & \bar{\bar{O}} \\ \bar{\bar{O}} & \varepsilon_r \bar{\bar{R}}^{(1)\dagger} \\ \varepsilon_r \bar{\bar{Q}}^{(1)\dagger} & \bar{\bar{O}} \end{bmatrix} \bar{\bar{A}} \tag{6.23a}$$

$$\bar{x} = [\bar{b}^T \quad \bar{c}^T \quad \bar{b}^{(1)T} \quad \bar{c}^{(1)T}]^T \tag{6.23b}$$

The matrix dimension of the eigenvalue problem in (23a) is $4M \times 4M$. In the above equation, only λ depends on wavenumber while all the other matrices are independent of

wavenumber. Thus the eigenvalue problem is linear with all the eigenvalues and eigenvectors solved simultaneously giving the multi-band solutions.

Knowing the eigenvalues λ, the mode wavenumbers k^2 are obtained from the relation of $\lambda = \frac{1}{k^2 - k_L^2}$, (Eq. (9c)). The modal surface currents distributions $\bar{p}$ and $\bar{q}$ are calculated from the eigenvectors through Eq. (20). Knowing $\bar{p}$ and $\bar{q}$, we can also compute the modal field distribution ψ and ψ_1 everywhere in the lattice by Eq. (2). The authenticity of the eigenmodes can also be checked by the extinction theorem (Eq. (2)) away from the boundaries.

6.4 Numerical results

We consider the triangular lattices with lattice constant a as shown in Figure VI.1. The dielectric background has permittivity ε_b, and the scatterers are circular air voids of radius b drilled in the background with $\varepsilon_p = \varepsilon_0$, where ε_0 is the free space permittivity. We consider two cases with case 1 $b = 0.2a$, $\varepsilon_b = 8.9\varepsilon_0$ and filling ratio of 14.5% and case 2 of $b = 0.48a$, $\varepsilon_b = 12.25\varepsilon_0$ and filling ratio of 83.6%. We calculate the solutions using BBGFL method. We also calculate the solutions using the plane wave method [86] and the KKR method [98] and compare the results of BBGFL with these two methods.

In Appendix A, we describe the calculations of g_P and g_{1P} at the respective single low wavenumbers of k_L and k_{1L} that include the calculations of D_n [98].The lattice vectors are given by

$$\bar{a}_1 = \frac{a}{2}\left(\sqrt{3}\hat{x} + \hat{y}\right)$$

$$\bar{a}_2 = \frac{a}{2}\left(-\sqrt{3}\hat{x} + \hat{y}\right)$$

and the reciprocal lattice vectors are

$$\bar{b}_1 = \frac{2\pi}{a}\left(\frac{1}{\sqrt{3}}\hat{x} + \hat{y}\right)$$

$$\bar{b}_2 = \frac{2\pi}{a}\left(-\frac{1}{\sqrt{3}}\hat{x} + \hat{y}\right)$$

The Γ, M, and K points are

$$\Gamma: \bar{k}_i = 0\bar{b}_1 + 0\bar{b}_2 = 0$$

$$M: \bar{k}_i = \frac{1}{2}\bar{b}_1 + 0\bar{b}_2 = \frac{\pi}{a}\left(\frac{1}{\sqrt{3}}\hat{x} + \hat{y}\right)$$

$$K: \bar{k}_i = \frac{1}{3}\bar{b}_1 + \frac{1}{3}\bar{b}_2 = \frac{4\pi}{3a}\hat{y}$$

We plot the band solutions with $\bar{k}_i = \beta_1\bar{b}_1 + \beta_2\bar{b}_2$ following $\Gamma \to M \to K \to \Gamma$.

The normalized frequency $f_N(k)$ is defined as

$$f_N(k) = \frac{ka}{2\pi}\sqrt{\frac{\varepsilon_0}{\varepsilon_b}}$$

In the following computations, we choose the low wavenumber k_L such that $f_N(k_L) = 0.2$. The choice of k_L is quite arbitrary as k_L values in a range will work. This makes BBGFL method robust. In the examples, the maximum number of two-dimensional (2D) Bloch waves in BBGFL is 441 corresponding to $-10 \le m, n \le 10$, so that the highest m, n index is 10. This leads to an eigenvalue problem of maximum dimension $4M = 1764$.

Case 1: $b = 0.2a$**,** $\varepsilon_b = 8.9\varepsilon_0$**,** $\pi b^2/\Omega_0 = 14.5\%$

The band diagram is plotted in Figure VI.2, with MoM discretization $N = 80$, and D_n (as defined in Eq. (27)) at order 4 to compute g_P and $\hat{n}' \cdot \nabla' g_P$ at the single low wavenumber k_L. We compute solutions using the plane wave method with 1681 Bloch waves. Note that we only use 441 Bloch waves in the BBGFL method. The agreements between the two methods are excellent.

In Figure VI.3, the surface modal currents, unnormalized, are plotted for the first few modes near Γ point with $\bar{k}_i = 0.05\bar{b}_1$.

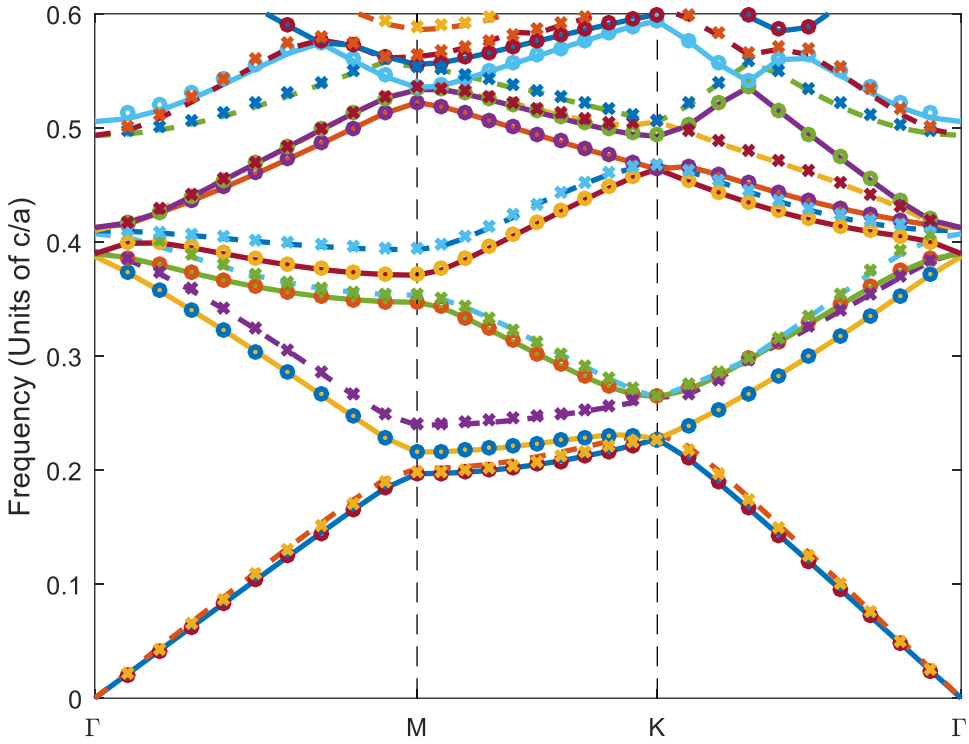

Figure VI.2. Band diagram of the hexagonal structure with background dielectric constant of 8.9 and air voids of radius $b = 0.2a$. The results of BBGFL are shown by the solid curves for TMz polarization and by the dashed curves for the TEz polarization. The circles and crosses are the results of planewave method for the TMz and TEz polarizations, respectively.

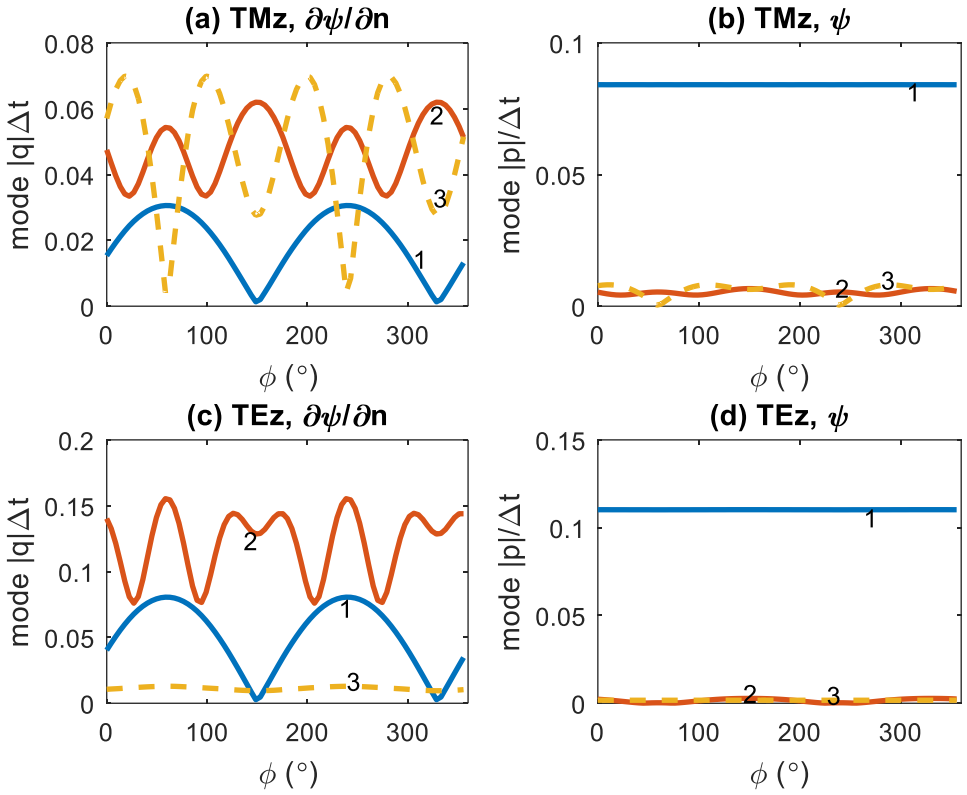

Figure VI.3. Modal surface currents distribution near Γ point at $\bar{k}_i = 0.05\bar{b}_1$ corresponding to the first few modes of the hexagonal structure with background dielectric constant of 8.9 and air voids of radius $b = 0.2a$. (a) TMz, surface electric currents $J_z \propto \partial\psi/\partial n$; (b) TMz, surface magnetic current $M_t \propto \psi$; (c) TEz, surface magnetic currents $M_z \propto \partial\psi/\partial n$; (d) TEz, surface electric current $J_t \propto \psi$. The corresponding normalized mode frequencies are 1: 0.0208, 2: 0.3736, 3: 0.3864 for TMz wave, and 1: 0.02224, 2: 0.3847, 3: 0.404 for TEz wave, respectively.

In Table VI-1, the convergence of the lowest mode with respect to the number of Bloch waves used in BBGFL using different low wavenumber k_L are tabulated for TMz polarization with $\bar{k}_i = 0.05\bar{b}_1$. It is noted that the choice of k_L is robust, and fewer Floquet modes are needed as one choses a lower k_L.

Table VI-1. The convergence of the lowest mode with respect to the number of Bloch waves used in BBGFL using different low wavenumber k_L. The results are tabulated for TMz polarization with $\bar{k}_i = 0.05\bar{b}_1$, where 0.020798 is the first band solution.

f_N	$M = 9$	$M = 49$	$M = 121$	$M = 441$
$f_N(k_L) = 0.001$	0.020798	0.020798	0.020798	0.020798
$f_N(k_L) = 0.1$	0.020780	0.020798	0.020798	0.020798
$f_N(k_L) = 0.2$	0.020806	0.020797	0.020797	0.020798
$f_N(k_L) = 0.5$	0.020888	0.020792	0.020794	0.020798

Case 2: $b = 0.48a$**,** $\varepsilon_b = 12.25\varepsilon_0$**,** $\pi b^2/\Omega_0 = 83.6\%$

The parameters for this case are the same as in [98]. The area ratio of scatterers to background is high at 83.6%. The dielectric constant ratio of $\varepsilon_b/\varepsilon_p$ is as high as 12.25. In this case, the field varies more rapidly along the perimeter of the scatterer than the previous case and we choose the MoM discretization to be $N = 180$, and D_n (as defined in Eq. (27)) is selected at order 8 to compute g_P and $\hat{n}' \cdot \nabla' g_P$ at the single low wavenumber k_L. The band diagram is plotted in Figure VI.4. For the planewave method we used 6561 Bloch waves which is significantly larger than M=441 Floquet modes for BBGFL. The KKR solution of the first few modes at the points of M, and K are also given (Ref. [98] has the complete KKR results). The band gap between the third and fourth bands is noted. The agreements between the three methods are in general good. Note that the planewave method predicts slightly larger higher order modes than the BBGFL. The differences decrease as more Bloch waves are included in the planewave expansion. Note that the planewave method results shown are not exactly the same as the results reported in [98], possibly due to the different treatment of the Fourier series expansion of the dielectric function [86, 175]. In our implementation, we do not apply any smearing function to the permittivity profile $\varepsilon(r)$, and directly compute the Fourier transform of $\varepsilon^{-1}(r)$. For the KKR method, more terms in the D_n series are needed as frequency increases. In Figure VI.5, the unnormalized surface modal currents

are plotted for the first few modes near Γ point with $\bar{k}_i = 0.05\bar{b}_1$. The modal currents tend to have more variations as the modal wavenumbers increase.

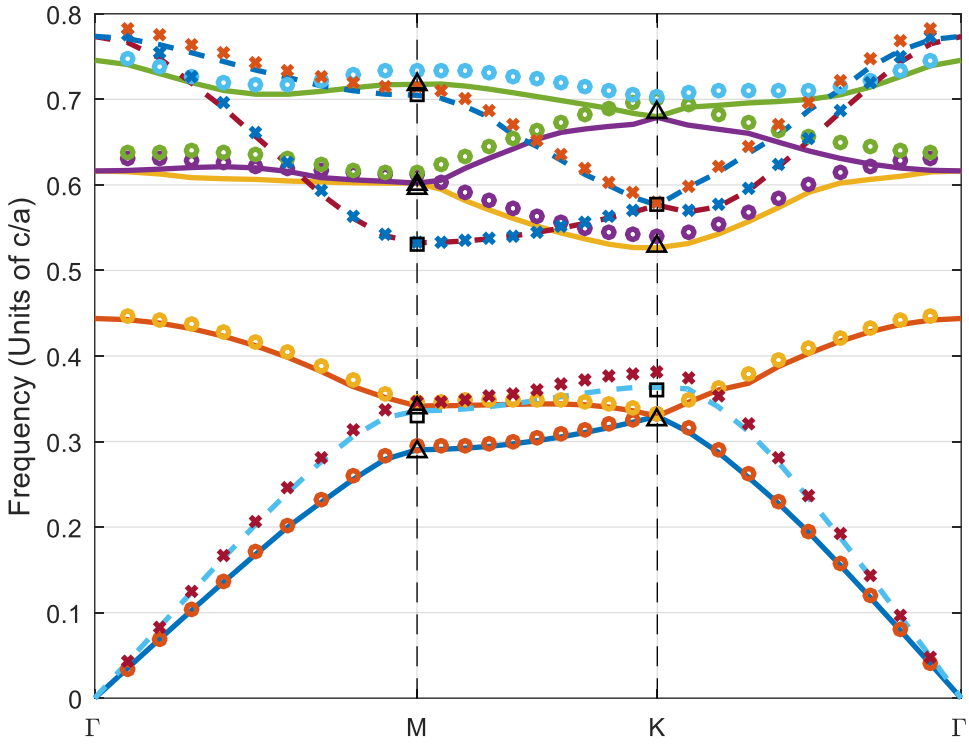

Figure VI.4. Band diagram of the hexagonal structure with background dielectric constant of 12.25 and air voids of radius b=0.48a. The results of BBGFL are shown by the solid curves for TMz polarization and by the dashed curves for the TEz polarization. The circles and crosses are the results of planewave method for the TMz and TEz polarizations, respectively. The triangles and squares are the results of the KKR method for the TMz and TEz polarizations, respectively.

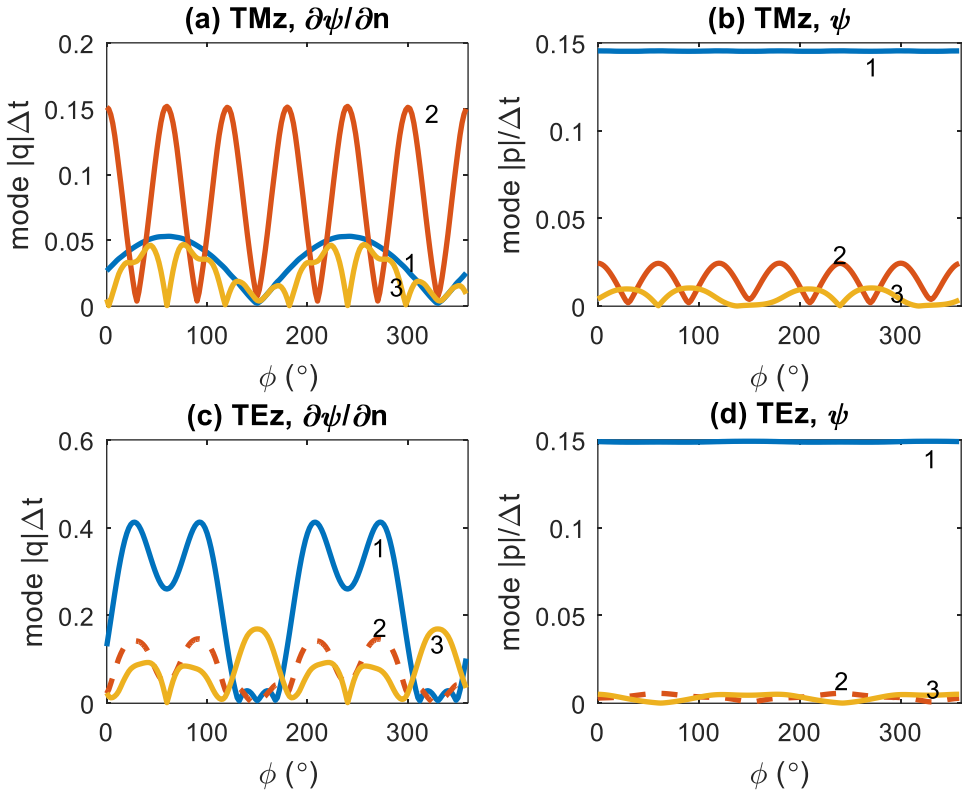

Figure VI.5. Modal surface currents distribution near Γ point at $\bar{k}_i = 0.05\bar{b}_1$ corresponding to the first few modes of the hexagonal structure with background dielectric constant of 12.25 and air voids of radius $b = 0.48a$. (a) TMz, surface electric currents $J_z \propto \partial\psi/\partial n$; (b) TMz, surface magnetic current $M_t \propto \psi$; (c) TEz, surface magnetic currents $M_z \propto \partial\psi/\partial n$; (d) TEz, surface electric current $J_t \propto \psi$. The corresponding normalized mode frequencies are 1: 0.03437, 2: 0.4425, 3: 0.6154 for TMz wave, and 1: 0.04145, 2: 0.7669, 3: 0.7710 for TEz wave, respectively.

The eigenvalues of the BBGFL approach include spurious modes. All the spurious modes are quickly rejected based on the following simple calculations. The spurious modes do not satisfy the extinction theorem as given in Eq. (2). If we evaluate the field inside the scatterers using g_P, or evaluate the field outside the scatterers using g_{1P}, we get non-zero values for the spurious modes. These modes can be identified by several points calculations inside or outside the scattering using the surface integrals. Some of the spurious modes do not satisfy one of the two surface integral equations Eq. (4), and for these modes, their modal currents ψ and $\partial\psi/\partial n$ on the

boundary are essentially zeros and trivial. For the rest of the spurious modes, they satisfy the surface integral equations Eq. (4), but do not obey the extinction theorem Eq. (2), and these modes are shown to be nearly invariant with respect to $\bar{k}_i$, with values close to the roots of $J_n(kb)$, where J_n is the n-th order Bessel function.

The CPU time is recorded when running the BBGFL code in Mat lab R2014b to compute the band diagram on an HP ProDesk 600 G1 desktop with Intel Core i7-4790 CPU @ 3.60 GHz and 32 GB RAM. Since the computation for different $\bar{k}_i$ are independent, the CPU time for one $\bar{k}_i$ will be described. For case 2 with the larger N and higher order of D_n, it takes a total of ~96 sec to complete the mode analysis at one $\bar{k}_i$, of which ~11s is spent on the eigenvalue analysis. More than 80% CPU time is spent on computing the matrices $\bar{\bar{S}}$, $\bar{\bar{L}}$, $\bar{\bar{S}}^{(1)}$, and $\bar{\bar{L}}^{(1)}$ at the single low wavenumbers k_L and k_{1L} respectively for background periodic Green's function and scatterer periodic Green's function. The calculation of D_n (and $D_n^{(1)}$ by changing k to k_1) as defined in Appendix A to facilitate the computation of g_P and g_{1P} takes ~24s, and the calculation of the low wavenumber matrices using D_n takes ~27s on the boundary. Another ~28s are needed for solutions away from the boundary as needed in checking the extinction theorem. The time recorded is for one polarization, and for the second polarization the added time is very small since only the eigenvalue problem is to be resolved. The approach is much more efficient than the KKR approach which is based on the evaluation of D_n at every frequency that needed to be used to search the band solution k, with one band at a time. The BBGFL can also be more efficient than the planewave method when the planewave method requires significantly larger number of Bloch waves as in the second case with large dielectric contrast and large filling ratio. Note that for the case of infinite contrast of perfect electric conductor (PEC), BBGFL also works.

6.5 Low frequency dispersion relations, effective permittivity and propagation constants

In this section, we illustrate the low frequency dispersion relations which are useful for the design of devices in photonics and metamaterials.

In metamaterials, the scatterers and the lattice spacings are subwavelengths. Effective permittivities and effective propagation constants have been calculated for random media of dielectric mixtures [15, 26, 34, 183-186]. In random medium, the positions of scatterers are random creating random phase in propagating waves. Every realization has different positions of scatterers although each realization has the same statistics and the field solutions of different realizations are different. The waves are decomposed into coherent waves and incoherent waves. The coherent wave has definite amplitude and phase while the incoherent waves have random amplitudes and phases giving speckle. In low frequency, the coherent waves dominate while at higher frequencies, the incoherent waves dominate. In random medium, the effective permittivity and the effective propagation constant are that of the coherent waves. On the other hand, the geometry in a periodic structure is deterministic with a single solution. The quasistatic method has been used to calculate the effective permittivity of a periodic medium [185]. It is interesting to note that at very low frequency, the effective permittivities as derived for random medium and for periodic medium are the same. In the following, we associate effective permittivity and effective propagation constant with the low frequency dispersion relation of the lowest band in the vicinity of the Γ point.

In Figure VI.6 and Figure VI.7, we plot the ω-k lowest band near the Γ point for case a and case b, respectively. These will be labeled as low frequency dispersion curves. The dispersion relation curves are plotted for $\bar{k}_i$ moving along the line of ΓM, and along the line of ΓK in the first Brillouin zone, respectively. The points M and K represent the largest anisotropy in the first

irreducible Brillouin zone. In Appendix B we derived the effective permittivity and effective propagation constants [34]. The corresponding dispersion curves are straight lines and are also plotted in Figure VI.6 and Figure VI.7.

The low frequency dispersion relations of the lowest band are close to the effective permittivity curves at low frequency and deviate as $|\bar{k}_i|$ increases. At higher frequencies, towards the M and K points, they show significant departures when $\bar{k}_i$ are close to M and K point. Thus as frequency increases, the effective propagation constants and effective permittivity are dispersive and anisotropic. The dispersion relations are plotted for both TM polarization and TE polarization. For the same ω, TM wave in general has a slightly larger k. The difference between the two polarization increases as the permittivity contrast and the scatterer filling ratio increases.

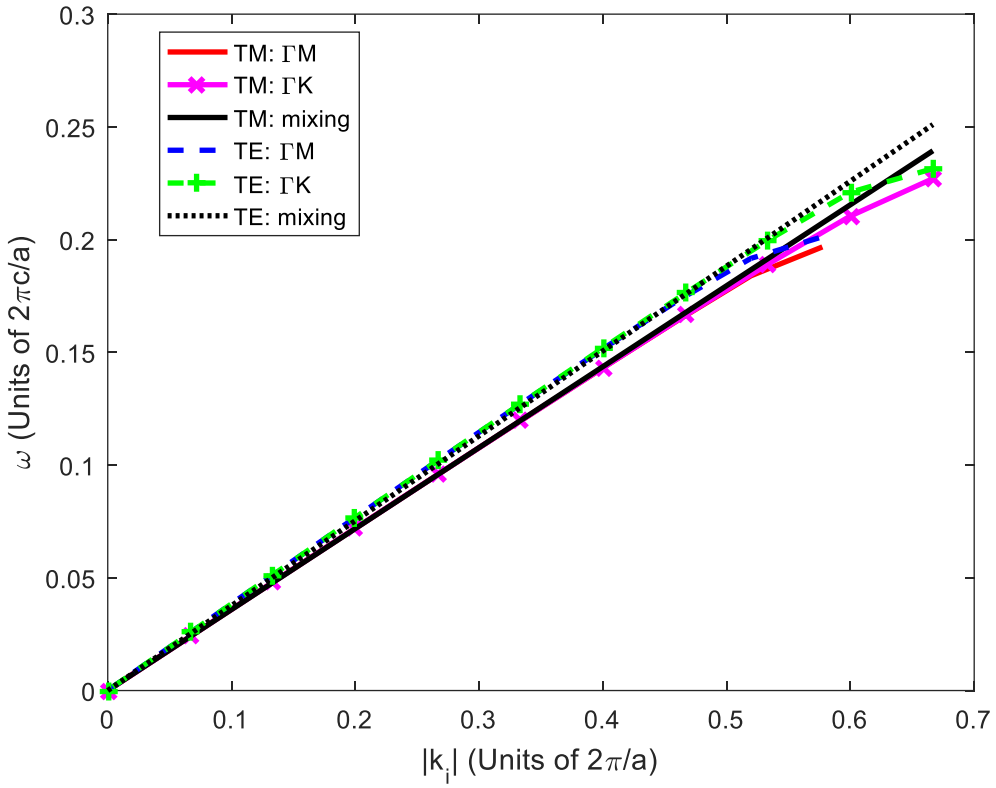

Figure VI.6. Dispersion relationship of the hexagonal structure with background dielectric constant of 8.9 and air voids of radius $b = 0.2a$.

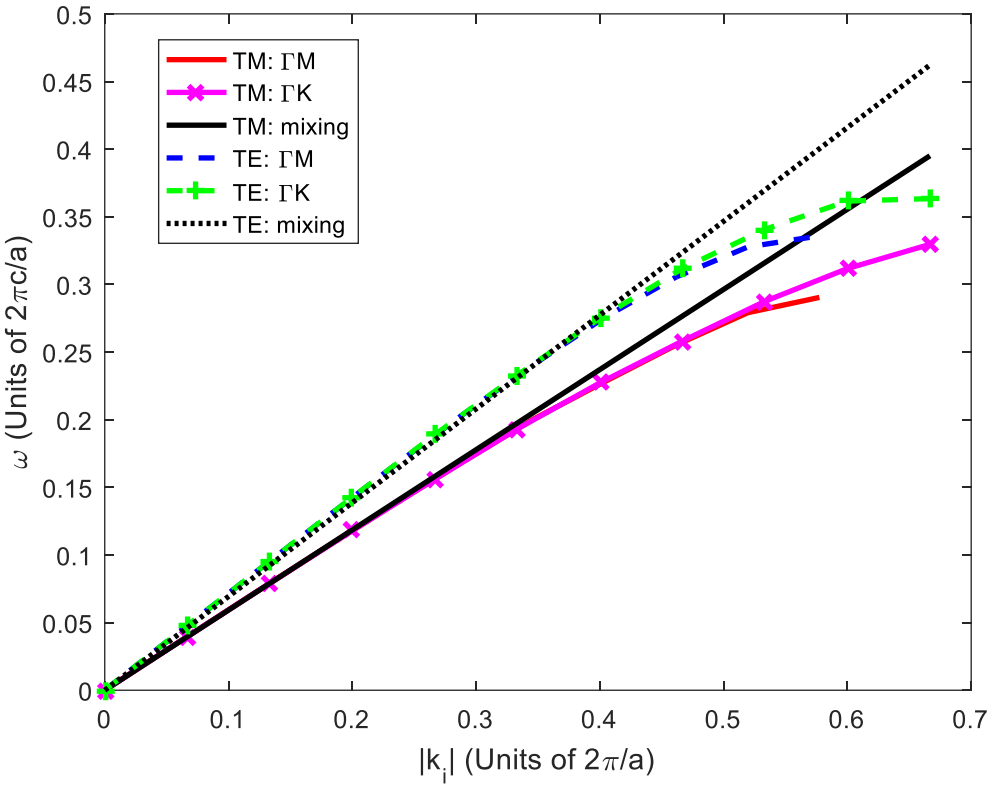

Figure VI.7. Dispersion relationship of the hexagonal structure with background dielectric constant of 12.25 and air voids of radius $b = 0.48a$.

The BBGFL method also works for infinite permittivity contrast as in the case of PEC [80]. In Figure VI.8, we plot the ω-k dispersion relation for the PEC scatterer case, with the PEC cylinder radius $b = 0.2a$, and the background permittivity $\varepsilon_b = 8.9\varepsilon_0$. The behavior of the TE wave is similar to that of the dielectric case. But for the TM wave, as indicated by the quasistatic mixing formula that the mixture does not have a finite quasistatic effective permittivity. The ω-k dispersion relation from the lowest band has similar behavior to that of the plasma [186]. The periodic structure behaves like a plasma for the TM wave that the wave could only propagate when its frequency is larger than the corresponding plasma frequency.

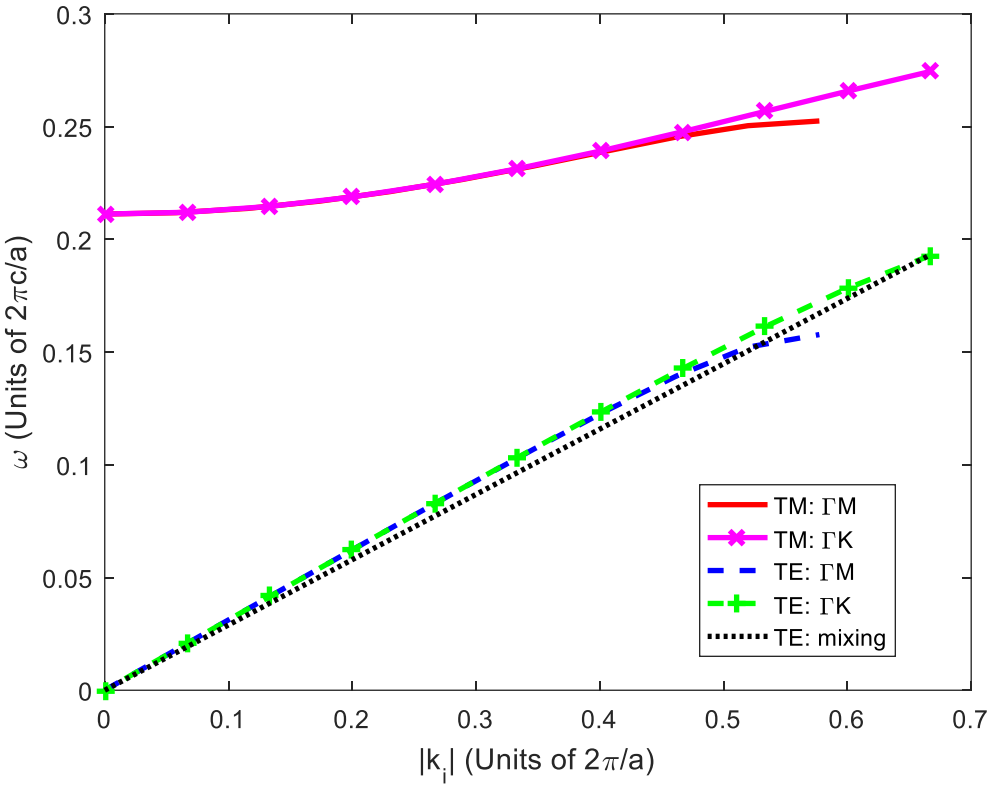

Figure VI.8. Dispersion relationship of the hexagonal structure with background dielectric constant of 8.9 and PEC cylinders of radius $b = 0.2a$.

6.6 Conclusions

In this chapter we have applied the BBGFL approach, previously used for Dirichlet boundary conditions [80], to calculate band solutions and the low frequency dispersion relations of dielectric periodic structures in 2D problem with 2D periodicity. In the BBGFL approach, we solve the dual surface integral equations with MoM using the broadband periodic Green's function of both the background and the scatterer. The Broadband periodic Green's functions are fast convergent because of low wavenumber extraction. The low wavenumber component represents evanescent near field which converge slowly. Because MoM is applied, the method is applicable to arbitrary scatterer shapes and arbitrary filling ratio and permittivity contrasts. The BBGFL approach has the form of a linear eigenvalue problem. The method is shown to be efficient and

accurate. The choice of the low frequency wavenumber has been shown to be robust because MoM is applied. The method, in principle, is applicable to arbitrary scatterer shapes and arbitrary filling ratio and permittivity contrasts. We are studying these cases. We are also extending the method to 3D problems with 3D periodicity.

Appendix A: Evaluation of periodic Green's function and the matrix elements at the single low wavenumber

We only need to compute the matrix elements S_{mn} , L_{mn} and $S_{mn}^{(1)}$, $L_{mn}^{(1)}$ as defined in Eq. (6), at the respective single low wavenumbers of k_L and k_{1L}. The spatial and spectral series summations as given in Eq. (3) converge slowly especially when $\bar{\rho} \to \bar{\rho}'$. Thus we seek to subtract the primary contribution [80, 98], separating $g_P\left(k, \bar{k}_i; \bar{\rho}, \bar{\rho}'\right)$ into the primary part $g(k; \bar{\rho}, \bar{\rho}')$ and the response part $g_R\left(k, \bar{k}_i; \bar{\rho}, \bar{\rho}'\right)$.

$$g_P\left(k, \bar{k}_i; \bar{\rho}\right) = g(k; \bar{\rho}) + g_R\left(k, \bar{k}_i; \bar{\rho}\right) \tag{6.24}$$

$$g(k; \bar{\rho}) = \frac{i}{4} H_0^{(1)}(k\rho) = \frac{i}{4} J_0(k\rho) - \frac{1}{4} N_0(\, k\rho) \tag{6.25}$$

where $J_0(w)$ and $N_0(w)$ are the zeroth order Bessel and Neumann function, respectively.

Since there is no singularity in g_R, we express it as

$$g_R\left(k, \bar{k}_i; \bar{\rho}\right) = \sum_{n=-\infty}^{\infty} E_n J_n(k\rho) \exp(in\phi) \tag{6.26}$$

It follows that

$$g_P\left(k, \bar{k}_i; \bar{\rho}\right) = -\frac{1}{4} N_0(k\rho) + \sum_{n=-\infty}^{\infty} D_n J_n(k\rho) \exp(in\phi) \tag{6.27}$$

where

$$D_n = E_n + \frac{i}{4}\delta_{n0} \tag{6.28}$$

and δ_{n0} is the Kronecker delta function.

Expanding the Bloch wave $\exp\left(i\bar{k}_{i\alpha}\cdot\bar{\rho}\right)$ into Bessel functions in the spectral domain expression of g_P (Eq. (3)),

$$g_P\left(k,\bar{k}_i;\bar{\rho}\right) = \frac{1}{\Omega_0}\sum_{\alpha}\frac{1}{\left|\bar{k}_{i\alpha}\right|^2 - k^2}\sum_{n=-\infty}^{\infty} i^n \exp(-in\phi_{i\alpha})\, J_n\left(\left|\bar{k}_{i\alpha}\right|\rho\right)\exp(in\phi) \tag{6.29}$$

where $\phi_{i\alpha}$ is the polar angle of $\bar{k}_{i\alpha}$, and ϕ is the polar angle of $\bar{\rho}$.

Balancing the coefficients of $\exp(in\phi)$ in Eq. (27) and (29), it follows that

$$D_n = \frac{1}{J_n(k\rho)}\left[i^n\frac{1}{\Omega_0}\sum_{\alpha}\frac{\exp(-in\phi_{i\alpha})\, J_n\left(\left|\bar{k}_{i\alpha}\right|\rho\right)}{\left|\bar{k}_{i\alpha}\right|^2 - k^2} + \frac{1}{4}N_0(k\rho)\delta_{n0}\right] \tag{6.30}$$

and for real k,

$$D_{-n} = D_n^* \tag{6.31}$$

Note that ρ is arbitrarily chosen in this expression. ρ should avoid the zeros of $J_n(k\rho)$ and not be too close to 0. The number of Floquet modes used in the above expression is much larger than in evaluation of g_B using Eqs. (8, 10). However, the series of g_R in Eq. (26) converges in a few terms, usually $|n| \le 8$ for moderately low wavenumber k_L.

For the normal derivative $\hat{n}'\cdot\nabla' g_P\left(k,\bar{k}_i;\bar{\rho},\bar{\rho}'\right)$, using Eqs. (24-26), we have

$$\hat{n}'\cdot\nabla' g_P\left(k,\bar{k}_i;\bar{\rho},\bar{\rho}'\right) = \hat{n}'\cdot\nabla' g(k;\bar{\rho},\bar{\rho}') + \hat{n}'\cdot\nabla' g_R\left(k,\bar{k}_i;\bar{\rho},\bar{\rho}'\right) \tag{6.32}$$

$$\hat{n}'\cdot\nabla' g(k;\bar{\rho},\bar{\rho}') = \frac{i}{4}kH_1^{(1)}(k|\bar{\rho}-\bar{\rho}'|)\left(\hat{n}'\cdot\frac{\bar{\rho}-\bar{\rho}'}{|\bar{\rho}-\bar{\rho}'|}\right) \tag{6.33}$$

$$\hat{n}'\cdot\nabla' g_R\left(k,\bar{k}_i;\bar{\rho},\bar{\rho}'\right) = \hat{n}'\cdot\nabla'\sum_{n=-\infty}^{\infty} E_n J_n(k|\bar{\rho}-\bar{\rho}'|)\exp\left(in\phi_{\bar{\rho}\bar{\rho}'}\right) \tag{6.34}$$

With addition theorem,

$$J_n(k|\bar{\rho}-\bar{\rho}'|)\exp\left(in\phi_{\bar{\rho}\bar{\rho}'}\right)=\sum_{m=-\infty}^{\infty}J_m(k\rho)J_{m-n}(k\rho')\exp(im\phi-i(m-n)\phi') \tag{6.35}$$

Eq. (34) is readily evaluated,

$$\begin{aligned}\hat{n}'\cdot\nabla' g_R\left(k,\bar{k}_i;\bar{\rho},\bar{\rho}'\right)&\\ =\sum_{n=-\infty}^{\infty}E_n\sum_{m=-\infty}^{\infty}J_m(k\rho)\exp(im\phi)\,\hat{n}'&\\ \cdot\left(\hat{\rho}'kJ'_{m-n}(k\rho')+\hat{\phi}'\frac{1}{\rho'}J_{m-n}(k\rho')[-i(m-n)]\right)\exp(-i(m-n)\phi')&\end{aligned} \tag{6.36}$$

The summation over m also has fast convergence. In practice, it suffices to use the same upper limit as n of Eq. (26).

Note that $g_R\left(k,\bar{k}_i;\bar{\rho}-\bar{\rho}'\right)$ and $\hat{n}'\cdot\nabla' g_R\left(k,\bar{k}_i;\bar{\rho}-\bar{\rho}'\right)$ are all smooth functions for arbitrary $\bar{\rho}-\bar{\rho}'$. Using Eqs. (6), (24-26), (32), (33), and (36),

$$S_{mn}=S_{mn}^{(P)}+S_{mn}^{(R)} \tag{6.37a}$$

$$L_{mn}=L_{mn}^{(P)}+L_{mn}^{(R)} \tag{6.37b}$$

where the superscripts (P) and (R) denote the contribution from the primary and the response part, respectively.

$$\begin{aligned}S_{mn}^{(P)}&=\frac{1}{\Delta t_n}\int_{S_{00}^{(n)}}dl'\hat{n}'\cdot\nabla' g(k,\bar{\rho}-\bar{\rho}')\,,\bar{\rho}\to\bar{\rho}_m^-\\ &=\begin{cases}-\dfrac{1}{2\Delta t_n}, & n=m\\ [\hat{n}'\cdot\nabla' g(k,\bar{\rho}-\bar{\rho}')]_{\bar{\rho}=\bar{\rho}_m,\bar{\rho}'=\bar{\rho}_n}, & n\neq m\end{cases}\end{aligned} \tag{6.38a}$$

$$S_{mn}^{(R)}=\frac{1}{\Delta t_n}\int_{S_{00}^{(n)}}dl'\hat{n}'\cdot\nabla' g_R(k,\bar{\rho}-\bar{\rho}')\,,\bar{\rho}\to\bar{\rho}_m^- \tag{6.38b}$$

$$= [\hat{n}' \cdot \nabla' g_R(k, \bar{\rho} - \bar{\rho}')]_{\bar{\rho}=\bar{\rho}_m, \bar{\rho}'=\bar{\rho}_n}$$

$$L_{mn}^{(P)} = \frac{1}{\Delta t_n} \int_{S_{00}^{(n)}} dl' g(k, \bar{\rho} - \bar{\rho}')$$

$$= \begin{cases} \frac{i}{4}\left[1 + \frac{i2}{\pi} \ln\left(\frac{\gamma k}{4e} \Delta t_n\right)\right], & n = m \\ [g(k, \bar{\rho} - \bar{\rho}')]_{\bar{\rho}=\bar{\rho}_m, \bar{\rho}'=\bar{\rho}_n}, & n \neq m \end{cases} \tag{6.38c}$$

$$L_{mn}^{(R)} = \frac{1}{\Delta t_n} \int_{S_{00}^{(n)}} dl' g_R(k, \bar{\rho} - \bar{\rho}'), \bar{\rho} \to \bar{\rho}_m^- \tag{6.38d}$$

$$= [g_R(k, \bar{\rho} - \bar{\rho}')]_{\bar{\rho}=\bar{\rho}_m, \bar{\rho}'=\bar{\rho}_n}$$

where $\gamma = 1.78107$ is the Euler's constant, and $e = 2.71828$ is the base of the natural logarithm.

The expressions for the elements of $\bar{\bar{S}}^{(1)}$ and $\bar{\bar{L}}^{(1)}$ are of the same form by changing k to k_1, except that

$$S_{mm}^{1(P)} = \frac{1}{2\Delta t_m}, \bar{\rho} \to \bar{\rho}_m^+ \tag{6.39}$$

Note that the matrices L and $L^{(1)}$ are symmetric.

Appendix B: 2D effective permittivity from quasistatic mixing formula

Consider scatterers with permittivity ε_p embedded in background media with permittivity ε. We derive the effective permittivity from the Lorentz-Lorenz law which states the macroscopic field $\bar{E}$ is the sum of the exciting field $\bar{E}^{\text{ex}}$ and the dipole field $\bar{E}_P$ [15, 34].

$$\bar{E}^{\text{ex}} = \bar{E} - \bar{E}_P \tag{6.40}$$

The effective permittivity ε_{eff} relates the macroscopic flux $\bar{D}$ and the macroscopic field $\bar{E}$,

$$\bar{D} = \varepsilon_{\text{eff}} \bar{E} \tag{6.41}$$

Also,

$$\bar{D} = \varepsilon \bar{E} + \bar{P} \tag{6.42}$$

and

$$\bar{P} = n_0 \alpha \bar{E}^{ex} \tag{6.43}$$

where n_0 is the number densities of scatterers per unit area, and α is the polarizability of each scatter. Expressing $\bar{E}_P$ in terms of P,

$$\bar{E}_P = -\chi \frac{\bar{P}}{\varepsilon} \tag{6.44}$$

where χ is a coefficient to be calculated.

Then substituting Eq. (44) into Eq. (40), and Eq. (40) into Eq. (43) yield

$$\bar{P} = \frac{n_0 \alpha \varepsilon}{\varepsilon - n_0 \alpha \chi} \bar{E} \tag{6.45}$$

Putting Eq. (45) into Eq. (42), and comparing with Eq. (41), we obtain

$$\varepsilon_{\text{eff}} = \varepsilon + \frac{n_0 \alpha \varepsilon}{\varepsilon - n_0 \alpha \chi} = \varepsilon \frac{1 + \frac{n_0 \alpha (1 - \chi)}{\varepsilon}}{1 - \frac{n_0 \alpha \chi}{\varepsilon}} \tag{6.46}$$

Equation (46) is known as the Clausius-Mossotti relation. Consider 2D cylindrical scatterers with circular cross section of radius b and cross section area $A_0 = \pi b^2$, we derive the expressions of α and χ by solving the 2D Laplace equation.

For TE polarization,

$$\alpha = A_0 y 2\varepsilon \tag{6.47a}$$

$$\chi = \frac{1}{2} \tag{6.47b}$$

where

$$y = \frac{\varepsilon_p - \varepsilon}{\varepsilon_p + \varepsilon} \tag{6.47c}$$

Thus,

$$\varepsilon_{\text{eff}} = \varepsilon \frac{1 + n_0 A_0 y}{1 - n_0 A_0 y} = \varepsilon \frac{1 + f_v y}{1 - f_v y} \tag{6.48}$$

where the area filling ratio is $f_v = n_0 A_0$. Equation (48) is known as the Maxwell-Garnett mixing formula.

Note that when scatter is of PEC material, $\varepsilon_p \to \infty$, $y \to 1$, thus $\varepsilon_{\text{eff}} = \varepsilon(1 + f_v)/(1 - f_v)$ is finite.

For TM polarization,

$$\alpha = A_0(\varepsilon_p - \varepsilon) \tag{6.49a}$$

$$\chi = 0 \tag{6.49b}$$

Thus

$$\varepsilon_{\text{eff}} = \varepsilon + n_0 A_0 \big(\varepsilon_p - \varepsilon\big) = (1 - f_v)\varepsilon + f_v \varepsilon_p \tag{6.50}$$

Note that when the scatterers are PEC$\varepsilon_p \to \infty$, $\varepsilon_{\text{eff}} \to \infty$. Thus ε_{eff} does not exist for TM wave with PEC scatterers. This is also clear from the dispersion relation of the lowest band case for the Dirichlet boundary condition that was treated previously [80].

CHAPTER VII

Constructing the Broadband Green's Function including Periodic Structures using the Concept of BBGFL

The Green's functions are physical responses due to a single point source in a periodic lattice. The single point source can also correspond to an impurity or a defect. In this Chapter, the Green's functions, including the scatterers, for periodic structures such as in photonic crystals and metamaterials are calculated. The Green's functions are in terms of the multiband solutions of the periodic structures. The Green's functions are broadband solutions so that the frequency or wavelength dependences of the physical responses can be calculated readily.

Using the concept of modal expansion of the periodic Green's function, we have developed the method of broadband Green's function with low wavenumber extraction (BBGFL) [80-83] that gives an accelerated convergence of the multiple band expansions. Using BBGFL, surface integral equations are formulated and solved by the method of moment (MoM) so that the method is applicable to scatterers of arbitrary shape. The determination of modal band solutions in this method is a linear eigenvalue problem, so that the multi-band solutions are computed for a Bloch wavenumber simultaneously. This is in contrast to using the usual free space Green's function or the KKR/ multiple scattering method [96-99] in which the eigenvalue problem is nonlinear. The modal field solutions are wavenumber independent. We have applied the BBGFL to calculate band diagrams of periodic structures. The BBGFL method is applicable to both PEC [80] and dielectric

periodic scatterers [81]. The method is broadband so that the frequency or wavelength dependences can be calculated readily. Our method has some similarities to the hybrid plane-wave and integral equation based method [187-189], where an integral-differential eigensystem is derived for an auxiliary extended problem which has smooth eigenfunctions.

The goal of this Chapter is to calculate the Green's function for periodic structures that includes infinite periodic scatterers and to illustrate physically the responses due to point sources in the periodic structures. Such physical responses also correspond to response due to an impurity or defect in the periodic structures. The mathematical steps are 1) to solve for the band modal fields and normalize the band modal fields [82], and 2) to calculate the periodic Green's function at a single low wavenumber k_L from surface integral equation and 3) the periodic Green's function at any wavenumber k using the accelerated modal representation for each Bloch wave-vector in the first Brillouin zone, and 4) to calculate the Green's function due to a single point source by integrating the periodic Green's function over to the Bloch wavenumber [74-79]. Our approach is related to [74-77] by representing the periodic Green's function in terms of multi-band solutions and in applying the phased-array method to obtain the point source response. But we apply surface integral equation with the method of moment (MoM) to solve for the multiple band solutions instead of using plane wave expansion, making the approach applicable to high permittivity contrast, arbitrary shape scatterers and non-penetrable scatterers. We use the low wavenumber extraction technique to accelerate the convergence of the band modal representation, making a broadband response ready to obtain.

Once we're equipped with the Green's function, we're ready to solve problems such as perturbations or defects in periodic structures, using integral equation based methods. Numerical

results are illustrated for the band modal fields, the periodic Green's functions and the single point source Green's functions for two-dimensional (2D) PEC scatterers in a 2D lattice.

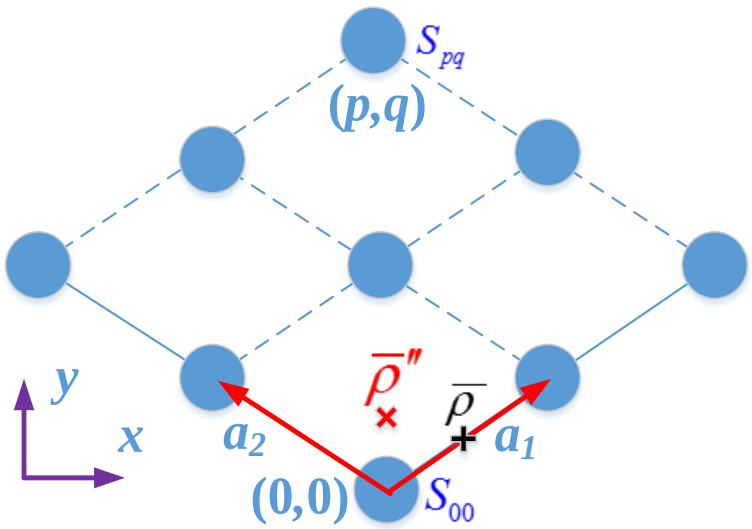

Figure VII.1. Illustration of periodic scatterers in 2D periodic lattice in xy plane. S_{pq} denotes the surface of the pq-th scatterer. $\bar{\rho}''$ and $\bar{\rho}$ represents the location of an arbitrary source and field point, respectively.

Figure VII.1 illustrates the geometry of the 2D periodic array we're considering in this chapter. The notations are the same as we used in Chapter VI, where a is the lattice constant, $\bar{a}_1$ and $\bar{a}_2$ are the primitive lattice vectors. We use Ω_0 to denote the primitive cell area, and the scatterer in the pq-th cell has boundary S_{pq} surrounding the region A_{pq}. $\bar{\rho}''$ and $\bar{\rho}$ represents the location of an arbitrary source and field point, respectively.

7.1 Representation of the Green's function using modal expansion with low wavenumber extraction

The periodic Green's function with empty lattice $g_p^0\left(k, \bar{k}_i; \bar{\rho}, \bar{\rho}'\right)$ is the response to an infinite array of periodic point sources with progressive phase shift, denoted by $\delta^\infty\left(\bar{\rho} - \bar{\rho}'; \bar{k}_i\right)$.

$$\delta^{\infty}\left(\bar{\rho}-\bar{\rho}';\bar{k}_i\right)=\sum_{p=-\infty}^{\infty}\sum_{q=-\infty}^{\infty}\delta\left(\bar{\rho}-\bar{\rho}'-\bar{R}_{pq}\right)\exp\left(i\bar{k}_i\bullet\bar{R}_{pq}\right) \tag{7.1}$$

where $\bar{R}_{pq}=p\bar{a}_1+q\bar{a}_2$.

In spectral domain representation,

$$g_P^0\left(k,\bar{k}_i;\bar{\rho},\bar{\rho}'\right)=\frac{1}{\Omega_0}\sum_{m,n}\frac{\exp\left(i\bar{k}_{i,mn}\bullet\left(\bar{\rho}-\bar{\rho}'\right)\right)}{\left|\bar{k}_{i,mn}\right|^2-k^2} \tag{7.2}$$

where $\bar{k}_{i,mn}=\bar{k}_i+m\bar{b}_1+n\bar{b}_2$. This can be viewed as modal expansion where $\left|\bar{k}_{i,mn}\right|$ is the modal frequency and the Bloch wave $\frac{1}{\sqrt{\Omega_0}}\exp\left(\bar{k}_{i,mn}\cdot\bar{\rho}\right)$ is the normalized modal field. The modal field satisfies the orthonormal condition.

Including the periodic scatterers, we represent the periodic Green's function as $g_P^S\left(k,\bar{k}_i;\bar{\rho},\bar{\rho}'\right)$. In terms of modal expansion,

$$g_P^S\left(k,\bar{k}_i;\bar{\rho},\bar{\rho}'\right)=\sum_{\alpha}\frac{\tilde{\psi}_\alpha\left(\bar{\rho},\bar{k}_i\right)\tilde{\psi}_\alpha^*\left(\bar{\rho}',\bar{k}_i\right)}{k_\alpha^2-k^2} \tag{7.3}$$

where k_α and $\tilde{\psi}_\alpha\left(\bar{\rho},\bar{k}_i\right)$ are the modal frequencies and the normalized modal fields, respectively. k_α and $\tilde{\psi}_\alpha\left(\bar{\rho},\bar{k}_i\right)$ are solved in Chapter VI in the modal analysis of the periodic structure, and in general both can be complex.

For (7.3) to be valid, $\tilde{\psi}_\alpha\left(\bar{\rho},\bar{k}_i\right)$ must satisfy the orthonormal condition,

$$\int_{\Omega_{00}}d\bar{\rho}\tilde{\psi}_\alpha^*\left(\bar{\rho},\bar{k}_i\right)\tilde{\psi}_\beta\left(\bar{\rho},\bar{k}_i\right)=\delta_{\alpha\beta} \tag{7.4}$$

Eq. (7.3) can be proved as follows.

Proof:

We have

$$\left(\nabla^2 + k^2\right) g_P^S\left(k, \bar{k}_i; \bar{\rho}, \bar{\rho}'\right) = -\delta^\infty\left(\bar{\rho} - \bar{\rho}'; \bar{k}_i\right)$$
$$\left(\nabla^2 + k_\alpha^2\right) \tilde{\psi}_\alpha\left(\bar{\rho}, \bar{k}_i\right) = 0$$

Since $\tilde{\psi}_\alpha\left(\bar{\rho}, \bar{k}_i\right)$ completes an orthonormal basis, we could represent both $g_P^S\left(k, \bar{k}_i; \bar{\rho}, \bar{\rho}'\right)$ and $\delta^\infty\left(\bar{\rho} - \bar{\rho}'; \bar{k}_i\right)$ using linear combination of $\tilde{\psi}_\alpha\left(\bar{\rho}, \bar{k}_i\right)$

$$g_P^S\left(k, \bar{k}_i; \bar{\rho}, \bar{\rho}'\right) = \sum_\alpha C_\alpha \tilde{\psi}_\alpha\left(\bar{\rho}, \bar{k}_i\right)$$
$$\delta^\infty\left(\bar{\rho} - \bar{\rho}'; \bar{k}_i\right) = \sum_\alpha \tilde{\psi}_\alpha^*\left(\bar{\rho}, \bar{k}_i\right) \tilde{\psi}_\alpha\left(\bar{\rho}, \bar{k}_i\right)$$

Substituting the representations into wave equation to solve for the coefficients C_α

$$C_\alpha = \frac{\tilde{\psi}_\alpha^*\left(\bar{\rho}', \bar{k}_i\right)}{k_\alpha^2 - k^2}$$

This completes the proof of (7.3).

■

As discussed before, (7.3) converges slowly with respect to the number of modes included. In order to improve the convergence, we subtract out a low wave number component $g_P^S\left(k_L, \bar{k}_i; \bar{\rho}, \bar{\rho}'\right)$, and define the remainder as the broadband Green's function $g_{P,B}^S\left(k, k_L, \bar{k}_i; \bar{\rho}, \bar{\rho}'\right)$.

$$\begin{aligned} g_{P,B}^S\left(k, k_L, \bar{k}_i; \bar{\rho}, \bar{\rho}'\right) &= g_P^S\left(k, \bar{k}_i; \bar{\rho}, \bar{\rho}'\right) - g_P^S\left(k_L, \bar{k}_i; \bar{\rho}, \bar{\rho}'\right) \\ &= \sum_\alpha \frac{k^2 - k_L^2}{\left(k_\alpha^2 - k^2\right)\left(k_\alpha^2 - k_L^2\right)} \tilde{\psi}_\alpha\left(\bar{\rho}, \bar{k}_i\right) \tilde{\psi}_\alpha^*\left(\bar{\rho}', \bar{k}_i\right) \\ &= \sum_\alpha \frac{1}{\frac{1}{k^2 - k_L^2} - \frac{1}{k_\alpha^2 - k_L^2}} \frac{\tilde{\psi}_\alpha\left(\bar{\rho}, \bar{k}_i\right) \tilde{\psi}_\alpha^*\left(\bar{\rho}', \bar{k}_i\right)}{\left(k_\alpha^2 - k_L^2\right)^2} \end{aligned} \tag{7.5}$$

Notice that $1/(k_\alpha^2 - k_L^2)$ are the eigenvalues of the band diagram problem and $\tilde{\psi}_\alpha\left(\bar{\rho}, \bar{k}_i\right)$ are the corresponding normalized modal fields.

Note that $g_{P,B}^{S}\left(k,k_L,\bar{k}_i;\bar{\rho},\bar{\rho}'\right)$ converges with respect to $1/k_\alpha^4$, in contrast to $1/k_\alpha^2$ as in $g_P^S\left(k,\bar{k}_i;\bar{\rho},\bar{\rho}'\right)$. Only a few modes are needed to construct the broadband Green's function $g_{P,B}^{S}\left(k,k_L,\bar{k}_i;\bar{\rho},\bar{\rho}'\right)$ at any k, from which $g_P^S\left(k,\bar{k}_i;\bar{\rho},\bar{\rho}'\right)$ is easily obtained by summing up $g_{P,B}^{S}\left(k,k_L,\bar{k}_i;\bar{\rho},\bar{\rho}'\right)$ and $g_P^S\left(k_L,\bar{k}_i;\bar{\rho},\bar{\rho}'\right)$. The maximum k_α included should be several times larger than the largest k of interest to ensure convergence.

$$g_P^S\left(k,\bar{k}_i;\bar{\rho},\bar{\rho}'\right)=g_P^S\left(k_L,\bar{k}_i;\bar{\rho},\bar{\rho}'\right)+g_{P,B}^S\left(k,k_L,\bar{k}_i;\bar{\rho},\bar{\rho}'\right) \tag{7.6}$$

Thus g_P^S is only needed to be evaluated at a single k_L, and the choice of k_L is robust subject to non-overlap with the modes k_α. This k_L can be different from the k_L used in the modal analysis of the periodic structure with BBGFL.

7.2 Solving for the Green's function at a single low wavenumber

7.2.1 The extinction theorem and surface integral equation

We solve directly the surface integral equation for the Green's function $g_P^S\left(k,\bar{k}_i;\bar{\rho},\bar{\rho}''\right)$ at a single k_L. To illustrate the idea without loss of generality, we simply assume that $\bar{\rho}''$ is the source position outside the scatterer, and $\bar{\rho}$ is the field point outside the scatterer, respectively. The extinction theorem governing $g_P^S\left(k,\bar{k}_i;\bar{\rho},\bar{\rho}''\right)$ is then given by

$$\begin{aligned}&g_P^S\left(k,\bar{k}_i;\bar{\rho},\bar{\rho}''\right)-g_P^0\left(k,\bar{k}_i;\bar{\rho},\bar{\rho}''\right)\\&=\int_{S_{00}}d\bar{\rho}'\Big[g_P^S\left(k,\bar{k}_i;\bar{\rho}',\bar{\rho}''\right)\hat{n}'\bullet\nabla' g_P^0\left(k,\bar{k}_i;\bar{\rho},\bar{\rho}'\right)\\&-g_P^0\left(k,\bar{k}_i;\bar{\rho},\bar{\rho}'\right)\hat{n}'\bullet\nabla' g_P^S\left(k,\bar{k}_i;\bar{\rho}',\bar{\rho}''\right)\Big]\end{aligned} \tag{7.7}$$

One can derive similar relations when $\bar{\rho}$ is the field point inside the scatterer, and when $\bar{\rho}''$ is the source position inside the scatterer respectively. In a general setup, we need four parts of $g_P^{S,(11)}\left(k,\bar{k}_i;\bar{\rho},\bar{\rho}''\right)$, $g_P^{S,(21)}\left(k,\bar{k}_i;\bar{\rho},\bar{\rho}''\right)$, $g_P^{S,(12)}\left(k,\bar{k}_i;\bar{\rho},\bar{\rho}''\right)$, and $g_P^{S,(22)}\left(k,\bar{k}_i;\bar{\rho},\bar{\rho}''\right)$, where

the superscripts denote the combination of the locations of the field point and source point, to completely describe the Green's function $g_P^S\left(k,\bar{k}_i;\bar{\rho},\bar{\rho}''\right)$. Then $g_P^{S,(11)}\left(k,\bar{k}_i;\bar{\rho},\bar{\rho}''\right)$ and $g_P^{S,(21)}\left(k,\bar{k}_i;\bar{\rho},\bar{\rho}''\right)$ are coupled and connected to each other at the surface through boundary conditions; and same for $g_P^{S,(12)}\left(k,\bar{k}_i;\bar{\rho},\bar{\rho}''\right)$, and $g_P^{S,(22)}\left(k,\bar{k}_i;\bar{\rho},\bar{\rho}''\right)$.

Note that we have used $g_P^0\left(k,\bar{k}_i;\bar{\rho},\bar{\rho}''\right)$ to denote the periodic Green's function in an empty lattice without the scatterer, which has the meaning of the direct excitation field due to a point source array. Thus the left hand side of (7.7) has the meaning of response field due to scattering from periodic scatterers with no singularity.

Eq. (7.7) can be derived as follows.

Proof:

We start from

$$\left(\nabla^2+k^2\right)g^0\left(k;\bar{\rho},\bar{\rho}'\right)=-\delta\left(\bar{\rho}-\bar{\rho}'\right)$$
$$\left(\nabla^2+k^2\right)g_P^S\left(k,\bar{k}_i;\bar{\rho},\bar{\rho}''\right)=-\delta^\infty\left(\bar{\rho}-\bar{\rho}'';\bar{k}_i\right)$$

We choose A to be the region outside all the scatterers, and S to be the joint boundary, and $\hat{n}$ to be the normal pointing out of A, thus pointing into the scatterer. Applying the 2D Green's theorem,

$$\begin{aligned}&\int_A d\bar{\rho}\left[g_P^S\left(k,\bar{k}_i;\bar{\rho},\bar{\rho}''\right)\nabla^2 g^0\left(k;\bar{\rho},\bar{\rho}'\right)-g^0\left(k;\bar{\rho},\bar{\rho}'\right)\nabla^2 g_P^S\left(k,\bar{k}_i;\bar{\rho},\bar{\rho}''\right)\right]\\&=\int_S d\bar{\rho}\left[g_P^S\left(k,\bar{k}_i;\bar{\rho},\bar{\rho}''\right)\hat{n}\cdot\nabla g^0\left(k;\bar{\rho},\bar{\rho}'\right)-g^0\left(k;\bar{\rho},\bar{\rho}'\right)\hat{n}\cdot\nabla g_P^S\left(k,\bar{k}_i;\bar{\rho},\bar{\rho}''\right)\right]\end{aligned}$$

Let both $\bar{\rho}'$ and $\bar{\rho}''$ to be in region A, and making use of the wave equations,

$$\begin{aligned}&\int_A d\bar{\rho}\left[g_P^S\left(k,\bar{k}_i;\bar{\rho},\bar{\rho}''\right)\nabla^2 g^0\left(k;\bar{\rho},\bar{\rho}'\right)-g^0\left(k;\bar{\rho},\bar{\rho}'\right)\nabla^2 g_P^S\left(k,\bar{k}_i;\bar{\rho},\bar{\rho}''\right)\right]\\&=\int_A d\bar{\rho}\left[-g_P^S\left(k,\bar{k}_i;\bar{\rho},\bar{\rho}''\right)\delta\left(\bar{\rho}-\bar{\rho}'\right)+g^0\left(k;\bar{\rho},\bar{\rho}'\right)\delta^\infty\left(\bar{k}_i;\bar{\rho}-\bar{\rho}''\right)\right]\\&=-g_P^S\left(k,\bar{k}_i;\bar{\rho}',\bar{\rho}''\right)+g_P^0\left(k,\bar{k}_i;\bar{\rho}',\bar{\rho}''\right)\end{aligned}$$

In the last equality, we have used the symmetry of $g^0(k;\bar{\rho},\bar{\rho}')$, the definition of $\delta^\infty(\bar{\rho},\bar{\rho}'';\bar{k}_i)$, and the definition of $g_P^0(k,\bar{k}_i;\bar{\rho}',\bar{\rho}'')$.

$$g^0\left(k;\bar{\rho},\bar{\rho}'\right)=g^0\left(k;\bar{\rho}',\bar{\rho}\right)$$

$$\delta^\infty\left(\bar{\rho}-\bar{\rho}'';\bar{k}_i\right)=\sum_{p=-\infty}^{\infty}\sum_{q=-\infty}^{\infty}\delta\left(\bar{\rho}-\bar{\rho}''-\bar{R}_{pq}\right)\exp\left(i\bar{k}_i\bullet\bar{R}_{pq}\right)$$

$$g_P^0\left(k,\bar{k}_i;\bar{\rho}',\bar{\rho}''\right)=\sum_{p=-\infty}^{\infty}\sum_{q=-\infty}^{\infty}g^0\left(k;\bar{\rho}',\bar{\rho}''+\bar{R}_{pq}\right)\exp\left(i\bar{k}_i\bullet\bar{R}_{pq}\right)$$

For the right hand side, it is possible to split the line integral into multiple integrals, and apply the Bloch wave condition of $g_P^S(k,\bar{k}_i;\bar{\rho},\bar{\rho}'')$, and separate out the definition of $g_P^0(k,\bar{k}_i;\bar{\rho},\bar{\rho}')$, then we get

$$\begin{aligned}&\int_S d\bar{\rho}\left[g_P^S\left(k,\bar{k}_i;\bar{\rho},\bar{\rho}''\right)\hat{n}\cdot\nabla g^0\left(k;\bar{\rho},\bar{\rho}'\right)-g^0\left(k;\bar{\rho},\bar{\rho}'\right)\hat{n}\cdot\nabla g_P^S\left(k,\bar{k}_i;\bar{\rho},\bar{\rho}''\right)\right]\\&=\int_{S_{00}}d\bar{\rho}\left[g_P^S\left(k,\bar{k}_i;\bar{\rho},\bar{\rho}''\right)\hat{n}\cdot\nabla g_P^0\left(k;\bar{\rho}',\bar{\rho}\right)-g_P^0\left(k;\bar{\rho}',\bar{\rho}\right)\hat{n}\cdot\nabla g_P^S\left(k,\bar{k}_i;\bar{\rho},\bar{\rho}''\right)\right]\end{aligned}$$

Equating the left hand side with right hand side, we arrive at,

$$\begin{aligned}&-g_P^S\left(k,\bar{k}_i;\bar{\rho}',\bar{\rho}''\right)+g_P^0\left(k,\bar{k}_i;\bar{\rho}',\bar{\rho}''\right)\\&=\int_{S_{00}}d\bar{\rho}\left[g_P^S\left(k,\bar{k}_i;\bar{\rho},\bar{\rho}''\right)\hat{n}\cdot\nabla g_P^0\left(k;\bar{\rho}',\bar{\rho}\right)-g_P^0\left(k;\bar{\rho}',\bar{\rho}\right)\hat{n}\cdot\nabla g_P^S\left(k,\bar{k}_i;\bar{\rho},\bar{\rho}''\right)\right]\end{aligned}$$

Now change the definition of $\hat{n}$ to be pointing outward from the scatterer into A, and then exchange variable $\bar{\rho}$ with $\bar{\rho}'$, we get the final form of the extinction theorem,

$$\begin{aligned}&-g_P^S\left(k,\bar{k}_i;\bar{\rho},\bar{\rho}''\right)+g_P^0\left(k,\bar{k}_i;\bar{\rho},\bar{\rho}''\right)\\&=-\int_{S_{00}}d\bar{\rho}'\left[g_P^S\left(k,\bar{k}_i;\bar{\rho}',\bar{\rho}''\right)\hat{n}'\cdot\nabla' g_P^0\left(k;\bar{\rho},\bar{\rho}'\right)-g_P^0\left(k;\bar{\rho},\bar{\rho}'\right)\hat{n}'\cdot\nabla' g_P^S\left(k,\bar{k}_i;\bar{\rho}',\bar{\rho}''\right)\right]\end{aligned}$$

where both $\bar{\rho}$ and $\bar{\rho}''$ are outside of the scatterer in region A. This is identical to (7.7).

■

To proceed and illustrate the idea, we stick to $g_P^{S,(11)}\left(k,\bar{k}_i;\bar{\rho},\bar{\rho}''\right)$ and assume a Dirichlet boundary condition of $g_P^S\left(k,\bar{k}_i;\bar{\rho},\bar{\rho}''\right)$ on the scatterer surface. This is the case when we examine the electric field response due to a $\hat{z}$-polarized line source outside of a periodic array of PEC scatterers. The fields are polarized TM to z.

For $\bar{\rho}'$ to be on the boundary,

$$g_P^S\left(k,\bar{k}_i;\bar{\rho}',\bar{\rho}''\right)=0 \tag{7.8}$$

The extinction theorem is then much simplified,

$$\begin{aligned} &g_P^S\left(k,\bar{k}_i;\bar{\rho},\bar{\rho}''\right)-g_P^0\left(k,\bar{k}_i;\bar{\rho},\bar{\rho}''\right) \\ &=-\int_{S_{00}} d\bar{\rho}'\left[g_P^0\left(k,\bar{k}_i;\bar{\rho},\bar{\rho}'\right)\hat{n}'\bullet\nabla' g_P^S\left(k,\bar{k}_i;\bar{\rho}',\bar{\rho}''\right)\right] \end{aligned} \tag{7.9}$$

Note that in (7.9), $\bar{\rho}$ can still be anywhere outside the scatterers, and this is the equation to calculate $g_P^S\left(k,\bar{k}_i;\bar{\rho},\bar{\rho}''\right)$. Letting $\bar{\rho}$ approaching the surface of the scatterer, we get the surface integral equation,

$$g_P^0\left(k,\bar{k}_i;\bar{\rho},\bar{\rho}''\right)=\int_{S_{00}} d\bar{\rho}'\left[g_P^0\left(k,\bar{k}_i;\bar{\rho},\bar{\rho}'\right)\hat{n}'\bullet\nabla' g_P^S\left(k,\bar{k}_i;\bar{\rho}',\bar{\rho}''\right)\right] \tag{7.10}$$

Define the surface currents $J\left(\bar{\rho}';\bar{k}_i\right)$,

$$J\left(\bar{\rho}';\bar{k}_i\right)=\hat{n}'\bullet\nabla' g_P^S\left(k,\bar{k}_i;\bar{\rho}',\bar{\rho}''\right) \tag{7.11}$$

Then

$$g_P^0\left(k,\bar{k}_i;\bar{\rho},\bar{\rho}''\right)=\int_{S_{00}} d\bar{\rho}'\left[g_P^0\left(k,\bar{k}_i;\bar{\rho},\bar{\rho}'\right)J\left(\bar{\rho}';\bar{k}_i\right)\right] \tag{7.12}$$

Notice that this is the same equation that governs the modal analysis problem as we developed in Chapter VI. We're simply replacing the right hand side (excitation) with the direct incidence field from the periodic point source array $g_P^0\left(k,\bar{k}_i;\bar{\rho},\bar{\rho}''\right)$. We can apply the same discretization scheme using pulse basis and point matching in MoM to solve it.

Let $q_n = \Delta t_n J(\bar{\rho}_n; \bar{k}_i) = \Delta t_n J_n$, then in matrix form

$$\bar{\bar{L}}^{(e)}\bar{q} = \bar{b}^{(e)} \tag{7.13}$$

where

$$L_{mn}^{(e)} = \frac{1}{\Delta t_n}\int_{S_{00}^{(n)}} d\bar{\rho}' g_P^0\left(k, \bar{k}_i; \bar{\rho}, \bar{\rho}'\right), \bar{\rho} = \bar{\rho}_m \tag{7.14}$$

$$b_m^{(e)} = g_P^0\left(k, \bar{k}_i; \bar{\rho}, \bar{\rho}''\right), \bar{\rho} = \bar{\rho}_m \tag{7.15}$$

The evaluation of the matrix elements and the right hand side directly follow the scheme we developed in Chapter VI.

After solving for the surface currents $J(\bar{\rho}'; \bar{k}_i)$, we reapply (7.7) or (7.9) to get the Green's function $g_P^S(k, \bar{k}_i; \bar{\rho}, \bar{\rho}'')$ anywhere.

Note that both $g_P^0(k, \bar{k}_i; \bar{\rho}, \bar{\rho}'')$ and $g_P^S(k, \bar{k}_i; \bar{\rho}, \bar{\rho}'')$ satisfy the Bloch wave condition, using $\psi(\bar{\rho})$ as a general representation of field,

$$\psi\left(\bar{\rho} + \bar{R}_{pq}\right) = \psi\left(\bar{\rho}\right)\exp\left(i\bar{k}_i \bullet \bar{R}_{pq}\right) \tag{7.16}$$

7.2.2 Illustration of numerical results

We illustrate numerical results considering a periodic array of circular PEC cylinders. The primary lattice vectors are defined by $\bar{a}_1 = \frac{a}{2}\left(\sqrt{3}\hat{x} + \hat{y}\right)$, and $\bar{a}_2 = \frac{a}{2}\left(-\sqrt{3}\hat{x} + \hat{y}\right)$, where $a = 1$ is the normalized lattice constant. $\bar{b}_1 = 2\pi\frac{\bar{a}_2 \times \hat{z}}{\Omega_0}$ and $\bar{b}_2 = -2\pi\frac{\bar{a}_1 \times \hat{z}}{\Omega_0}$ are the reciprocal lattice vectors, and $\Omega_0 = (\bar{a}_1 \times \bar{a}_2) \cdot \hat{z}$ is the lattice area. The cylinders have radii of $b = 0.2a$ centered at $\bar{R}_{pq} = p\bar{a}_1 + q\bar{a}_2$, where $p, q = \cdots, -1, 0, 1, \ldots$. The background region outside of the cylinders has permittivity of $\varepsilon_b = 8.9\varepsilon_0$. We put the source point at $\bar{\bar{\rho}}'' = \frac{1}{3}(\bar{a}_1 + \bar{a}_2)$, and are interested in

the field response $g_P^S\left(k_L, \bar{k}_i; \bar{\rho}, \bar{\rho}''\right)$ over the lattice. We choose $k_L = \frac{2\pi}{a} f_{nL} \sqrt{\frac{\varepsilon_b}{\varepsilon_0}}$ where $f_{nL} = 0.001$, and let $\bar{k}_i = \beta_1 \bar{b}_1 + \beta_2 \bar{b}_2$, where $\beta_1 = 0.1$, $\beta_2 = 0.05$. The position of the cylinder and the source point in the unit lattice are illustrated in Figure VII.2. We also depict a special field point at $\bar{\rho} = \frac{7}{16} \bar{a}_1$ where we're going to examine the $\bar{k}_i$ dependence more carefully.

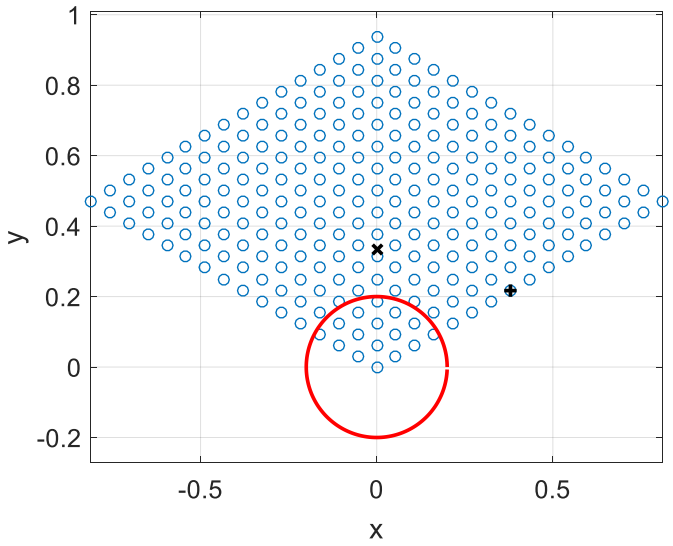

Figure VII.2. Geometry of the cylinder (red circle) and the source point (black cross) inside the unit cell. Blue circles denotes the points at which we probe the fields. Black + denotes a special field point to be examined more closely.

The surface currents on the cylinder are shown in Figure VII.3, which demonstrate a peak at $\phi = 90°$, closest to the source point.

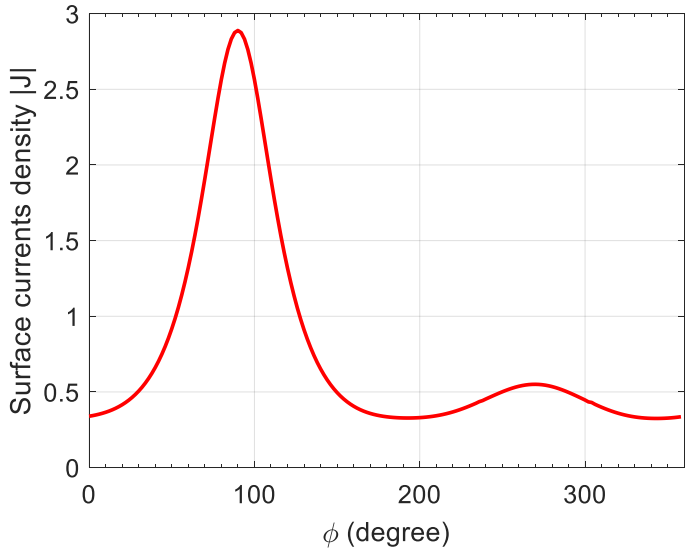

Figure VII.3. Magnitude of the surface currents on the PEC cylinder

The field distribution of $g_P^S(k_L, \bar{k}_i; \bar{\rho}, \bar{\rho}'')$ over the lattice is depicted in Figure VII.4. The field repeats itself under Bloch wave conditions. The repeating of the point sources is obvious from the magnitude of the field distribution. The phase progression according to $\bar{k}_i$ is manifested in the real and imaginary part of the field distributions.

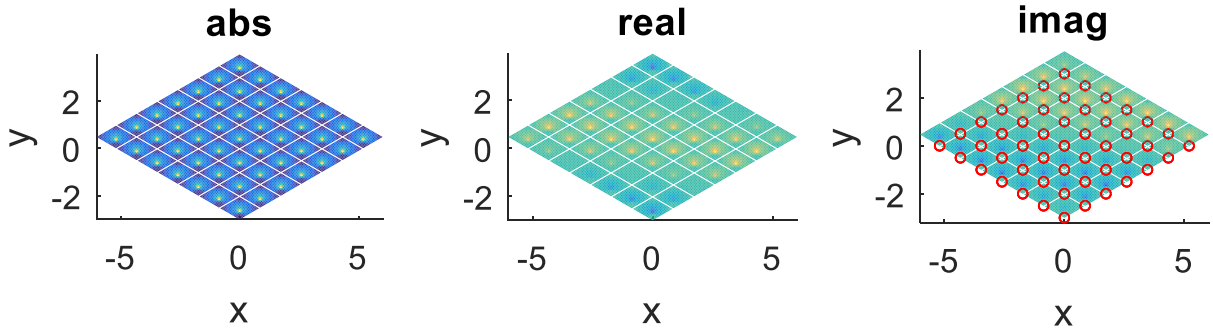

Figure VII.4. Field distribution of $g_P^S(k_L, \bar{k}_i; \bar{\rho}, \bar{\rho}'')$ over the lattice: (a) left: magnitude, (b) middle: real part; (c) right: imaginary part.

7.3 Efficient Modal Field Normalization

7.3.1 Calculation and representation of the modal field

For the modal expansion of (7.3) to be valid, $\tilde{\psi}_\alpha(\bar{\rho};\bar{k}_i)$ must satisfy the orthonormal condition of (7.4), where $\tilde{\psi}_\alpha(\bar{\rho};\bar{k}_i)$ is the normalized modal field distribution. In this section, we describe the conditions imposed on the modal field $\psi_\alpha(\bar{\rho};\bar{k}_i)$ to make it orthonormal.

We limit ourselves to the case of PEC scatterers with TMz polarization. Then for a specific mode α, the modal field $\psi_\alpha(\bar{\rho};\bar{k}_i)$ is governed by the extinction theorem from the modal current $J_\alpha(\bar{\rho}')$ and the modal wavenumber k_α, which are obtained out of the modal analysis problem,

$$\psi_\alpha\left(\bar{\rho};\bar{k}_i\right)=\int_{S_{00}} d\bar{\rho}'\left[g_P^0\left(k_\alpha,\bar{k}_i;\bar{\rho},\bar{\rho}'\right)J_\alpha\left(\bar{\rho}'\right)\right] \tag{7.17}$$

Applying low wavenumber extraction, where k_L can be different from the one used in (7.5),

$$\psi_\alpha\left(\bar{\rho};\bar{k}_i\right)=\int_{S_{00}} d\bar{\rho}'\left[g_P^0\left(k_L,\bar{k}_i;\bar{\rho},\bar{\rho}'\right)+g_{P,B}^0\left(k_\alpha,k_L,\bar{k}_i;\bar{\rho},\bar{\rho}'\right)\right]J_\alpha\left(\bar{\rho}'\right) \tag{7.18}$$

The normalized modal field will then become

$$\tilde{\psi}_\alpha\left(\bar{\rho},\bar{k}_i\right)=\frac{\psi_\alpha\left(\bar{\rho},\bar{k}_i\right)}{\sqrt{\int_{\Omega_{00}} d\bar{\rho}\left|\psi_\alpha\left(\bar{\rho},\bar{k}_i\right)\right|^2}} \tag{7.19}$$

We will show that under the condition of $k_L\to 0$, i.e., $k_L \ll k_\alpha$ and $k_L \ll \left|\bar{k}_{i\alpha}\right|$, where both k_α and $\bar{k}_{i\alpha}$ depends on $\bar{k}_i$,

$$\psi_\alpha\left(\bar{\rho};\bar{k}_i\right)\to\frac{1}{k_\alpha^2}\sum_{\alpha'}\tilde{\psi}_{\alpha'}^0\left(\bar{\rho};\bar{k}_i\right)b_{\alpha'\alpha} \tag{7.20}$$

where $\tilde{\psi}_{\alpha'}^0(\bar{\rho};\bar{k}_i)=\frac{1}{\sqrt{\Omega_0}}\exp(\bar{k}_{i\alpha'}\cdot\bar{\rho})$ is the normalized Floquet mode, which is orthonormal, and $b_{\alpha'\alpha}$ is the projection of surface currents $J_\alpha(\bar{\rho}')$ on the Floquet mode $\tilde{\psi}_{\alpha'}^0(\bar{\rho};\bar{k}_i)$.

$$b_{\alpha'\alpha} = \frac{k_\alpha^2 - k_L^2}{\left|\bar{k}_{i\alpha'}\right|^2 - k_\alpha^2} \int_{S_{00}} d\bar{\rho}' \left[\tilde{\psi}_{\alpha'}^{0*}\left(\bar{\rho}'; \bar{k}_i\right) J_\alpha\left(\bar{\rho}'\right) \right] \tag{7.21}$$

It is easy to show that Eq. (7.21) is identical to the definition of $\bar{b}$ in Chapter VI,

$$\bar{b} = \bar{\bar{W}}\bar{\bar{R}}^\dagger \bar{q} \tag{7.22}$$

Thus $b_{\alpha'\alpha}$ is simply the α'-th component of the eigenvector $\bar{b}$ corresponding to the eigen mode of k_α.

Eq. (7.20) is proved as follows.

Proof:

Start from (7.18) and substitute $g_{P,B}^0$ using modal expansion in the form of (7.5),

$$\begin{aligned} \psi_\alpha\left(\bar{\rho}; \bar{k}_i\right) = & \int_{S_{00}} d\bar{\rho}' g_P^0\left(k_L, \bar{k}_i; \bar{\rho}, \bar{\rho}'\right) J_\alpha\left(\bar{\rho}'\right) \\ & + \sum_{\alpha'} \frac{\tilde{\psi}_{\alpha'}^0\left(\bar{\rho}, \bar{k}_i\right)}{\left(\left|\bar{k}_{i\alpha'}\right|^2 - k_L^2\right)} \frac{\left(k_\alpha^2 - k_L^2\right)}{\left(\left|\bar{k}_{i\alpha'}\right|^2 - k_\alpha^2\right)} \int_{S_{00}} d\bar{\rho}' \tilde{\psi}_{\alpha'}^{0*}\left(\bar{\rho}', \bar{k}_i\right) J_\alpha\left(\bar{\rho}'\right) \end{aligned} \tag{7.23}$$

Using the definition of $b_{\alpha'\alpha}$ in (7.21), and considering,

$$\begin{aligned} \left(\nabla^2 + k_L^2\right) g_P^S\left(k_L, \bar{k}_i; \bar{\rho}, \bar{\rho}'\right) &= -\delta^\infty\left(\bar{\rho} - \bar{\rho}'; \bar{k}_i\right) \\ \left(\nabla^2 + \left|\bar{k}_{i\alpha'}\right|^2\right) \tilde{\psi}_{\alpha'}^2\left(\bar{\rho}, \bar{k}_i\right) &= 0 \\ \left(\nabla^2 + k_\alpha^2\right) \tilde{\psi}_\alpha\left(\bar{\rho}, \bar{k}_i\right) &= 0 \end{aligned}$$

which leads to

$$\begin{aligned} \nabla^2 g_P^S\left(k_L, \bar{k}_i; \bar{\rho}, \bar{\rho}'\right) &= -\delta^\infty\left(\bar{\rho} - \bar{\rho}'; \bar{k}_i\right) - k_L^2 g_P^S\left(k_L, \bar{k}_i; \bar{\rho}, \bar{\rho}'\right) \\ \nabla^2 \tilde{\psi}_{\alpha'}^2\left(\bar{\rho}, \bar{k}_i\right) &= -\left|\bar{k}_{i\alpha'}\right|^2 \tilde{\psi}_{\alpha'}^2\left(\bar{\rho}, \bar{k}_i\right) \\ \tilde{\psi}_\alpha\left(\bar{\rho}, \bar{k}_i\right) &= -\frac{\nabla^2 \tilde{\psi}_\alpha\left(\bar{\rho}, \bar{k}_i\right)}{k_\alpha^2} \end{aligned}$$

Thus

$$\psi_\alpha\left(\bar{\rho};\bar{k}_i\right)=\frac{k_L^2}{k_\alpha^2}\int_{S_{00}}d\bar{\rho}'g_P^0\left(k_L,\bar{k}_i;\bar{\rho},\bar{\rho}'\right)J_\alpha\left(\bar{\rho}'\right)+\frac{1}{k_\alpha^2}\sum_{\alpha'}\frac{\left|\bar{k}_{i\alpha'}\right|^2\tilde{\psi}_{\alpha'}^0\left(\bar{\rho},\bar{k}_i\right)}{\left(\left|\bar{k}_{i\alpha'}\right|^2-k_L^2\right)}b_{\alpha'\alpha} \tag{7.24}$$

We arrive at (7.20) under the limit of $k_L\to 0$, i.e., $k_L\ll k_\alpha$ and $k_L\ll\left|\bar{k}_{i\alpha}\right|$.

■

After (7.20), and invoking the orthonormal condition of $\tilde{\psi}_{\alpha'}^0\left(\bar{\rho};\bar{k}_i\right)$, it immediately follows that,

$$\int_{\Omega_{00}}d\bar{\rho}\psi_\alpha^*\left(\bar{\rho},\bar{k}_i\right)\psi_\beta\left(\bar{\rho},\bar{k}_i\right)=\frac{1}{k_\alpha^{*2}k_\beta^2}\sum_{\alpha'}\bar{b}_{\alpha'\alpha}^*\bar{b}_{\alpha'\beta}=\frac{1}{k_\alpha^{*2}k_\beta^2}\left\langle\bar{b}_\alpha,\bar{b}_\beta\right\rangle=\frac{1}{k_\alpha^{*2}k_\beta^2}\bar{b}_\alpha^\dagger\bar{b}_\beta \tag{7.25}$$

where $\langle\bar{b}_\alpha,\bar{b}_\beta\rangle$ denotes the inner product of the two eigenvectors $\bar{b}_\alpha$ and $\bar{b}_\beta$. When $k_\alpha\neq k_\beta$, those valid (physical) eigenvectors satisfy $\langle\bar{b}_\alpha,\bar{b}_\beta\rangle=0$, following the Sturm-Liouville theory; when $k_\alpha=k_\beta$, $\bar{b}_\alpha$ and $\bar{b}_\beta$ can be always orthonormalized through a Gram-Schmidt process. Using the orthonormal basis of the eigenvectors, (7.25) is reduced

$$\int_{\Omega_{00}}d\bar{\rho}\psi_\alpha^*\left(\bar{\rho},\bar{k}_i\right)\psi_\beta\left(\bar{\rho},\bar{k}_i\right)=\frac{\left\langle\bar{b}_\alpha,\bar{b}_\alpha\right\rangle}{\left|k_\alpha\right|^4}\delta_{\alpha\beta}=\frac{1}{\left|k_\alpha\right|^4}\delta_{\alpha\beta} \tag{7.26}$$

Thus the normalized modal field distribution $\tilde{\psi}_\alpha\left(\bar{\rho};\bar{k}_i\right)$

$$\tilde{\psi}_\alpha\left(\bar{\rho},\bar{k}_i\right)=\left|k_\alpha\right|^2\psi_\alpha\left(\bar{\rho},\bar{k}_i\right) \tag{7.27}$$

satisfies the orthonormal condition of (7.4).

The modal field itself can be calculated from either (7.18) or (7.20). Note (7.20) is only valid for $k_L\to 0$ ($k_L\ll k_\alpha$ and $k_L\ll\left|\bar{k}_{i\alpha}\right|$). A combination of (7.20) and (7.27) leads to

$$\tilde{\psi}_\alpha\left(\bar{\rho},\bar{k}_i\right)=\frac{\left|k_\alpha\right|^2}{k_\alpha^2}\sum_{\alpha'}\tilde{\psi}^0_{\alpha'}\left(\bar{\rho};\bar{k}_i\right)b_{\alpha'\alpha} \tag{7.28}$$

where the normalization of modal field $\tilde{\psi}\left(\bar{\rho},\bar{k}_i\right)$ is guaranteed. Note for real k_α, (7.28) is simplified to

$$\tilde{\psi}_\alpha\left(\bar{\rho},\bar{k}_i\right)=\sum_{\alpha'}\tilde{\psi}^0_{\alpha'}\left(\bar{\rho};\bar{k}_i\right)b_{\alpha'\alpha} \tag{7.29}$$

suggesting the physical meaning of $\bar{b}_\alpha$ as the coefficients of plane wave expansion of modal fields.

Below we show the orthogonality of $\psi_\alpha\left(\bar{\rho};\bar{k}_i\right)$ and $\psi_\beta\left(\bar{\rho};\bar{k}_i\right)$ for $k_\alpha \neq k_\beta$ (assuming real k_α). The conclusion can be generalized to the complex case.

$$\int_{\Omega_{00}} d\bar{\rho}\psi^*_\alpha\left(\bar{\rho},\bar{k}_i\right)\psi_\beta\left(\bar{\rho},\bar{k}_i\right)=0 \tag{7.30}$$

Proof:

Starting from

$$\left(\nabla^2+k_\alpha^2\right)\psi_\alpha\left(\bar{\rho},\bar{k}_i\right)=0$$
$$\left(\nabla^2+k_\beta^2\right)\psi_\beta\left(\bar{\rho},\bar{k}_i\right)=0$$

We have

$$\left(k_\beta^2-k_\alpha^{*2}\right)\psi^*_\alpha\left(\bar{\rho},\bar{k}_i\right)\psi_\beta\left(\bar{\rho},\bar{k}_i\right)=\psi_\beta\left(\bar{\rho},\bar{k}_i\right)\nabla^2\psi^*_\alpha\left(\bar{\rho},\bar{k}_i\right)-\psi^*_\alpha\left(\bar{\rho},\bar{k}_i\right)\nabla^2\psi_\beta\left(\bar{\rho},\bar{k}_i\right)$$

Then

$$\begin{aligned}&\left(k_\beta^2-k_\alpha^{*2}\right)\int_{\Omega_{00}} d\bar{\rho}\psi^*_\alpha\left(\bar{\rho},\bar{k}_i\right)\psi_\beta\left(\bar{\rho},\bar{k}_i\right)\\&=\int_{\Omega_{00}} d\bar{\rho}\left[\psi_\beta\left(\bar{\rho},\bar{k}_i\right)\nabla^2\psi^*_\alpha\left(\bar{\rho},\bar{k}_i\right)-\psi^*_\alpha\left(\bar{\rho},\bar{k}_i\right)\nabla^2\psi_\beta\left(\bar{\rho},\bar{k}_i\right)\right]\\&=\int_{\partial\Omega_{00}} d\bar{\rho}\left[\psi_\beta\left(\bar{\rho},\bar{k}_i\right)\hat{n}\cdot\nabla\psi^*_\alpha\left(\bar{\rho},\bar{k}_i\right)-\psi^*_\alpha\left(\bar{\rho},\bar{k}_i\right)\hat{n}\cdot\nabla\psi_\beta\left(\bar{\rho},\bar{k}_i\right)\right]\end{aligned}$$

It is easy to argue the right hand side to be zero considering the Bloch wave condition, such that the integral over $\partial\Omega_{pq}$ are equal for any pq-th cell, but these contour integrals cancel each other since the normal are opposite to each other. It directly follows that

$$\int_{\Omega_{00}} d\bar{\rho}\psi_\alpha^*\left(\bar{\rho},\bar{k}_i\right)\psi_\beta\left(\bar{\rho},\bar{k}_i\right)=0,\ \text{for } k_\beta^2 \neq k_\alpha^{*2}$$

■

7.3.2 Illustration of results on the modal fields $\boldsymbol{\psi_\alpha}\left(\bar{\boldsymbol{\rho}},\bar{\boldsymbol{k}}_{\boldsymbol{i}}\right)$

We use the same periodic array of PEC cylinders as described in section 7.2.1 to illustrate the modal fields and its orthonormalization. We choose the same $\bar{k}_i$ and k_L as well. In Figure VII.5, we show the modal fields out of (7.18) for the lowest three modes. The field extinguishes inside the PEC cylinder, and it exhibits more complicated pattern over the lattice as the normalized modal frequency increases. The field patterns are orthogonal to each other.

In Figure VII.6, we check the accuracy of using (7.20) to approximate (7.18). Their relative error in the root mean square (RMS) sense is plotted as a function of modal frequency. The accuracy decreases as the modal frequency increases.

The validity of (7.20) assures the orthonormal relation in the normalized modal field of (7.28). In Figure VII.7, we explicitly check the orthogonal relation of the eigenvectors $\bar{b}_\alpha$ corresponding to different modes. The cross inner products of the eigenvectors $\bar{b}_\alpha$ in general vanishes. One must ensure dense enough spatial sampling in evaluating (7.4) if using (7.18) and (7.19) to check the orthonormal condition of modal fields.

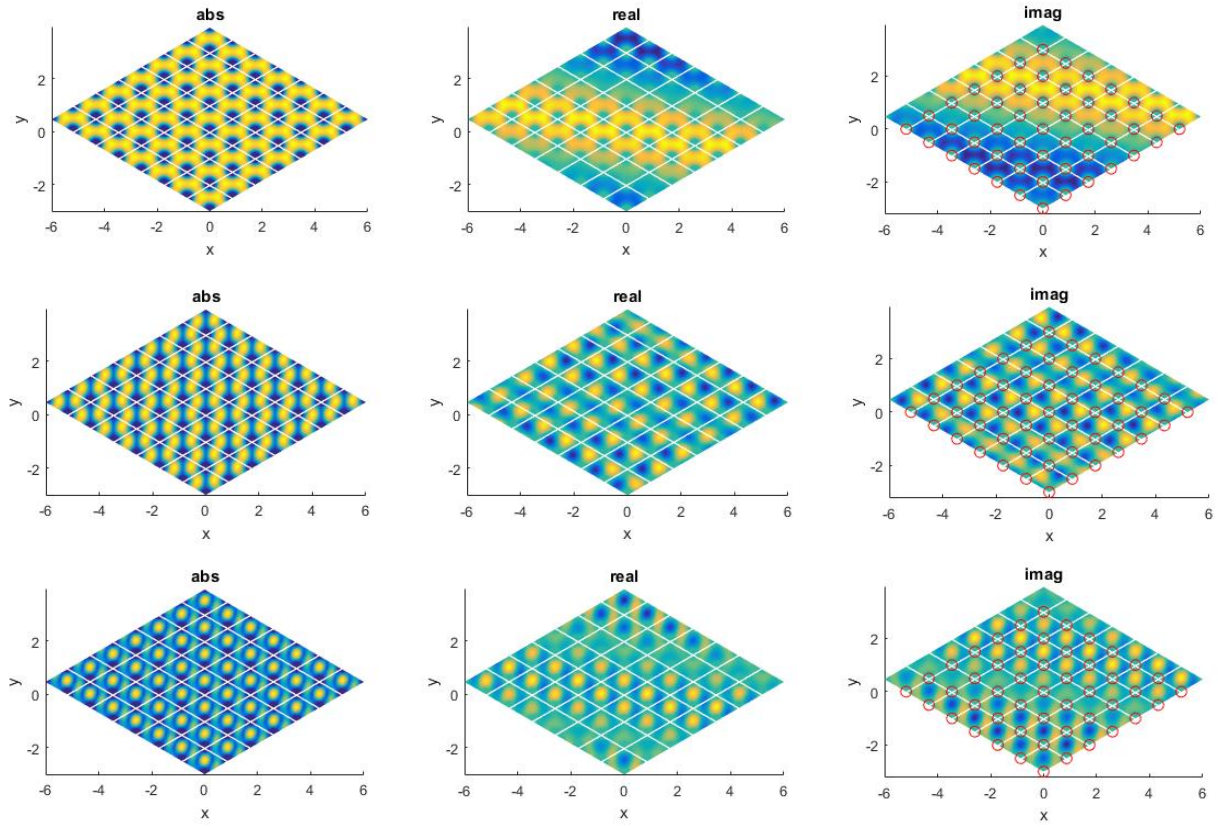

Figure VII.5. Modal field distribution for the lowest three modes (a) top: $f_n = 0.216$ (b) middle: $f_n = 0.368$ (c) bottom: $f_n = 0.413$. From left to right are the magnitude, real, and imaginary part of the modal fields, respectively.

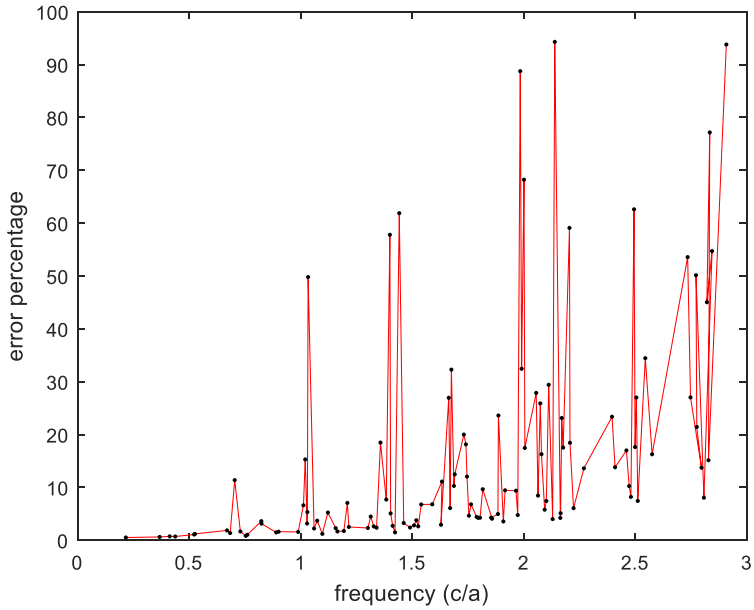

Figure VII.6. The relative RMSE of using (7.20) to approximate (7.18) as a function of normalized modal frequency.

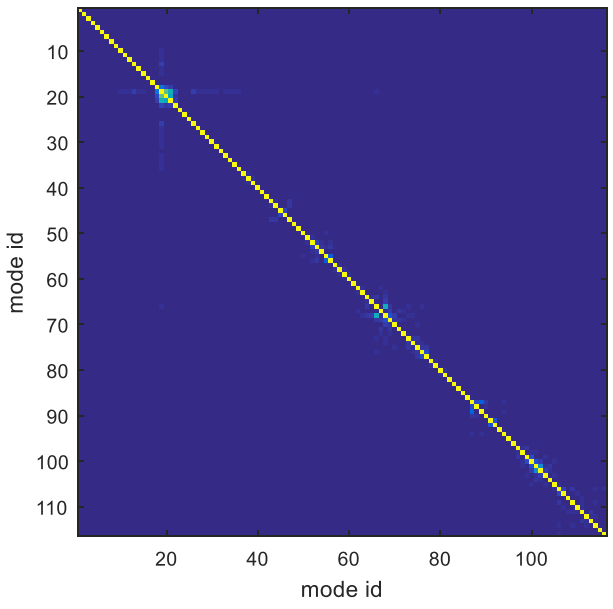

Figure VII.7. Inner products of the eigenvectors $\bar{b}_\alpha$ corresponding to different modes.

7.3.3 Illustration of results on the Green's function $g_P^S(\boldsymbol{k}, \bar{\boldsymbol{k}}_i; \bar{\boldsymbol{\rho}}, \bar{\boldsymbol{\rho}}'')$

The orthonormalization of the modal field supports the modal expansion of the Green's function with low wave number expansion as discussed in section 7.1. In this subsection, we test the accuracy of using (7.6) with modal expansion to evaluate the Green's function of $g_P^S(k, \bar{k}_i; \bar{\rho}, \bar{\rho}'')$ as compared to the direct solution from surface integral equation (SIE) as discussed in section 7.2. The advantage of (7.6) is that we only need to solve SIE once.

We first illustrate the results of $g_{P,B}^S(k, k_L, \bar{k}_i; \bar{\rho}, \bar{\rho}')$ following (7.5) at $f_n = 0.2$ using all the modes with $k_\alpha \leq k_{\max} = 8k$, including 49 modes. The results are given in Figure VII.8. Comparing to the results of $g_P^S(k_L, \bar{k}_i; \bar{\rho}, \bar{\rho}')$ as shown in Figure VII.4, the behavior of $g_{P,B}^S(k, k_L, \bar{k}_i; \bar{\rho}, \bar{\rho}')$ is well and smooth without singularity. It is also seen that the spatial variation of $g_{P,B}^S$ is close to the modal field distribution of $\tilde{\psi}_\alpha(\bar{\rho}, \bar{k}_i)$ at $f_{n\alpha} = 0.216$ as shown in Figure VII.5. This is a result of f_n being close to $f_{n\alpha}$ thus the contribution from the corresponding mode becomes dominant in shaping the broadband Green's function $g_{P,B}^S$.

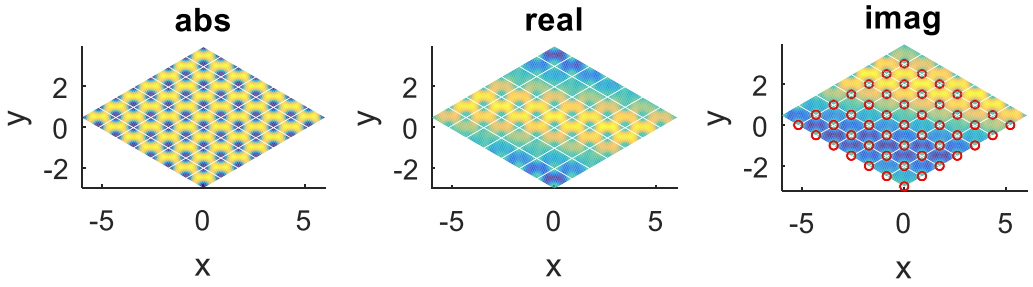

Figure VII.8. Spatial variation of $g_{P,B}^S(k, k_L, \bar{k}_i; \bar{\rho}, \bar{\rho}')$ at $f_n = 0.2$ with $f_{nL} = 0.001$ and $\bar{k}_i = 0.1\bar{b}_1 + 0.05\bar{b}_2$. From left to right are the magnitude, real, and imaginary part of the fields, respectively.

Using $k_{\max} = 8k$ as the benchmark, we calculate the relative error in evaluating $g_{P,B}^{S}$ as the number of modes included. The errors are plotted in Figure VII.9 in terms of $k_{\max}$, confirming the rapid convergence of $g_{P,B}^{S}$ with respect to the number of modes. In this case a $k_{\max} = 3k$ yields error less than 1%. The mode density in general increases as the frequency increases.

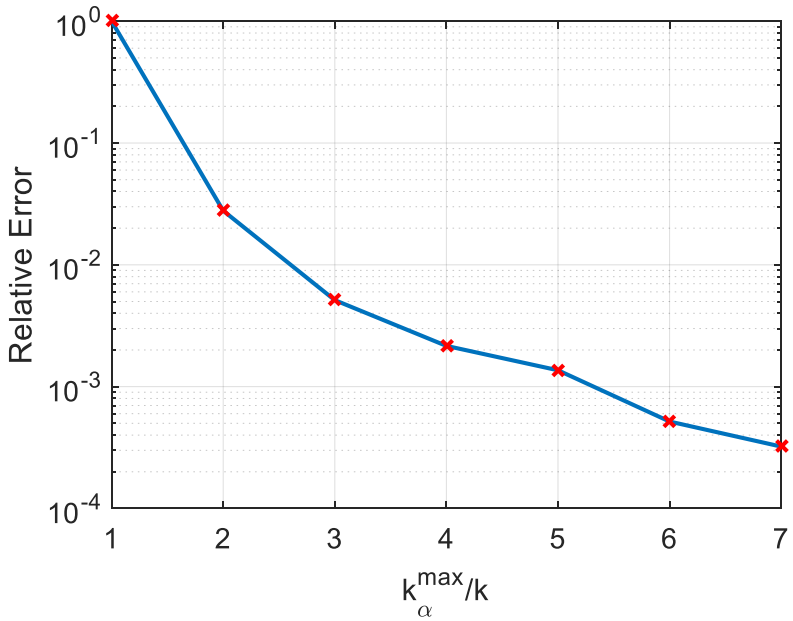

Figure VII.9. Relative error in evaluating $g_{P,B}^{S}$ as a function of $k_{\max}$ with $k_{\alpha} \leq k_{\max}$

We then use (7.6) to evaluate $g_{P}^{S}\left(k, \bar{k}_i; \bar{\rho}, \bar{\rho}''\right)$ at three different k's corresponding to $f_n =$ 0.1, 0.2, and 0.4, respectively. The spatial variation of g_{P}^{S} are plotted in Figure VII.10 as well as the number of modes included in calculating $g_{P,B}^{S}$ with $k_{\alpha} \leq k_{\max} = 8k$. As depicted, the Green's function $g_{P}^{S}\left(k, \bar{k}_i; \bar{\rho}, \bar{\rho}''\right)$ at a specific $\bar{k}_i$ varies significantly with respect to k.

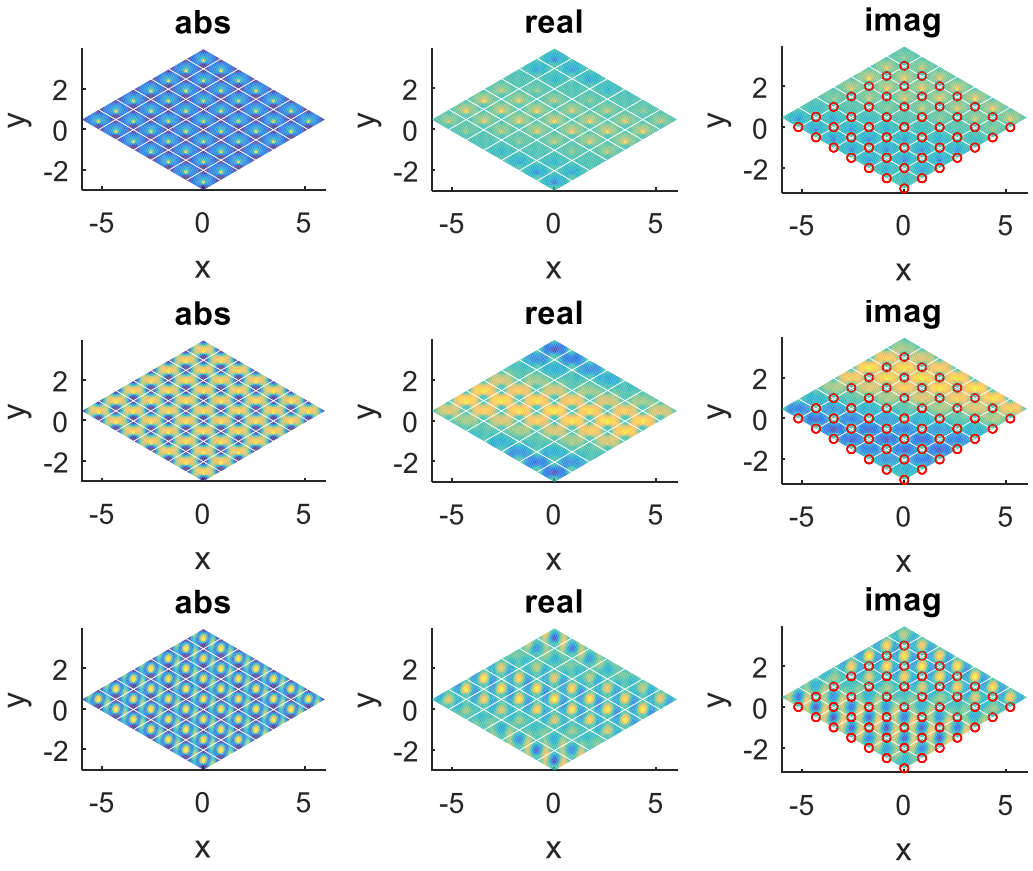

Figure VII.10. $g_P^S\left(k, \bar{k}_i; \bar{\rho}, \bar{\rho}''\right)$ at three different k's: $f_n = 0.1$ (top), 0.2 (middle), and 0.4 (bottom). From left to right are the magnitude, real, and imaginary part of the modal fields, respectively. The number of modes included in g_B^S are 12, 49, and 116, respectively.

In Figure VII.11, we plot $g_P^S\left(k, \bar{k}_i; \bar{\rho}, \bar{\rho}''\right)$ as a function of the normalized frequency f_n at field point $\bar{\rho} = \frac{7}{16}\bar{a}_1$, and source point $\bar{\rho}'' = \frac{1}{3}(\bar{a}_1 + \bar{a}_2)$. We performed the calculation for two cases: (a) lossless background with $\varepsilon_b = 8.9\varepsilon_0$, and (b) lossy background with $\varepsilon_b = 8.9(1 + 0.11i)\varepsilon_0$. In both cases we have used a real low wavenumber k_L corresponding to $f_{nL} = 0.001$. The results of (7.6) with BBGFL are compared to the results of (7.9) by solving SIE directly. For the lossless case, the results agree well except close to $f_n = 0.22$, which is close to the modal frequency of $f_n = 0.216$. The poles in the modal expansion of the Green's function causes the

suffer in accuracy. The agreement is much improved in the lossy case that by using a complex k, the resonance issue is avoided.

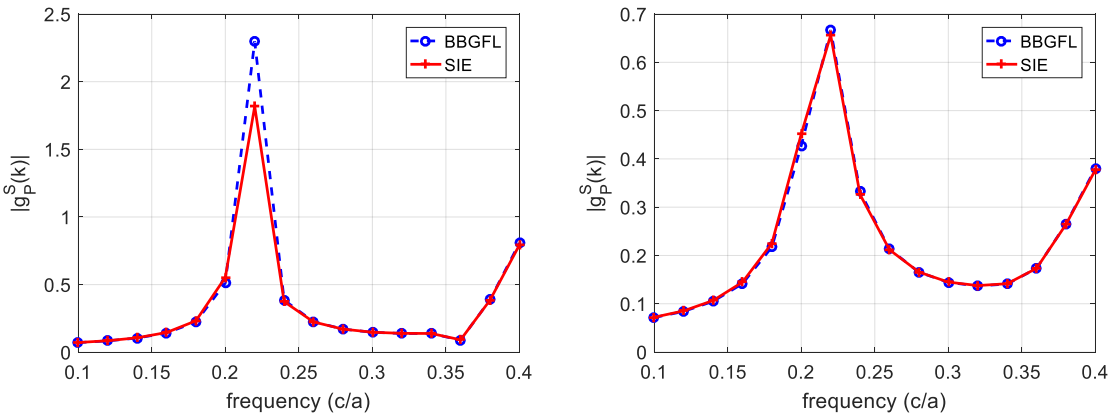

Figure VII.11. $g_P^S(k, \bar{k}_i; \bar{\rho}, \bar{\rho}'')$ as a function of the normalized frequency f_n (a) left, $\varepsilon_b = 8.9\varepsilon_0$ (b) right, $\varepsilon_b = 8.9(1 + 0.11i)\varepsilon_0$

The relative errors are plotted in Figure VII.12. We calculate the relative error both point-wisely and in the root mean square (RMS) sense. The RMSE are calculated from the field values at the 16×16 grid points as depicted in Figure VII.2 in blue circles. Both errors exhibit similar trends and magnitudes as a function of frequency. The errors are generally within 5% except close to modal frequencies. Again we see modal expansion is less accurate as frequency is close to resonance, and the lossy case suffers less from resonance.

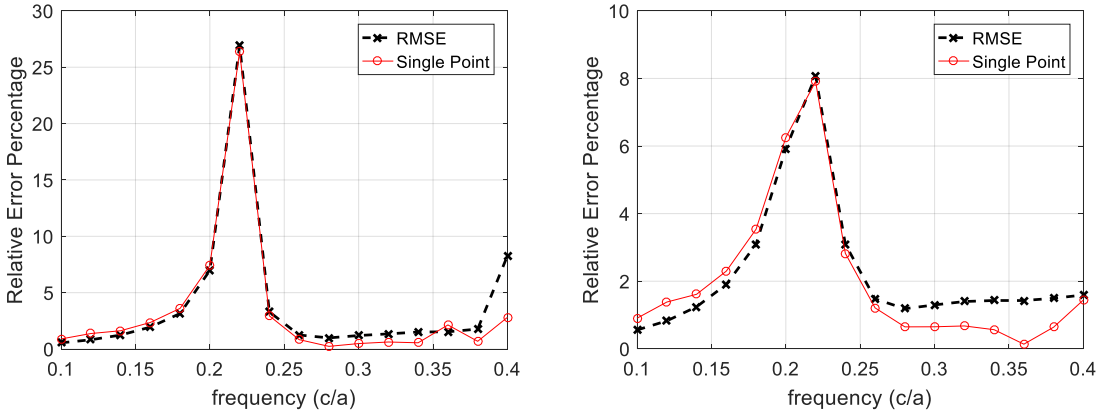

Figure VII.12. Relative error as a function of the normalized frequency in evaluating $g_P^S\left(k,\bar{k}_i;\bar{\rho},\bar{\rho}''\right)$ (a) left, $\varepsilon_b = 8.9\varepsilon_0$ (b) right, $\varepsilon_b = 8.9(1+0.11i)\varepsilon_0$.

7.4 The Array Scanning Method

7.4.1 Integration over the Brillouin zone

Our eventual goal is to find the Green's function $g^S(k;\bar{\rho},\bar{\rho}')$ due to a single point source $\delta(\bar{\rho}-\bar{\rho}')$ in the lattice including periodic scatterers. It is different from the periodic Green's function $g_P^S\left(k,\bar{k}_i;\bar{\rho},\bar{\rho}'\right)$ responding to a periodic point source array with progressive phase shift $\delta^\infty\left(\bar{\rho}-\bar{\rho}';\bar{k}_i\right)$ as given in (7.1). In this section we seek the relations between $g^S(k;\bar{\rho},\bar{\rho}')$ and $g_P^S\left(k,\bar{k}_i;\bar{\rho},\bar{\rho}'\right)$.

One can readily show that $\delta(\bar{\rho}-\bar{\rho}')$ can be represented by integrating $\delta^\infty\left(\bar{\rho}-\bar{\rho}';\bar{k}_i\right)$ over the first Brillouin zone.

$$\delta\left(\bar{\rho}-\bar{\rho}'\right)=\int_0^1 d\beta_1\int_0^1 d\beta_2\delta^\infty\left(\bar{\rho}-\bar{\rho}';\bar{k}_i\left(\beta_1,\beta_2\right)\right) \tag{7.31}$$

where $\bar{k}_i(\beta_1,\beta_2)=\beta_1\bar{b}_1+\beta_2\bar{b}_2$, and $\bar{b}_1$, $\bar{b}_2$ are the reciprocal lattice vectors, that are in-plane with the primary lattice vectors $\bar{a}_1$, $\bar{a}_2$, and satisfy $\bar{a}_i\cdot\bar{b}_j=2\pi\delta_{ij}$.

It immediately follows from (7.31) and the linearity of the system that

$$g^S\left(k;\bar{\rho},\bar{\rho}''\right)=\int_0^1 d\beta_1\int_0^1 d\beta_2 g_P^S\left(k,\bar{k}_i\left(\beta_1,\beta_2\right);\bar{\rho},\bar{\rho}''\right) \tag{7.32}$$

Now considering (7.6),

$$g^S\left(k;\bar{\rho},\bar{\rho}"\right)=\int_0^1 d\beta_1\int_0^1 d\beta_2\left[g_P^S\left(k_L,\bar{k}_i;\bar{\rho},\bar{\rho}"\right)+g_{P,B}^S\left(k,k_L,\bar{k}_i;\bar{\rho},\bar{\rho}"\right)\right] \tag{7.33}$$

Realizing the integrand is a periodic function with respect to $\bar{k}_i$, we apply the mid-point rectangular quadrature rule for its numerical evaluation [79],

$$g^S\left(k;\bar{\rho},\bar{\rho}"\right)=\left(\Delta\beta\right)^2\sum_{m=1}^{N_b}\sum_{n=1}^{N_b}\left[g_P^S\left(k_L,\bar{k}_i\left(\beta_m,\beta_n\right);\bar{\rho},\bar{\rho}"\right)+g_{P,B}^S\left(k,k_L,\bar{k}_i\left(\beta_m,\beta_n\right);\bar{\rho},\bar{\rho}"\right)\right] \tag{7.34}$$

where $\Delta\beta=1/N_b$, $\beta_n=(n-1/2)\Delta\beta$, $n=1,2,\ldots,N_b$.

7.4.2 Dealing with self-point singularity

Note that $g^S(k;\bar{\rho},\bar{\rho}')$ is singular when $\bar{\rho}=\bar{\rho}'$, and this self-point singularity is embedded in the low wave number component in (7.33). In consideration of (7.7) or (7.9), we separate $g_P^S\left(k_L,\bar{k}_i;\bar{\rho},\bar{\rho}'\right)$ into the primary contribution $g_P^0\left(k_L,\bar{k}_i;\bar{\rho},\bar{\rho}'\right)$, which is the direct incidence field, and the response contribution $g_P^R\left(k_L,\bar{k}_i;\bar{\rho},\bar{\rho}'\right)$, which is the scattering field,

$$g_P^S\left(k_L,\bar{k}_i;\bar{\rho},\bar{\rho}"\right)=g_P^0\left(k_L,\bar{k}_i;\bar{\rho},\bar{\rho}"\right)+g_P^R\left(k_L,\bar{k}_i;\bar{\rho},\bar{\rho}"\right) \tag{7.35}$$

Then

$$\begin{aligned}g^S\left(k;\bar{\rho},\bar{\rho}"\right)=&\int_0^1 d\beta_1\int_0^1 d\beta_2 g_P^0\left(k_L,\bar{k}_i;\bar{\rho},\bar{\rho}"\right)\\&+\int_0^1 d\beta_1\int_0^1 d\beta_2\left[g_P^R\left(k_L,\bar{k}_i;\bar{\rho},\bar{\rho}"\right)+g_{P,B}^S\left(k,k_L,\bar{k}_i;\bar{\rho},\bar{\rho}"\right)\right]\end{aligned} \tag{7.36}$$

Realizing that the first term is simply the free space Green's function $g^0(k_L;\bar{\rho},\bar{\rho}'')$,

$$\int_0^1 d\beta_1\int_0^1 d\beta_2 g_P^0\left(k_L,\bar{k}_i;\bar{\rho},\bar{\rho}"\right)=g^0\left(k_L;\bar{\rho},\bar{\rho}"\right)=\frac{i}{4}H_0^{(1)}\left(k_L\left|\bar{\rho}-\bar{\rho}"\right|\right) \tag{7.37}$$

Proof:

We start from the integral representation of $g^{(0)}(k;\bar{\rho},\bar{\rho}')$,

$$g^0\left(k;\bar{\rho},\bar{\rho}'\right)=\frac{1}{\left(2\pi\right)^2}\int_{-\infty}^{\infty}dk_x\int_{-\infty}^{\infty}dk_y\,\frac{\exp\left(ik_x\left(x-x'\right)+ik_y\left(y-y'\right)\right)}{k_x^2+k_y^2-k^2}$$

Let

$$\bar{k}_t=\hat{x}k_x+\hat{y}k_y$$

then

$$g^0\left(k;\bar{\rho},\bar{\rho}'\right)=\frac{1}{\left(2\pi\right)^2}\iint d\bar{k}_t\,\frac{\exp\left(i\bar{k}_t\cdot\left(\bar{\rho}-\bar{\rho}'\right)\right)}{\left|\bar{k}_t\right|^2-k^2}$$

Now let

$$\bar{k}_t=\bar{k}_i+m\bar{b}_1+n\bar{b}_2=\bar{k}_{i,mn}$$

We can transform the integral domain from the infinite $\left(k_x,k_y\right)$ plane to within the first Brillouin zone.

$$g^0\left(k;\bar{\rho},\bar{\rho}'\right)=\frac{1}{\left(2\pi\right)^2}\sum_{m,n}\iint d\bar{k}_i\,\frac{\exp\left(i\bar{k}_{i,mn}\cdot\left(\bar{\rho}-\bar{\rho}'\right)\right)}{\left|\bar{k}_{i,mn}\right|^2-k^2}=\frac{1}{\left(2\pi\right)^2}\iint d\bar{k}_i\sum_{m,n}\frac{\exp\left(i\bar{k}_{i,mn}\cdot\left(\bar{\rho}-\bar{\rho}'\right)\right)}{\left|\bar{k}_{i,mn}\right|^2-k^2}$$

Identifying

$$g_P^0\left(k;\bar{\rho},\bar{\rho}'\right)=\frac{1}{\Omega_0}\sum_{m,n}\frac{\exp\left(i\bar{k}_{i,mn}\cdot\left(\bar{\rho}-\bar{\rho}'\right)\right)}{\left|\bar{k}_{i,mn}\right|^2-k^2}$$

We immediately get

$$g^0\left(k;\bar{\rho},\bar{\rho}'\right)=\frac{\Omega_0}{\left(2\pi\right)^2}\iint d\bar{k}_i\,g_P^0\left(k,\bar{\rho};\bar{\rho}'\right)$$

With

$$\bar{k}_i = \beta_1 \bar{b}_1 + \beta_2 \bar{b}_2, 0 \le \beta_1, \beta_2 \le 1$$

Using the Jacobian,

$$\frac{\partial(k_x, k_y)}{\partial(\beta_1, \beta_2)} = \begin{vmatrix} \frac{\partial k_x}{\partial \beta_1} & \frac{\partial k_x}{\partial \beta_2} \\ \frac{\partial k_y}{\partial \beta_1} & \frac{\partial k_y}{\partial \beta_2} \end{vmatrix} = \frac{(2\pi)^2}{\Omega_0}$$

It readily follows

$$g^0(k; \bar{\rho}, \bar{\rho}') = \int_0^1 d\beta_1 \int_0^1 d\beta_2 g_P^0\left(k, \bar{k}_i; \bar{\rho}, \bar{\rho}'\right)$$

■

Then

$$g^S(k; \bar{\rho}, \bar{\rho}") = g^0(k_L; \bar{\rho}, \bar{\rho}") + \int_0^1 d\beta_1 \int_0^1 d\beta_2 \left[g_P^R\left(k_L, \bar{k}_i; \bar{\rho}, \bar{\rho}"\right) + g_{P,B}^S\left(k, k_L, \bar{k}_i; \bar{\rho}, \bar{\rho}"\right) \right]$$

(7.38)

The first term is singular at $\bar{\rho} = \bar{\rho}''$, while the second term is spatially well-behaved. The techniques to deal with the singularity of $g^0(k_L; \bar{\rho}, \bar{\rho}'')$ in the method of moments (MoM) is well developed.

Note that the integrand in (7.38) in general varies much more rapidly with $\bar{k}_i$ than the integrand of (7.33). The integrand of (7.37) cancel out with (7.38) to yield a smoother integrand of (7.33). Thus care must be taken to use (7.38) to ensure the convergence of the integral. A complex *k* helps to smooth out the integrand.

7.4.3 Illustration of results of the Green's function $g^S(k; \bar{\rho}, \bar{\rho}'')$

We now examine the performance of BBGFL when used to calculate $g^S(k; \bar{\rho}, \bar{\rho}'')$ over a wide frequency band after integrating $g_P^S\left(k, \bar{k}_i; \bar{\rho}, \bar{\rho}''\right)$ over the Brillouin zone.

In Figure VII.13, we plot the integrand of (7.32) as a function of $\bar{k}_i$. We also decompose the integrand of $g_P^S\left(k, \bar{k}_i; \bar{\rho}, \bar{\rho}''\right)$ into the primary contribution $g_P^0\left(k, \bar{k}_i; \bar{\rho}, \bar{\rho}''\right)$ and the response contribution $g_P^R\left(k, \bar{k}_i; \bar{\rho}, \bar{\rho}''\right)$, and show each parts as a function of $\bar{k}_i$. The results are evaluated at $f_n = 0.2$, $\bar{\rho}'' = \frac{1}{3}(\bar{a}_1 + \bar{a}_2)$, and $\bar{\rho} = \frac{7}{16}\bar{a}_1$. A lossless background with $\varepsilon_b = 8.9\varepsilon_0$ is assumed. It is noted that both the primary and response components change rapidly as a function of $\bar{k}_i$. The singular parts cancel each other, yielding a smooth integrand of $g_P^S\left(k, \bar{k}_i; \bar{\rho}, \bar{\rho}''\right)$ as $\bar{k}_i$ changes.

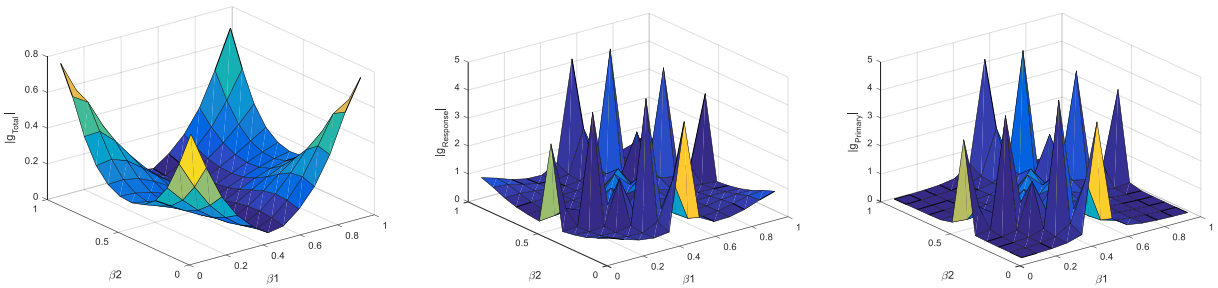

Figure VII.13. Magnitude of the integrand as a function of $\bar{k}_i$: (a) left, $g_P^S\left(k, \bar{k}_i; \bar{\rho}, \bar{\rho}''\right)$, (b) middle, $g_P^0\left(k, \bar{k}_i; \bar{\rho}, \bar{\rho}''\right)$, (c) right, $g_P^R\left(k, \bar{k}_i; \bar{\rho}, \bar{\rho}''\right)$. $\varepsilon_b = 8.9\varepsilon_0$

We should notice that $g_P^S\left(k, \bar{k}_i; \bar{\rho}, \bar{\rho}''\right)$ is smooth in this case because the chosen frequency is in the stop band of the band structure, thus no poles / modes is encountered over the entire Brillouin zone. Behavior is different in the passband. In Figure VII.14 (a), we plot the integrand of $g_P^S\left(k, \bar{k}_i; \bar{\rho}, \bar{\rho}''\right)$ at $f_n = 0.26$ with a lossless background $\varepsilon_b = 8.9\varepsilon_0$. The integrand is singular when the modes k_α hit k. In Figure VII.14 (b), the same plot is given with a lossy background $\varepsilon_b = 8.9(1 + 0.11i)\varepsilon_0$. The complex k avoids the real modes k_α, which helps to smooth out the integrand substantially.

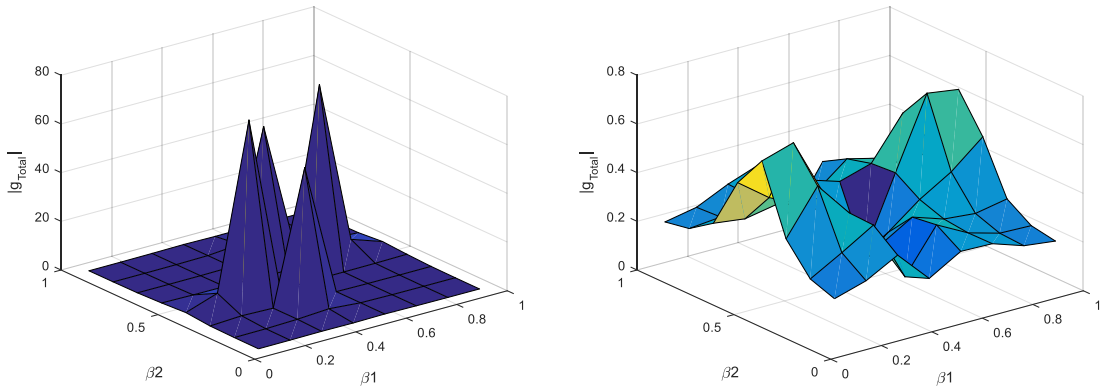

Figure VII.14. Magnitude of $g_P^S\left(k, \bar{k}_i; \bar{\rho}, \bar{\rho}''\right)$as a function of $\bar{k}_i$ at $f_n = 0.26$: (a), $\varepsilon_b = 8.9\varepsilon_0$ (b) right, $\varepsilon_b = 8.9(1 + 0.11i)\varepsilon_0$.

In Figure VII.15, we plot the spatial variation of $g^S(k; \bar{\rho}, \bar{\rho}'')$ following (7.32) using the mid-point rectangular quadrature rule. A lossless background with $\varepsilon_b = 8.9\varepsilon_0$ is assumed. To test the convergence with respect to the sampling density of $\bar{k}_i$, the relative RMSE is calculated using $N_b = 8$, and $N_b = 12$, achieving a relative error as small as $8.45 \times 10^{-6}\%$. Thus $N_b = 8$ is large enough to give accurate results of $g^S(k; \bar{\rho}, \bar{\rho}'')$.

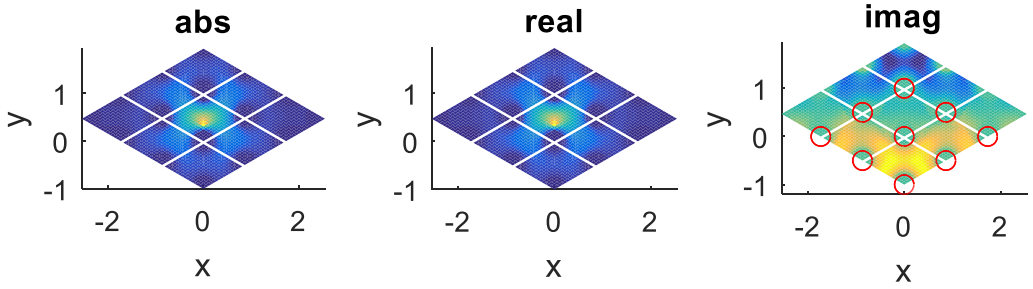

Figure VII.15. Spatial variation of $g^S(k; \bar{\rho}, \bar{\rho}'')$ following (7.32) at $f_n = 0.2$. From left to right are the magnitude, real, and imaginary part of the fields, respectively. $\varepsilon_b = 8.9\varepsilon_0$

In Figure VII.16, we again plot the spatial variations of $g^S(k; \bar{\rho}, \bar{\rho}'')$ at $f_n = 0.1$, $f_n = 0.2$, and $f_n = 0.4$, respectively. The results are now calculated following (7.33) invoking the low

wavenumber extraction technique. Note there is no requirement to keep k_L constant as we sweep $\bar{k}_i$. k_L can be chosen to facilitate the efficient normalization of modal fields as given in (7.28). To be simple, in computing these results, we have chosen a constant $f_{nL} = 0.001$ over the entire Brillouin zone. Note that the worse visual agreement in the pattern of the imaginary part when comparing Figure VII.16 (b) to Figure VII.15 is due to the fact that the imaginary part varies in a range much smaller than the real part and is close to zero. Comparing to the band diagram of the periodic structure as given in [99], it is interesting to see that the field spreads more out at $f_n = 0.4$ as it is in the passband.

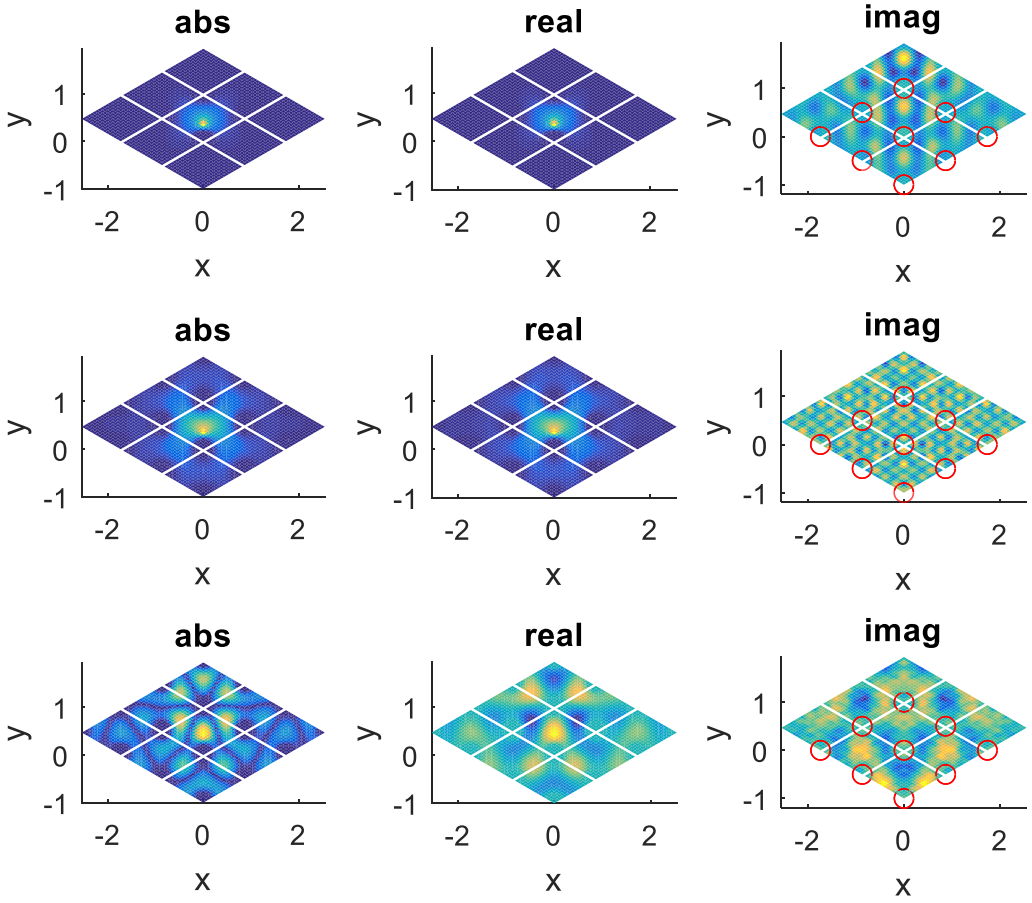

Figure VII.16. Spatial variations of $g^S(k; \bar{\rho}, \bar{\rho}'')$ following (7.33). (a) top, $f_n = 0.1$; (b) middle, $f_n = 0.2$ (c) bottom, $f_n = 0.4$. From left to right are the magnitude, real, and imaginary part of the fields, respectively. $\varepsilon_b = 8.9\varepsilon_0$.

In Figure VII.17, we plot $g^S(k;\bar{\rho},\bar{\rho}'')$ as a function of the normalized frequency. The results are again evaluated at $\bar{\rho}'' = \frac{1}{3}(\bar{a}_1 + \bar{a}_2)$, and $\bar{\rho} = \frac{7}{16}\bar{a}_1$. The values of the Green's function obtained with BBGFL as in (7.33) are compared to the results from (7.32) by solving SIEs directly. Note that other than the peak value at $f_n = 0.26$, the agreement is in general good. The oscillation of the Green's function is closely related to the band diagrams of the periodic structure. It is suppressed in the stop band below $f_n = 0.2$, and behaves more complexed beyond that. One should notice the value of $g^S(k;\bar{\rho},\bar{\rho}'')$ out of SIE is also subject to errors when entering the passband due to the poles of the integrand. But the comparison of the BBGFL solution and SIE solution is still meaningful as the same quadrature points are used in performing the $\bar{k}_i$ integral.

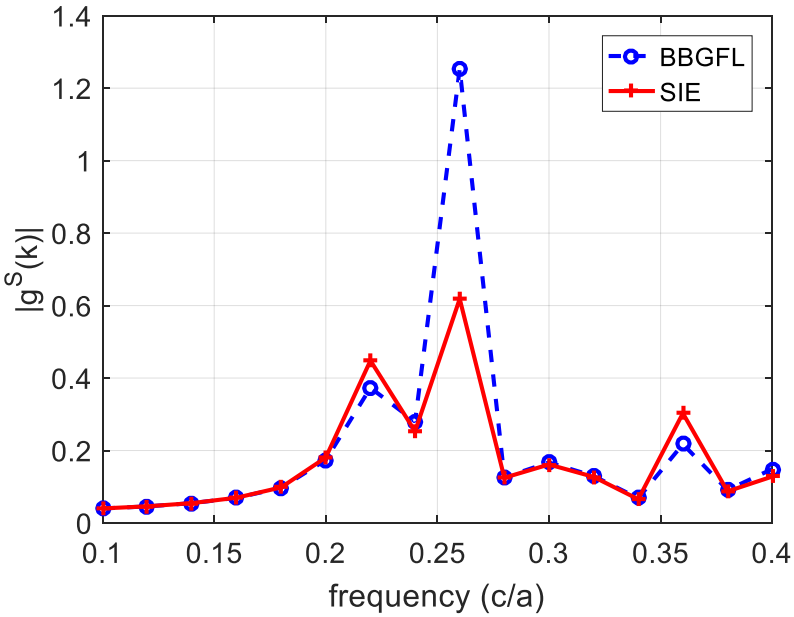

Figure VII.17. $g^S(k;\bar{\rho},\bar{\rho}'')$ as a function of the normalized frequency. $\varepsilon_b = 8.9\varepsilon_0$.

In Figure VII.18, we plot the relative error in computing $g^S(k;\bar{\rho},\bar{\rho}'')$ as a function of the normalized frequency following (7.33). The results of (7.32) are taken as benchmark. The errors

are calculated both in the RMS sense and at the single point. The trend and scale of the two error agree well. The relative error is general less than 2% at frequencies below 0.2, and becomes larger beyond 0.2. The reason for the enlarged error when the frequency enters the passband of the periodic array is due to the poles in the modal expansion.

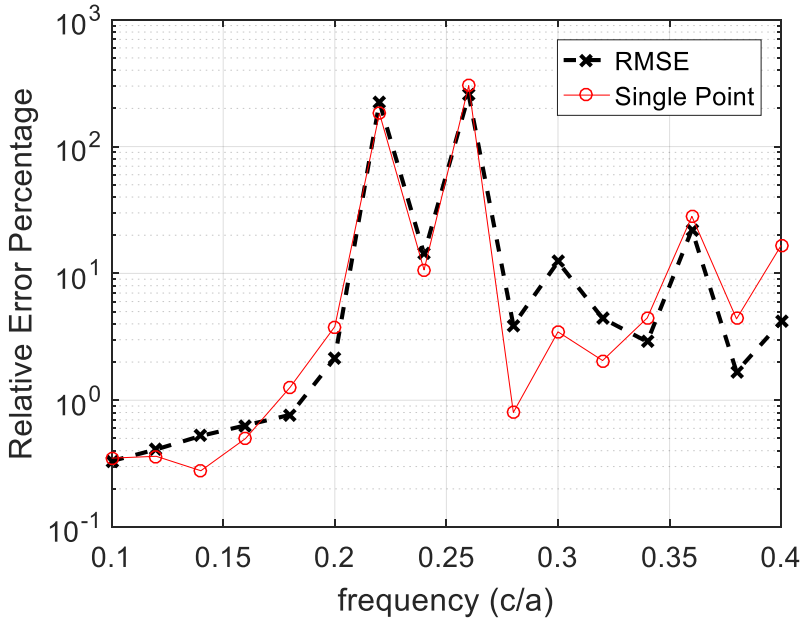

Figure VII.18. Relative error in calculating $g^S(k;\bar{\rho},\bar{\rho}'')$ as a function of the normalized frequency. $\varepsilon_b = 8.9\varepsilon_0$.

A second example with complex k

We examine a second example with a complex background permittivity of $\varepsilon_b = 8.9(1 + 0.11i)\varepsilon_0$. This will yield a complex k, and avoid the poles in the modal expansion when the frequency falls in the pass band of the periodic structure. The other parameters are kept unchanged. Note that although ε_b becomes complex, we can still apply a real k_L in the BBGFL. In Figure VII.19, we compare $g^S(k;\bar{\rho},\bar{\rho}'')$ as a function of the normalized frequency, and in Figure VII.20, we show the relative error in computing $g^S(k;\bar{\rho},\bar{\rho}'')$. Comparing with Figure VII.17 and Figure

VII.18, respectively, the errors are greatly reduced. The spatial variations of $g^S(k;\bar{\rho},\bar{\rho}'')$ are plotted in Figure VII.21, showing improved accuracy in imaginary parts. And the expansion of field in the passband of $f_n = 0.4$ is suppressed due to material loss.

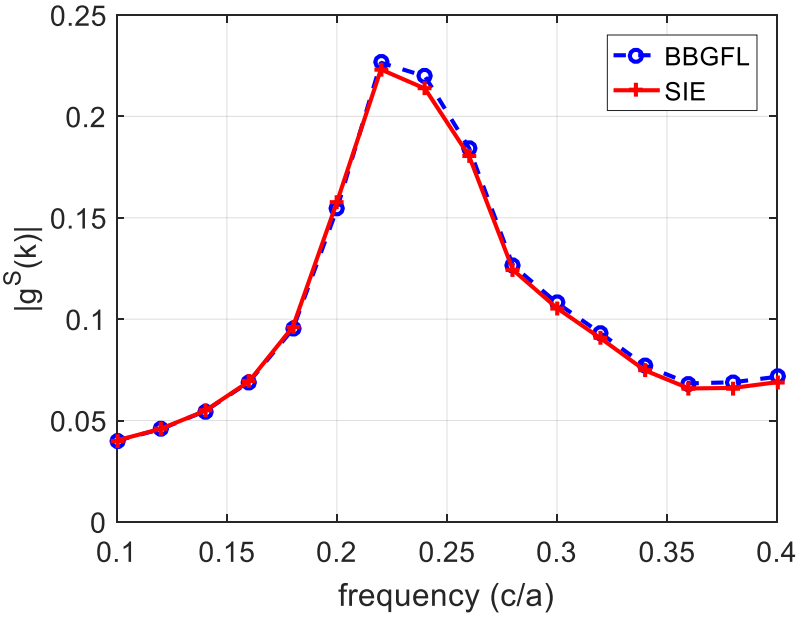

Figure VII.19. $g^S(k;\bar{\rho},\bar{\rho}'')$ as a function of the normalized frequency. $\varepsilon_b = 8.9(1+0.11i)\varepsilon_0$

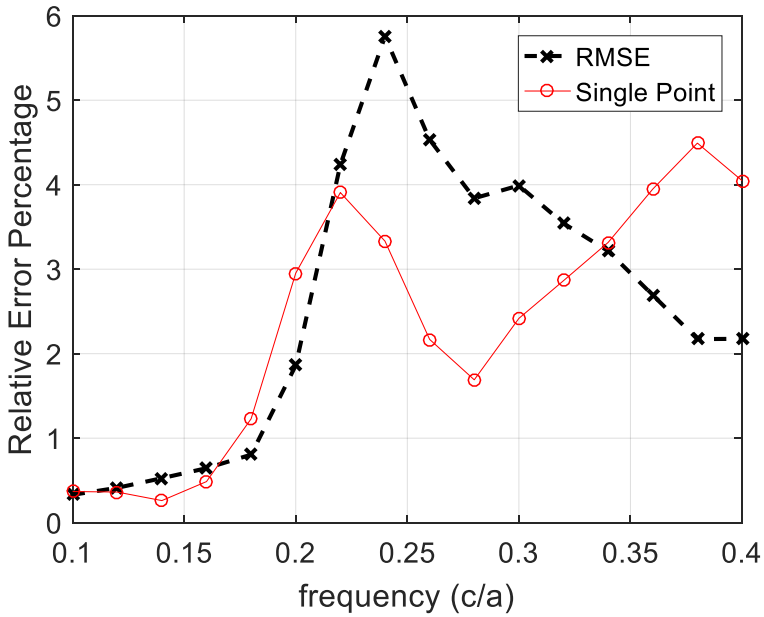

Figure VII.20. Relative error in calculating $g^S(k;\bar{\rho},\bar{\rho}'')$ as a function of the normalized frequency. $\varepsilon_b = 8.9(1+0.11i)\varepsilon_0$

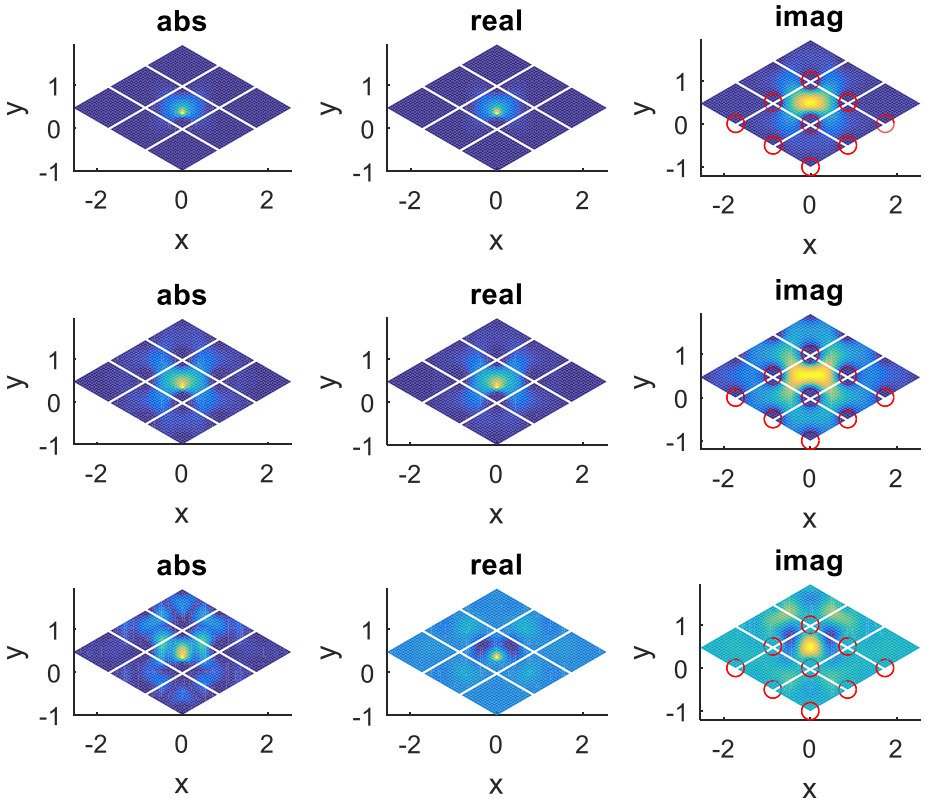

Figure VII.21. Spatial variations of $g^S(k;\bar{\rho},\bar{\rho}'')$ following (7.33). (a) top, $f_n = 0.1$; (b) middle, $f_n = 0.2$ (c) bottom, $f_n = 0.4$. From left to right are the magnitude, real, and imaginary part of the fields, respectively. $\varepsilon_b = 8.9(1 + 0.11i)\varepsilon_0$

7.5 Conclusions

In this chapter, we discussed the procedure to construct the Green's function due to a point source inside a periodic array of scatterers. The Green's function is in a form of integration over the Brillouin zone, which transforms the modes from discrete at a given $\bar{k}_i$ to a continuum over the entire Brillouin zone. By representing the periodic Green's function including the scatterers at each elementary $\bar{k}_i$ using modal expansion, and extracting out a low wavenumber component, we get a form of the Green's function that is broadband. The Green's function suffers from loss of accuracy when the wave frequency approaches the modal frequency of the periodic structure.

However, by introducing loss, the complex k bypasses the poles of Green's function, which substantially improved the accuracy in evaluating the broadband Green's function.

The Green's functions provide physical understanding of the propagation and scattering in periodic structures. We have illustrated Green's functions in the bandgap and in the passband. We are presently using this Greens function to formulate integral equations that can be used to model excitations, impurities, displacement of scatterers, disorder, defects, and finite size periodic structures. Extensions to the 3D case are also presently studied.

CHAPTER VIII

Conclusions

The thesis is focused on electromagnetic scattering theory. It has promoted the state of art knowledge in electromagnetic scattering of random media and periodic structure.

In dense volumetric random media scattering, both partially coherent method and fully coherent method are developed. In the partially coherent approach, cyclical corrections are introduced to the dense media radiative transfer (DMRT) solution, accounting for the backscattering enhancement effects, and this enables the model applicable to combined active and passive snow remote sensing, using the same set of physical parameters of snowpack. The consistent combination of information from active and passive microwave measurements, is an active and ongoing research topic that is to bring about significant improvement in the accuracy of snowpack retrieval algorithms from microwave observables.

In the fully coherent approach, Maxwell equations are solved numerically over the entire snowpack including a bottom half space, directly calculating the complex scattering matrix of the scene, including both amplitude and phase. For the first time, through efficient techniques of computational electromagnetics and the high performance parallel computing, the historically impossible problem is solved. Not only does this fundamentally new approach generates consistent active and passive results, it provides a benchmark solution to traditional approaches that involve approximations. The model predicted scattering matrix opens a new era to study polarimetric,

interferometric, and tomographic radar signatures of the snowpack in microwave remote sensing. This full wave approach is currently used to study scattering behavior of the thin snow layers on sea ice, and the model is being further developed to incorporate a rough bottom interface, such that volume scattering from ice grains and surface scattering from rough interfaces can be coherently combined.

In characterizing the microstructure of the snowpack, the bicontinuous random media is for the first time used to represent the anisotropic snowpack. The full wave solution of Maxwell's equation is used to extract the uniaxial effective permittivity of the anisotropic bicontinuous media, and to derive the co-polarization phase difference arising from an anisotropic snow layer, that is linearly proportional to the thickness of the snow layer. This new approach has much wider range of validity as compared to strong permittivity fluctuation theory and Maxwell-Garnett mixing formulae.

In layered random media scattering, both fully coherent and partially coherent models are developed for polar ice sheet emission at 0.5~2.0GHz. The models are developed to examine the effects of rapid density fluctuation in alternating the ice sheet thermal emission spectrum. The coherent model reveals distinct coherent layer effects that are not captured by traditional incoherent models when the thicknesses of the ice layers are close to wavelengths. The partially coherent model preserves the signatures of the fully coherent model but runs more efficiently and stably than the fully coherent approach. These models are currently deployed to analyze the ultra-wideband radiometry (UWBRAD) brightness temperatures collected over Greenland to derive the internal temperature profile of the ice sheet.

In electromagnetic wave propagation and scattering in periodic structure such as photonic crystals and metamaterials, we have developed a new representation the periodic Green's function

in terms of multiple band solutions with fast convergence, no singularity, and simple wavenumber dependence. These advantages are obtained by subtracting out a low wavenumber component. The low wavenumber component is related to evanescent waves and near field interactions, and is the source of poor convergence and singularity. The technique, named broadband Green's function with low wavenumber extraction (BBGFL), is used to derive band solutions of periodic scatterers in the framework of method of moments (MoM), applicable to both penetrable and non-penetrable scatterers of arbitrary shape and filling ratio. The band solution is converted into a linear eigenvalue problem with small matrix dimensions, providing all the modes simultaneously. We have further applied the technique to construct Green's functions including periodic scatterers in terms of multiple band solutions of the periodic structure. The Green's function is physically connected to the field solutions due to excitations, defects, distortions, and truncations of the periodic structure. Such Green's function, when applied to an integral equation formulation, can significantly reduce the number of unknowns in the analysis and design of periodic wave functional materials.

BIBLIOGRAPHY

[1] M. Sturm, M. Durand, D. Robinson, and M. Serreze, *Got Snow? the need to monitor earth's snow resources*, Edited by A. Gautier, Brochure printed by National Snow and Ice Data Center.

[2] M. A. Webster, I. G. Rigor, S. V. Nghiem, N. T. Kurtz, S. L. Farrell, D. K. Perovich, and M. Sturm, "Interdecadal changes in snow depth on arctic sea ice," *J. of Geophys. Res.: Oceans*, 119, 5395-5406, doi:10.1002/2014JC009985, 2014.

[3] T. P. Barnett, J. C. Adam, and D. P. Lettenmaier, "Potential impacts of a warming climate on water availability in snow-dominated regions," *Nature*, 438(7066), 303-309, doi:10.1038/nature04141, 2005.

[4] J. R. Laghari, "Melting glaciers bring energy uncertainty," *Nature, 502*(7473), pp.617-618, 2013.

[5] Board, Space Studies, *Earth science and applications from space: National imperatives for the next decade and beyond*. National Academies Press, 2007.

[6] ESA, *Report for Mission Selection: CoReH2O*, European Space Agency, Noordwijk, The Netherlands, ESA SP-1324/2 (3 volume series), 2012.

[7] S. H. Yueh, S. J. Dinardo, A. Akgiray, R.West, D.W. Cline, and K. Elder, "Airborne Ku-band polarimetric radar remote sensing of terrestrial snow cover," *IEEE Trans. Geosci. Remote. Sens.*, vol. 47, no. 10, pp. 3347–3364, Oct. 2009.

[8] J. Shi *et al*., "WCOM: The science scenario and objectives of a global water cycle observation mission," *IGARSS*, Quebec, Canada, Jul. 13–18, 2014.

[9] J. *Shi et al.*, "The Water cycle observation mission (WCOM): overview," *IGARSS*, Beijing, China, July 10-15, 2016.

[10] J. T. Pulliainen, J. Grandell and M. T. Hallikainen. "HUT snow emission model and its applicability to snow water equivalent retrieval," *IEEE. Trans. Geosci. Remote Sens.*, vol. 37 no. 3, pp. 1378-1390, 1999.

[11] J. Lemmetyinen, J. Pulliainen, A. Rees, A. Kontu, Y. Qiu and C. Derksen, "Multiple-layer adaptation of HUT snow emission model: comparison with experimental data," *IEEE Trans. Geosci. Remote Sens*., vol. 48, no. 7, pp. 2781-2794, July 2010.

[12] A. Wiesmann, and C. Mätzler, "Microwave Emission Model of Layered Snowpacks," *Remote Sensing of Environment*, vol. 70, pp307-316, 1999

[13] C. Mätzler, "HPACK, A bistatic radiative transfer model for microwave emission and backscattering of snowpacks, and validation by surface-based experiments," Inst. Appl. Phys., Univ. Bern, Bern, Switzerland, IAP-Research Report 2000-4, Jun. 2000.

[14] G. Picard, L. Brucker, A. Roy, F. Dupont, M. Fily, A. Royer and C. Harlow, "Simulation of the microwave emission of multi-layered snowpacks using the Dense Media Radiative transfer theory: the DMRT-ML model," *Geosci. Model Dev.*, 6: 1061-1078, 2013.

[15] L. Tsang, J. A. Kong and R. T. Shin, *Theory of Microwave Remote Sensing*. Wiley-Interscience, New York, 1985.

[16] L. Tsang and J. A. Kong, *Scattering of electromagnetic waves, vol. 3, Advanced Topics*, Wiley-Interscience, 2001.

[17] L. Tsang, C. T. Chen, A. T. C. Chang, J. Guo and K. H. Ding, "Dense Media Radiative Transfer Theory Based on Quasicrystalline Approximation with Application to Passive Microwave Remote Sensing of Snow," *Radio Sci.*, 35: 741-749, 2000.

[18] L. Tsang, J. Pan, D. Liang, Z. Li, D. W. Cline and Y. Tan, "Modeling active microwave remote sensing of snow using dense media radiative transfer (DMRT) theory with multiple-scattering effects," *IEEE Trans. Geosci. Remote Sens.*, vol. 45, no. 4, pp. 990-1004, Apr. 2007.

[19] K.-H. Ding; X. Xu; L. Tsang, "Electromagnetic Scattering by Bicontinuous Random Microstructures With Discrete Permittivities," *IEEE Trans. Geosci. Remote Sens.*, vol.48, no.8, pp.3139,3151, Aug. 2010.

[20] X. Xu, L. Tsang, S. Yueh,, "Electromagnetic Models of Co/Cross-polarization of Bicontinuous/DMRT in Radar Remote Sensing of Terrestrial Snow at X- and Ku-band for CoReH2O and SCLP Applications," *IEEE J. Sel. Topics Appl. Earth Obser. Remote Sens.*, vol.5, no.3, pp.1024-1032, June 2012.

[21] W. Chang, S. Tan, J. Lemmetyinen, L. Tsang, X. Xu, and S. Yueh, "Dense Media Radiative Transfer Applied To SnowScat and SnowSAR," *IEEE J. Sel. Topics Appl. Earth Obser. Remote Sens.*, vol. 7, no. 9, pp. 3811-3825, 2014.

[22] D. Liang, X. Xu, L. Tsang, K. M. Andreadis, and E. G. Josberger, "The effects of layers in dry snow on its passive microwave emissions using dense media radiative transfer theory based on the Quasicrystalline Approximation (QCA/DMRT)," *IEEE Trans. Geosci. Remote Sens.*, vol. 46, no. 11, pp. 3663-3671, Nov. 2008.

[23] S. Chandrasekhar, *Radiative Trasfer*, Dover, New York, 1960.

[24] L. Tsang, J. A. Kong and K. H. Ding, *Scattering of Electromagnetic Waves, vol. 1. Theory and Applications*. Hoboken, NJ: Wiley-interscience, 2000.

[25] M. T. Hallikainen, F. T. Ulaby, and T. E. V. Deventer, "Extinction behavior of dry snow in the 18- to 90- GHz range," *IEEE Trans. Geosci. Remote Sens.*, vol. GE-25, no. 6, pp. 737-745, 1987.

[26] L. Tsang and J. A. Kong, "Scattering of electromagnetic waves from random media with strong permittivity fluctuations," *Radio Sci.*, vol. 16, no. 3, pp. 303–320, May/Jun. 1981.

[27] A. Stogryn, "Correlation functions for random granular media in strong fluctuation theory," *IEEE Trans. Geosci. Remote Sens.*, vol. GE-22, no. 2, pp. 150–154, Mar. 1984.

[28] W. Chang, K.-H. Ding, L. Tsang and X. Xu, "Microwave scattering and medium characterization for terrestrial snow with QCA-Mie and bicontinuous models: comparison studies," *IEEE Trans. Geosci. Remote. Sens.*, vol. 54, no. 6, pp. 3637-648, Jun. 2016.

[29] L. Tsang, C. E. Mandt, and K.-H. Ding, "Monte Carlo simulations of the extinction rate of dense media with randomly distributed dielectric spheres based on solution of Maxwell's equations," *Optics Lett.*, vol. 17, no. 5, pp. 314-316, 1992.

[30] K. K. Tse, L. Tsang, C. H. Chan, K. H. Ding, and K. W. Leung, "Multiple scattering of waves by dense random distributions of sticky particles for applications in microwave scattering by terrestrial snow," *Radio Sci.*, vol. 42, 2007, RS5001.

[31] L. Tsang and A. Ishimaru, "Backscattering enhancement of random discrete scatterers," *J. Opt. Soc. Am. A*, vol. 1, no. 8, pp. 836-839, Aug. 1984.

[32] L. Tsang and A. Ishimaru, "Theory of backscattering enhancement of random discrete isotropic scatterers based on the summation of all ladder and cyclical terms," *J. Opt. Soc. Am. A*, vol. 2, no. 8, pp. 1331-1338, Aug. 1985.

[33] S. Tan, W. Chang, L. Tsang, J. Lemmetyinen, and M. Proksch, "Modeling both active and passive microwave remote sensing of snow using dense media radiative transfer (DMRT) theory with multiple scattering and backscattering enhancement," *IEEE J. Sel. Topics Applied Earth Observ. Remote Sens.*, vol. 8, no. 9, pp. 4418-4430, 2015.

[34] L. Tsang, J. A. Kong, K.-H. Ding, and C. O. Ao, *Scattering of electromagnetic waves, vol. 2, Numerical simulations*, New York: Wiley-Interscience, 2001.

[35] S. Tan, X. Xu, and L. Tsang, "A Fully Coherent Snowpack Full Wave Scattering Model Based on Numerical Simulation of Maxwell's Equation Using Bicontinuous Media and Half Space Green's Function," *IGARSS 2015*, Milan, July 2015.

[36] S. Tan, J. Zhu, L. Tsang and S. V. Nghiem, "Numerical Simulations of Maxwell's Equation in 3D (NMM3D) Applied to Active and Passive Remote Sensing of Terrestrial Snow and Snow on Sea Ice," PIERS 2016, Shanghai, Aug. 8-11, 2016.

[37] K. S. Chen, L. Tsang, K. L. Chen, T. H. Liao, and J. S. Lee (2014), "Polarimetric simulations of SAR at L-band over bare soil using scattering matrices of random rough surfaces from numerical 3D solutions of Maxwell equations," *IEEE Trans. Geosci. Remote Sens.*, vol. 52, no. 11, pp. 7048-7058.

[38] S. Tebaldini, and L. Ferro-Famil (2014), "Retrieved vertical structure consistent with snowpack hand-hardness from snow-pit measurement," ESA AlpSAR Final Report.

[39] S. Leinss, G. Parrella, and I. Hajnsek, "Snow Height Determination by Polarimetric Phase Differences in X-band SAR Data," *IEEE J. Sel. Topics Appl. Earth Obser. Remote Sens.*, vol. 7, no. 9, pp. 3794-3810, 2014.

[40] S. Leinss, A. Wiesmann, J. Lemmetyinen, and I. Hajnsek, "Snow Water Equivalent of Dry Snow Measured by Differential Interferometry," *IEEE J. Sel. Topics Appl. Earth Obser. Remote Sens.*, vol. 8, no. 8, pp. 3773-3790, 2015.

[41] S. Leinss, J. emmetyinen, A. Wiesmann, and I. Hajnsek, "Interferometric and Polarimetric Methods to Determine SWE, Fresh Snow Depth and the Anisotropy of Dry Snow,"

Geoscience and Remote Sensing Symposium (IGARSS), 2015 IEEE International, pp. 4029-1032, DOI: 10.1109/IGARSS.2015.7326709.

[42] S. Leinss, H. Löwe, M. Proksch, J. Lemmetyinen, A. Wiesmann, and I. Hajnsek, "Anisotropy of seasonal snow measured by polarimetric phase differences in radar time series," *The Cryosphere Discuss.*, 9, 6061-6123, 2015.

[43] A. Sihvola, "Mixing rules with complex dielectric coefficients," *Subsurf. Sens. Technol. Appl.*, vol. 1, no. 4, pp. 393-415, 2000.

[44] S. Tan, C. Xiong, X. Xu, and L. Tsang, "Uniaxial effective permittivity of anisotropic bicontinuous random media using NMM3D," *IEEE Geosci. Remote Sens. Lett.*, vol. 13, no. 8, pp. 1168-1172, 2016.

[45] W. C. Chew, J. A. Friedrich, and R. Geiger, "A multiple scattering solution for the effective permittivity of a sphere mixture," *IEEE Trans. Geosci. Remote Sens.*, vol. 28, no. 2, pp. 207-214, 1990.

[46] P. R. Siqueira, and K. Sarabandi, "Method of moments evaluation of the two dimensional quasi-crystalline approximation," *IEEE Trans. Ant. Prop.*, vol. 44, no. 8, pp. 1067-1077, 1996.

[47] P. R. Siqueira, and K. Sarabandi. "Determination of effective permittivity for three-dimensional random media," In *Antennas and Propagation Society International Symposium*, 1996. AP-S. Digest, vol. 3, pp. 1780-1783, IEEE, 1996.

[48] Y. H. Kerr, et al. "The SMOS mission: New tool for monitoring key elements ofthe global water cycle." *Proceedings of the IEEE*, vol. 98, no. 5, pp. 666-687, 2010.

[49] D. M. Le Vine, et al. "Aquarius: An instrument to monitor sea surface salinity from space." *IEEE Trans. Geosci. Remote Sens.*, vol. 45, no. 7, pp. 2040-2050, 2007.

[50] D. Entekhabi, et al. "The soil moisture active passive (SMAP) mission." *Proceedings of the IEEE*, vol. 98, no.5, pp. 704-716, 2010.

[51] K. Jezek, J. T. Johnson, M. R. Drinkwater, G. Macelloni, L. Tsang, M. Aksoy and M. Durand, "Radiometric Approach for Estimating Relative Changes in Intra-Glacier Average Temperature," *IEEE Trans. Geosci. Remote Sens.*, vol. 53, no. 1, pp. 134-143, Jan. 2015.

[52] M. Aksoy, J. T. Johnson, K. C. Jezek, M. Durand, M. R. Drinkwater, G. Macelloni, L. Tsang, "An examination of multi-frequency microwave radiometry for probing subsurface ice sheet temperatures," in *2014 IEEE Geoscience and Remote Sensing Symposium*, pp. 3614-3617, 2014.

[53] J. T. Johnson et al, "The ultra-wideband software-defined radiometer (UWBRAD) for ice sheet internal temperature sensing: instrument status and experiment plans," *IGARSS* 2015.

[54] G. Macelloni, M. Brogioni, S. Pettinato, R. Zasso, A. Crepaz, J. Zaccaria, B. Padovan and M. Drinkwater, "Ground-based L-band Emission Measurements at Dome-C Antarctica: The DOMEX-2 Experiment," *IEEE Trans. Geosci. Remote Sens.*, vol. 51, no. 9, pp. 4718-4730, Sep 2013

[55] M. Brogioni, G. Macelloni, F. Montomoli, and K. C. Jezek, “Simulating Multifrequency Ground-Based Radiometric Measurements at Dome C—Antarctica”, *IEEE J. Sel. Topics Appl. Earth Observ. Remote Sens.*, vol. 8, no. 9, pp. 4405-4417, 2015.

[56] L. Brucker, E. P. Dinnat, G. Picard, and N. Champollion, “Effect of Snow Surface Metamorphism on Aquarius L-Band Radiometer Observations at Dome , Antarctica,” *IEEE Trans. Geosci. Remote Sens.*, vol. 52, no. 11, pp. 7408-7417, Nov. 2014.

[57] M. Leduc-Leballeur, G. Picard, A. Mialon, L. Arnaud, E. Lefebvre, P. Possenti, and Y. Kerr, “Modeling L-band brightness temperature at Dome C in Antarctica and comparison with SMOS observations,” *IEEE Trans. Geosci. Remote Sens.*, vol. 53, no. 7, pp. 4022-4032, Feb. 2015.

[58] S. Tan, M. Aksoy, M. Brogioni, G. Macelloni, M. Durand, K. C. Jezek, T.-L. Wang, L. Tsang, J. T. Johnson, M. R. Drinkwater, and L. Brucker, “Physical models of layered polar firn brightness temperatures from 0.5 to 2 GHz,” *IEEE J. Sel. Topics Appl. Earth Obser. Remote Sens.*, vol. 8, no. 7, pp. 3681-3691, Jul. 2015.

[59] L. Tsang, T.-L. Wang, J. T. Johnson, K. C. Jezek, and S. Tan, “A partially coherent microwave emission model for polar ice sheets with density fluctuations and multilayer rough interfaces from 0.5 to 2GHz,” *Geoscience and Remote Sensing Symposium (IGARSS), 2016 IEEE International*, 2016.

[60] T.-L. Wang, L. Tsang, J. T. Johnson, K. C. Jezek, and S. Tan, “Partially coherent model for the microwave brightness temperature of layered snow firn with density variations and interface roughness,” *Geoscience and Remote Sensing Symposium (IGARSS), 2015 IEEE International*, 2015.

[61] T. Wang, L. Tsang, J. T. Johnson, and S. Tan, “Scattering and transmission of waves in multiple random rough surfaces: energy conservation studies with the second order small perturbation method,” *Progress In Electromagnetics Research*, Vol. 157, 1-20, 2016.

[62] M. Sanamzadeh, L. Tsang, J. T. Johnson, R. J. Burkholder, and S. Tan, “Scattering of electromagnetic waves from 3D multi-layer random rough surfaces based on the second order small perturbations method (SPM2): energy conservation, reflectivity and emissivity,” submitted to JOSAA, Nov. 2016.

[63] J. D. Joannopoulos, S. G. Johnson, J. N. Winn, and R. D. Meade, *Photonic crystals: molding the flow of light*, Princeton University, 2011.

[64] S. Tretyakov, Analytical modeling in applied electromagnetics, Artech House, 2003.

[65] J. B. Pendry, A. J. Holden, D. J. Robbins, an W. J. Stewart, “Magnetism from conductors and enhanced nonlinear phenomena,” *IEEE Trans. Microwave Theory Tech.*, 47 (11), 2075-2084, 1999.

[66] D. R. Smith, W. J. Padilla, D. C. Vier, S. C. Nemat-Nasser, and S. Schultz, “Composite medium with simultaneously negative permeability and permittivity,” *Physcial Review Letters*, 84 (18), 4184-4187, 2000.

[67] S. Yang, J. H. Page, Z. Liu, M. L. Cowan, C. T. Chan, and P. Sheng, “Focusing of sound in a 3D phononic crystal,” *Physical Review Letters*, 93 (2), 024301, 2004.

[68] A. B. Khanikaev, S. H. Mousavi, W.-K. Tse, M. Kargarian, A. H. MacDonald, and G. Shvets, “Photonic topological insulators,” *Nature Materials*, 12, 233-239, 2013.

[69] Z. Yang, F. Gao, X. Shi, X. Lin, Z. Gao, Y. Chong, and B. Zhang, “Topological Acoustics,” *Physical Review Letters*, 114, 114301, 2015.

[70] Z. Wang, Y. D. Chong, J. D. Joannopoulos, and M. Soljacic, “Reflection-free one-way edge modes in a gyromagnetic photonic crystal,” *Physical Review Letters*, 100, 013905, 2008.

[71] M. Silveirinha, and C. Fernandes, “Effective permittivity of metallic crystals: A periodic Green’s function formulation,” *Electromagnetics*, 23(8), 647-663, 2003.

[72] M. G. Silveirinha, “Metamaterial homogenization approach with application to the characterization of microstructured composites with negative parameters,” *Phys. Rev. B*, 75, 115104, 2007.

[73] M. G. Silveirinha, “Generalized Lorentz-Lorenz formulas for microstructured materials,” *Phys. Rev. B*, 76, 245117, 2007.

[74] T. Suzuki, and P. K. I. Yu, “Emission power of an electric dipole in the photonic band structure of the fcc lattice,” *J. Opt. Soc. Am. B*, 12(4), 570-582, 1995.

[75] C. Caloz, D. Curcio, A. Alvarez-Melcon, A. K. Skrivervik, and F. E. Gardiol, “Slot antenna on a photonic crystal substrate Green’s function study,” in *44th SPIE Annu. Terahertz Gigahertz Photon. Meeting Exhibition*, 3795, 176-187, 1999.

[76] C. Caloz, A. K. Skrivervik, and F. E. Gardiol, “An efficient method to determine Green’s functions of a two-dimensional photonic crystal excited by a line source ---- the phased-array method,” *IEEE Trans. Microwave Theory Tech.*, 50(5), 1380-1391, 2002.

[77] M. G. M.V. Silveirinha, and C. A. Fernandes, “Radiation from a short vertical dipole in a disk-type PBG material,”in *Antennas and Propagation Society International Symposium, 2003 IEEE*, 3, 990-993, 2003.

[78] F. Capolino, D. R. Jackson, and D. R. Wilton, “Fundamental properties of the field at the interface between air and a periodic artificial material excited by a line source,” *IEEE Trans. Anten. Propag.*, 53(1), 91-99, 2005.

[79] F. Capolino, D. R. Jackson, D. R. Wilton and L. B. Felsen, "Comparison of methods for calculating the field excited by a dipole near a 2-D periodic material," *IEEE Trans. Anten. Propag.*, 55(6), 1644--1655, 2007.

[80] L. Tsang, "Broadband Calculations of Band Diagrams in Periodic Structures Using the Broadband Green's Function with Low Wavenumber Extraction (BBGFL)," *Prog. Electromag. Res.*, 153, 57--68, 2015.

[81] L. Tsang and S. Tan, "Calculations of band diagrams and low frequency dispersion relations of 2D periodic dielectric scatterers using broadband Green’s function with low wavenumber extraction (BBGFL)," *Optics Express*, 24(2), 945--965, 2016.

[82] L. Tsang and S. Huang, “Broadband Green’s function with low wave number extraction for arbitrary shaped waveguide with applications to modeling of vias in finite power/ground plane,” *Prog. Eletromag. Res.*, 152, 105--125, 2015.

[83] S. Huang, and L. Tsang, “Fast electromagnetic analysis of emissions from printed circuit board using broadband Green’s function method,” *IEEE Trans. Electro. Compa.*, 58(5), 1642-1652, 2016.

[84] K.M. Ho, C.T. Chan, and C.M. Soukoulis, “Existence of a photonic gap in periodic dielectric structures,” *Physical Review Letters*, 16, 3152--3155, 1990.

[85] KM Leung and YF Liu, “Full vector wave calculation of photonic band structures in face-centered-cubic dielectric media,” *Physical Review Letters*, 65, 2646--2649, 1990.

[86] RD Mead, KD Brommer, AM Rappe, and JD Joannopoulos, “Existence of a photonic bandgap in two dimensions,” *Applied Physics Letters*, 61, 495--497, 1992.

[87] H. S. Sozuer, J. W. Haus, and R. Inguva, “Photonic bands: Convergence problems with the plane-wave method,” *Phys. Rev. B*, 45(24), 13962--13972, 1992.

[88] R. D. Meade, A. M. Rappe, K. D. Brommer, J. D. Joannopoulos, and O. L. Alerhand, “Accurate theoretical analysis of photonic band-gap materials,” *Phys. Rev. B*, 48, 8434-8437, 1993. Erratum: S. G. Johnson, ibid 55, 15942, 1997.

[89] M. Plihal, and A. A. Maradudin, “Photonic band structure of two-dimensional systems: The triangular lattice,” *Phys. Rev. B*, 44(16), 8565--8571, 1991.

[90] V. Kuzmiak, A. A. Maradudin, and F. Pincemin, “Photonic band structures of two-dimensional systems containing metallic components,” *Phys. Rev. B*, 50(23), 16835--16844, 1994.

[91] S. G. Johnson, and J. D. Joannopoulos, “Block-iterative frequency domain methods for Maxwell’s equations in a planewave basis,” *Optics Express*, 8(3), 173--190, 2001.

[92] S. Fan, PR Villeneuve, and JD Joannopoulos, “Large omnidirectional band gaps in metallodielectric photonic crystals,” *Phy. Rev. B*, 54(16), 11245--11251, 1996.

[93] A. J. Ward and J. B. Pendry, “Calculating photonic Green's function using a nonorthogonal finite-difference time-domain method,” *Phys. Rev. B*, 58(11), 7252--7259, 1998.

[94] BP Hiett, JM Generowicz, SJ Cox, M Molinari, DH Beckett, and KS Thomas, “Application of finite element methods to photonic crystal modelling,” *IEE Proc-Sci Measurement Technology*, 149(5), 293--296, 2002.

[95] M Luo, QH Liu, and Z Li, “Spectral element method for band structures of two-dimensional anisotropic photonic crystals,” *Physical Review E*, 79(2), 026705, 2009.

[96] J Korringa, “On the calculation of the energy of a Bloch wave in a metal,” *Physica*, 13(6), 392--400, 1947.

[97] W Kohn and N. Rostoker, “Solution of the Schrödinger Equation in Periodic Lattices with an Application to Metallic Lithium,” *Phys Rev.*, 94, 1111--1120, 1954.

[98] K. M. Leung, and Y. Qiu, “Multiple-scattering calculation of the two-dimensional photonic band structure,” *Physical Review B*, 48(11), 7767--7771, 1993.

[99] W. Zhang, C. T. Chan and P. Sheng, “Multiple scattering theory and its application to photonic band gap systems consisting of coated spheres,” *Optics Express*, 8(3), 203-208, 2001.

[100] S. Tan, and L. Tsang, “Green’s functions, including scatterers, for photonic crystals and metamaterials,” in preparation, Dec. 2016.

[101] T.-H. Liao, S.-B. Kim, S. Tan, L. Tsang, C. Su and T. J. Jackson, “Multiple Scattering effects with cyclical correction in active remote sensing of vegetated surface using vector radiative transfer theory,” *IEEE J. Sel. Topics Appl. Earth Observ.*, vol 9, no. 4, pp. 1414-1429, Apr. 2016.

[102] H. Rott, S. H. Yueh, D. W. Cline, C. Duguay, R. Essery, C. Haas, F. Heliere, M. Kern, G. Macelloni, E. Malnes, T. Nagler, J. Pulliainen, H. Rebhan and A. Thompson, "Cold Regions Hydrology High-Resolution Observatory for Snow and Cold Land Processes," *Proceedings of the IEEE* , vol.98, no.5, pp.752,765, May 2010.

[103] J. Lemmetyinen, A. Kontu, J. Pulliainen, A. Wiesmann, C. Werner, T. Nagler, H. Rott and M. Heidinger, *Technical Assistance for the Deployment of an X- to Ku-Band Scatterometer during the NoSREx II Experiment*, Final Report, ESA ESTEC Contract No. 22671/09/NL/JA, Dec. 2011.

[104] J. Lemmetyinen, A. Kontu, K. Rautiainen, J. Vehviläinen, J. Pulliainen, T. Nagler, F. Müller, M. Heidinger, R. Sandner, H. Rott and A. Wiesmann, *Technical Note NoSRex Consolidated Datasets*, ESA ESTEC Contract No. 22671/09/NL/JA, Nov. 2013.

[105] T. E. Durham, “An 8-40 GHz Wideband Instrument for Snow Measurements,” *Earth Science Technology Forum*, 5 pp., 2011 [Online]. Available: http://esto.nasa.gov/conferences/estf2011/papers/ Durham_ESTF2011.pdf.

[106] R. H. Lang and J. S. Sidhu, “Electromagnetic backscattering from a layer of vegetation: a discrete approach,” *IEEE Trans. Geo. Remote Sensing*, vol. GE-21, no. 1, pp. 62-71, Jan. 1983.

[107] S. Huang; L. Tsang; E. G. Njoku, and K. S. Chen, "Backscattering Coefficients, Coherent Reflectivities, and Emissivities of Randomly Rough Soil Surfaces at L-Band for SMAP Applications Based on Numerical Solutions of Maxwell Equations in Three-Dimensional Simulations," *IEEE Trans. Geosci. Remote Sens.*, vol.48, no.6, pp.2557,2568, June 2010

[108] S. Huang, L. Tsang, “Electromagnetic Scattering of Randomly Rough Soil Surfaces Based on Numerical Solutions of Maxwell Solutions of Maxwell Equations in Three-Dimensional Simulations Using a Hybrid UV/PBTG/SMCG Method,” *IEEE Trans. Geosci. Remote Sens.*, vol. 50, no. 10, pp. 4025-4035, Oct. 2012

[109] C. Fierz, R. L. Armstrong, Y. Durand, P. Etchevers, E. Greene, D. M. McClung, K. Nishimura, P. K. Satyawali and S. A. Sokratov, “*The international classification for seasonal snow on the ground*,” in “*IHP Tech. Doc. in Hydrol. Ser.*,” UNESCO-IHP, Paris, No. 83, IACS Contribution No. 1, 2009.

[110] X. Xu, L. Tsang, W. Chang, and S. Yueh, “Bicontinuous DMRT model extracted from multi-size QCA with application to terrestrial snowpack,” in *Proc. XXXIth URSI Gen. Assem. Sci. Symp. (URSI GASS’14)*, Beijing, China, Aug. 2014, pp. 1-3, doi: 10.1109/URSIGASS.2014.6929662.

[111] W. Chang, *Electromagnetic Scattering of Dense Media with Application to Active and Passive Microwave Remote Sensing of Terrestrial Snow*, Ph. D. dissertation, Department of Electrical Engineering, Univ. Washington, Seattle, WA, USA, 2014.

[112] M. A. Webster, I. G. Rigor, S. V. Nghiem, N. T. Kurtz, S. L. Farrell, D. K. Perovich, and M. Sturm, "Interdecadal changes in snow depth on Arctic sea ice," *J. Geophys. Res. Oceans*, 119, 5395-5406, doi:10.1002/2014JC009985, 2014.

[113] S. Tan, X. Xu, and L. Tsang, "Towards a Fully Coherent Snowpack Scattering Model Based on Numerical Simulation of Maxwell's Equation Using Bicontinuous Media and Half Space Green's Function," *PIERS 2015*, Prague, July 2015.

[114] S. Tan, L. Tsang, X. Xu, and K.-H. Ding, "Snowpack Characterization and Scattering Modeling Using Both DMRT and A Fully Coherent Approach," *MicroSnow2 and SnowEx Workshops*, Columbia, MD, USA, July 13-16, 2015.

[115] S. Tan, L. Tsang, X. Xu, and K.-H. Ding, "Snowpack microstructure characterization and partial coherent and fully coherent forward scattering models in microwave remote sensing," *AGU Fall Meeting*, San Francisco, Dec. 2015.

[116] S. Tan, J. Zhu, X. Xu, K.-H. Ding, and L. Tsang, "The fully and partially coherent approaches applied to snowpack remote sensing based on 3D numerical solutions of Maxwell's equations," *APS and URSI 2016*, Puerto Rico, June 26 to July 1, 2016.

[117] L. Tsang,, S. Tan, X. Xu, and K.-H. Ding, "Emission and scattering models for microwave remote sensing of snow using numerical solutions of Maxwell equations," *IGARSS 2016*, Beijing, July 2016.

[118] S. Tan, J. Zhu, L. Tsang and S. V. Nghiem, "Numerical Simulations of Maxwell's Equation in 3D (NMM3D) Applied to Active and Passive Remote Sensing of Terrestrial Snow and Snow on Sea Ice," *PIERS 2016*, Shanghai, Aug. 8-11, 2016.

[119] T. J. Cui, and W. C. Chew, "Fast Algorithm for Electromagnetic Scattering by Buried 3-D Dielectric Objects of Large Size," *IEEE Trans. Geosci. Remote Sens.*, vol. 37, no. 5, pp. 2597-2608, 1999.

[120] L. Ferro-Famil, S. Tebaldini, M. Davy, and F. Boute, "3D SAR imaging of the snowpack at X- and Ku-Band: results from the AlpSAR campaign," *EUSAR 2014*, pp. 1-4, 2014.

[121] M. Abramowitz, and A. Stegun, "Handbook of mathematical functions," *Applied mathematics series*, 55, p. 62, 1966.

[122] A. Reigber, and A. Moreira, "First demonstration of airborne SAR tomography using multibaseline L-band data," *IEEE Trans. Geosci. Remote Sens.*, vol. 38, no. 5, pp. 2142-2152, 2000.

[123] D. H. T. Minh, T. L. Toan, F. Rocca, S. Tebaldini, M. M. d'Alessandro, and L. Villard, "Relating P-band synthetic aperture radar tomography to tropical forest biomass," *IEEE Trans. Geosci. Remote Sens.*, vol. 52, no. 2, pp. 967-979, 2014.

[124] L. Ferro-Famil, S. Tebaldini, M. Davy, C. Leconte, F. Boutet, "Very high resolution three-dimensional imaing of natural environments using a tomographic ground-based SAR system," *8th European Conference on Antennas and Propagation* (EuCAP 2014), pp. 3221-3224, 2014.

[125] L. Ferro-Famil, S. Tebaldini, M. Davy, F. Boute, "3D SAR imaging of the snowpack in presence of propagation velocity changes: results from the AlpSAR campaign," *IGARSS 2014*, Quebec, Canada, 3370-3373, 2014.

[126] T. G. Yitayew, L. Ferro-Famil, T. Eltoft, "High resolution three-dimensional imaging of sea ice using ground-based tomographic SAR data," *EUSAR 2014*, pp. 1325-1328, 2014.

[127] T. G. Yitayew, L. Ferro-Famil, T. Eltoft, "3-D imaging of sea ice using ground-based tomographic SAR data and comparison of the measurements with TerraSAR-X data," *IGARSS 2014*, Quebec, Canada, 1329-1332, 2014.

[128] L. M. H. Ulander, H. Hellsten, G. Stenstrom, "Synthetic-aperture radar processing using fast factorized back-projection," *IEEE. Trans. Aerospace Electronic Systems*, vol. 39, no. 3, pp. 760-776, 2003.

[129] P. Jeong, S. Han, K. Kim, "Efficient time-domain back projection algorithm for penetration imaing radar," *Microwave Optical Technology Letters*, vol. 53, no. 10, 2406-2411, 2011.

[130] G. Zhang, and L. Tsang, "Application of angular correlation function of clutter scattering and correlation imaging in target dectection," *IEEE Trans. Geosci. Remote Sens.*, vol. 36, no. 5, pp. 1485-1493, 1998.

[131] W. C. Chew, *Waves and fields in inhomogeneous media*, New York: IEEE Press, 1995.

[132] A. Banos, *Dipole Radiation in the pressence of a conducting half-space*, Pergamon, Oxford, 1966.

[133] M. A. Taubenblatt, and K. T. Tuyen, "Calculation of light scattering from particles and structures on a surface by the coupled-dipole method," *J. Opt. Soc. Am. A*, vol. 10, no. 5, pp. 912-919, 1993.

[134] Y. Saad, and M. H. Schultz, "GMRES: A generalized minimal residual algorithm for solving nonsymmetric linear systems," *SIAM Journal on scientific and statistical computing*, *7*(3), pp.856-869, 1986.

[135] R. Schmehl, B. M. Nebeker, and E. D. Hirleman, "discrete-dipole approximation for scattering by features on surfaces by means of a two-dimensional fast Fourier transform technique," *J. Opt. Soc. Am. A*, vol. 14, no. 11, 3026-3036, 1997.

[136] M. Frigo, and S. G. Johnson, FFTW open source parallel FFT library, http://www.fftw.org/, last visit: 12/11/2015.

[137] M. Frigo, and Steven G. Johnson, "The Design and Implementation of FFTW3," *Proceedings of the IEEE*, 93 (2), 216–231, 2005.

[138] S. H. Lou, L. Tsang, C. H. Chan, and A. Ishimaru, "Application of finite element method to Monte Carlo simulations of scattering of waves by random rough surfaces with the periodic boundary condition," *Journal of Electromagnetic Waves and Applications*, vol. 5, no. 8, pp. 835-855, 1991.

[139] S. H. Lou, L. Tsang, and C. H. Chan, "Application of the finite element method to Monte Carlo simulations of scattering of waves by random rough surfaces: peetrable case," *Waves in Random Media*, vol. 1, no. 4, pp. 287-307, 1991.

[140] M. E. Veysoglu, H. A. Yueh, R. T. Shin, and J. A. Kong, "Polarimetric Passive Remote Sensing of Periodic Surfaces," *Journal of Electromagnetic Waves and Applications*, vol. 5, no. 3, pp. 267-280, 1991.

[141] S. G. Johnson, Faddeeva Package, http://ab-initio.mit.edu/wiki/index.php/Faddeeva_Package.

[142] A. Kustepeli, and A. Q. Martin, "On the slitting parameter in the Ewald method," *IEEE Trans. Microwave Guided Wave Lett.*, vol. 10, no. 5, pp. 168-170, 2000.

[143] S. Campione, and F. Capolino, "Ewald method for 3D periodic dyadic Green's functions and complex modes in composite materials made of spherical particles under the dual dipole approximation," *Radio Science*, vol. 47, RS0N06: 1-11, doi:10.1029/2012RS005031, 2012.

[144] L. Tsang, K.-H. Ding, G. Zhang, C. C. Hsu, and J. A. Kong, "Backscatterng enhancement and clustering effects of randomly distributed dielectric cylindres overlying a dielectric half-space based on Monte-Carlo simulations," *IEEE Trans. Antennas Propgat.*, vol. 43, no. 5, pp. 488-499, 1995.

[145] F. Vallese, and J. A. Kong, "Correlation function studies for snow and ice," *J. Appl. Phys.*, vol. 52, no. 8, pp. 4921-4925, 1981.

[146] C. Mätzler, "Relation between grain-size and correlation length of snow," *Journal of Glaciology*, vol. 48, no. 162, pp. 461-466, 2002.

[147] N. F. Berk, "Scattering properties of the leveled-wave model of random morphologies," *Phys. Rev. A., Gen. Phys.*, vol. 44, no. 8, pp. 5069-5079, 1991.

[148] M. C. Rechtsman, and S. Torquato, "Effective dielectric tensor for electromagnetic wave propagation in random media," *J. Appl. Phys.*, 103: 084901-1:15, 2008.

[149] H. Löwe, F. Riche, and M. Schneebeli, "A general treatment of snow microstructure exemplified by an mproved relation for thermal conductivity," *The Cryosphere*, 7: 1743-1480, 2013.

[150] H. Löwe, J. K. Spiegel, M. Schneebeli, "Interfacial and structural relaxations of snow under isothermal conditions," *J. Glaciol.*, vol. 57, no. 203, pp. 499-510, 2011.

[151] J. Van der Veen, *Fundamentals of Glacier Dynamics*. Rotterdam: A. A. Balkema, pp. 462, 1999.

[152] G. Macelloni, M. Brogioni, M. Aksoy, J. T. Johnson, K. C. Jezek and M. Drinkwater, "Understanding SMOS data in Antarctica," *IGARSS 2014*, Quebec, Canada, July 2014.

[153] H. J. Zwally, "Microwave emissivity and accumulation rate of polar firn," *J. Glaciol.*, vol. 18, no. 79, pp. 195-215, 1977.

[154] C. Mätzler and A. Wiesmann, "Extension of the Microwave Emission Model of Layered Snowpacks to Coarse-Grained Snow," *Remote Sens. Environ.*, 70:317-325, 1999

[155] L. Brucker, G. Picard, L. Arnaud, J.-M. Barnola, M. Schneebeli, H. Brunjail, E. Lefebvre and M. Fily, "Modeling time series of microwave brightness temperature at Dome C, Antarctica, using vertically resolved snow temperature and microstructure measurements," *J. Glaciology*, vol. 57, no. 201, pp. 171-182, 2011.

[156] L. Brucker, G. Picard and M. Fily, "Snow grain-size profiles deduced from microwave snow emissivities in Antarctica," *J. Glaciology*, vol. 56, no. 197, pp. 514-526, 2010.

[157] M. Brogioni, S. Pettinato, F. Montomoli and G. Macelloni, "Snow layering effects on L-band passive Measurements at Dome C-Antarctica," in *Proc. 13th Specialist Meet. Microw. Radiometry Remote Sens. Environ. (MicroRad'14)*, pp. 61-64, Pasadena, CA, USA.

[158] R. D. West, D. P. Winebrenner, L. Tsang and H. Rott, "Microwave emission from density-stratified Antarctic firn at 6 cm wavelength," *Journal of Glaciology*, vol. 42, no. 140, pp. 63-76, 1996.

[159] A. W. Bingham and M. R. Drinkwater, "Recent Changes in the Microwave Scattering Properties of the Antarctic Ice Sheet," *IEEE Trans. Geosci. Remote Sens.*, vol. 38, no. 4, pp. 1810-1820, July 2000.

[160] M. R. Drinkwater, N. Floury, M. Tedesco, "L-band ice-sheet brightness temperatures at Dome C, Antarctica: spectral emission modeling, temporal stability and impact of the ionosphere," *Annals of Glaciology* 39, pp. 391-396, 2004

[161] R. B. Alley, J. F. Bolzan and I. M. Whillans, "Polar firn densification and grain growth," *Annals of Glaciology* 3, pp. 7-11, 1982

[162] A. J. Gow, *Depth-Time-Temperature Relationships of Ice Crystal Growth in Polar Glaciers*, Research Report 300, Cold Regesions Res. Eng. Lab., Hanover, NH, USA, Oct. 1971.

[163] F. T. Ulaby, T. H. Bengal, M. C. Dobson, J. R. East, J. B. Garvin and D. L. Evans, "Microwave Dielectric Properties of Dry Rocks," *IEEE Trans. Geosci. Remote Sens.*, vol. 28, no. 3, pp. 325-336, 1990.

[164] T. Meissner, and F. Wentz, "The Complex Dielectric Constant of Pure and Sea Water from Microwave Satellite Observations," *IEEE Trans. Geosci. Remote Sens.*, vol.42, no.9, pp. 1836-1849, Sep 2004.

[165] C. Mätzler, "Microwave permittivity of dry snow," *IEEE Trans. Geosci. Remote Sens.*, vol. 34, no. 2, pp. 573-581, Mar. 1996.

[166] M. E. Tiuri, A. H. Sihvola, E. G. Nyfors and M. T. Hallikainen, "The complex dielectric constant of Snow at Microwave Frequencies," *IEEE J. Oceanic Engineering*, vol. OE 9, no. 5, pp. 377-382, Dec. 1984.

[167] C. Mätzler, "Microwave dielectric properties of ice," In *Thermal Microwave Radiation: Applications for Remote Sesning*, eds. C. Mätzler, P. Rosenkranz, A. Battaglia and J. P. Wigneron, *IET Electromagnetic Waves Series*, vol. 52, Institute of Engineering and Technology, Stevenage, U. K., p. 455-462, 2006.

[168] B. Bereiter, H. Fischer, J. Schwander, B. Stauffer and T.F. Stocker, "Diffusive equilibration of N2, O2 and CO2 mixing ratios in a 1.5 Million Years Old Ice Core," *The Cryosphere*, 8, 245–256, 2014.

[169] C. T. Swift, P. S. Hayes, J. S. Herd, W. L. Jones, and V. E. Delnore, "Airborne Microwave Measurements of the Southern Greenland Ice Sheet," *J. Geophysical Research*, vol. 90, no. B2, pp. 1983-1994, 1985.

[170] L. Tsang, S. Tan, T. Wang, J. Johnson, and K. Jezek, "A partially coherent model of layered media with random permittivities and roughness for polar ice sheet emission in UWBRAD," *MicroRad 2016*, Espoo, Finland, April 11-14, 2016.

[171] S. Tan, L. Tsang, T.-L. Wang, M. Sanamzadeh, J. T. Johonson, K. Jezek, "Modeling polar ice sheet emission from 0.5 to 2.0GHz with a partially coherent model of layered media with random permittivities and roughness," *Eastern Snow Conerfence*, Columbus, Ohio, June 2016.

[172] L. Tsang, S. Tan, H. Xu, T. Wang, M. Sanamzadeh, J. Johnson, and K. Jezek, "Effects of layered media with random permittivities and roughness on ice sheet emissions from 0.5-2.0 GHz," *PIERS 2016*, Shanghai, Aug. 8-11, 2016.

[173] K. C. Jezek, *Surface roughness measurements on the western Greenland ice sheet*, Byrd Polar Research Center Technical Report 2007-01, Byrd Polar Research Center, The Ohio State University, Columbus, OH, 20 pages, 2007.

[174] L. Tsang, T.-L. Wang, J. Johnson, K. Jezek, and S. Tan, "Modeling the Effects of Multi-layer Surface Roughness on 0.5-2 GHz Passive Microwave Observations of the Greenland and Antarctic Ice Sheets," *2015 AGU Fall Meeting. Agu*, 2015.

[175] M. Kafesaki, and CM Soukoulis, "Historical perspective and review of fundamental principles in modelling three-dimensional periodic structures with emphasis on volumetric EBGs," Chapter 8 of *Metamaterials*, ed by N Engheta and RW Ziolkowski John Wiley and Sons, 2006.

[176] Z. Liu, CT Chan, P Sheng, AL Goertzen and JH Page, "Elastic wave scattering by periodic structures of spherical objects: Theory and experiment," *Physical Review B*, 62, 2446--2457, 2000.

[177] RW Ziolkowski and M. Tanaka, "FDTD analysis of PBG waveguides, power splitters and switches," *Optical and Quantum Electronics*, 31, 843--855, 1999.

[178] J.-M. Jin and DJ Riley, *Finite Element Analysis of Antennas and Arrays*, Hoboken, Wiley, 2009.

[179] L. Tsang, and S. Huang, *Full Wave Modeling and Simulations of The Waveguide Behavior of Printed Circuit Boards Using A Broadband Green's Function Technique*, Provisional U.S. Patent No. 62/152.702 (2015).

[180] S. Huang, *Broadband Green's Function and Applications to Fast Electromagnetic Analysis of High-Speed Interconnects*. Ph.D. dissertation, Dept. Elect. Eng., Univ. Washington, Seattle, WA (2015).

[181] S. Huang, and L. Tsang, "Broadband Green's Function and Applications to Fast Electromagnetic Modeling of High Speed Interconnects," *IEEE International Symposium on Antennas and Propagation*, Vancouver, BC, Canada, 2015.

[182] P. Arcioni, M. Bozzi, M. Bressan, G. Conciauro, and L. Perregrini, "The BI-RME method: An historical overview," *2014 International Conference on Numerical Electromagnetic Modeling and Optimization for RF, Microwave, and Terahertz Applications (NEMO)*, 1--4, 2014.

[183] L. Tsang and J. A. Kong, "Multiple scattering of electromagnetic waves by random distributions of discrete scatterers with coherent potential and quantum mechanical formulism," *Journal of Applied Physics*, 51(7), 3465--3485, 1980.

[184] A. H. Sihvola, *Electromagnetic mixing formulas and applications*, IET 47, 1999.

[185] A. Ishimaru, S. W. Lee, Y. Kuga, and V. Jandhyala, "Generalized constitutive relations for metamaterials based on the quasi-static Lorentz theory,". *Antennas and Propagation, IEEE Transactions on*, 51(10), 2550--2557, 2003.

[186] J. B. Pendry, J. A. Holden, J. D. Robbins, and J. W. Stewart, "Low frequency plasmons in thin-wire structures," *J. Phys. Condensed Matter*, 10, 4785--4809, 1998.

[187] M. G. Silveirinha, and C. A. Fernandes, "Efficient calculation of the band structure of artificial materials with cylindrical metallic inclusions," *IEEE Trans. Microwave Theory Tech.*, 51(5), 1460-1466, 2003.

[188] M. G. Silveirinha, and C. A. Fernandes, "A hybrid method for the efficient calculation of the band structure of 3-D metallic crystals," *IEEE Trans. Microwave Theory Tech.*, 53(3), 889-902, 2004.

[189] M. G. Silverinha, and C. A. Fernandes, "Computation of the electromagnetic modes in two-dimensional photonic crystals: A technique to improve the convergence rate of the plane wave method," *Electromagnetics*, 26(2), 175-187, 2006.